

*Polyphosphoester colloids:
from biomedical to optical applications*

Ph.D. Thesis

Evandro M. Alexandrino





MAX-PLANCK-GESELLSCHAFT

Max-Planck-Institut
für Polymerforschung

Max Planck Institute
for Polymer Research



Dissertation

Polyphosphoester colloids: from biomedical to optical applications

Zur Erlangung des akademischen Grades

“Doktor der Naturwissenschaften”

im Promotionsfach Chemie,

eingereicht am Fachbereich

Chemie, Pharmazie und Geowissenschaften

der Johannes Gutenberg - Universität Mainz,

erstellt am

Max - Planck - Institut für Polymerforschung Mainz

von

Evandro M. Alexandrino

geboren am 09.07.1986

in Osasco, Brasilien.

Mainz, im Juli 2015



Für meine Familie.



Erklärung

Hiermit erkläre ich, dass ich diese Arbeit eigenständig und nur unter Verwendung der angegebenen Hilfsmittel angefertigt habe. Alle Stellen, die im Sinn oder Wortlaut anderen Arbeiten entnommen wurden, sind durch entsprechende Quellenangaben kenntlich gemacht.

Evandro Alexandrino

Mainz, den 24. Juli 2015

Amtierender Dekan: Prof. Dr. Dirk Schneider

Erster Gutachter: Prof. Dr. Katharina Landfester

Zweiter Gutachter: Prof. Dr. Michael Maskos

Tag der Prüfung: 24.07.2015



Abstract	1
Zusammenfassung	3
1 Preface	5
2 Fundaments	7
2.1 Principles of miniemulsion	7
2.1.1 Definitions	7
2.1.2 General mechanism	7
2.1.3 Miniemulsion/solvent-evaporation process	10
2.1.4 Miniemulsion/solvent-evaporation: morphology	11
2.1.5 Interfacial polymerization in miniemulsion	13
2.2 Polyphosphoesters	21
2.2.1 Brief history and synthesis approach	21
2.2.2 Applications	28
2.3 Methods	33
2.3.1 Dynamic light scattering (DLS)	33
2.3.2 Zeta potential	35
2.3.3 Scanning electron microscopy (SEM)	36
2.3.4 Transmission electron microscopy (TEM)	38
2.3.5 Luminescence spectroscopy	40
2.3.6 Heteronuclear multiple-bond correlation spectroscopy (HMBC)	41
2.3.7 Magic angle spinning solid state NMR spectroscopy (MAS-NMR)	41
3 Results and discussion	45
3.1 PPE nanoparticles for potential bone cancer therapy	45
3.1.1 Motivation	46
3.1.2 Experimental part	48
3.1.2.1 Materials	48
3.1.2.2 Nanoparticle preparation	48
3.1.2.3 Thermal characterization	49
3.1.2.4 Encapsulation efficiency	49

3.1.2.5 Calcium phosphate attachment studies	50
3.1.2.6 Cell viability assays	51
3.1.2.7 Interaction experiments and magic spinning angle solid state NMR measurements	52
3.1.2.8 Calcium phosphate crystallization experiments	53
3.1.3 Synthesis of PPE nanoparticles by miniemulsion/solvent-evaporation approach	53
3.1.4 Evaluation of bone adhesion	59
3.1.5 PPEs and their interaction with calcium ions	62
3.1.6 Paclitaxel loaded PPE nanoparticle synthesis	74
3.1.7 Drug encapsulation efficiency	76
3.1.8 Thermal characterization	77
3.1.9 Effect of PPE-NPs and PPE-NPs loaded with paclitaxel on <i>in vitro</i> cell viability	78
3.1.10 Calcium phosphate attachment studies of drug- loaded nanoparticles	82
3.1.11 Conclusion	83
3.2 Core and shell PPE nanocapsules for potential oxygen and temperature detection	85
3.2.1 Motivation	86
3.2.2 Experimental part	87
3.2.2.1 Materials	87
3.2.2.2 Nanodroplet and nanoparticle preparation	88
3.2.2.3 Nanocapsule preparation	88
3.2.2.4 TTA – UC measurements	89
3.2.3 Organophosphate core shell PPE colloids for TTA upconversion	91
3.2.4 Effect of emitter concentration	99
3.2.5 hbUPPE nanodroplets and core/PPE shell nanocapsules	102
3.2.6 Core/shell PPE colloids interactions with O ₂	106
3.2.7 Temperature dependent measurements	109
3.2.8 Conclusion	114

3.3 Kinetics of copper-free azide-alkyne cycloaddition polymerization (Cu-free AACP) in miniemulsion	117
3.3.1 Motivation	118
3.3.2 Experimental part	120
3.3.2.1 Materials	120
3.3.2.2 Miniemulsion polyaddition of HDDP and BAP	120
3.3.2.3 Solution polymerization of HDDP and BAP	121
3.3.2.4 <i>In-situ</i> surfactant formation in direct miniemulsion	121
3.3.2.5 2D ^1H - ^{15}N HMBC analysis	122
3.3.2.6 2D DOSY ^1H NMR analysis	122
3.3.2.7 Gel permeation chromatography (GPC) analysis	123
3.3.2.8 Statistics analysis	123
3.3.3 Kinetics evaluation: miniemulsion vs solution	123
3.3.4 Effect of the temperature	127
3.3.5 Evaluation of the method in the polymer structure features	127
3.3.6 <i>In-situ</i> surfactant formation by Cu-free azide-alkyne cycloaddition	133
3.3.7 Conclusion	136
3.4 Polyphosphoester colloids: efficiency of miniemulsion vs interfacial polycondensation	139
3.4.1 Motivation	140
3.4.2 Experimental part	141
3.4.2.1 Materials	141
3.4.2.2 Synthesis of BPA-PPE by inverse miniemulsion	141
3.4.2.3 Synthesis of BPA-PPE by interfacial polymerization	143
3.4.2.4 ^1H and $^{31}\text{P}\{\text{H}\}$ NMR analysis	143
3.4.2.5 ^1H - ^{31}P HMBC analysis	143
3.4.2.6 Size exclusion chromatography (SEC) analysis	144
3.4.3 Bisphenol A-based polyphosphate by inverse miniemulsion: miniemulsion vs classic interfacial polymerization	144

3.4.4	Morphological analysis of BPA-PPE colloids obtained by inverse miniemulsion	151
3.4.5	Conclusion	155
3.5	Stabilization of nanoparticles synthesized by miniemulsion polymerization using “green” amino-acid based surfactants	157
3.5.1	Motivation	158
3.5.2	Experimental part	158
3.5.1.1	Materials	158
3.5.1.2	Synthesis of polystyrene nanoparticles (PS-NPs)	159
3.5.1.3	Synthesis of poly(L-lactide) nanoparticles (PLLA-NPs) and polyphosphate nanoparticles (PP-NPs)	159
3.5.1.4	MTS assay for determination of cell viability	160
3.5.3	Results and discussion	161
3.5.4	Conclusion	166
4	Outlook	167
5	Appendix	169
5.1	Curriculum Vitae	169
5.2	Acknowledgements	171
6	References	172

Abstract

Polyphosphoesters (PPE) are structurally versatile and potentially biocompatible and biodegradable materials. These properties allow the development of tailored materials, suitable for different applications. The combination between these new polymers and colloidal science is a powerful tool for the development of solutions in diverse areas. This thesis covers the preparation of polyphosphoester-based nanoparticles and nanocapsules using the miniemulsion/solvent-evaporation strategy and their application in biomedical and optical fields and the study of step-growth polymerizations in inverse miniemulsion.

In a first approach, the interaction of synthetic polyphosphoesters (PPEs) with calcium ions was explored. PPE nanoparticles were prepared using the miniemulsion/solvent-evaporation strategy and evaluated in relation to their adhesion properties towards the surface of a calcium phosphate cement, usually applied for bone-replacement therapies.¹⁻³ The specificity and structural requirements for this interaction were studied with a model compound. Up to 15 wt% of a potent anti-cancer drug, paclitaxel, were encapsulated in the nanoparticles and showed highly efficiency against a bone cancer cell line (SaOs-2), providing a potential more efficient platform for the treatment of bone cancer, one of the most painful types of cancer. Toxicity tests were performed in collaboration with Dr. Sandra Ritz.

A second approach this work presents the use of polyphosphoesters and organophosphates in the development of triplet-triplet annihilation upconversion (TTA-UC) colloids. The protective properties of unsaturated PPEs and organophosphates against oxygen was applied for the development of nanoparticulate upconversion systems which presented high ratios of upconversion emission in comparison to phosphorescence, were also capable to produce upconverted photons in the presence of oxygen and showed a reproducible temperature depending efficiency. Such properties create platforms for the development of applications as bioimaging, oxygen sensing and nanothermometers.

In a third approach this thesis presents the influences of the increase of the surface area in the behavior of two types of step-growth polymerizations in inverse miniemulsion. Firstly, an azide-alkyne copper free polyaddition was evaluated and an increase of the kinetics and reduction of the formation of cycles was observed in comparison to a solution polymerization.⁴ Secondly, a PPE was used for the comparison between a classical interfacial and an inverse miniemulsion polycondensation. The reduction of deactivation reactions was

observed, resulting in slightly higher molecular weights. Such knowledge is crucial for the development of PPE nanocapsules for biomedical applications in miniemulsion.

In a last approach the results of the preparation of polyphosphate nanoparticles with amino-acid based surfactants in the collaboration work performed with Baier *et al.* are presented. The stability and cytotoxicity of three different polymer nanoparticles were compared between a classic surfactant for direct miniemulsion (sodium dodecyl sulfate, SDS) and the three amino-acid based surfactants, revealing that these surfactants can be a more environmentally friend and biodegradable alternative to SDS.

Zusammenfassung

PPE sind strukturell vielseitige und potentiell biokompatible und –abbaubare Materialien. Diese Eigenschaften erlauben die Entwicklung von maßgeschneiderten Werkstoffen für unterschiedlichste Anwendungsgebiete. Die Kombination dieser neuen Polymere mit den Kolloidwissenschaften liefert ein wirkungsvolles Instrument für die Lösung von Fragestellungen in vielen unterschiedlichen Gebieten. Diese Doktorarbeit behandelt die Herstellung von PPE-basierten Nanopartikeln und Nanokapseln mit Hilfe der Miniemulsions- und der Lösungsmittelverdampfungstechnik für biomedizinische und optische Anwendungen. Zudem behandelt sie die Stufenwachstumspolymerisation in der inversen Miniemulsion.

Als Erstes wurde die Wechselwirkung von synthetischen Polyphosphoestern mit Calciumionen untersucht. PPE Nanopartikel wurden mit Hilfe der Miniemulsion/Lösungsmittelverdampfungsmethode hergestellt. Es wurde die Adhäsionseigenschaften dieser Nanopartikel auf einer Oberfläche bestehend aus Calciumphosphatzement untersucht, da dieses Material häufig für Knochenersatztherapien verwendet wird. Die spezifischen Eigenschaften und die strukturellen Anforderungen für diese Wechselwirkung wurden an Hand einer Modellschubstanz untersucht. Dafür wurden bis zu 15 Gewichts-% eines starken Antitumormittels, Paclitaxel, in die Nanopartikel eingekapselt. Diese Nanopartikel zeigten eine hohe Effizienz gegenüber knochentumorspezifischen Zelllinien (SaOs-2). Dadurch wäre eine potentiell effizientere Behandlung dieses Tumors möglich, das eines der schmerzlichsten Krebsarten darstellt. Toxizitätstests wurden in Zusammenarbeit mit Dr. Sandra Ritz durchgeführt.

Die Anwendung von PPE und Organophosphaten für die Entwicklung von Triplett-Triplett-Annihilation Aufkonversion (TTA-UC) wird als eine zweite Herangehensweise in dieser Arbeit vorgestellt. Die schützenden Eigenschaften der ungesättigten PPE und Organophosphate gegenüber Sauerstoff wurden verwendet, um nanopartikuläre Upconversion-Systeme zu entwickeln, die hohe Anteile an Upconversion-Emission im Vergleich zur Phosphoreszenz zeigen. Diese Systeme waren auch fähig hochkonvertierte Photonen in Gegenwart von Sauerstoff zu produzieren und zeigten reproduzierbar eine temperaturabhängige Effizienz. Solche Eigenschaften können dazu dienen, eine Plattform für die Entwicklung von Bioimaging, für Sauerstoffsensoren und Nanothermometer zu schaffen.

Als dritte Herangehensweise wird in dieser Arbeit der Einfluss einer wachsenden Oberfläche in das Verhalten von zwei Arten Stufenwachstumspolymerisation in der inversen Miniemulsion gezeigt. Als erstes wurde eine kupferfreie Azid-Alkin Polyaddition untersucht. Verglichen mit einer Polymerisation in Lösung, wurde ein Anstieg der Reaktionsgeschwindigkeit und eine verminderte Bildung von zyklischen Strukturen beobachtet. Als nächstes wurde für den Vergleich der klassischen Polykondensation an der Grenzfläche und in der inversen Miniemulsion ein PPE eingesetzt. In der inversen Miniemulsion wurden eine Abnahme der Deaktivierungsschritte und daraus resultierend etwas höhere Molekulargewichte beobachtet. Eine solche Kenntnis ist äußerst wichtig für die Entwicklung von PPE Nanokapseln für biomedizinische Anwendungen mit Hilfe der Miniemulsion.

Als letztes werden die Ergebnisse der Herstellung von Polyphosphatnanopartikeln vorgestellt, die mit aminosäurebasierten Tensiden in Zusammenarbeit mit G. Baier synthetisiert wurden. Die Stabilität und Zytotoxizität von drei verschiedenen polymeren Nanopartikeln wurden untersucht. Die Nanopartikel waren entweder mit einem klassischen Tensid für die direkte Miniemulsion (Natriumdodecylsulfat (SDS)) oder drei aminosäurebasierten Tensiden hergestellt worden. Die Untersuchungen ergaben, dass die aminosäurebasierten Tenside umweltfreundlicher und biologisch besser abbaubar sind als SDS.

1 Preface

As the popular proverb says “*Good things come in small packages*”. The development of new nanomaterials and the advances performed in nanoscience in the last decades are a perfect example of such concept. The development of new nanostructures and solutions for everyday problems is a topic of constant study by diverse scientists around the world, representing one of the most emergent areas in science nowadays, and between the many materials developed an especial emphasis must be made around the development of new colloidal systems, especially polymer colloids. Colloidal system are defined in the *Gold Book* from IUPAC as a state of subdivision, where molecules or polymolecular systems are dispersed in a medium and present in at least one direction a dimension between 1 nm and 1 μm .⁵ With the use of different polymerization approaches as emulsion, miniemulsion and microemulsion polymerization as well as the combination with solvent-evaporation strategies, polymer colloids with different morphologies, as particles or capsule-like system, and various properties have been prepared, offering a versatile platform for the development of new solutions in crucial fields, as healthcare and medicine, energy or agriculture for example, which, in combination with polymer chemistry, provides the tools for the preparation of the so-called smart systems, materials which can show higher efficiency in their application and are capable to answer to certain situations without the need of further human action.

In order to develop such “*smart*” solutions, new materials must be developed. One of the biggest scientists of the 20th century, Albert Einstein, once said “*Look deep into nature, and then you will understand everything better*”.⁶ The development of many new materials has been inspired in examples taken from natural systems and the simple observation of the living systems reveals that nature has chosen phosphate esters as the basis for life. Westheimer⁷ and more recently Warshel *et al.*⁸ reviewed the role of phosphate esters in the development of life, concluding that the polyvalence of the phosphorus center and the versatility to be degraded through different mechanisms other than nucleophilic attacks were decisive in the choice of these materials by nature. Besides the immensurable value of such phosphates in the formation of essential organic molecules as DNA and RNA, phosphate anions also have also a very important role in the development of life: hydroxyapatite, the main inorganic component in human bone, is a calcium phosphate mineral. Inspired by such properties, a class of synthetic polymers called polyphosphoesters was developed, which can provide at the same time structural versatility and potential

biodegradability and biocompatibility. Polyphosphoesters are therefore a valuable class of polymers for the development of new biomedical solutions, especially in the development of solutions for bone related diseases, as osteoporosis and bone cancer. In bone cancer tumors that have metastasized to bone are a great risk and can cause pathological bone fractures, pain, hypercalcaemia and spinal cord and nerve-compression syndromes.⁹ Bone metastases are normally a consequence of other cancers complications, principally breast and prostate cancer, reaching 65-80% of the patients of these types of cancer.⁹ The usual drugs used in the specific treatment of bone cancer, as for example bisphosphonates, still presents drawbacks as the fact that 30-50% of the patients present new bone metastases, skeletal complications and disease progression.⁹ Therefore, the development of new strategies is needed and the use of colloidal science for the development of more efficient systems in the treatment of cancer is an emergent topic, with potential for both diagnostics and treatment of different types of cancer.¹⁰ Thus, in this work, the potential of polyphosphoesters in the development of new strategies for bone cancer therapy was explored. The synthesis of new polyphosphoesters have been investigated by our group during the last years, producing a large library of new materials with variable properties, which could be further applied in the preparation of colloidal systems.^{2, 3, 11-16} This work explores primarily the interaction of the new synthetic polyphosphoesters with calcium-containing surfaces and the development of a new strategy for bone cancer treatment. In a second approach, the structural versatility of the polyphosphoesters synthesized and of the miniemulsion/solvent-evaporation approach was used in the development of photon upconversion systems, which presents potential applications in optical and energy fields, as well as in diagnostics strategies. In a third approach, an inverse miniemulsion was used in the preparation of polyphosphate colloids and the advantages concerning the minimization of the surface area, based in previous studies performed with an azide-alkyne and copper-free reaction in an inverse miniemulsion polymerization system, in comparison to a classical interfacial polymerization approach were compared.

2 Fundamentals

2.1 Principles of miniemulsion

This section describes the main principles of miniemulsion, covering the basic parameters involved in the so called miniemulsion/solvent-evaporation method for the preparation of stable nanoparticle and nanocapsule dispersions and the use of the miniemulsion technique for interfacial polymerizations.

2.1.1 Definitions

Accordingly to the IUPAC recommendation, miniemulsions (or sometimes also called nanoemulsions) are defined as emulsions, i.e. systems formed by one disperse and one continuous phase, with the dispersed phase having diameters between 50 nm and 1 μm .¹⁷ The systems are classified according to the composition in direct (oil-in-water) or inverse (water-in-oil) miniemulsions.¹⁸ Miniemulsions are kinetically stable systems, this means they are stabilized against coalescence and against diffusion degradation (Ostwald ripening).¹⁷⁻¹⁹ For stabilization against coalescence, the use of surfactants is essential. Ionic (anionic, cationic or zwitterionic) and non-ionic (mostly polymeric) surfactants can be used for the stabilization of different miniemulsions.¹⁸ The protection against diffusion destabilization is performed with the use of substances that are highly insoluble in the continuous phase.^{17, 18} These substances are called hydrophobes (direct miniemulsions) or lipophobes (inverse miniemulsions).¹⁸

2.1.2 General mechanism

A mechanical emulsification process starts with a pre-emulsification step, where the initial two phases and additives are mixed, generating droplets with a large size distribution which are then stabilized by surfactants.¹⁸ Depending on the system and type of device used, the size of droplets in the pre-emulsified system is found between 1-20 μm .²⁰ Diverse methods can be used for the formation of a miniemulsion system. Early methods as stirring or ultraturrax do not generated usually enough energy for the formation of small and fine distributed droplets dispersions.^{18, 21} Higher energy than the surface energy $\gamma\Delta A$ is necessary

to transform larger droplets in smaller ones.¹⁸ Nowadays, for bench scale experiments the main source of energy for the formation of stable and fine distributed miniemulsions systems is ultrasonication.¹⁸ Ultrasound waves between 20-100 kHz have the ability to produce chemical and physical transformations.²⁰ The vibration of a planar surface can generate longitudinal waves, which can propagate through the liquid medium and induce motion of the droplets through compressions and rarefactions under fluctuating pressure, resulting in the so called acoustic cavitation phenomena.^{20, 22} Li and Fogler^{23, 24} described the phenomena of the acoustic waves in the emulsification process as phenomena comprised by two steps. Firstly, dispersed phase droplets or gas bubbles should be incorporated to the continuous phase under the influence of Rayleigh-Taylor instability, which represents the acceleration of one fluid into another promoted by ultrasonic waves at the interface.²⁵ In a second step, larger droplets were disrupted into smaller ones through the cavitation process, which generates a series of effects as shock waves, micro-jets, turbulence and shear forces that contribute to the formation of the final miniemulsion.²⁰ The general steps for the formation of a miniemulsion through the acoustic cavitation phenomena are represented in Figure 2.1 – 1.²⁶

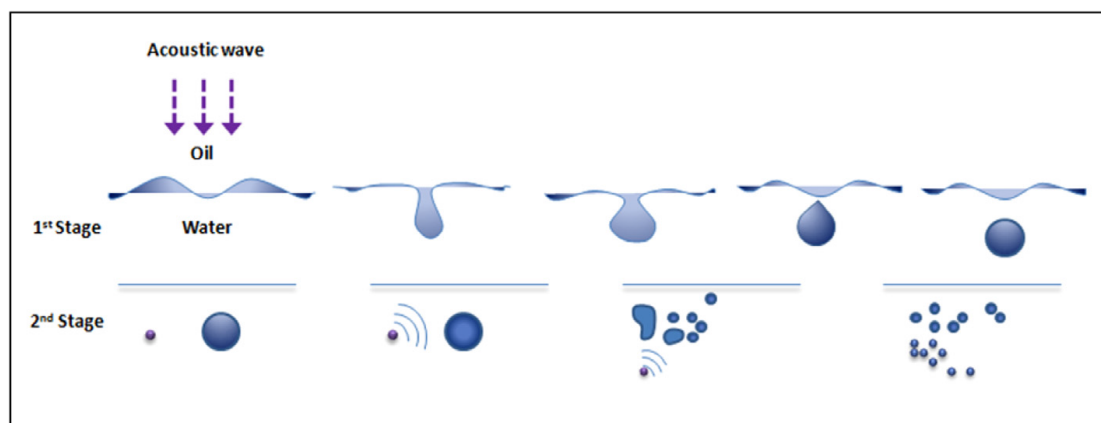


Fig. 2.1 – 1 Schematic representation of an acoustic cavitation mechanism in the formation of a miniemulsion system (Reprinted from Publication *Ultrason. Sonochem.*, 21(6), Sivakumar M., Tang S.Y., Tan K.W., Cavitation technology - a greener processing technique for the generation of pharmaceutical nanoemulsions, 2069-2083, Copyright © 2014, with permission from Elsevier).²⁶

Miniemulsions are metastable systems. Surfactants and an osmotic pressure agent (hydro- or lipophobes) and a high amount of energy are crucial elements in the formation stable systems for longer periods of time. The formation of a miniemulsion system and the influence of the previous parameters can be understood based on the thermodynamic

involved in the mixture of oil and water.²⁶ Gibbs free energy, ΔG , for a two components system can be expressed as

$$\Delta G = \mu_2 - \mu_1 \quad (1)$$

where μ_2 and μ_1 are the chemical potentials of states 1 and 2. If $\Delta G > 0$, the mixture is thermodynamically impossible; for $\Delta G = 0$ the two components are in thermodynamic equilibrium; and if $\Delta G < 0$ the system transforms spontaneously from a two component to a emulsion system. The configurational entropy change in the mixture process, ΔS_{conf} , can be described as

$$\Delta S_{conf} = -nk_B \left[\ln \phi + \left\{ \frac{(1 - \phi)}{\phi} \right\} \ln(1 - \phi) \right] \quad (2)$$

here, n represents the number of droplets of the dispersed phase, k_B is the Boltzmann constant and ϕ is the disperse phase volume fraction. Through the combination of equations (1) and (2), the Gibbs free energy can be described as

$$\Delta G = \gamma \Delta A - T \Delta S_{conf} \quad (3)$$

with the free energy for the formation of the new interface is represented by the surface energy $\gamma \Delta A$. In order to obtain $\Delta G < 0$, $\gamma \Delta A$ must be much lower than $T \Delta S_{conf}$ and surfactants act here to lower the interfacial tension values. Nevertheless, the formation of a miniemulsion is still not a spontaneous process and high energy is needed to form the small droplets. This energy can be represented by the Laplace pressure,²⁷ which relates the pressure difference between two phases and the curvature of the surface:

$$\Delta P = \gamma \left(\frac{1}{R_1} + \frac{1}{R_2} \right) = \frac{\gamma}{2R} \quad (4)$$

Equation (4) can be reduced for spherical droplets where $R_1 = R_2$. The energy necessary to create a miniemulsion must surpass the Laplace pressure and ultrasonication or high pressure homogenization are the most efficient methods. The final size and size distribution of the obtained droplets in the miniemulsion depends on the shear rate and emulsion rheology, which will vary depending on the ultrasonication conditions, process parameters and the system physicochemical properties.²⁰

After the formation of the droplets, another parameter can affect the stability of the formed miniemulsion: Ostwald ripening. In general, Ostwald ripening describes the growth of larger droplets at the cost of the consumption of smaller ones.²⁷ Ostwald ripening is a consequence of the higher surface energy, and hence high Gibbs free energy, of smaller droplets in comparison to bigger ones. The Ostwald ripening can be counterbalanced with the use of highly hydrophobic or lipophobic molecules, depending on the type of system, inside of the droplets forming the disperse phase. A low content of a homogeneously distributed hydro-/lipophobe in the droplets, which can hardly diffuse through the continuous phase and exchange between the droplets, generates an increase in the osmotic pressure, $\Pi_{osm} = RTc/M$, counterbalancing partially and generating a final state of equal pressure inside of the droplets. Thus, a final steady-state miniemulsion is obtained.¹⁸

2.1.3 Miniemulsion/solvent-evaporation process

The preparation of nanoparticles and nanocapsules starting from preformed polymers is the combination between the miniemulsion and the emulsion solvent-evaporation techniques. The emulsion solvent-evaporation technique was developed by Burton and O'Farrel in the end of the 1970's.²⁸ In this method, a polymer or mixture of polymers and other additives is initially diluted in a suitable solvent, forming a homogeneous phase which is next dispersed in a continuous phase containing a surfactant to form stable emulsions. The solvent is afterwards evaporated through heating or application of low vacuum, resulting in a stable latex.²⁹ This process can be easily combined with the miniemulsion technique, especially with direct miniemulsions as depicted in Figure 2.1 – 2.

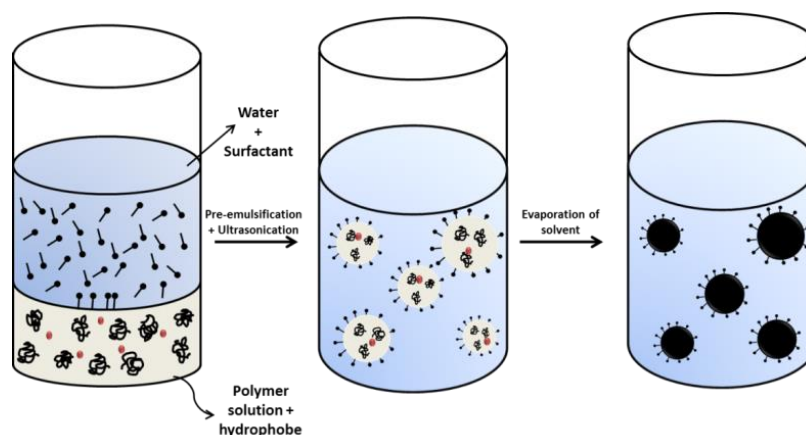


Fig. 2.1 – 2 General scheme of the miniemulsion/solvent-evaporation technique.

During the slow evaporation of the emulsified droplets with the polymer dissolved, a precipitation process of the polymer starts by nucleation at the interfacial region of the droplets.³⁰ The solvent evaporation rate depends on the temperature and solubility of it in the continuous phase.²⁹ The continuous phase is usually saturated with the solvent of the dispersed phase and the diffusion of the solvent in the continuous phase is normally faster than the evaporation kinetics, making the chemical nature of the solvent and the continuous phase crucial in the hardening process.²⁹ The evaporation process and hardening of the particles is one of the processes that will influence the size and size distribution of the final dispersion. The particle size is intimately linked to the size of the droplet which it originated from, and therefore all the parameters discussed about the stability of a miniemulsion system in section 2.1.2 will affect the final dispersion obtained. The evaporation process is relatively slow and coalescence can result in broadening of the size distribution. However, Staff *et al.*³¹ showed recently with dual color cross-correlation fluorescence spectroscopy that in systems with efficient stabilization, coalescence during the evaporation process could be considered to play a minor role.

2.1.4 Miniemulsion/solvent-evaporation: morphology

The miniemulsion/solvent-evaporation technique attracts great attention in the development of nanoparticles and nanocapsules for diverse fields, using a large library of functional polymers, as for example biodegradable polymers^{1,32-34}, electrical semi-conductive polymers,³⁵ stimuli-responsive polymers³⁶ etc. The control of the morphology is crucial to obtain materials suitable for the desired applications. The pioneer work of Torza and Mason described the thermodynamically stable morphologies, which can be possibly obtained when three immiscible liquids are mixed.³⁷ The authors described the conditions to the capsule morphology formation, where two of the immiscible liquids are components of the disperse phase, using the spreading coefficient S_i , defined as

$$S_i = \gamma_{jk} - (\gamma_{ij} - \gamma_{ik}) \quad (5)$$

which, as represented in equation (5), is defined as the interfacial tension (γ) between two liquids for the three liquids i , j and k . Figure 2.1 – 3³⁸ shows the scenarios predictable for a system consisting of three phases 1, 2 and 3. According with the signals of the coefficients S_1, S_2 and S_3 the following situations can possibly be obtained: a singular and completely

encapsulated system (A); multiple occluded cores (B); partially engulfed systems (C) and completely non-encapsulated system (D).

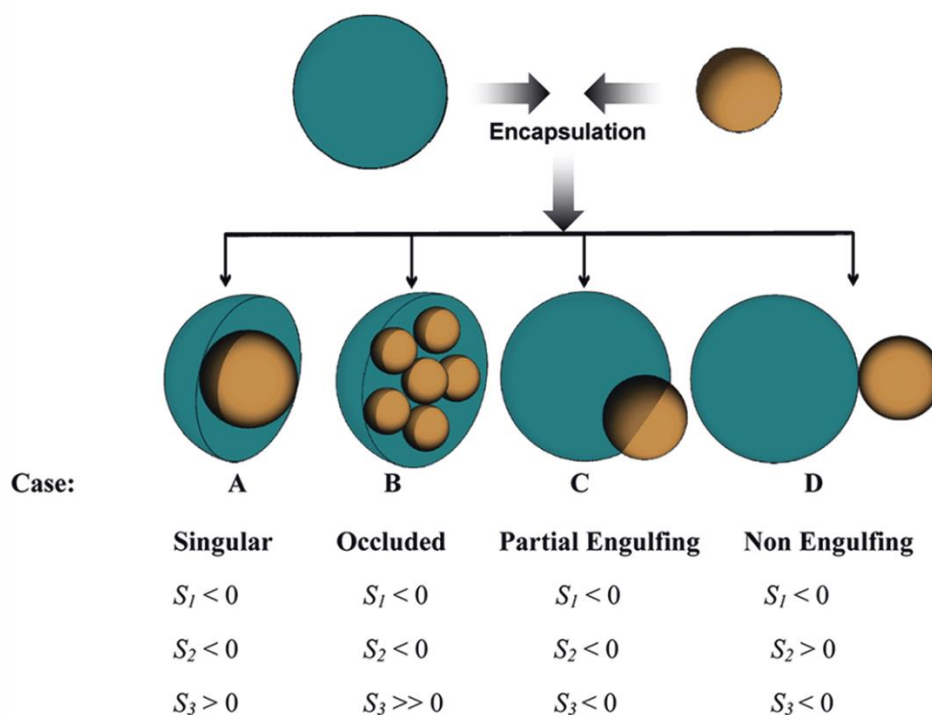


Fig. 2.1 – 3 The four possible morphologies observed at systems composed by three immiscible liquids. The two droplets (green and yellow) represent the two immiscible liquids compounding the disperse phase, with the third immiscible liquid as continuous phase. In the miniemulsion/solvent-evaporation technique the two immiscible disperse liquids are initially dissolved in a common solvent and during the evaporation process the phase separation occur, producing one of the four scenarios (Adapted with permission from Trongsatitkul T., Budhlall, Multicore-shell PNIPAm-co-PEGMA microcapsules for cell encapsulation, *Langmuir*, 27, 2011, 13468-13480. Copyright © 2011 American Chemical Society).³⁸

Therefore, the final morphology is a process determined by thermodynamic parameters of the system. The final morphology obtained should correspond to the lowest free Gibbs enthalpy (G_S):²⁹

$$G_S = \sum_{i,j}^n \gamma_{ij} A_{ij} \quad (6)$$

composed by the surface tension (γ_{ij}) and the interfacial area (A_{ij}) between the phases i and j . Surfactant and ratio between the two phases are the two parameters with highest influence in the final morphology. Nevertheless, during the evaporation process it is possible that G_S is not minimized and in this situation the final morphology is a metastable state, kinetically stabilized, but not thermodynamically.²⁹ In this scenario, parameters involving the mobility of the components of the system, as crystallinity and viscosity, which can influence severely the final morphology.³⁹⁻⁴²

Among the four different morphologies, the capsule morphology is of highest interest. The capsule morphology in polymeric nanocapsules is formed by a liquid core, which can be or not reactive, and a polymeric material as the shell and the engineering of the systems can create application in the most varied fields, from biomedical to optical areas. Zhao and Fickert^{43, 44} have used the miniemulsion/solvent-evaporation approach in the development of nanocapsules containing encapsulated self-healing agents, as monomers and catalysts, which could not be encapsulated by other means as radical polymerization reaction due to their reactivity. More recently, Zhao⁴⁵ presented a similar approach for the encapsulation of functionalized polymers for self-healing purposes. Wohnhaas *et al.*⁴⁶ used the miniemulsion/solvent-evaporation technique for the development of nanocapsules systems for bioimaging, through the encapsulation of an upconversion dye system. The encapsulation allowed the use of the upconversion effect in aqueous media with high efficiency.

This thesis uses the miniemulsion/solvent-evaporation technique for two different strategies: the development nanoparticles systems as nanocarriers of anti-cancer drug, aiming especially new bone cancer therapies; and the development of fully biodegradable nanocapsules system, containing an encapsulated upconversion system, for potential oxygen and temperature sensors. The development and characterization of these systems is presented in the following chapters.

2.1.5 Interfacial polymerization in miniemulsion

The use of the interface as shortcut for production of new molecules and macromolecules is a classical topic in chemistry, with its starting point in the early works of Schotten⁴⁷ and Baumann.⁴⁸ Applications of liquid-liquid interfacial approaches are found in the most varied fields including electrochemistry, drug and gene delivery, membranes and

biocatalysis.^{49, 50} Between the numerous possible applications, the use of the interfacial polymerization (mostly polycondensation) in combination with micro- and miniemulsions is a valuable tool in the preparation of nanoparticles, aiming the encapsulation of different materials.

In the classical interfacial polymerization two immiscible solvents containing the monomers, initiator and/or catalysts are mixed, and may or may not be submitted to agitation to increase the contact between the two phases.⁵¹ Moreover, to such systems may be added additives called phase-transfer catalysts (PTC), molecules that help in the migration of the monomers between both phases. Classic PTC molecules are quaternary ammonium salts and crown ethers.⁵¹ Micro- and miniemulsions are excellent alternatives to the classical interfacial polymerization approach, due to the special chemical features of such systems and the possibility to produce unique morphologies and applications. Such systems present a series of structural and compositional similarities, but there are still important differences.⁵² Both systems are basically formed by an oil phase, an aqueous phase and surfactant. The droplets, in most of the cases, can present a radius $r < 100$ nm. Nevertheless, one of the most important differences between both systems is found in their stability: while microemulsions are defined as thermodynamically stable systems, containing a high amount of surfactant and possibly a co-surfactant in their formulation, miniemulsions are kinetically stable systems, prepared with the use of lower amount of surfactant and the application of a high amount of mechanical energy.⁵² In this work, miniemulsion systems were the focus for the preparation of nanocapsules and understanding of the influence of the surface area in polymerization features as the polymer structure, molecular weight and end groups. The use of the miniemulsion in combination with varied polymerization techniques is summarized below.

Polycondensation and polyaddition in miniemulsion

Step-growth polymerization is one of the most applied approaches in the preparation of micro- and nanocapsules and its usefulness for the development of encapsulated systems is well known since the early works of Chang⁵³ for encapsulation of aqueous solutions of proteins within polymeric shells. Miniemulsion has been used in diverse works in the development of nanocapsules, with both inverse and direct miniemulsion systems, and step-growth reactions have been used in the preparation of linear as well as cross-linked polymeric films at the interfacial region. Based on this strategy, the chemistry of polyurethanes and polyureas stands out. Crespy *et al.*⁵⁴ produced a

systematic study of the synthesis of polyurea, polythiourea and polyurethane nanocapsules by interfacial polycondensation and crosslinking reactions using an inverse miniemulsion system to produce hollow nanocapsules. The authors were able to show how the nature of the monomers and the continuous phase could influence strongly the formation and morphology of the capsules. Besides, with control of the amount of the monomer in the disperse phase (in the case diethylenetriamine) the wall thickness could also be controlled. Gaudin and Sintés-Zydowicz⁵⁵ studied the effect of the droplet size in the molecular and thermal properties in polymer shells of poly(urethane-urea) nanocapsules. The authors used a direct miniemulsion approach and compared the properties of the formed membranes at droplets of 70 or 200 nm, concluding that no influence in the final chemical properties of the shell was observed, obtaining polymers in both case with molar mass around 2000 g mol^{-1} due to the inevitable hydrolysis of the diisocyanate monomer. The authors compared in this work two samples with relatively small mean diameter difference and the size distribution of miniemulsions could make the influence of the size in both systems to be even smaller. Together with the fact that a direct miniemulsion was used, where the high water concentration could increase the ratio of hydrolysis, make the conclusion that the size of droplets does not affects the polycondensation reaction a matter still open for further discussions. The kinetics of the shell formation by interfacial polycondensation has also been discussed in the literature. Zhang *et al.*⁵⁶ evaluated the kinetics and modeled the formation of waterborne polyurethanes shells in direct miniemulsion system, relating diffusion processes through the formed polymer membrane and reactivity of the monomers: while high reactive aromatic isocyanates showed a diffusion controlled fast reaction process, the moderate reactivity of aliphatic isocyanates resulted in a reaction-controlled process.

The importance of the isocyanate chemistry in the preparation of nanocapsules can be easily observed by the number of different works found in the literature involving the preparation of polyurethanes or polyurea nanocapsules or with isocyanates as cross-linkers. In the formulation of nanocapsules for biomedical applications, different monomers have been cross-linked using isocyanate chemistry. For example, Taheri *et al.*⁵⁷ produced hybrid nanocapsules based on silver and potato starch using toluene diisocyanate (TDI) as the crosslinker, resulting in nanocapsules with mean diameter between 290 and 370 nm and different shell thicknesses depending on the concentration of TDI. The nanocapsules showed effective antibacterial properties against *Staphylococcus epidermidis* and *Escherichia coli*. Another example of a biodegradable natural polymer used for the formation of nanocapsules by crosslinking reactions with TDI was lignin: hollow nanocapsules have been

prepared, which released their content in the presence of laccase, an enzyme produced by certain fungi, generating an important strategy for the development of delivery systems for agricultural applications.⁵⁸ A similar approach was applied by Piradashvili *et al.*⁵⁹ for the preparation of protein nanocontainers based on albumin and TDI, resulting in a biocompatible and biodegradable system with efficient drug delivery properties. Condensation reactions have also been used in the preparation of inorganic shells at the surface of droplets in miniemulsion. Fickert *et al.*⁶⁰ produced silica nanocapsules containing thiol or amine groups at the surface using a direct miniemulsion approach. Hydrolysis occurred at the interface between the aqueous continuous phase and the droplets composed by the monomers for the shell formation, originating the condensation reaction for the formation of the silica membrane. The droplets also contained a hydrophobe and the self-healing monomer or the catalyst. A second approach was applied with one monomer dispersed in the organic droplets and a second monomer which was added drop-wise after emulsification. In both systems a similar size and size distribution were obtained and the thickness of the shell could be controlled upon control of the formulation.

“Click” and olefin metathesis in miniemulsion

Many other examples can be found in the literature using the chemistry of polyurethanes and TDI for the preparation of nanocontainers.⁶¹⁻⁶⁵ Nevertheless some drawbacks are found in this approach, mainly due to the limitation on the types of molecules which can be efficiently encapsulated through this strategy, resulted of the competitive reactions in case of the presence of nucleophilic –NHR, –SH and –OH groups in the chemical structure of the molecule targeted for encapsulation, and the hard control between the formation of polyurethane and polyurea films at the interface. In order to provide more selective strategies for the formation of nanocapsules different step-growth polymerization approaches have been used in miniemulsion. Click chemistry reactions are often referred if bioorthogonal reactions are demanded. They are specific reactions which are performed between specific pairs of chemical groups that are typically not found in natural materials. Therefore, the introduction of click chemistry for the preparation of nanocapsules in miniemulsion is an attractive strategy for the encapsulation of biomolecules and a large number of therapeutic molecules. Roux *et al.*⁶⁶ presented an approach for the preparation of glyco-nanocapsules using a copper catalyzed azide-alkyne (CuAAC) interfacial polyaddition. In this work, 6,6'-diazido-6,6'-dideoxysucrose was clicked with bis(propargyloxy)butane in direct emulsion systems, with or without the use of microwaves to increase the kinetics of

the reaction, producing capsules with an average mean diameter of 200 nm.⁶⁶ Besides the fact that the monomers and the core of the formulation were biocompatible and that the use of the click approach would create the opportunity for encapsulation of other biomolecules sensitive to the TDI chemistry, as for example siRNA, the use of copper would probably be a cause of concern for future applications of this system due to the toxicity issues related to this metal.⁶⁷ Siebert *et al.*⁶⁸ presented a copper-free alkyne-azide click polyaddition for the preparation of nanocapsules using electron deficient alkynes. The approach produced polymers with molecular weights up to $M_w = 33,600 \text{ g mol}^{-1}$ in miniemulsion, smaller than the ones obtained in the solution approach ($M_w = 45,500 \text{ g mol}^{-1}$), and nanocapsules with a mean diameter of around 280 nm. Copper-free alkyne-azide click reactions are generally temperature dependent and relatively high temperature for the encapsulation of biomolecules as proteins or siRNA was needed for satisfactory kinetics (in this work 50 °C). Nevertheless, it was demonstrated that the use of the miniemulsion approach leads to an acceleration of the kinetics involving this click reaction, probably due the increase of local concentrations, making possible to use this approach for lower temperatures as 25 °C.⁴ Besides the alkyne-azide reaction, another click strategy used for the preparation of nanocapsules in miniemulsion was the thiol-ene step-growth polymerization. Paiphansiri and coworkers⁶⁹ produced glutathione-responsive DNA-based nanocapsules using the thiol-disulfide exchange and the thiol-ene click approach for the preparation of biodegradable and fluorescent labeled systems, with potential for theranostic applications. Chen and coworkers⁷⁰ used the thiol-ene approach for the preparation of chitosan nanocapsules through the crosslinking of *N*-maleoyl-functionalized chitosan, used both as a surfactant and precursor in the system, and bis(3-mercapto-propionate) as the crosslinker. As many other thiol-ene approaches, this reaction is initiated by UV-light and this is one of the main drawbacks for this reaction in miniemulsion. The scattering caused in the emulsion system lowers the efficiency of the reaction, what probably explains the fact that the conversion was increased with the decrease of the droplet size.

Another possible strategy for the replacement of the classical isocyanate chemistry in the preparation of nanocapsules is the use of olefin metathesis. Malzahn and coworkers⁷¹ presented a bioorthogonal interfacial olefin cross metathesis for the preparation of dextran-alkylphosphate hollow nanocapsules. Metathesis is a reaction which can be performed at mild conditions and the use of phosphate based cross-linkers also offered the possibility of further addition of functionalities to the polymeric shell, as for example the addition of fluorescent units. EDX and ICP-OES analysis revealed efficient removal of the

ruthenium catalyst, which makes olefin metathesis a tool of high interest for the development of new nanocapsules for biomedical applications. Up to date few studies involving metathesis in miniemulsion are available in the literature. Cardoso *et al.*⁷² studied the efficiency of the acyclic diene metathesis reaction of natural oil in direct miniemulsion systems, evaluating the influence of the different types of surfactant, showing that Ru-indenylidene catalysts and nonionic surfactants were more effective in comparison to Ru-benzylidene and ionic surfactants, respectively. Ring-opening metathesis polymerization has also been explored in the preparation of latex particles in miniemulsion. Quemener *et al.*^{73, 74} explored the polymerization of polynorbornene latexes in direct miniemulsions and observed that the use of a *in situ* generated ruthenium catalyst in the water-phase resulted in stable dispersions with average diameter between 200-500 nm, with $M_n = 15,000 \text{ g mol}^{-1}$ and PDI 1.6, while the strategy with the oil-soluble catalyst resulted in large and poorly stabilized dispersions. The *in situ* approach also resulted in the increase of the conversion from 16% to 90%. Following these studies, the authors developed a water soluble PEO-based ruthenium carbene and obtained stable latexes with average diameter 200-250nm. The authors observed that high molecular weight macroinitiators formed latexes with less coagulation.

Ionic polymerizations in miniemulsion

Ionic polymerizations are commonly considered very sensitive to water in reaction media and are therefore carried out under strictly anhydrous conditions. However, an increasing number of catalytic systems stable in aqueous media have been developed in the past decade enabling the use of milder and more robust experimental conditions.⁷⁵

For cationic polymerizations at the droplet/particle interface, a combination of initiator and surfactant (INISURF) can be used.⁷⁶ Cauvin and coworkers used dodecylbenzenesulfonic acid as the INISURF for the cationic polymerization of *p*-methoxystyrene (pMOS) in miniemulsion.⁷⁷ However, only oligomers with $M_n < 1,000 \text{ g mol}^{-1}$ were achieved due to the decreasing surface activity of the dormant species with increasing chain length. The group obtained higher molecular weights (up to $3,000 \text{ g mol}^{-1}$) in an inverse miniemulsion by combining dodecylbenzenesulfonic acid with the Lewis acid ytterbium triflate as the initiator. The authors propose that the triflate anions generate a bulky strong Brønsted superacid $\text{H}^+\text{Yb}(\text{OTf})_4^-$ that acts as the initiator. Chain growth appears rapidly and the termination reaction is retarded due to the increasing hydrophobicity of the interface caused by oligomers.⁷⁸ These systems still suffer from a high

termination rate producing only oligomers. The hydrophobicity of the growing polymer chains results in a loss of their surface activity (commonly referred to as the “critical DP effect”).⁷⁹ For this reason, research has been focused on transferring the chain growth from the interface to the droplet core by designing Lewis acid-surfactant combined catalysts (LASC).⁸⁰ The solubility of LASC in the monomer phase is enhanced through an electrosteric surfactant bearing poly(ethylene glycol) chains which repel the ligated water from the ytterbium atom.⁸¹ The authors achieved M_n up to 40,000 g mol⁻¹ after 100 h but without control over the polymerization.

Similar to cationic polymerization, the number of reported anionic polymerizations in emulsion or heterophase is limited due to the high sensitivity of the propagating species towards water. Still, living/controlled polymerization is highly desired since well-defined polymers with narrow molecular weight distributions can be obtained. Anionic emulsion polymerization has mostly been reported for the ring-opening polymerization of cyclic siloxanes,^{82, 83} glycidyl ethers⁸⁴ and the polymerization of cyanoacrylates.^{85, 86} Cyclosiloxanes and cyanoacrylates as reactive monomers start to polymerize at the interface until the growing chains collapse into the particle core. For this reason, high molecular weights are, similar to cationic polymerization, limited through the critical DP effect. Condensation and transfer reactions lead to an increase in molar mass but also to a broadening of the molecular weight distribution (MWD).⁸⁷ Barrère *et al.* compared the ring-opening anionic polymerization of octamethylcyclotetrasiloxane in miniemulsion and bulk.⁸⁸ At 70% conversion they obtained a narrow MWD in miniemulsion. Initiation, propagation, and reversible termination occur at the interface. Backbiting reactions also occur similar to bulk polymerization but in contrast to the latter, predominantly small cycles (four to five membered rings) are produced which can be easily removed. As backbiting takes place at the interface, steric constraints through ion-pairing limit the size of the rings and macrocycles as found in bulk polymerization were not observed. For 1,3,5-tris(trifluoropropylmethyl)cyclotrisiloxane, Barrère and coworkers even obtained higher yields than in bulk or solution polymerization as backbiting reactions were suppressed through the steric hindrance of the surfactant.⁸² Maitre *et al.* showed that the polymerization kinetics for phenyl glycidyl ether (PGE) in bulk differ from polymerization in miniemulsion.⁸⁴ The initiation, propagation and termination step could be found in both systems. However, transfer reactions did not occur in miniemulsion. Cyclic monomers such as ϵ -caprolactam and ϵ -caprolactone were successfully anionically polymerized in non-aqueous miniemulsions.^{89, 90} In the first case, the monomer ϵ -caprolactam, the initiator

NaH and the activator *N*-acetylcaprolactam were dissolved in DMSO, constituting the polar, dispersed phase. For the continuous phase, isoparaffinic oil was used. By this method anisotropic polyamide-6 nanoparticles were obtained with molecular weights up to 40,000 g mol⁻¹. In addition the absence of structural defects which often lead to poor mechanical properties was shown.

Radical polymerization in miniemulsion

Controlled radical polymerization (CRP) opens up the way for the formation of polymeric nanoparticles with precise control over molecular weight and distribution. It combines the advantages of ionic polymerization concerning livingness and of free radical polymerization in terms of industrial implementation.⁹¹ Nitroxide mediated polymerization (NMP), atom transfer radical polymerization (ATRP) and reversible addition-fragmentation chain transfer polymerization (RAFT) represent the most popular and successful methods for the synthesis of functional polymeric nanoparticles.⁹²

In emulsion polymerization, the compartmentalization effect needs to be considered: In free radical emulsion polymerization the radicals are confined in different particles and thus termination reactions are hampered. This leads to an increase in overall polymerization rate and higher molecular weights for decreasing particle size. For controlled polymerizations based on activating/deactivating mechanisms, such as NMP and ATRP, partitioning of the controlling agent and the growing radical between droplets, continuous phase and forming particles also plays a crucial role in the control over MWD, polymerization rate, and colloidal stability.^{93, 94} It has been demonstrated that for CRP the rate of polymerization decreases with decreasing particle size and the rates of deactivation and termination are higher compared to bulk as the controlling agent and the growing polymer chain are confined in a small volume.⁹⁵ These characteristics for CRP in emulsions results in a higher control and narrower MWD in comparison to what is usually obtained in bulk systems. A decrease of the concentration of the deactivating species inside the droplet affects therefore the control over the chain growth adversely.⁹⁶ Hence, the use of hydrophobic controlling agents, where the entry into the water phase is more unlikely, leads usually to a better control over the kinetics and the molecular weight.⁹⁷ For ATRP, Cunningham and coworkers showed in simulations, that while the rate of polymerization in bulk is dependent on the equilibrium ratio of the Cu(I)/Cu(II) species, in emulsions with small particle sizes the rate is controlled by the size dependent relative concentrations of Cu(I) and Cu(II).⁹⁸ In emulsion, additionally the choice of the surfactant has to be considered since

anionic surfactants interact with the catalyst. Therefore, nonionic surfactants such as Brij98 (PEG20-oleyl ether) or Tween80 (PEG20-sorbitan monooleate) and the cationic surfactant CTAB (cetyl trimethylammonium bromide) are preferentially used.⁹⁹ Thus, CRP in emulsion is preferentially performed in systems with confined space such as in miniemulsion where each droplet can be considered as single microreactors and transportation and partitioning plays a minor role. The use of high-energy shear devices for the generation of a miniemulsion is argued as the major drawback of this method. However, Guo *et al.* reported a NMP of styrene without the use of such homogenization devices by *in situ* formation of the surfactant potassium oleate. The system exhibited good control (MWD below 1.22) and high colloidal stability.^{100, 101} The miniemulsion technique, by carefully choosing the conditions can be even superior than bulk systems. By combining the ultrasonication with the *in situ* surfactant formation the same group achieved an increase in the polymerization rate and a better control over polymerization compared to the corresponding bulk system.¹⁰² For ATRP, where the activator, for example the Cu(I) species, is sensitive to air and thus not well suited for miniemulsion preparation, reverse ATRP techniques have been developed.¹⁰³

2.2 Polyphosphoesters

2.2.1 Brief history and synthesis approaches

The estimated age of the planet Earth is 4.5 billion years. During this long process, innumerable changes on the environment provided the perfect scenario for the development of the most varied forms of life through the evolutionary process. In the development of living organisms, nature has found great support in a certain element: phosphorus. Phosphorus is an essential element in the composition of important molecules in living systems, being part especially of the genetic information transmission, in the form of DNA and RNA, or the flow of energy, as adenosine phosphate derivatives (Figure 2.2 – 1).¹⁰⁴

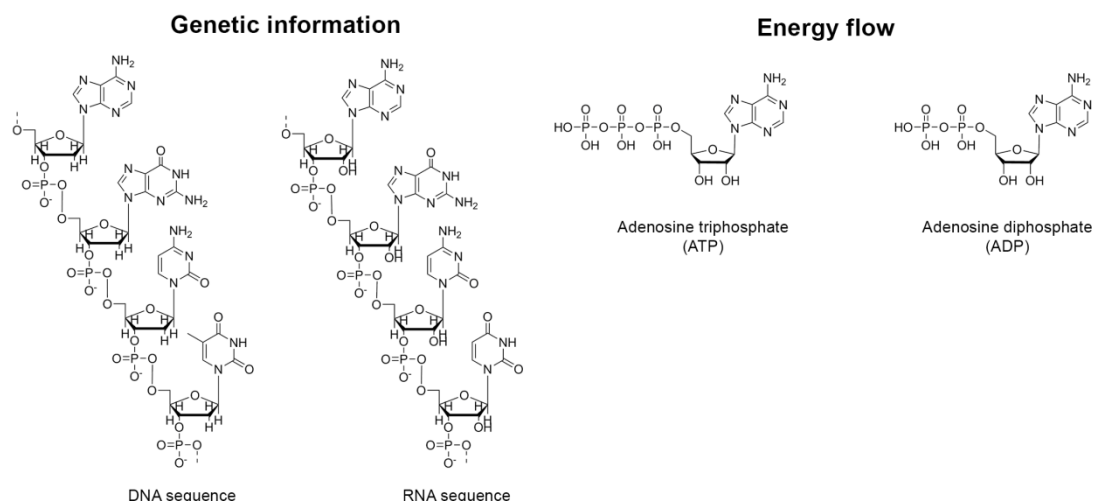


Fig. 2.2 – 1 Chemical structure of some of the most important phosphorus containing biomolecules: general DNA and RNA sequences, responsible by genetic information transmission, and ATP and ADP, essential for the energetic flow in living systems.

Macromolecules containing repeating phosphoester units in the backbone, as in the case of DNA and RNA, belong to a special class of polymers called polyphosphoesters.¹⁰⁵ Polyphosphoesters are a structurally versatile class of polymers, a factor that allows the tailoring of materials with suitable structures for varied applications, from flame retardant materials to tissue engineering.¹⁰⁶ Through the control of the side chains and backbone structures, polyphosphoesters are classified in different sub-classes: polyphosphates, polyphosphonates and polyphosphoramidates (Figure 2.2 – 2). Such structural versatility provides a wide range of chemical and mechanical properties to these materials, varying from amorphous to crystalline, water-soluble to highly lipophilic and biocompatible or toxic materials. Adding to this versatility the fact that the phosphoester moiety is a potentially biodegradable unit, both by enzymatic and hydrolytic degradation, polyphosphoesters are highly attractive materials for the development of biomedical applications.^{105, 106}

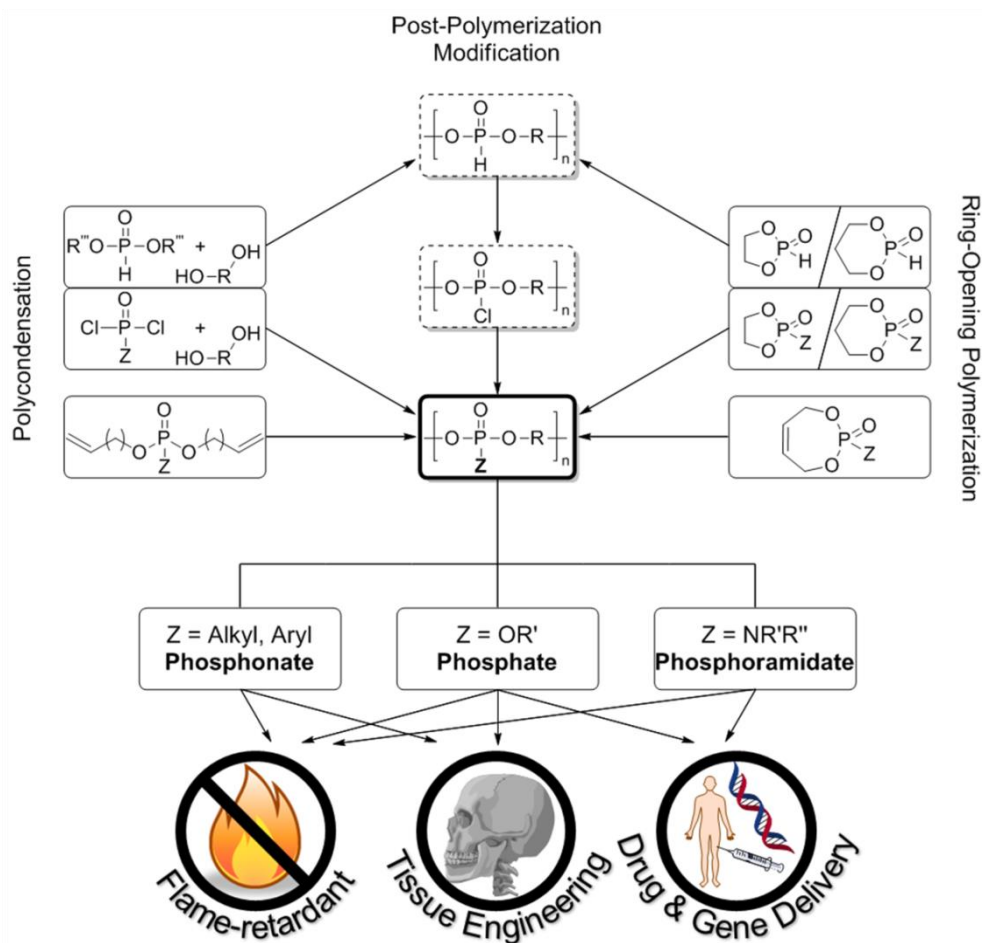


Fig. 2.2 – 2 Main synthetic routes for the preparation of polyphosphoesters and related application fields (Reproduced from reference ¹⁰⁶, Copyright © 2015 WILEY-VCH Verlag GmbH & Co. KGaA, Weinheim).

In order to achieve such variety of properties, different synthetic strategies (Figure 2.2 – 2) have been applied in the development of polyphosphoesters in the last decades.¹⁰⁶ In fact, one should look back to 1934 to find the first synthetic polyphosphoester, prepared by Arvin through the polycondensation between phosphorus oxychloride with bisphenol-A and phenol.¹⁰⁷ Following these efforts, a library of polyphosphates was prepared with flame-retardant properties demonstrated by Cass.¹⁰⁸ Nevertheless, low molecular weight values and high cost made the interest by such materials to decrease quickly. Polycondensation can be performed in different approaches, e.g. in melt, solution or at the interface, providing a platform for the formation of varied structures. Maiti *et al.*,¹⁰⁹ for example, used an interfacial polycondensation to produce polyimidophosphonates through the reaction between dihydroxybisimide and dichlorophenylphosphine oxide, obtaining polymers with M_n 5,000-6,000 $g\ mol^{-1}$ and flame

retarding properties. Most of the polycondensation approaches make use of phosphorus chloride monomers, which can be highly toxic in some cases, especially in the case of POCl_3 , one of the most common phosphorylating agent.¹¹⁰ An important alternative is the use of phosphoric acid. Recently, Penczek and coworkers¹¹¹ reviewed the use H_3PO_4 as building block for the preparation of polyphosphates through the polycondensation with polyols, as for example ethylene glycol and glycerol, leading to the preparation of linear as well as branched structures. Figure 2.2 – 3 shows some examples of polycondensations for the achievement of polyphosphoesters.

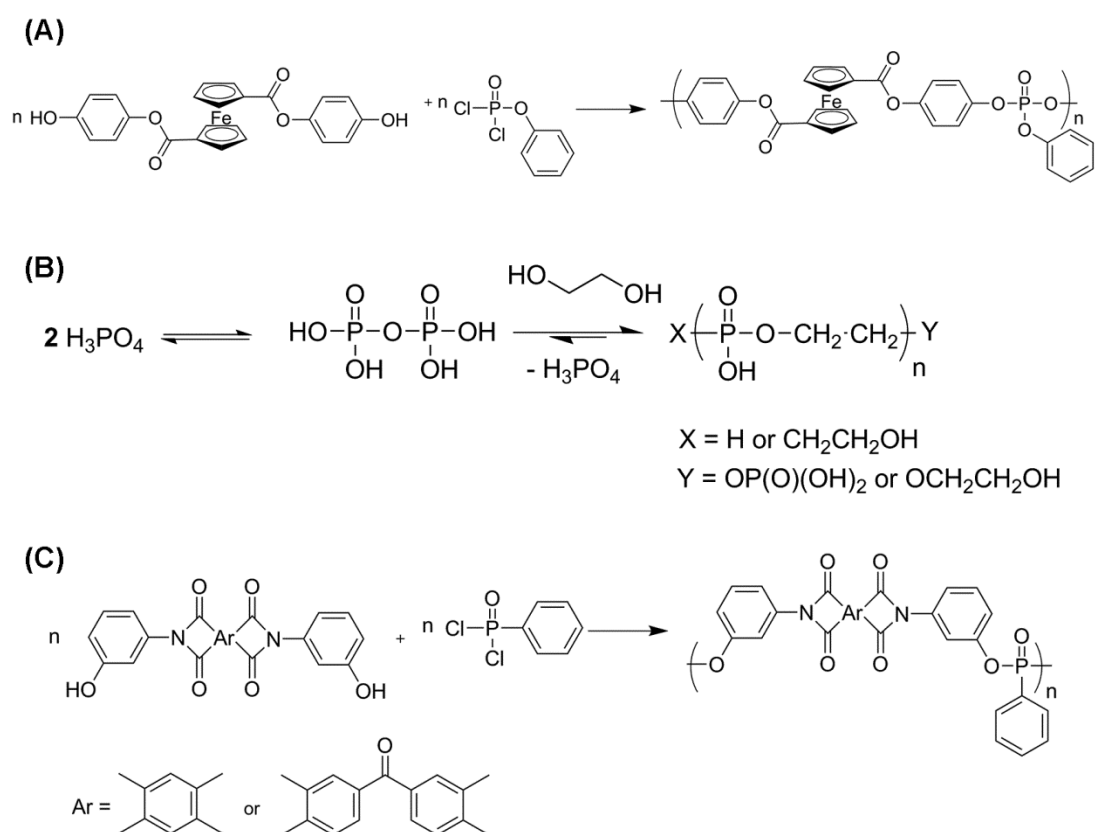


Fig. 2.2 – 3 Examples of polyphosphoesters structures obtained by polycondensation approaches: (A) ferrocene-containing polyphosphate (Adapted from reference ¹¹², © 2003 WILEY-VCH Verlag GmbH & Co. KGaA, Weinheim); (B) polyphosphate obtained from the reaction between phosphoric acid and ethylene glycol (Adapted from reference ¹¹³, Copyright © 2014 Royal Society of Chemistry); (C) synthesis of polyimidophosphonates from dihydroxybisimide monomers (Reproduced from reference ¹⁰⁹, Copyright © 2003 WILEY-VCH Verlag GmbH & Co. KGaA, Weinheim).

Another important approach in the history of polyphosphoester synthesis is the use of chain-growth techniques, especially the use of ring-opening polymerization (ROP). Even though the difficulty to synthesize the monomers used in such approaches has limited its application on industrial level today, many efforts in the academic world go in this direction. Penczek and coworkers pioneered the development of the synthesis of polyphosphoesters using ROP.¹¹³ The controlled polymerization of different five- and six-membered cyclic alkylene phosphates have been summarized already in the 1970's.^{114, 115} Steinbach *et al.* prepared cyclic alkylene phosphonate monomers, which have been used for the synthesis water-soluble polyphosphonates using organocatalysis.¹¹ The structural control afforded by the use of ROP approaches also enabled the development of well-defined block, graft and hyperbranched copolymer structures.¹¹³ The synthesis was performed using many different catalysts, including strong organic bases as DBU (1,8-Diazabicyclo[5.4.0]undec-7-ene) or DMAP (4-(dimethylamino)pyridine), cationic and especially anionic initiators, as for example triisobutylaluminium, Grignard reagents or butyl lithium, and metal carboxylates, where tin(II) 2-ethylhexanoate (Sn(Oct)₂) stands out.¹⁰⁶ For example, Wen and Zhuo¹¹⁶ used an enzyme-catalyzed approach for the ring-opening polymerization of a cyclic phosphate (ethylene isopropyl phosphate), but only obtained oligomers. Figure 2.2 – 4 shows a general approach for the synthesis of polyphosphoesters by ROP and Figure 2.2 – 5 presents a selection of monomers synthesized up-to-date.

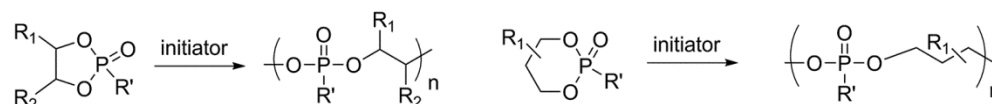
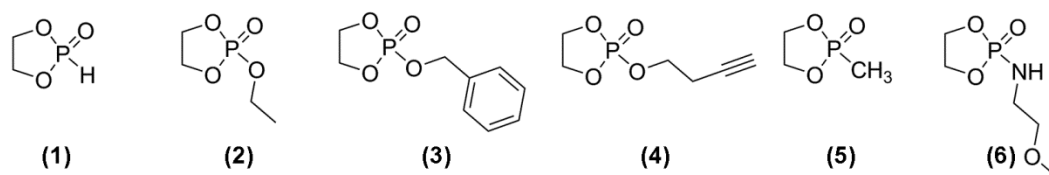


Fig. 2.2 – 4 General ring-opening polymerization strategy for the preparation of polyphosphoester structures.

Five - membered



Six - membered

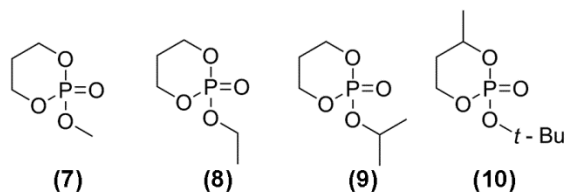


Fig. 2.2 – 5 Selection of monomers applied in the polymerization of polyphosphoesters by ring-opening polymerization: **(1)** 2-hydroxy-2-oxo-1,3,2-dioxaphospholane;¹¹⁷ **(2)** ethyl ethylenephosphate (EEP);¹¹⁸ **(3)** 2-benzyloxy-2-oxo-1,3,2-dioxaphospholane (BP);¹¹⁹ **(4)** 2-(but-3-yn-1-yloxy)-2-oxo-1,3,2-dioxaphospholane (BYP);¹²⁰ **(5)** 2-methyl-1,3,2-dioxaphospholane 2-oxide (MeEP);¹¹ **(6)** *N*-methoxyethyl phospholane amidate (MOEPA);¹²¹ **(7)** 2-methoxy-2-oxo-1,3,2-dioxaphosphorinane;¹²² **(8)** 2-ethoxy-2-oxo-1,3,2-dioxaphosphorinane;¹²³ **(9)** 2-isopropoxy-2-oxo-1,3,2-dioxaphosphorinanes;¹²³ **(10)** 2-*t*-butoxy-2-oxo-1,3,2-dioxaphosphorinanes.¹²⁴

Historically, ROP and polycondensation have been the most used approaches in the preparation of synthetic polyphosphoesters. Nevertheless, other polymerization techniques have also attracted the academic interest in the development of new polyphosphoesters. Polyadditions have been performed between phosphoric acid with bisepoxides (Figure 2.2 – 6) and bisoxetanes.^{111, 125} But recently, another approach has successfully been developed in the preparation especially of hydrophobic polyphosphoesters: the olefin metathesis polymerization. High molecular weight polymers and versatile structures, with possibilities of functionalization in the end-groups and side-chain, were made accessible through the use of easy to handle monomers and different versions of the Grubbs catalyst, providing varied synthetic routes through step-growth or chain-growth polymerization strategies. Polycondensation approaches (acyclic diene metathesis or ADMET) and chain-growth strategies (ring-opening metathesis polymerization or ROMP) have been successfully applied in the development of new synthetic polyphosphoesters and were especially important in the development of this thesis. Our group pioneered the use of such strategies in the development of new synthetic polyphosphoesters. Up-to-date, linear and hyperbranched polyphosphates and linear polyphosphonates have been successfully

developed using the ADMET strategy, providing materials with varied backbone and possible control of the crystallinity and thermal properties,¹⁶ functional and reactive side-chains,^{15, 126} telechelic materials¹³ and the possibility of further post-polymerization reactions using the Horner-Wadsworth-Emmons reaction.¹²⁷ A similar metathesis approach was used in the development of unsaturated hyperbranched polyphosphates, with different phosphorus contents.^{14, 128} A olefin cross-metathesis approach have been applied successfully by the same group in the development of dextran-polyphosphate hollow nanocapsules.⁷¹ A ROMP approach was used by Steinbach *et al.*³ to produce unsaturated homopolymers and copolymers with cyclooctene from novel seven-membered phosphate monomers, achieving molecular weights up to 50,000 g mol⁻¹).

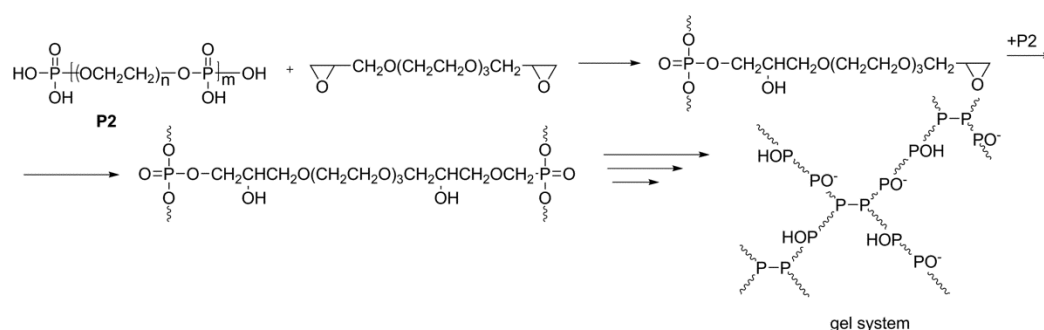


Fig. 2.2 – 6 Schematic representation of the reaction approach presented by Kazanskii *et al.*¹²⁹ for the synthesis of polyphosphate gel based on poly(PEG phosphate) and diglycidyl ether of triethylene glycol (Reprinted from *Polymer Gels and Networks*, 4 (4), Kazanskii, K., Kuznetsova, V., Pretula, J., Penczek, S., Ionizable hydrogels of new type based on poly(ethylene glycol)phosphates, 335-349, Copyright © 1996, with permission from Elsevier).

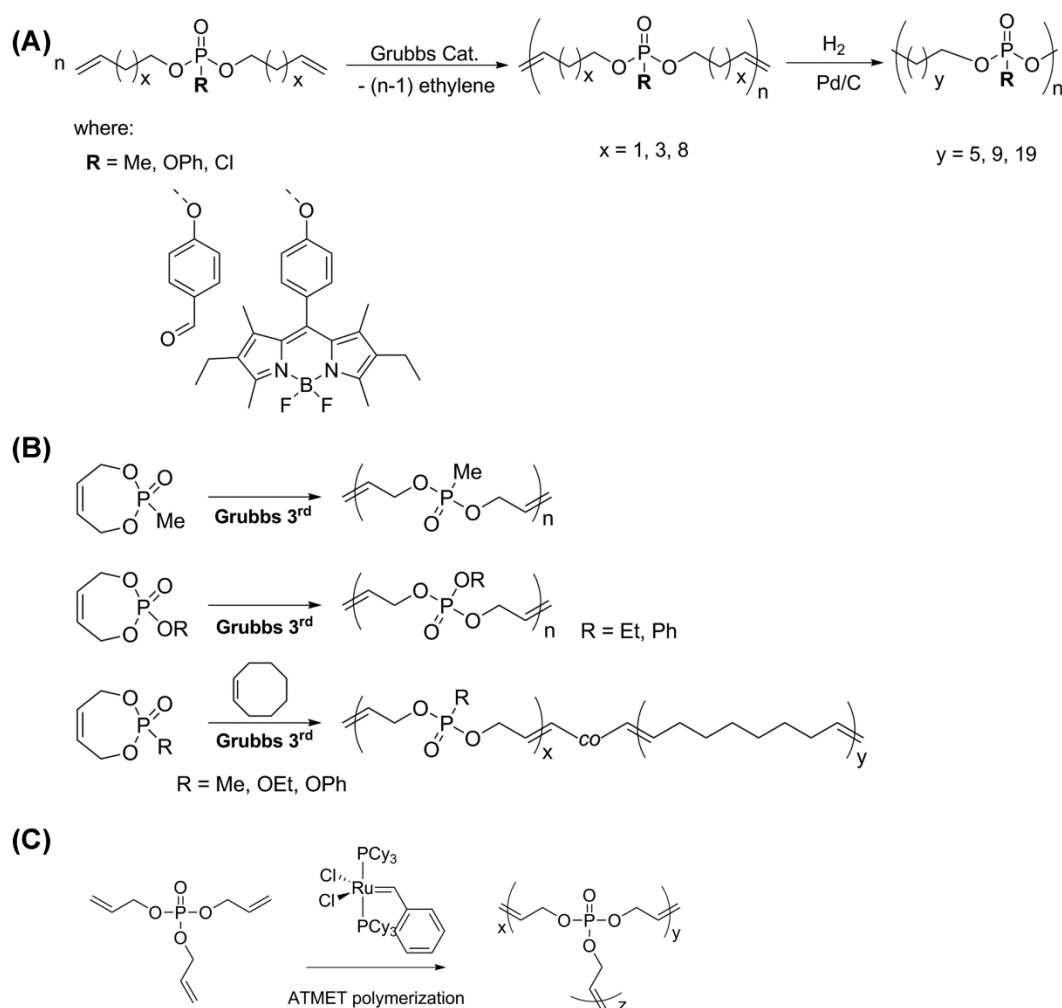


Fig. 2.2 – 7 Examples of polyphosphoesters structures obtained by olefin metathesis approaches: (A) acyclic diene metathesis approach for the synthesis of linear unsaturated and saturated polyphosphates^{15, 16, 126} and polyphosphonates;^{2, 127} (B) ring-opening metathesis polymerization approach for the synthesis of polyphosphates and polyphosphonates homopolymers and copolymers;³ (C) acyclic triene metathesis polymerization for the preparation of unsaturated hyperbranched polyphosphates.¹²⁸

2.2.2 Applications

Polyphosphoesters are potentially biocompatible and biodegradable materials. Nevertheless, these materials attracted at first the interest for their application as flame retardants additives. As previously mentioned, in the 1930's Cass and coworkers¹⁰⁸ had already synthesized a library of polyphosphoesters and analyzed their potential flame retardant properties. Even though by that time costs and the reached properties made the

interest in such applications shrink, nowadays the use of polyphosphates and polyphosphonates for this type of applications is again of high interest.¹³⁰ Due to the introduction of REACH (Registration, Evaluation, Authorization and Restriction of Chemicals) by the European Union in 2007 and the consequent elimination of the use of potentially carcinogenic halogenated polycyclic aromatics flame retardant additives, polyphosphoesters raised again as an optimal choice in Europe. The use of polymers and oligomers as flame retardants brings others advantages as lowering of leaching and blooming out events.^{128, 131} The use of phosphorus-containing polymers as flame retardant additives has been already well reviewed.¹³²

Even though historically the interest on polyphosphoesters was initially concentrated on its flame retardant properties, the structural versatility of this materials and potential properties made with this class of polymers could also attract interest beyond this field. The potential hydrolytic and enzymatic degradation of polyphosphoesters and biocompatibility has been reviewed by Wang *et al.*¹⁰⁵ These properties made polyphosphoesters perfect candidates for the development of new biomedical solutions. Between the possible applications, drug and gene delivery as well as tissue engineering stands out. In drug delivery strategies, nano- and microparticles^{133, 134} have been developed using polyphosphoesters homo- and copolymers for the encapsulation of anti-cancer drugs as paclitaxel or doxorubicin by different groups.^{1, 135-138} In most of these works, loading contents up to 10 wt% were obtained and many efforts have been made to increase such numbers. Wooley and coworkers^{134, 139} developed, for example, an elegant strategy which resulted in loading capacity of paclitaxel up to 65 wt%. Poly(ethylene oxide)-*block*-polyphosphoesters-graft-paclitaxel conjugates were prepared using a combination of the structural versatility of the polyphosphoesters prepared by ROP and alkyne-azide or thiol-ene click chemistry for the further post-polymerization modification (Figure 2.2 – 8). The use of polyphosphoesters in gene delivery has also been topic of many studies.^{105, 140-143} Leong and coworkers¹⁴³ have prepared a successful system in the early 2000s for the delivery of plasmid DNA using poly(2-aminoethyl propylene phosphate) (PPE-EA), a biodegradable water-soluble polyphosphoester, which presented positive charges in the side chain. The positive side chains were used for the formation of conjugates with plasmid-DNA and the polymer presented higher tissue compatibility in comparison to other classic options for gene delivery as polyethylenimine and poly-L-lysine, resulting in enhanced β -galactosidase expression. Triblockcopolymers of PPE-EA with monoethoxy poly(ethylene glycol) and poly(ϵ -caprolactone) have also been successfully

synthesized and used for the preparation of micellar nanoparticles loaded with siRNA after the particle formation without change in the uniformity. These micellar nanoparticles demonstrated to be effective in GFP expression silencing in HEK293 cells.¹⁴⁴

Another attractive field in the development of biomedical solutions nowadays is the establishment of theranostical systems, which are systems that combine therapeutics, as drug delivery, and diagnostics, as imaging, skills at the same time.¹⁴⁵ Wooley and coworkers¹⁴⁶ prepared with success polymeric nanotheranostics systems using thiol-yne chemistry for the post modification of a blockcopolymer composed of PLLA and an alkyne-functionalized poly(butynyl ethylenephosphate), obtaining micelles with different surface charges depending on the thiol-derivative used in the post modification reaction. Figure 2.2 – 9 shows a scheme of the strategy used in the preparation of these nanotheranostic systems.

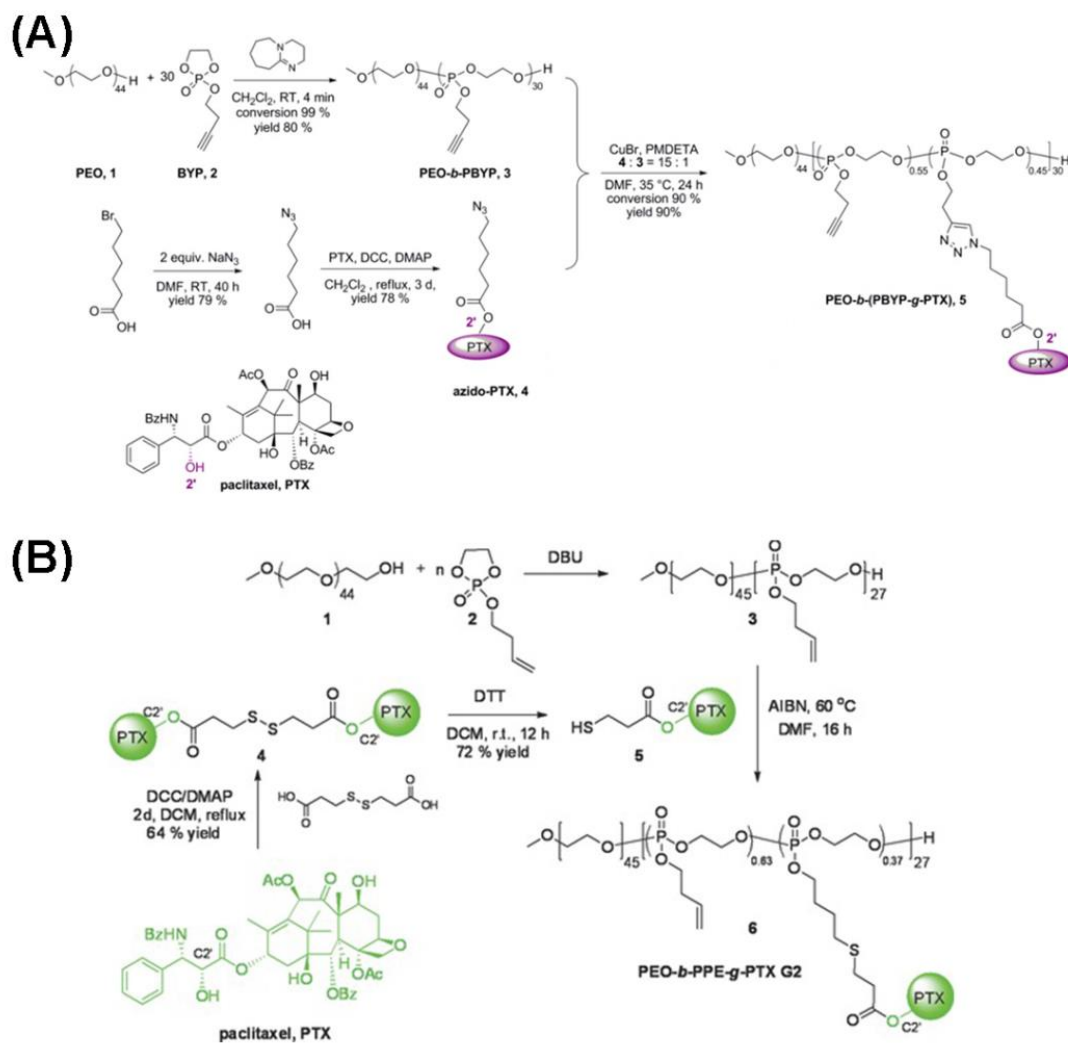


Fig. 2.2 – 8 Synthetic strategy of the poly(ethylene oxide)-*block*-polyphosphoesters-graft-paclitaxel conjugates: (A) first generation (Reproduced from ¹³⁹ with permission of The Royal Society of Chemistry) and (B) second generation conjugates synthesized by Wooley *et al* (Reproduced from reference ¹³⁴, © 2003 WILEY-VCH Verlag GmbH & Co. KGaA, Weinheim).

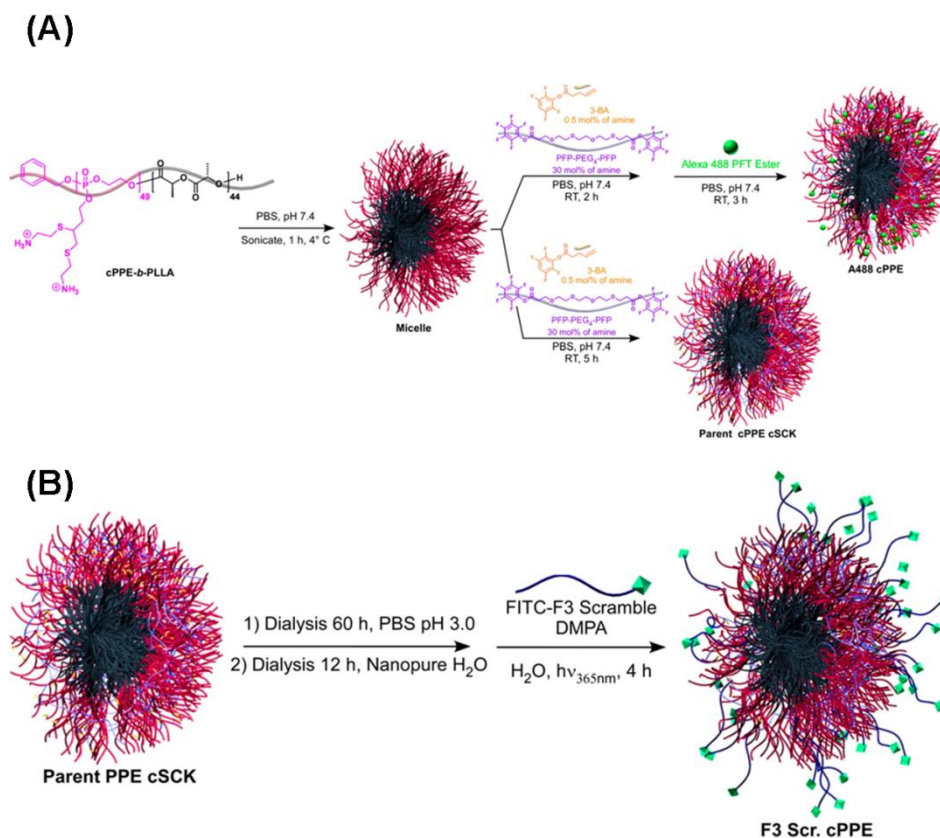


Fig. 2.2 – 9 Nanotheranostics micellar systems based on PPE-PLLA block copolymers produced by Gustafson *et al.*: (A) Synthesis of Parent and A488-Labeled cPPE-*b*-PLLA cSCKs and (B) Conjugation of FITC-Labeled F3 scr. Peptide to cPPE₄₉-*b*-PLLA₄₄ cSCKs (Reprinted with permission from Gustafson *et al.* Holistic Assessment of covalently labeled core-shell polymeric nanoparticles with fluorescent contrast agents for theranostic applications, *Langmuir*, 2014, 30 (2), pp 631–641. Copyright © 2014 American Chemical Society).¹⁴⁶

Tissue engineering is another field of potential for polyphosphoesters. A copolymer of bis(hydroxyethyl)terephthalate and ethyl *ortho*-phosphodichloridate, followed by chain extension with terephthaloyl chloride was produced using polycondensation and applied in the development of conduits for nerve regeneration.¹⁴⁷ This was one of the pioneering works involving polyphosphoesters and tissue engineering. Most recent efforts in the production of polyphosphoester scaffolds have been directed for bone tissue regeneration strategies, due the potential of such phosphorus-containing polymers to influence positively the proliferation of osteoblasts, a fact that have been previously reported to inorganic polyphosphates and polymers containing phosphate groups as side chains.^{148, 149} Leong and coworkers¹⁵⁰ conjugated acrylate groups to the side chains of PPE-HA and formed hydrogels through a photocrosslinking reaction. The hydrogels obtained showed biodegradability

dependent of the crosslinking level and no toxicity against bone marrow-derived mesenchymal stem cells from goat, resulting in clear mineralization after three weeks of incubation of these cells in the hydrogels. Another interesting example was brought to light by Wang and coworkers,¹⁵¹ who produced block copolymers of PLLA and poly(ethyl ethylene phosphate) further used to modify PLLA surfaces by spin-coating process, providing in this way a surface capable to enhance the proliferation of osteoblasts significantly in comparison to the pure PLLA.

Besides the already established flame retardant properties and biomedical applications of polyphosphoesters, other fields have been demonstrated as potential application. Recently, the potential of hyperbranched polyphosphoesters as an active oxygen protective matrix for the triplet-triplet annihilation upconversion phenomenon was introduced (which is discussed later on as one of the topics in this work).¹⁴ The use of polyphosphoesters in the controlled crystallization of inorganic salts has also been topic of a recent review¹¹¹ and the demonstrated structural versatility from polyphosphoesters make believable that the full potential of this class of polymers is still to be discovered.

2.3 Methods

2.3.1 Dynamic light scattering (DLS)^{152, 153}

When light interacts with matter, an oscillating polarization of the electrons in the material is induced by light electric field. The molecules of the matter act, therefore, as a secondary source of light and radiate (scatter) light.¹⁵⁴ If the particles are moving, the fluctuations of the scattered light intensity will reflect the Brownian motion. The motion of scattering polymers or particles in solution can be determined by dynamic light scattering (DLS), also called quasi-elastic light scattering (QELS) and photon correlation spectroscopy (PCS).¹⁵² Figure 2.3 – 1 shows a basic scheme of the measurement system for DLS.

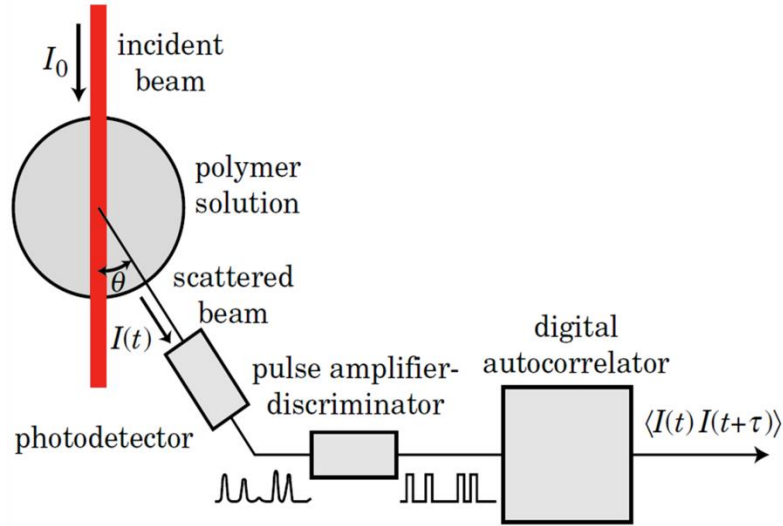


Fig. 2.3 – 1 Basic scheme of a DLS measurement system. A pulse-amplifier discriminator converts the analog signal of the photodetector, $I(t)$, into a digital signal, which is further converted by the autocorrelator (Reproduced from reference¹⁵², © 2002 WILEY-VCH Verlag GmbH & Co. KGaA, Weinheim).

Dynamic light scattering allows the determination of the hydrodynamic radius R_H of scattering particles in movement, through the determination of the selfdiffusion coefficient D_S . The selfdiffusion coefficient is determined using a time-intensity-autocorrelation function:

$$F_S(\vec{q}, \tau) = \int G_S(\vec{r}, \tau) \exp(i\vec{q}\vec{r}) d\vec{r} \quad (7)$$

which represents a certain number of scattering particles, fluctuating with time due to Brownian motion in a very small sub volume of the scattering volume centered at position \vec{r} in a given time t .¹⁵³ This function is actually the integral of the so-called van Hove self-correlation function:

$$G_S(\vec{r}, \tau) = \langle n(\vec{0}, t)n(\vec{r}, t + \tau) \rangle_{V,T} \quad (8)$$

For very dilute solutions, $G_S(\vec{r}, \tau)$ gives the probability of finding a given scattering particle at time $t + \tau$ and position \vec{r} , for a particle found at time t at position $\vec{0}$. From the average $\langle \rangle$ measured over the total measuring time and whole volume and for an isotropic diffusive particle motion (or “random walk”), the mean-square displacement of a scattering particle $\langle \Delta R(\tau)^2 \rangle$ can be determined as:

$$\langle \Delta R(\tau)^2 \rangle = 6D_S\tau \quad (9)$$

which denotes the average squared distance travelled by a scattering particle in a certain time τ . The use of a Fourier transform results in the corresponding dynamic structure factor:

$$F_S(q, \tau) = \exp(-q^2 \langle \Delta R^2(\tau) \rangle_V \tau/6) = \exp(-D_S q^2 \tau) \quad (10)$$

The concept of the self-diffusion coefficient can be extended to non-spherical particles. Instead of a self-diffusion coefficient, the center-of-mass diffusion coefficient D can be determined (Figure 2.3 – 2) for a sample with known temperature T and solvent viscosity η directly through the Stokes-Einstein-equation:

$$D = \frac{k_B T}{f} = \frac{k_B T}{6\pi\eta R_H} \quad (11)$$

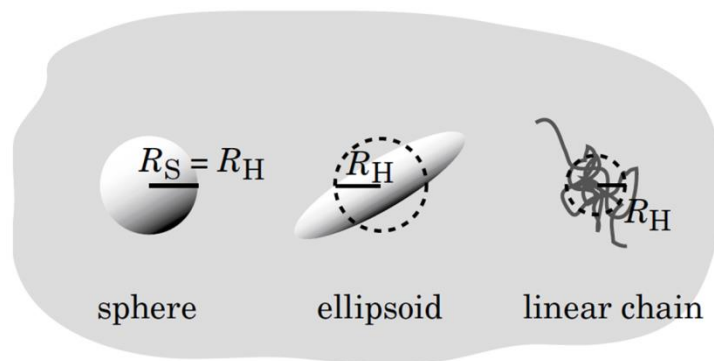


Fig. 2.3 – 2 In the center-of-mass motion approach, an ellipsoid with a hydrodynamic radius R_H receives the same friction as a sphere of radius R_H does. In the same approach, for a polymer chain with R_H the diffusion coefficient must also be the same (Reproduced from reference¹⁵², © 2002 WILEY-VCH Verlag GmbH & Co. KGaA, Weinheim).

2.3.2 Zeta potential

Around a charged particle dispersed in an electrolyte solution, a layer will be formed by ions presenting opposite charges to the ones at the particle surface. An ionic cloud can be formed in the surrounding of the particle, with a high concentration of counter-ions. This behavior of the counter-ions in the proximity of the particle surface is described by the Stern-Gouy-Chapman theory, which previews the drop of the surface potential across two layers: one compact inner layer and one diffuse outer layer.¹⁵⁵ The distribution of ions in

these two layers will depend upon the concentration of ions in the electrolyte solution, the charges, the solvent and the potential at the boundary region between the compact and the diffuse layers. When submitted to a flow field, a shear plane is developed at the interface between the compact and the diffuse layers, and the potential difference in this shear plane is the so-called zeta (ζ) potential (Figure 2.3 – 3).

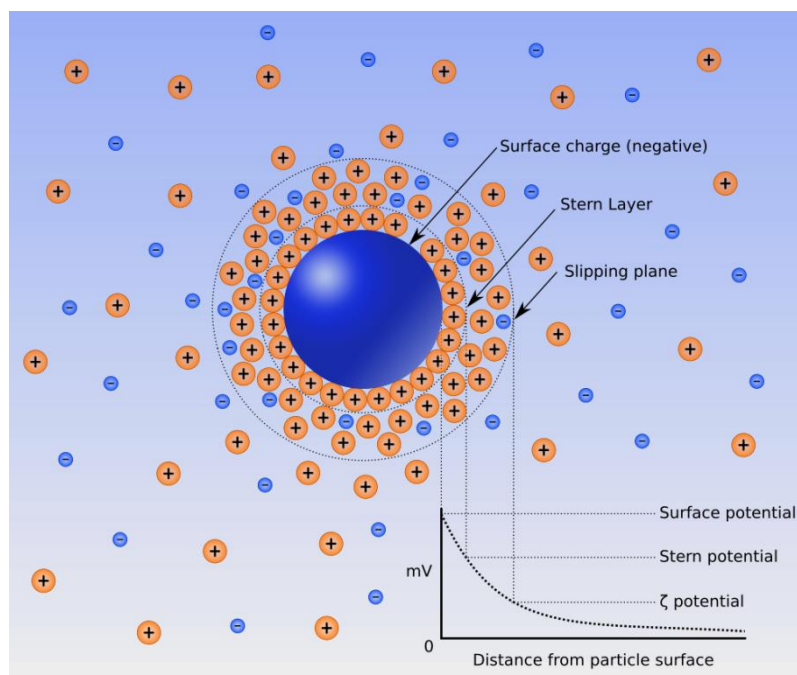


Fig. 2.3 – 3 Schematic representation of the compact and diffuse layers formation in the surrounding of a charged particle in an electrolyte and the determination of the zeta potential at the shear plane. Even though the zeta potential is not equal to the Stern potential and the electric surface potential, its determination provide important knowledge about the electric stabilization of the colloidal dispersion.

The determination of the zeta potential can be conducted by electrokinetics experiments, as electrophoresis and electroacoustic phenomena, where the current or voltage applied are related to the relative flow between two phases in the suspension.¹⁵⁵

2.3.3 Scanning electron microscopy (SEM)

Scanning electron microscopy has become a fundamental tool in the study of materials morphology, composition and surface interactions. Basically, a beam of electrons is firstly focused in a small spot and then scanned over the sample. When the electrons of

the beam hit the surface either radiation is emitted from the atoms composing the sample, according to the energy of the beam and the binding energy of the electrons of the atom to its electronic layer, or electrons of the beam are scattered. In any case, the radiation originating from the interaction between the electron beam and the sample is collected and results in an image.¹⁵⁶ Figure 2.3 – 4 shows a schematic diagram of a scanning electron microscope (model JSM – 5410, JEOL).

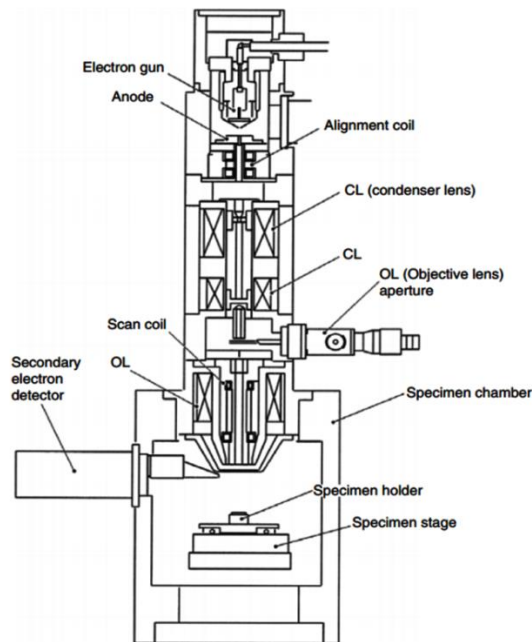


Fig. 2.3 – 4 Schematic diagram of a scanning electron microscope, model JSM – 5410 (JEOL, USA) (Scanning microscopy for nanotechnology: Techniques and applications, 2007, 1-40, Fundamentals of scanning electron microscopy (SEM), Zhou W., Apkarian, R., Wang Z. L., Figure 1, copyright © Springer. Reproduced with kind permission from Springer Science and Business Media).¹⁵⁷

The limits for resolution are dependent of the wavelength of the light source used. It means that the resolution provided by scanning electron microscope will be related to the wavelength of the electron beam. Abbe's equation relates the resolution and the wavelength:

$$d = 0.612\lambda/n \sin\alpha \quad (12)$$

where d is the smallest distance that can be resolved, λ the wavelength of the radiation source, n is the index of refraction of the medium between point source and lens, relative to free space, α is equal to half the angle of the cone of light from sample plane accepted by

the objective (half aperture angle, radians).¹⁵⁷ The wavelength of an electron beam is calculated based in the de Broglie equation, assuming relativistic effects due to the high electron velocity due to the accelerating potential usually applied. The electron beam can reach velocity in the order of 20% of the speed of light with an accelerating potential of 10 kV. Thus, a wavelength of the order of 12 pm can be obtained, resulting in very good resolution.

Besides the resolution, the quality of the image formed in a scanning electron microscope is dependent on the interaction between sample and electron beam. These interactions can be classified as elastic and inelastic.¹⁵⁷ An elastic scattering is the result of deflection of an incident electron by the atomic nucleus or shell electrons of similar energy composing the sample, which results in negligible energy loss by the incident electrons and a wide-angle directional change.¹⁵⁷ In case the scattering angle is more than 90°, the electrons are called as backscattered electrons (BSE), which are normally used in order to obtain compositional and topographic information of the sample.¹⁵⁷ Inelastic scattering will happen in the case the electron beam interacts with the sample, which is basically related to energy transfer of the incident electrons to the atoms of the sample. The amount of energy transferred is dependent of how the sample is excited (single molecules and atoms or groups) and the binding energy of the electron to a determined atom shell.¹⁵⁷ Ionization of the sample generates the so-called secondary electrons (SE), normally used to image and analyze the sample. Besides secondary electrons, characteristic X-rays, Auger electrons and cathodoluminescence are also produced. Characteristic X-rays are of special interest in the analytical chemical investigation of samples. The exploitation of these property resulted in the development of energy-dispersive X-ray spectroscopy analysis coupled to scanning electron microscopes, a popular elemental analysis tool.

2.3.4 Transmission electron microscopy (TEM)

Together with SEM analysis, transmission electron microscopy is an essential technique in the characterization of materials, especially in the nanoscale. As well as scanning electron microscopes, transmission electron microscopes also are based in the use of electron beam accelerated by high voltages, allowing the production of very low wavelengths and therefore high resolution. Nevertheless, while for SEM microscopes beam energy of the order of 10 keV-40 keV is used, TEM microscopes use energy in the order of

100 keV-400 keV, thus resulting in smaller wavelengths and consequently higher resolution.¹⁵⁸

In a classical TEM microscope, a thin specimen is irradiated by the high energy electron beam, generated in the electron gun by thermionic, Schottky or field emission. A three or four-stage condenser-lens controls the illumination aperture and the area of the sample illuminated. The lens system is responsible for the imaging of the electron intensity distribution behind the sample.¹⁵⁹ Figure 2.3 – 5 shows a schematic ray path for a transmission electron microscope.

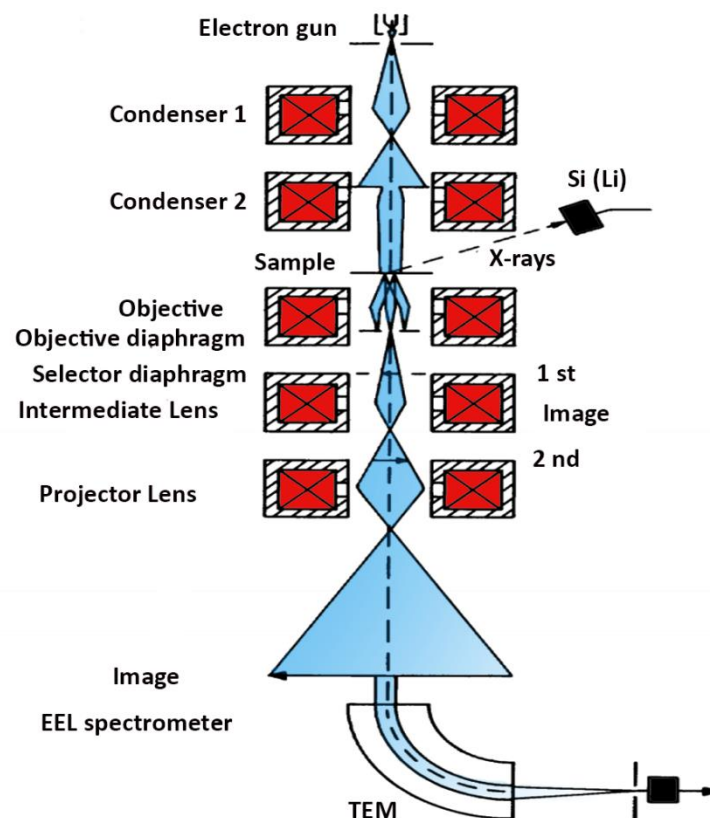


Fig. 2.3 – 5 Schematic electron beam pathway in a conventional transmission electron microscope.

As well as for SEM microscopes, the image generated by a TEM microscope is result of the interaction of the high energetic electron beam with the sample, which can result in a series of different signals. These signals can be detected by the different kinds of detector, generating image and the possibility of compositional analysis as EDX or electron-loss spectrometry (EELS).¹⁵⁸

TEM analysis is of special interest in the study of core-shell morphologies, allowing the investigation of important information as particle size, core size, shell thickness, uniformity etc. TEM image contrast results of the scattering of the electron beam with the sample. Bright field images are caused mainly due to amplitude contrast, which results of variations in the mass or thickness of the components of the sample. For core-shell like materials, the difference of composition and dimensions between the core and the shell will produce high contrast in bright field images, what makes TEM analysis of special importance in the study of nanocapsules systems.¹⁶⁰

2.3.5 Luminescence spectroscopy

Luminescence spectroscopy is a useful method in the determination of the electronic structure of localized centers and energy transfer processes. In contrast with the photoacoustic spectroscopy, based on the detection of absorbed photons through the transformation of the generated heat energy into mechanical (sound) energy,¹⁶¹ luminescence spectroscopy makes use of radiative deactivation of an previously excited sample through fluorescence, which is the result of an allowed transition from the first singlet excited state to the a singlet ground state ($S_1 \rightarrow S_0$), or phosphorescence, a spin-forbidden transition from a triplet excited state to the singlet ground state ($T_1 \rightarrow S_0$) generated by a previous intersystem crossing process (ISC).¹⁶¹

Different methods can be used for sample excitation in luminescence spectroscopy. Photoluminescence method has photons as excitation source, cathodo-luminescence uses cathode rays, electro-luminescence by electric fields and thermo-luminescence makes use of the thermal release of energy stored in solids previously excited.¹⁶² In this work, photoluminescence was the method used for investigation of emission phenomena in upconversion colloidal systems. Figure 2.3 – 5 shows a general scheme of a basic set-up for luminescence spectra recording using a photoluminescence excitation source. Luminescence or emission spectra are recorded by scanning the monochromator, which will analyze the energy emitted from the sample at a certain excitation condition. The photons emitted can have lower energy than the photons used for excitation (Stokes emission) or higher energy than the energy of the photons provided by the excitation source (anti-Stokes emission).¹⁶²



Fig. 2.3 – 5 General set-up for the recording of luminescence spectra with a photon excitation source.

Besides recording the emission, luminescence lifetime measurements are also of great interest. In this method, the decay of a certain excited state is followed with time and the luminescence lifetime is defined as the time necessary for a decrease of $1/e$ of the initial intensity of the luminescent process.¹⁶¹

2.3.6 Heteronuclear multiple-bond correlation spectroscopy (HMBC)

One of the most usual solution NMR experiments in the elucidation of organic molecules structure is the heteronuclear multiple-bond correlation spectroscopy (HMBC), a technique based on multiple quantum experiments once proposed by Müller¹⁶³ and further developed by Bax and Sammers.¹⁶⁴ HMBC is normally used as a 2D technique, usually to establish long-range correlations, i.e. over two or more bonds correlations, between protons and heteronuclei as ^{31}P , ^{15}N , ^{13}C or ^{19}F for example.¹⁶⁵ To illustrate the principles of HMBC, a ^1H - ^{13}C HMBC is here explained. In two-dimensional NMR experiments in general, the signal is recorded as a function of two times variables, t_1 or evolution and t_2 or detection, which are preceded by a preparation period, where the sample is excited, and a mixing period respectively. In a classic inverse detection experiment, the abundant nucleus (^1H) is first excited. The magnetization is then transferred to the less abundant and low- γ (gyromagnetic ratio) nucleus, in this particular case ^{13}C . After an evolution period, the magnetization of the ^{13}C nuclei is transferred back to the high- γ nuclei, ^1H , to obtain the FID under broadband decoupling of ^{13}C nuclei to give signals free of ^1H - ^{13}C couplings.¹⁶⁶

2.3.7 Magic angle spinning solid state NMR spectroscopy (MAS-NMR)

The absence of molecular motion in solids can influence severely the line width $\Delta\omega$, in NMR spectra resulting in very large $\Delta\omega$ and consequently difficulties in the study of

electron shielding and indirect spin interactions for example. The cause of such a characteristic in solid-state NMR spectroscopy is the direct dipole-dipole interactions presents in the sample. Magic-angle spinning (MAS) is one of the simplest methods to eliminate these dipole-dipole interactions and anisotropic chemical shift broadening while keeping the isotropic chemical shift. To produce such an effect, the MAS frequency must be higher or equal to proton dipolar line width, being this, therefore, an essential limitation for this technique.¹⁶⁷

The influence of the macroscopic spinning in the sample line width can be understood according as follows: in the presence of dipole-dipole interactions the NMR spectrum is defined by the secular part of the dipole-dipole Hamiltonian, which can be written as follows for the nuclei of the same magnetic species:¹⁶⁸

$$\hat{\mathcal{H}}_d = \gamma^2 \hbar^2 / 2 \sum_{ji} r_{ij}^{-3} (3 \cos^2 \theta_{ij} - 1) (\hat{I}_i \hat{I}_j - 3 \hat{I}_{zi} \hat{I}_{zj}) \quad (13)$$

and for the nuclei of different magnetic species:

$$\hat{\mathcal{H}}_d = 1/2 \sum_{ji} \gamma_{ij} \hbar^2 r_{ij}^{-3} (1 - 3 \cos^2 \theta_{ij}) (\hat{I}_{zi} \hat{I}_{zj}) \quad (14)$$

The application of a certain angular velocity ω_{rot} make that each internuclear vector \vec{r}_{ij} describes a cone about the z' axis, as depicted in Figure 2.3 – 6.

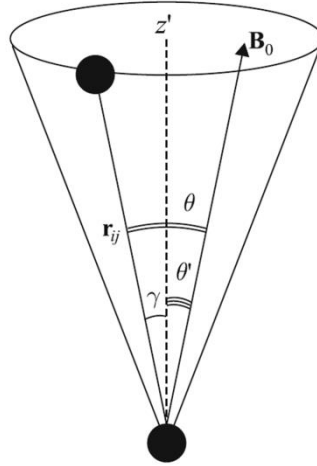


Fig. 2.3 – 6 Reorientation of the internuclear vector \vec{r}_{ij} when submitted to rotation at a certain angular velocity under an external magnetic field \mathbf{B}_0 (Magnetic resonance and its applications, 2014, 273-346, Nuclear magnetic resonance in diamagnetic solids, Chizhik, V. I., Chernyshev, Y. S., Donets, A. V., Frolov, V. V., Komolkin, A. V., Shelyapina, M. G., Figure 5.11, copyright © Springer. Reproduced with kind permission from Springer Science and Business Media).¹⁶⁸

Accordingly to Figure 2.3 – 6, $\cos(\theta_{ij})$ can be defined as:

$$\cos(\theta_{ij}) = \cos\theta' \cos\gamma_{ij} + \sin\theta' \sin\gamma_{ij} \cos(\omega_{rot}t + \phi_{0ij}) \quad (15)$$

which can be substituted in equation 13 , resulting in:

$$\begin{aligned} \hat{\mathcal{H}}_d = 1/2 \sum_{ij} \gamma^2 \hbar^2 r_{ij}^{-3} [& 1/2(3\cos^2\theta' - 1)(3\cos^2\gamma_{ij} - 1) \\ & + 3/2\sin 2\theta' \sin 2\gamma_{ij} \cos(\omega_{rot}t + \phi_{0ij}) \\ & + 3/2\sin^2\theta' \sin^2\gamma_{ij} \cos(2\omega_{rot}t \\ & + \phi_{0ij})] (\hat{I}_i \hat{I}_j - 3\hat{I}_{zi} \hat{I}_{zj}) \quad (16) \end{aligned}$$

The first term in the brackets can be considered constant, while the other two contributions are periodic and have average result equals to zero. Thus, the first term of the Hamiltonian can be described as:

$$\hat{\mathcal{H}}_d = \frac{1}{2} (3\cos^2\theta' - 1) \frac{\gamma^2 \hbar^2}{2} \sum_{ij} r_{ij}^{-3} (3\cos^2\gamma_{ij} - 1) (\hat{I}_i \hat{I}_j - 3\hat{I}_{zi} \hat{I}_{zj}) \quad (17)$$

It will determine the contribution of the dipole-dipole interaction in the MAS-NMR spectrum, while the second and third terms, corresponding to the frequencies ω_{rot} and $2\omega_{rot}$ respectively will correspond to the rotational side bands found at frequencies $\omega_0 \pm n\omega_{rot}$, which will decrease in intensity with increasing spinning frequency ω_{rot} . If the angle θ' between the rotation axis and the magnetic field vector \vec{B}_0 can satisfy the condition:

$$(3\cos^2\theta' - 1) = 0,$$

at a high rotation speed $\omega_{rot} > \Delta\omega$ (decreasing the influence of the second and the third term of equation 27), the theoretical value of the line width caused by dipole-dipole interactions should be zero. This condition is achieved for $\theta = 54^\circ 44'$, the so called "magic" angle. Therefore, MAS experiments are a tool of great value in the analysis of solids, achieving not only the reduction or elimination of dipole-dipole interactions interferences, but also the magnetic shielding anisotropy as well as first order quadrupolar interactions, affording high resolution solid state NMR spectra recording.¹⁶⁸

3 Results and discussions

3.1 PPE nanoparticles for potential bone cancer therapy¹⁻³

This section covers the development of PPE nanoparticles obtained using a direct miniemulsion/solvent-evaporation technique. New synthetic polyphosphoesters developed by acyclic diene metathesis (ADMET) or ring opening metathesis polymerization (ROMP) (in collaboration with Dr. Filippo Marsico and Dr. Tobias Steinbach) were applied in the preparation of nanoparticles. The surface interaction with a bone substitute material, a calcium phosphate-based cement, was evaluated. The principles behind the control of the specific interaction between PPEs and calcium were evaluated by solid state NMR experiments. Paclitaxel, an anti-mitotic drug, was loaded up to 15 wt% in the PPE nanoparticles with the most promising adhesion properties and the effects in the colloid properties, bone adhesion and in the *in vitro* activity against HeLa and SaOs-2 cells was evaluated in collaboration with Dr. Sandra Ritz. This chapter contains content of three previously published papers.¹⁻³



(Alexandrino *et al.*; *J. Mater. Chem. B*, 2014,2, 1298-1306, <http://pubs.rsc.org/en/Content/ArticleLanding/2014/TB/c3tb21295e#!divAbstract> - Reproduced by permission of The Royal Society of Chemistry.)

3.1.1 Motivation

Bone as a site of cancer growth can be either by: bone sarcomas, which include osteosarcoma and Ewing's sarcoma,¹⁶⁹ or - more common - it can be a consequence of other tumors that spread by metastasis to the bone tissue.^{170, 171} Among the types of cancer that spread by metastases to the bone tissue, breast and prostate cancer stand out, presenting metastases in approximately 70% - 80% in advanced stages of the disease.¹⁷⁰⁻¹⁷² The most common treatment for primary bone tumors or bone metastases is a combination of different techniques, such as surgical removal, fixation and chemotherapy, treatment with radioisotopes or by radiation strategies.¹⁷¹ The chemotherapeutic treatment is normally performed after the surgical intervention; with the main purpose of slowing down the tumor growth and metastases outgrowth.¹⁷³ Drugs are selected on the basis of the susceptibility of the primary tumor. For breast and ovarian tumors this would include doxorubicin^{174, 175} and paclitaxel (PTX).^{173, 176} PTX (Figure 3.1 – 1) has a high potency against many different types of cancer by stabilizing the tubulin system,¹⁷⁷ which leads to a suppression of the microtubule dynamics, mitotic arrest, and finally to death by apoptosis.^{177 178, 179}

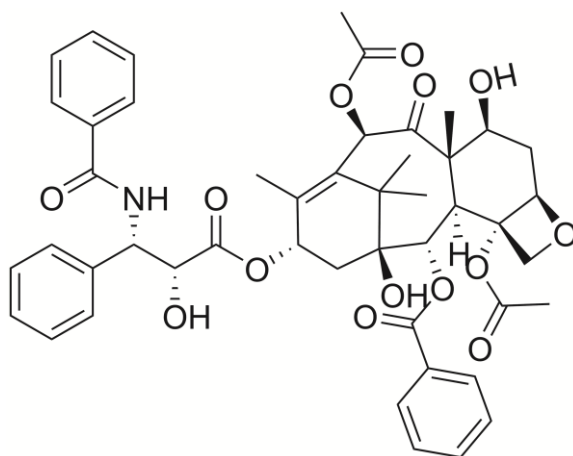


Fig. 3.1 – 1 Chemical structure of Paclitaxel.

Despite of these interesting properties, PTX shows poor water solubility¹⁷⁸ and does not have any bone surface targeting specificity. Higher solubility was achieved by the use of macroglycerolricinoleat (Cremophor EL[®]) and ethanol to solubilize the drug.^{178, 179} However, the toxicity of Cremophor EL created the necessity for the development of new carrier systems for the PTX application like nanoparticles or liposomes.^{178, 180-187}

Biodegradable polymer nanoparticles based on 'conventional' poly-(C)-esters were intensively studied with promising results concerning the encapsulation and activity of

hydrophobic drugs.¹⁸⁷ Recently, polyesters,¹⁸⁸⁻¹⁹⁰ poly(benzyl-L-glutamate),¹⁹¹ poly[N-(2-hydroxypropyl) methacrylamid],¹⁹² poly(ethylene imine)), and poly-L-lysine¹⁹³ based micro- and nanoparticles for targeted delivery to bone have been reported. The targeting profile depends mainly on the nanoparticle surface-chemistry, which is typically achieved by the introduction of targeting groups at the nanoparticle surface,^{187, 194} such as bisphosphonates and derivatives,¹⁹⁵ or oligopeptides¹⁹⁶ that can specifically target bone.^{197, 198} Due to the high affinity to the bone mineral hydroxyapatite (HA), bisphosphonates have emerged as a great option for a bone targeted therapy and have been studied intensively.^{171, 199} However, side effects have been reported for bisphosphonates as osteonecrosis of the jaw (ONJ), atrial fibrillation, and renal insufficiency.^{199, 200}

A promising alternative for the production of biodegradable nanoparticles with a potential inherent bone targeting ability are polyphosphoesters. Polyphosphoesters (PPE) are a major class of polymers composed by the sub-classes polyphosphates, polyphosphonates, polyphosphoramidates and polyphosphines, which are highly versatile biodegradable materials that allow easy modification of backbone, side chains, and end groups to tailor the functionality and solubility profile, features that stimulated the interest in these materials recently.^{121, 201} No other polymeric material shows this high versatility that is mainly due to the ability of phosphorus to form triesters and, in addition, having the possibility to interact with calcium. Further, the pendant ester results in usually less crystalline polymers compared to poly-(C)-esters. Even more, PPEs can be degraded both enzymatically and hydrolytically which makes them interesting also for long term use *in vivo* as no accumulation should occur.

In this thesis, we present the formation of PPE-nanoparticles (PPE-NPs) prepared by the miniemulsion/solvent-evaporation technique, the loading of this nanoparticles with Paclitaxel and the interaction with calcium phosphates cements.^{1-3, 202} These PPE homopolymers were prepared by a recently developed general synthetic protocol via olefin metathesis (via acyclic diene metathesis (ADMET) and ring-opening metathesis (ROMP) polymerization) in collaboration with Dr. Filippo Marsico and Dr. Tobias Steinbach.^{3, 16, 203} These novel hydrophobic PPEs were used for the preparation of potentially biodegradable and biocompatible nanoparticles that were efficiently loaded with PTX and that prove a strong interaction with calcium phosphate surfaces. The evaluation of the cytotoxicity properties against HeLa and Saos-2 cell lines was performed in collaboration with Dr. Sandra Ritz.

3.1.2 Experimental part

3.1.2.1 Materials

The synthesis of the polyphosphates by ADMET (Scheme 3.1 – 1), with molecular weight in the range of M_w 6,000 - 20,000 g mol⁻¹, was done in collaboration with Dr. Filippo Marsico and previously described.^{13, 16} The synthesis of polyphosphates by ROMP (Scheme 3.1 – 3), with M_w of around 43,000 g mol⁻¹, was done in collaboration with Dr. Tobias Steinbach, as well the synthesis of polyphosphonates - M_w 24,000 g mol⁻¹ - by ADMET (Scheme 3.1 – 2); both works were previously described.^{2, 3, 204} The hydrogenation catalyst (Sigma-Aldrich 5% Pd/C) was used as received. Sodium dodecyl sulfate (SDS) was purchased from Sigma-Aldrich. Chloroform analytical grade used for nanoparticle synthesis was purchased from VWR and water was purified by reverse osmosis (Milli-Q, Millipore®). The BODIPY-dye was synthesized according to reference method.²⁰⁵ Paclitaxel for research use was obtained from LC Laboratories and Taxomedac® (6 mg mL⁻¹) was purchased from medac (Wedel, Germany). A cellulose membrane from Carl Roth GmbH type 20/32 (molecular weight cut off 14,000 g mol⁻¹) was used for the dialysis purification process. The HPLC grade solvents THF, methanol and 0.1 % trifluoroacetic aqueous solution were obtained from Sigma-Aldrich, VWR and Merck respectively. HCl solution (37%) was obtained from Sigma-Aldrich. A micro-macro porous biphasic calcium phosphate cement (MBCP+), composed of 80% hydroxyapatite and 20% β -tricalcium phosphate, was donated from Biomatlante (Vigneux de Bretagne, France). Anhydrous CaCl₂, NaCl and Tris buffer were obtained from Sigma – Aldrich and used without further purification.

3.1.2.2 Nanoparticle preparation

PPE nanoparticles were synthesized using an adopted combination of the miniemulsion technique and the solvent-evaporation strategy.²⁰² 30 mg of the polymer were dissolved in 1.25 g of chloroform. To this solution, 0.05 mg of Bodipy or a given amount of paclitaxel was added. 5 g of Milli-Q water containing 10 mg of SDS were added to the chloroform solution and stirred during over a period of 60 min for the formation of the pre-emulsion. Then, the pre-emulsion was submitted to a pulsed ultrasonication process under an ice bath during 120 s (30 s sonicated and 10 s paused) at 70% amplitude in a ¼" tip Brason 450 W sonifier. The obtained miniemulsion was kept at 30 °C in an oil bath over a period of 8 h to completely evaporate the organic solvent. The obtained nanoparticles

dispersion was further purified by exhaustive dialysis against water before being used for further studies.

The average particle size and particle size distribution were obtained by dynamic light scattering (DLS) in a submicron particle sizer NICOMP® 380 equipped with a detector to measure the scattered light at 90°. The multi-angle dynamic light scattering measurement was performed in a ALV/CGS3 compact goniometer system with a He / Ne laser (632.8 nm), correlator ALV/LSE-5004 and evaluated with the ALV5000 software. The zeta-potential of the solutions were obtained using a Zetasizer NanoZ using as dispersive phase an aqueous 1×10^{-3} M KCl solution. The particle morphology was studied by scanning electron microscopy (SEM) using a microscopy Zeiss LEO Gemini 1530. Previous to the measurement a thin carbon coating layer was deposited using a vacuum coating system Leica EM MED020. Transmission electron microscopy (TEM) was performed in a JEOL 1400 microscope, after drop cast of the nanoparticle dispersion onto a carbon coated copper grid.

3.1.2.3 Thermal characterization

For evaluation of crystallinity of the paclitaxel loaded - polyphosphate nanoparticles and the influence of the dispersion of paclitaxel in the nanoparticles on the degree of crystallization, as well as the evaluation of the different additives in the crystallization of UPPE-C20-Hydroxy, differential scanning calorimetry (DSC) of the samples was performed in a Perkin Elmer DSC 8500, with a single heating ramp from -80 °C to 240 °C, at a heating rate of 10 °C min⁻¹. For the experiments, the nanoparticle samples were centrifuged at 18,000 rpm at 4 °C over a period of 30 min, the supernatant was decanted, and the residue was lyophilized.

3.1.2.4 Encapsulation efficiency

The quantity of the encapsulated paclitaxel in the polyphosphate nanoparticles was analyzed in triplicate on a HPLC (Hewlett Packard Series 1100). A reverse phase Spherisorb® ODS-2 column (250 x 4 mm i.d., pore size 5 µm, Lichrocart) was selected. A given amount of the nanoparticle dispersion was centrifuged at 18000 rpm at 4 °C over a period of 30 min, the supernatant was decanted, and the residue was lyophilized (this typically resulted in 1-3 mg of solid). The solid was dissolved in 1 mL of a mixture of THF: 0.1% aqueous

trifluoroacetic acid (70:30), ultrasonicated when necessary to help the dilution process, and filtered through a 0.45 μm PVDF filter before injection. A 10 μL injection was performed using an auto-sampler of the Agilent 1200 series. The mobile phase consisted of first an isocratic mixture of methanol: 0.1% aqueous trifluoroacetic:THF (40:40:20) over a period of 8 min to elute the drug at 1 mL min^{-1} (its retention time under these conditions is approximately 6.6 min) and after a gradient until a pure THF mobile phase was performed in the next 5 min, followed for a 3 min isocratic flow of 100% THF for the elution of the polymer. Detection was accomplished with a UV-Vis detector (Soma S-3702) at a wavelength of 227 nm. To determine the amount of paclitaxel, the set up was calibrated with paclitaxel in the range of 50 ng mL^{-1} -30,000 ng mL^{-1} . The encapsulation efficiency was determined as the ratio between the theoretical concentrations of paclitaxel expected for the starting amount of nanoparticles diluted to the concentration result obtained from the HPLC measurements, expressed in percentage.

3.1.2.5 Calcium phosphate attachment studies

The calcium phosphate particles (MBCP+, 80-200 μm , Biomatlante) have been dispersed in ultrapure water (10 mg mL^{-1} , Millipore) and washed for 30 min under horizontal agitation (200 rpm) before use. NP-PPE particles were dissolved in deionized water at an initial concentration of 1-3% and were diluted to application concentrations of 0.01% with deionized water in 1.5 mL Eppendorf centrifuge vials (1 mL nanoparticle solution volume). The calcium phosphate granules were left in the nanoparticle solution for 30 min immediately following deposition. The samples were placed on a shaker table at 180 rpm in order to expose all sides of the particles to the nanoparticles and stimulate attachment. After attachment the tubes were centrifuged at 1,000 rpm for 5 min, the majority of the liquid was pipetted from the tube and removed, and the tube was refilled with deionized water and vortexed to remove the loose and weakly attached nanoparticles from the calcium-phosphate granules. This process of centrifuging, removing the liquid, replacing the liquid with fresh deionized water, and vortexing was repeated two additional times. After the three rinses were complete, the samples centrifuged again and stored dry or in water before observation in the scanning electron microscopy (SEM, Zeiss LEO Gemini 1530). Previous to the measurement a thin carbon coating layer was deposited using a vacuum coating system Balzer Union (BAE250) (Figure 3.1 – 2).

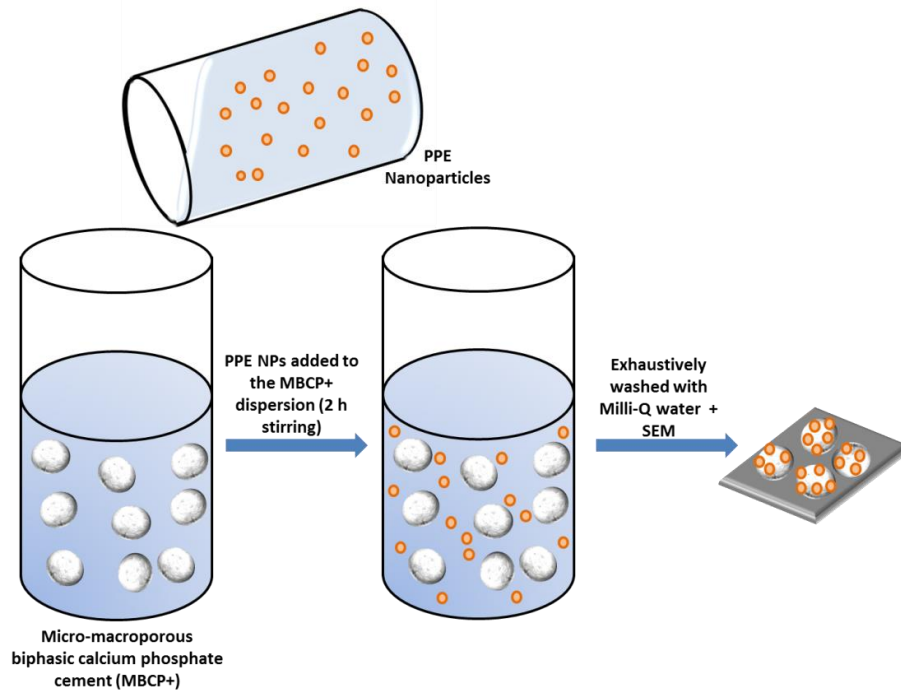


Fig 3.1 – 2 Experimental scheme of the nanoparticles attachment in MBCP+ experiment.

3.1.2.6 Cell viability assays

The evaluation of the cell viability was performed in cooperation with Dr. Sandra Ritz. Human cervix carcinoma cells, HeLa cells (#ACC57, DMSZ, Germany), were cultured in DMEM medium (Invitrogen) and human osteosarcoma cells, SaOS-2 (#ACC 243, DSMZ, Germany) were cultured in RPMI (Invitrogen) medium in a humidified incubator at 37°C/5% CO₂. Both media were supplemented with 10% fetal calf serum (FCS, Gibco), 100 units penicillin and 100 mg mL⁻¹ streptomycin (Life Technologies).

The effect of PTX (10 mM stock solution in DMSO), NP-PPE, and Taxomedac[®] (6 mg mL⁻¹ containing 527 mg mL⁻¹ macroglycerolricinoleat and 395 mg mL⁻¹ ethanol) on cell viability was measured by CellTiter-Glo or PrestoBlue[™] staining (Invitrogen) according to the manufactures protocol. Briefly, HeLa or Saos-2 cells (1.5 x10⁴ cells/well) were diluted in the indicated cell culture medium and seeded in 96 well-plates (black plate, clear bottom, corning, Amsterdam, Netherlands). The culture medium was replaced after ~16 h by compound supplemented medium (200 µL, DMEM, 10% FCS, 0.1% DMSO) or medium without compound (DMEM, 10% FCS, 0.1% DMSO) as a specific control. After 24 h and 48 h, viable cells were stained with 20 µL PrestoBlue Reagent per well and incubated for 20 min at

37 °C/5% CO₂. Metabolically active cells reduce the cell permeable dye resazurin into fluorescent resorufin, which was measured with a fluorescence plate reader (excitation wavelength 560 nm, emission wavelength 590 nm, Tecan Infinite M1000, Austria).

3.1.2.7 Interaction experiments and magic-spinning angle solid state NMR measurements

Solid-state NMR measurements were performed with the polymers UPPE-C20-Hydroxy, PPE-C20-Phenoxy and PPE-C20-Methyl before and after exposition to aqueous solutions of determined additives (NaCl, CaCl₂, tris(hydroxymethyl)aminomethane (Tris) and a mixture of Tris + CaCl₂). The general procedure for the preparation of each sample is described: 30 mg of polymer in powder form (granulometry was not controlled) were washed during a period of 8 h with 5 mL of a 100 mmol solution of one of the additives. Solution and polymer were put in closed 10 mL glass vials and let shaking during the washing time. After the washing period, the solution excess was extracted with a syringe and the sample was further lyophilized for extraction of the all residual water. The final powders were packed into 2.5 mm zirconia rotors suitable for magic angle spinning (MAS) NMR experiments up to 35 kHz MAS spinning frequency. Using a commercial double-resonance MAS probe supporting rotors of 2.5 mm outer diameter, ³¹P MAS NMR single pulse and cross-polarization MAS (CP-MAS) NMR measurements were performed with Bruker Avance III spectrometer operating at 500 MHz at room temperature. Single pulse measurements with high power 1H decoupling acquisition (Bruker pulse program: hpdec) and CP-MAS NMR measurements (rgvacp modified version of Bruker pulse program: vacp with 2D extension for CP-HETCOR measurements) have been recorded at 10 kHz MAS spinning speed. The ¹³C{¹H} CP heteronuclear correlation (CP-HETCOR) measurements were performed with a Bruker Avance III spectrometer operating at 850 MHz 1H Larmor frequency, under controlled temperature conditions ($T = 298$ K) and 25 kHz MAS spinning speed. Wide angle XRD diffraction of the samples used for the solid state NMR experiments were performed between $2\theta=1^{\circ}$ - 40° in a Philips Pulverdiffraktometer PW 1820, with wavelength Cu 1.5418 Å.

3.1.2.8 Calcium phosphate crystallization experiment

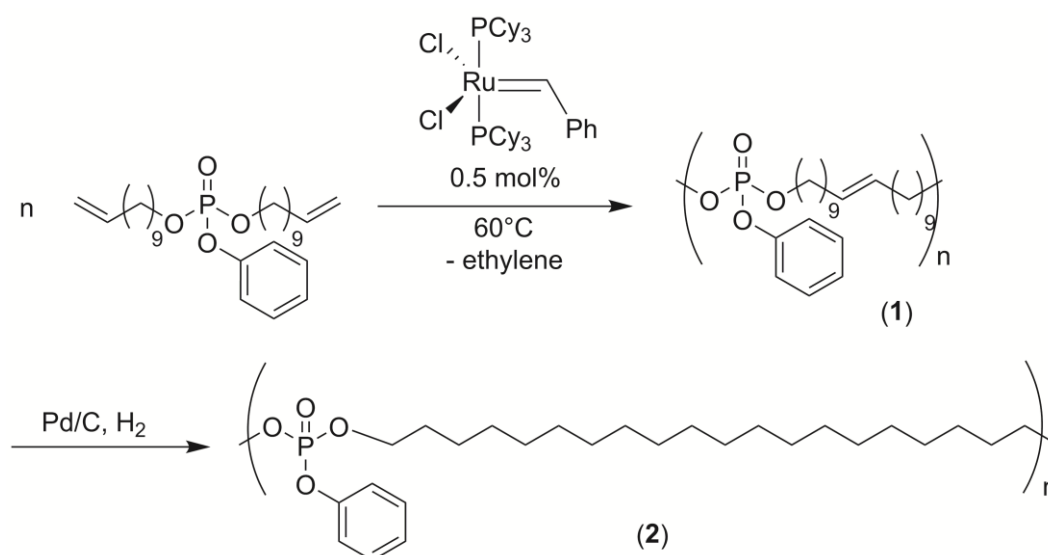
A calcium phosphate crystallization experiment was performed using nanoparticles synthesized from the polymer PPE-C20-Phenoxy. Firstly, nanoparticle dispersions were prepared according to the procedure in 3.1.2.2, with substitution of 10 mg of SDS as surfactant by the same amount of Vitamin E TPGS, a non-ionic surfactant molecule. Such change was carried out in order to lower the amount of negative charges in the surface of the particles. The dispersions were exhaustively dialyzed in a cellulose membrane (molecular weight cut-off 14,000 g mol⁻¹) against 2 L of Milli-Q water (ca. 5 days, with the whole water being renewed once per day) prior the experiments, to lower the amount of free surfactant in solution. 40 mL solution were prepared with 100 mg particles mL⁻¹ and 10 mM CaCl₂·2H₂O in Milli-Q water. The pH value of the solution was or was not adjusted to 10 with the addition of KOH. This first solution was stirred during 1 h at 300 rpm to allow the coordination of calcium ions to the surface of the particles. Meanwhile, 10 mL of a sodium hydrogen phosphate aqueous solution were prepared in order to obtain a final ratio of 5:3 phosphate to calcium (16.7 mM). The phosphate solution was added drop-wise, during 30 min-1 h, at 300 rpm stirring, and solution was left stirring at 37 °C during 24 h. At the end of this period, the sample was allowed to cool down to room temperature and was centrifuged at 4000 rpm, being freeze dried in the sequence. The final material obtained was analyzed by SEM microscopy.

3.1.3 Synthesis of PPE nanoparticles by miniemulsion/solvent-evaporation approach

Charged polyphosphates can present strong interactions with Ca²⁺ and other ions,²⁰⁶⁻²⁰⁸ being this property a good indication that these materials could present a strong interaction with calcium phosphate surfaces, like the bone inorganic matrix. Aiming potential strategies for bone cancer therapy, the use of hydrophobic polymers that can be loaded with highly hydrophobic drugs and can be used in the development of nanocarriers with bone “targeting” properties is of high interest. In addition, it would be also desirable to avoid tedious chemical post-modification steps to attach targeting moieties or ionic groups that could further interfere with the drug loading process. Accordingly to the good interaction results observed in literature for the interaction of inorganic polyphosphates with Ca²⁺,¹⁴⁸ we envisioned that PPEs would be ideal candidates to exhibit an inherent

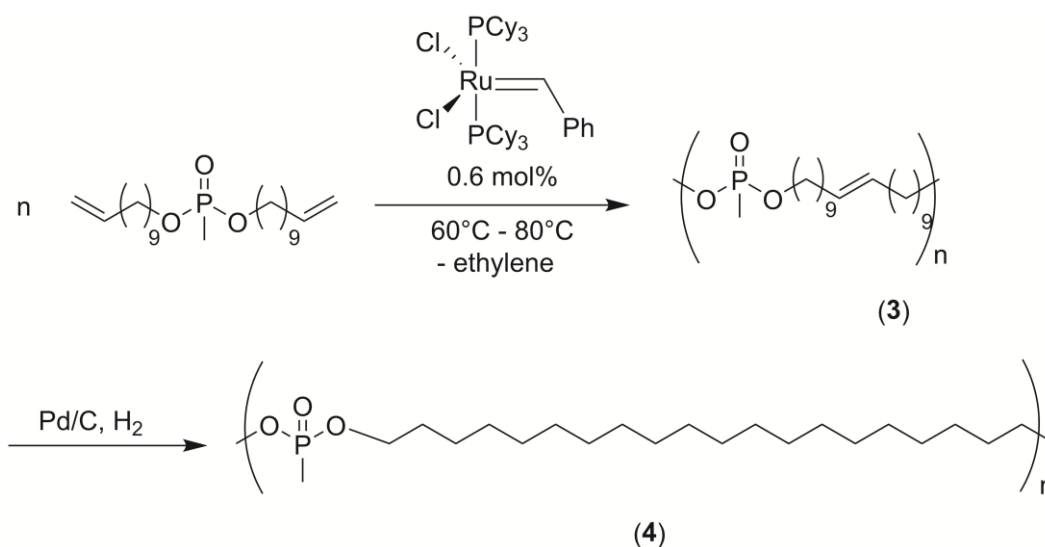
bone-targeting motive due to the multiple phosphates along the polymer backbone. Further, due to the neutral triesters, efficient loading with hydrophobic drugs should be ensured.

As a first approach, several polyphosphates with a variable number of methylene units (6, 10 or 20 carbons) between the phosphate groups were synthesized via an ADMET protocol. Scheme 3.1 – 1 presents exemplarily the synthesis of the polymer having a 20 methylene long spacer between the phosphate groups, i.e. PPE-C20-Phenoxy. After the ADMET reaction, unsaturated PPE (**1**) are obtained that are amorphous for C6 and C10 or exhibit a rather low melting point ($-7\text{ }^{\circ}\text{C}$ for C20). These polymers were hydrogenated in order to remove the double bonds that act as defects during the crystallization and to generate saturated and crystalline PPE (**2**). Nevertheless, the saturated PPE-C20-Phenoxy was still the only semi-crystalline material, with a melting point of ca. $50\text{ }^{\circ}\text{C}$ (see below).



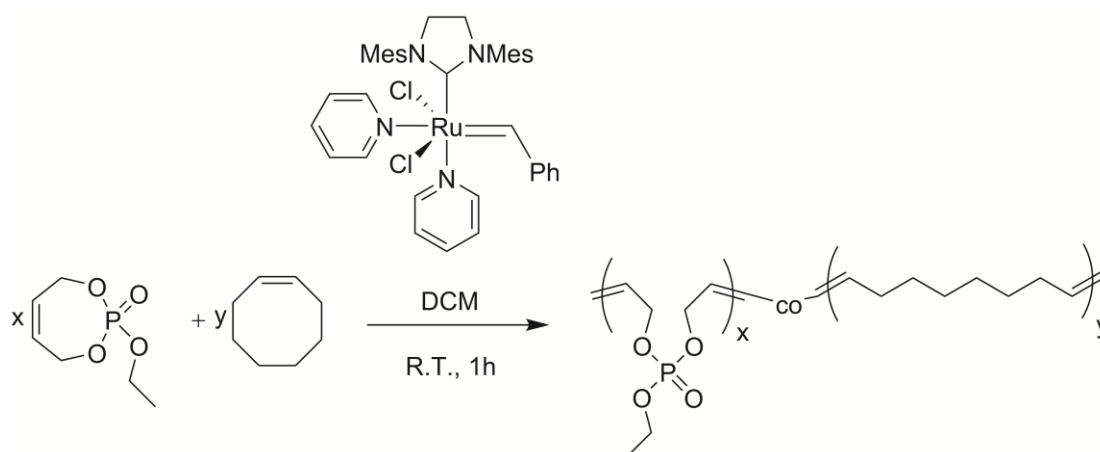
Scheme 3.1 – 1 Reaction scheme for the synthesis of the unsaturated (**1**) and saturated (**2**) polyphosphate PPE-C20-Phenoxy via acyclic diene metathesis polymerization (synthetic route developed by Dr. Filippo Marsico).

The acyclic diene metathesis polymerization approach was also applied in the preparation of new polyphosphonates, which, in comparison to the previous polyphosphates obtained, presented a less labile side chain in terms of hydrolysis. The new polyphosphonate synthesized presented a methyl group at the side chain (Scheme 3.1 – 2) and also 20 methyl groups between the phosphoesters units. The unsaturated PPE-C20-Methyl (**3**) is a semi-crystalline polymer with T_g at around $-40\text{ }^{\circ}\text{C}$ and T_m at around $20\text{ }^{\circ}\text{C}$. After hydrogenation (**4**) the T_g and T_m values raised to approximately $-15\text{ }^{\circ}\text{C}$ and $65\text{ }^{\circ}\text{C}$.



Scheme 3.1 – 2 Reaction scheme for the synthesis of the unsaturated (3) and saturated (4) polyphosphonate PPE-C20-Methyl via acyclic diene metathesis polymerization (synthetic route developed by Dr. Tobias Steinbach).

ADMET was not the only method used to obtain polymer with suitable properties for the preparation of nanoparticles by miniemulsion/solvent-evaporation. A ring-opening metathesis polymerization (ROMP) protocol was applied to obtain copolymers between a new seven membered cyclic phosphate monomer and *cis*-cyclooctene (Scheme 3.1 – 3). Copolymers with a ratio of cyclooctene:phosphate units of 10:1 (determined via ^1H NMR) and melting point around 55 °C were selected for preparation of nanoparticles. Due to the low phosphorus content, these nanoparticles were not used for further bone adhesion evaluation.



Scheme 3.1 – 3 Reaction scheme for the copolymerization of the polymer PPE-co-CO via ring opening metathesis polymerization (synthetic route developed by Dr. Tobias Steinbach).

All the polymers were used for the preparation of polymer nanoparticles by the miniemulsion/solvent-evaporation process. This method allows the easy incorporation of hydrophobic dyes and/or drugs in the nanoparticles, generating solid solutions after the evaporation of the solvent (Figure 3.1 – 3). The mean hydrodynamic diameter of the particles obtained for each of the polymers and the zeta potential values are presented in the Table 3.1 – 1. The nanoparticles mean diameter ranged between 80-300 nm and all systems showed a negative zeta-potential value, due to the surfactant used (sodium dodecyl phosphate, SDS).

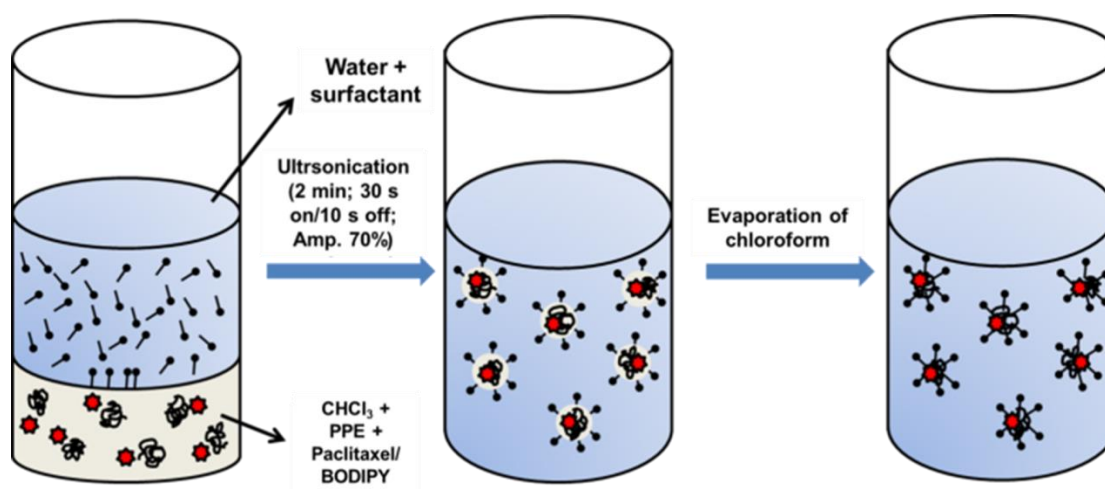


Fig 3.1 – 3 Miniemulsion/solvent-evaporation protocol used for the production of BODIPY or PTX loaded PPE nanoparticles (Alexandrino *et al.*; *J. Mater. Chem. B*, 2014,2, 1298-1306, <http://pubs.rsc.org/en/Content/ArticleLanding/2014/TB/c3tb21295e#!divAbstract> - Reproduced by permission of The Royal Society of Chemistry).

Table 3.1 – 1 Mean diameter and zeta potential for the PPE nanoparticles obtained from polyphosphates and polyphosphonate synthesized via ADMET and ROMP.

Sample	Mean diameter \pm S.D. (nm) ^a	Zeta potential (mV) ^b
PPE-NP-C6-Phenoxy	352 \pm 82	-64,3 \pm 6,3
PPE-NP-C10-Phenoxy	88 \pm 27	-59,2 \pm 11,8
PPE-NP-C20-Phenoxy	138 \pm 39	-47,4 \pm 12,5
PPE-NP-C20-Methyl	114 \pm 35	-51,7 \pm 7,7
PPE-co-CO-NP	91 \pm 37	-49,2 \pm 11,7

^a Determined via dynamic light scattering using a NICOMP Particle Size Analyzer;

^b Electrophoretic mobility determined using a Zetasizer.

From the miniemulsion/solvent-evaporation process the formation of spherical particles is expected.²⁰² The morphology of the PPE-NP-C20-Phenoxy nanoparticles has been investigated by dynamic light scattering revealing a rather uniform scattering intensity at different angles, indicating the formation of spherical nanoparticles in solution. Further, electron microscopy was used to visualize the shape of the nanoparticles. Due to the low melting point of PPE-C20-Phenoxy, we expected rather soft materials (Figure 3.1 – 4A, PPE-C6-Phenoxy and PPE-C10-Phenoxy were detected as droplets due to their amorphous structure). Compared to other polyesters, like polylactide, which has a melting point of ca. 180 °C, the low melting point is another characteristic of the herein presented PPEs. The lower degree in crystallinity may further influence the degradation kinetics. Figure 3.1 – 4B shows exemplarily scanning and transmission electron micrographs of the nanoparticles. Some of the nanoparticles suggest capsule-like morphologies, but the transmission electron microscopy analysis confirms the formation of solid particles. Figure 3.1 – 4C shows the morphology of the PPE-NP-C20-Methyl nanoparticles, which are similar to the PPE-NP-C20-Phenoxy nanoparticles, and Figure 3.1 – 4D presents the rather rounder nanoparticles obtained for the sample PPE-co-CO-NP.

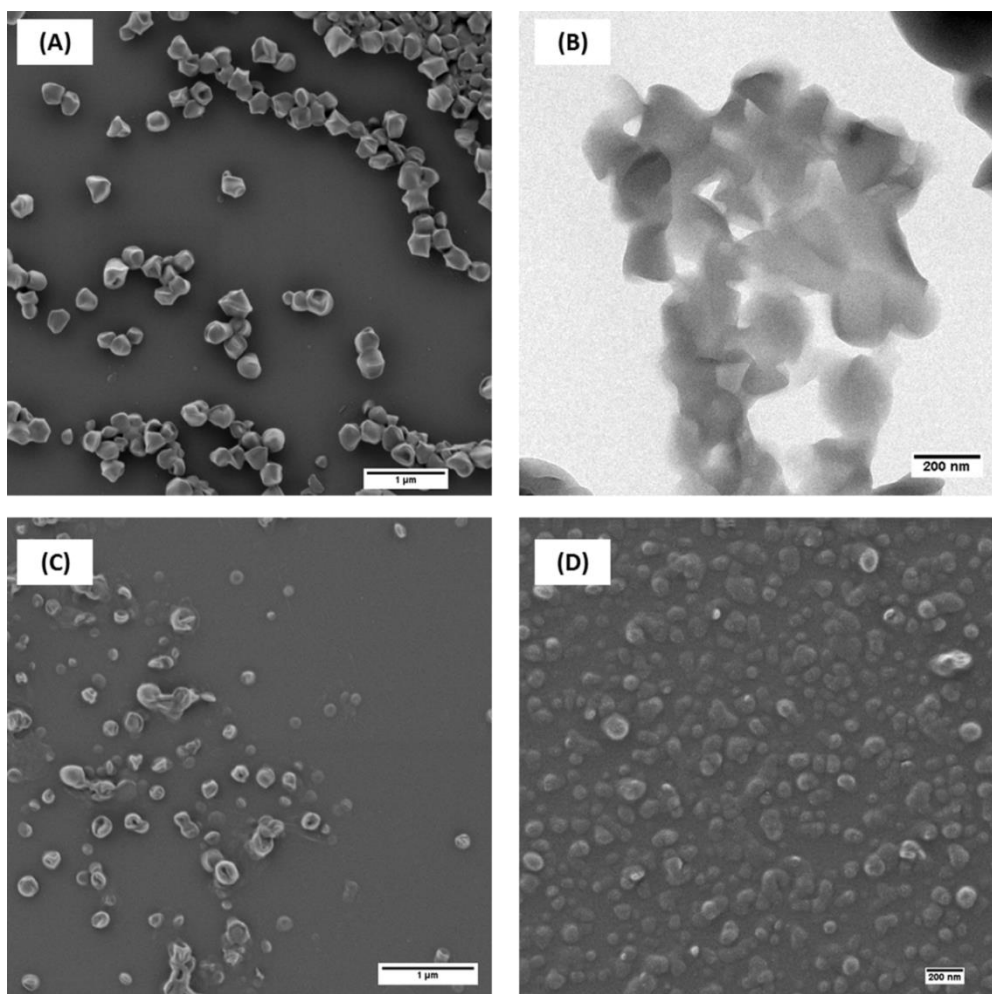


Fig. 3.1 – 4 Morphological evaluation of the nanoparticles: (A) scanning electron micrograph PPE-NP-C20-Phenoxy, scale bar 1 μm; (B) transmission electron micrograph PPE-NP-C20-Phenoxy, scale bar 200 nm (Alexandrino *et al.*; *J. Mater. Chem. B*, 2014, **2**, 1298-1306, <http://pubs.rsc.org/en/Content/ArticleLanding/2014/TB/c3tb21295e#!divAbstract> - Reproduced by permission of The Royal Society of Chemistry); (C) scanning electron micrograph PPE-NP-C20-Methyl, scale bar 1 μm (Reprinted with permission from Steinbach *et al.*, *Macromolecules*, 2014, **47** (15), 4884–4893. Copyright © 2014 American Chemical Society); (D) scanning electron micrograph PPE-co-CO-NP, scale bar 200 nm (Steinbach *et al.*; *Polym. Chem.*, 2013, **4**, 3800-3806, <http://pubs.rsc.org/en/Content/ArticleLanding/2013/PY/c3py00437f#!divAbstract> - Reproduced by permission of The Royal Society of Chemistry).

3.1.4 Evaluation of bone adhesion

The PPE nanoparticle dispersions were then evaluated with respect to their capacity to interact with bone surfaces. The MBCP+TM granules (Biomatlante) are a calcium phosphate material that have proven to be a good alternative to bone substitution since over 30 years,^{209, 210} and are currently used in spinal, tumoral, orthopedic and periodontal applications.^{211, 212} Biphasic calcium phosphate is usually composed of 20% hydroxyapatite (HA) and 80% β -tricalcium phosphate (β -TCP), a mixture that provides good bioactivity and osteoconduction properties.²¹¹ Due to these good bone substitution properties, MBCP+ was selected as a “model bone tissue” for the evaluation of the interaction with the PPE nanoparticles.

Firstly, the polyphosphate nanoparticles were evaluated. Fluorescent and non-fluorescent PPE nanoparticles (PPE-NP-C6-Phenoxy and -C10, -C20) were dispersed with the calcium phosphate granules and after extensive washing, the presence of the nanoparticles on the surface was evaluated by SEM and fluorescence microscopy (Figure 3.1 – 5). The fluorescence intensity on the granules increased with increasing number of methylene units between the phosphate groups, indicating that there is a strong attachment of these nanoparticles to the calcium phosphate granules (note that the scaling between the SEM and the fluorescence images is not the same!). This first indication was confirmed by SEM analysis as the PPE-NP-C20s can be clearly visualized on top of the cement (Figure 3.1 – 5B). This behavior can be related to the thermal properties of the three investigated polymers: as only PPE-NP-C20-Phenoxy is a crystalline solid at room temperature, the nanoparticles can attach effectively to the granules, while the nanoparticles from C6 and C10 probably form a polymer film on top of the granules, explaining that no distinct particles can be visualized via SEM. The weak fluorescence signal that is visible for amorphous materials (C6 and C10) is probably due to some remaining dye in the deposited film. The ADMET protocol herein presented is a useful tool to tailor the physical properties PPEs.

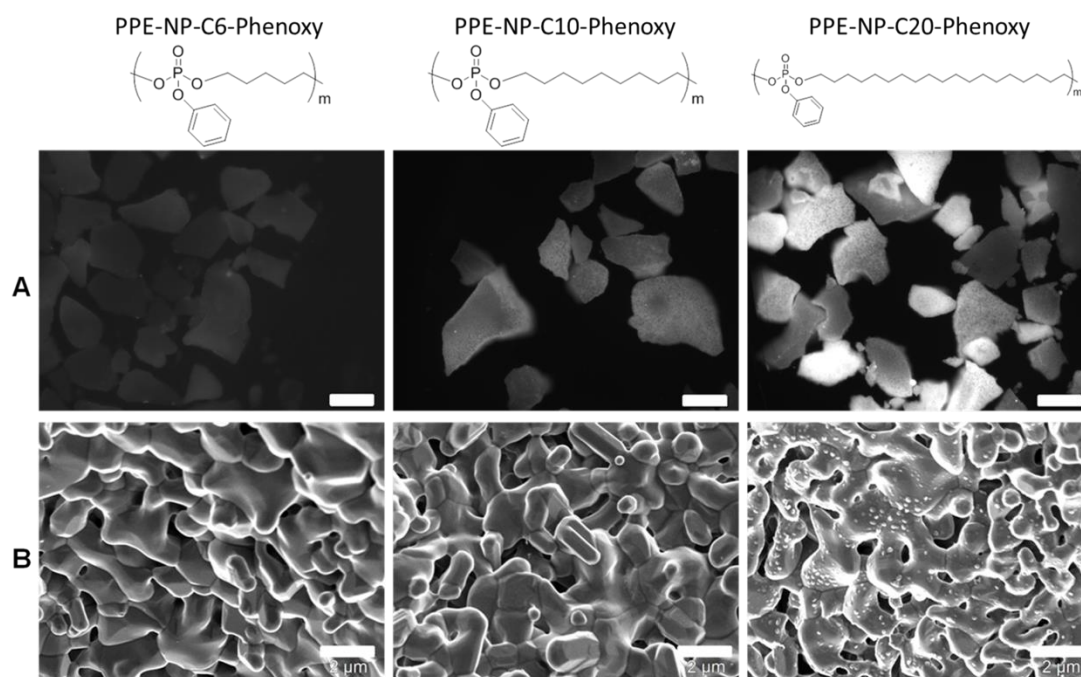


Fig. 3.1 – 5 Fluorescence images (scale bar 50 μm) (A) and scanning electron images (scale bar 2 μm) (B) of the calcium phosphate cement MBCP+ surface after exposition to a dispersion of nanoparticles NP-PPE with increasing carbon linker length (C6, C10, C20). MBCP+ is composed of 80% HA and 20% β -TCP (Alexandrino *et al.*; *J. Mater. Chem. B*, 2014, **2**, 1298-1306, <http://pubs.rsc.org/en/Content/ArticleLanding/2014/TB/c3tb21295e#!divAbstract> - Reproduced by permission of The Royal Society of Chemistry).

The attachment of the investigated PPEs is thought to be caused by the interaction of the phosphate moieties along the backbone either in their neutral state or by partial hydrolysis of the pendant (and more labile) phenyl ester. PPE-C20-Phenoxy was incubated with 0.1 M HCl to induce hydrolysis and the release of a low molecular weight compound (Figure 3.1 – 6) was detected by the UV detector during a SEC (size exclusion chromatography) experiment, while the apparent molecular weight of the polymer remained rather constant indicating that in this case the side chain is hydrolyzed first as reported previously by Baran and Penczek on similar PPEs.²¹³ In order to further confirm the hypothesis of the degradation of the phenol group during the miniemulsion preparation, the polymer was dissolved in THF and ultrasonicated from 1 to 30 min. Samples taken in this interval were analyzed by GPC and HPLC (Figure 3.1 – 7), showing the presence of a new low molecular compound (with the same retention time as phenol) and simultaneously a decrease of the UV signal of the polymer proving the loss of the aromatic side chain,

although the level of degradation that could occur during the ultrasonication step for the preparation of the miniemulsion could not be determined.

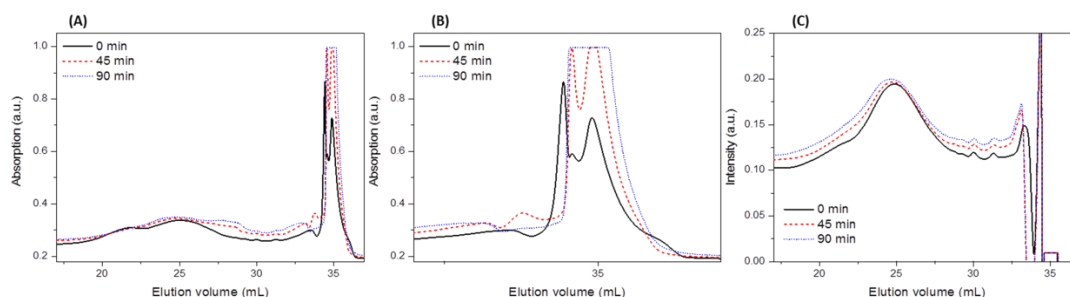


Fig. 3.1 – 6 SEC elugrams for the polymer PPE-C20-Phenoxy in THF and 0,1 M HCl: (A) UV-Vis signal; (B) highlight of the region at elution volume = 35 mL where a low molecular weight UV active product signal increased over time; (C) refractive index signal (Alexandrino *et al.*; *J. Mater. Chem. B*, 2014, **2**, 1298-1306, <http://pubs.rsc.org/en/Content/ArticleLanding/2014/TB/c3tb21295e#!divAbstract> - Reproduced by permission of The Royal Society of Chemistry).

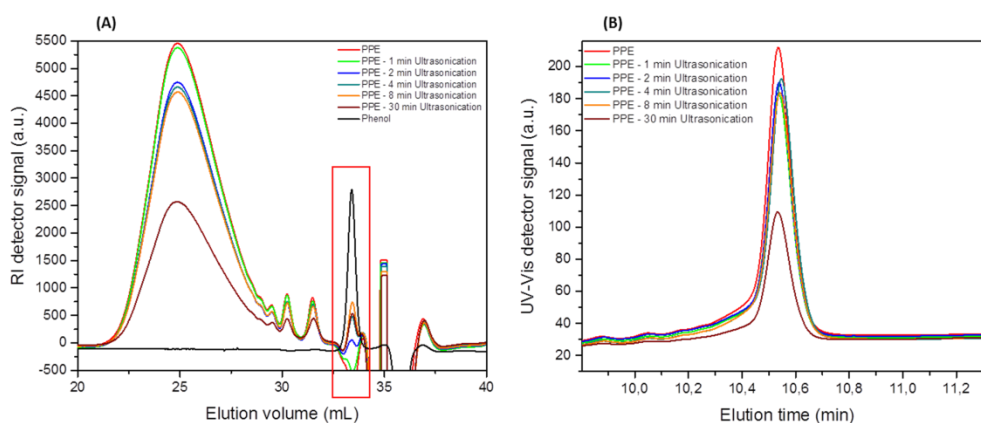


Fig. 3.1 – 7 (A) RI detector signal from the GPC elugram for the polymer PPE after the application of ultrasound (1/4" tip; 70% amplitude; 30 s on and 10 s off) for different periods of time and for phenol; (B) UV-Vis detector signal from HPLC elugram for the polymer PPE after the application of ultrasound (1/4" tip; 70% amplitude; 30 s on and 10 s off) for different periods of time (Alexandrino *et al.*; *J. Mater. Chem. B*, 2014, **2**, 1298-1306, <http://pubs.rsc.org/en/Content/ArticleLanding/2014/TB/c3tb21295e#!divAbstract> - Reproduced by permission of The Royal Society of Chemistry).

To also compare the effect that a labile group as phenoxy could have in the adhesion properties of the nanoparticles to the calcium phosphate surface, polyphosphonate

nanoparticles were also analyzed. The nanoparticles PPE-NP-C20-Methyl can be observed on the top of the cement (Figure 3.1 – 8), indicating that the presence of a labile side chain to produce charges was not necessary for the interaction of phosphorus containing polymers with calcium phosphate surfaces, although qualitatively the adhesion appears to happen in a major scale for PPE-C20-Phenoxy. This hypothesis is investigated in more detail in the next section.

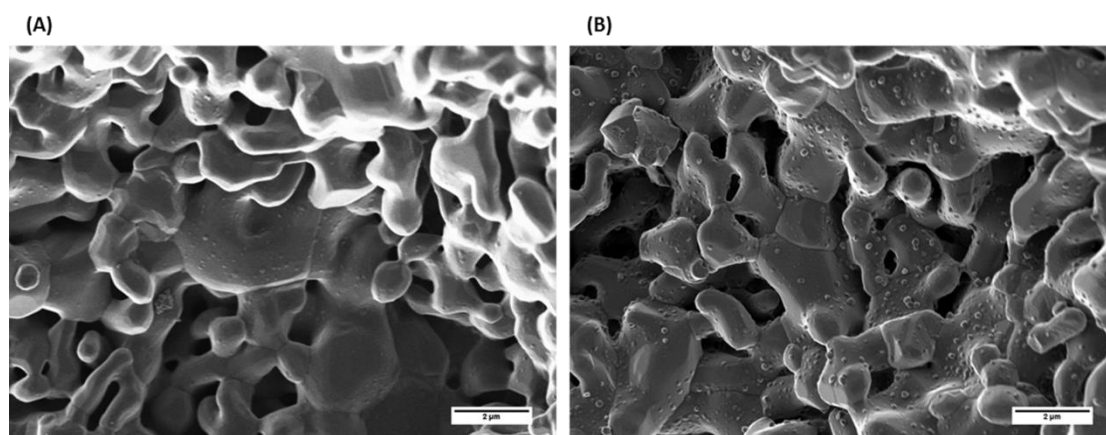
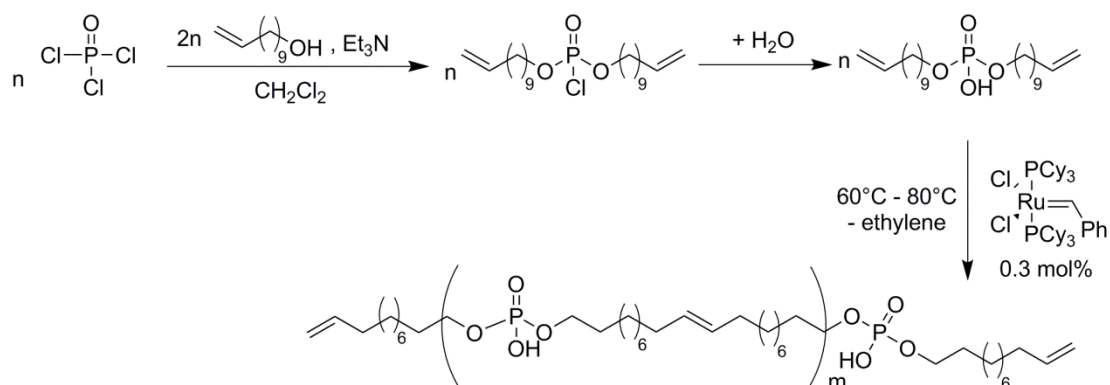


Fig. 3.1 – 8 Calcium phosphate cement MBCP+ surface after exposition to a dispersion of nanoparticles (A) PPE-NP-C20-Methyl and (B) PPE-NP-C20-Phenoxy (Alexandrino *et al.*; *J. Mater. Chem. B*, 2014, **2**, 1298-1306, <http://pubs.rsc.org/en/Content/ArticleLanding/2014/TB/c3tb21295e#!divAbstract> -

Reproduced by permission of The Royal Society of Chemistry).

3.1.5 PPEs and their interactions with calcium ions

As seen in section 3.1.4, polyphosphoester nanoparticles show effective surface interaction with calcium phosphate surfaces, which indicates the potential of such material for the development of tissue engineering applications. Nevertheless, the understanding and control of such interaction is essential in order to use the tailorability of PPEs in the development of adequate structures. As starting point, we use the hypothesis presented previously in section 3.1.4 that the phenoxy group in the side chain is liable and is partially degraded during the preparation of the nanoparticles, as suggested by Figure 3.1 – 7. In order to evaluate such a situation, a positive control polymer model was synthesized (Scheme 3.1 – 4) containing hydroxyl groups in the side chain.¹²⁶



Scheme 3.1 – 4 Reaction scheme for the synthesis of the unsaturated polyphosphate UPPE-C20-Hydroxy via acyclic diene metathesis polymerization.

The synthesis was confirmed by $^1\text{H-NMR}$ (Figure 3.1 – 4). The formation of the internal double bonds (δ 5.56 ppm) was observed. Small signals relative to the terminal double bonds are still visible, indicating that the molecular weight obtained is not too high (the estimated molecular weight by NMR is $10,200 \text{ g mol}^{-1}$). The material obtained was a powder even in the unsaturated form, which was almost not soluble in any solvent, except pyridine and other organic bases, which makes the preparation of nanoparticles from this material using the miniemulsion/solvent-evaporation strategy impossible.

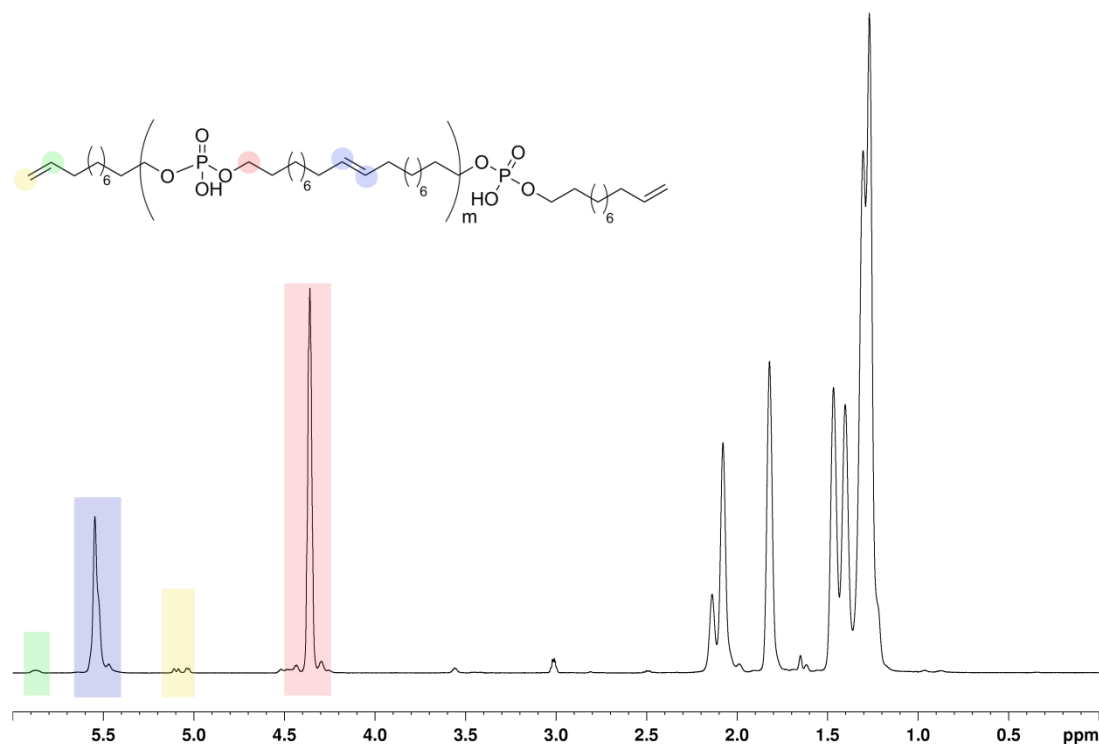


Fig. 3.1 – 9 ^1H NMR spectra in pyridine- d_6 (700 MHz, Avance III) at 298K from the polymer UPPE-C20-Hydroxy obtained by acyclic diene metathesis.

To evaluate the interaction between the polymer UPPE-C20-Hydroxy and three different types of additives (CaCl_2 , NaCl and tris(hydroxymethyl)aminomethane (Tris)), ^{31}P magic-spinning angle solid-state NMR spectra were measured, because the expected coordination of these ions should cause changes in the electronic shielding of the ^{31}P site. Initially, two types of experiments were performed: direct excitation or single-pulse excitation and cross-polarization (CP) measurements. The CP-MAS measurement enhances signals by a polarization transfer from ^1H to ^{31}P via heteronuclear dipolar couplings. This works best in regions with high structural order and low molecular mobility, as for example in crystalline structures, since the heteronuclear dipolar couplings in mobile regions are partially averaged out due to the molecular motion resulting in low signal intensities for short CP contact times. In contrast single-pulse experiments are less influenced by the difference in mobility, giving an overall impression of both mobile and rigid parts of the polymer, the relaxation delay is chosen sufficiently long. Figure 3.1 – 10 shows the spectra obtained for the UPPE-C20-Hydroxy.

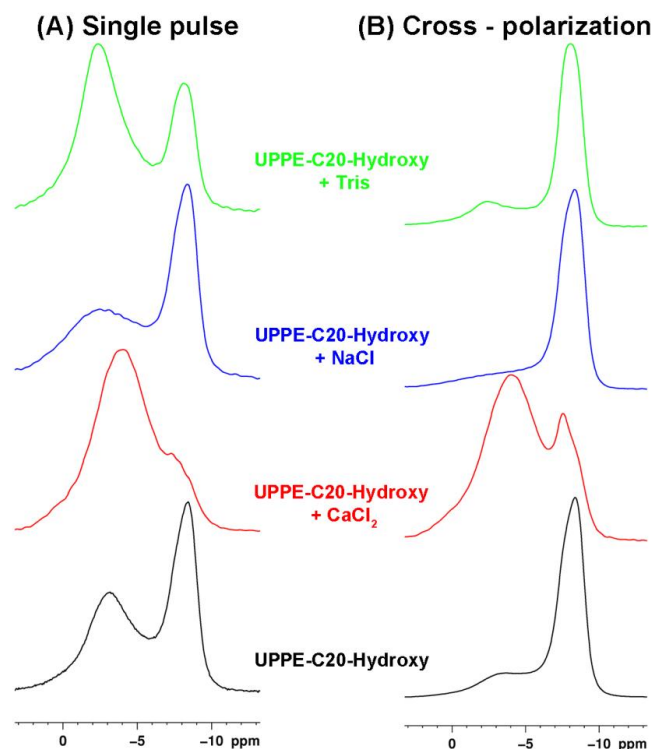


Fig. 3.1 – ^{31}P MAS NMR spectra (500 MHz ^1H Larmor frequency, Avance III) at 298K and 10 kHz MAS from the neat polymer PPE-C20-Hydroxy (black) and after exposition to Tris buffer (blue), CaCl_2 (green) or NaCl (lilac): (A) single-pulse and (B) cross-polarization experiments.

The single pulse experiment for the neat UPPE-C20-Hydroxy reveals two signals, at approximately $\delta - 3.3$ ppm and $\delta - 8.2$ ppm. The comparison of single-pulse spectra with the CP-MAS spectra shows that the high field signal results from a less mobile fraction, which is probably related to crystalline structures in the polymer. The addition of Tris buffer, an amine organic base, produces two changes in the single-pulse spectrum: firstly a change in the intensity ratio between the mobile and the rigid part; and second, the lower field signal is shifted by 1 ppm to lower field. Upon the mixing/dissolution in Tris buffer, as well as pyridine, small oligomers could have been washed out during the exposition of the polymer to this solution, which would explain the change of relative intensities between mobile and rigid phases. This hypothesis is supported by the fact that small oligomers could crystallize easier than bigger molecules and by a certain level of turbidity observed in the solution of Tris buffer after the exposition of the polymer. The analysis of the CP-MAS measurement reveals that the signal of the rigid fraction is very similar to that observed in the neat polymer, although an increase in the intensity of the signal at lower field is observed, which could result from protons of the counter-ion. The exposition of the polymer to a CaCl_2

solution brings substantial changes in the solid-state NMR spectra of UPPE-C20-Hydroxy. The single-pulse spectrum shows that the signal from the rigid fraction is almost completely suppressed, together with an increase in signal intensity of the more mobile parts. The CP-MAS spectrum presents a remarkable increase of the signal assigned to more mobile regions, which can be directly related to an increase of heteronuclear dipolar couplings in the system. This indicates that the introduction of CaCl_2 leads to a disturbance of the rigid, most likely crystalline structure in exchange for the formation of a different organized structure in response to Coulombic interactions between calcium ions and the phosphate units. The question that arises: is this interaction equal for every ion? Na^+ was chosen as the candidate for such analysis, since its radius is similar radius to that of Ca^{2+} and the single charge should not allow for the formation of a Coulombic network. As observed in the single-pulse experiment, changes in the spectrum are less pronounced than for Ca^{2+} when compared to the neat polymer. The peak assigned to the rigid fraction is almost the same as in the neat polymer, while a broadening of the more mobile fraction can be observed. Such broadening in the single – pulse spectrum can be related to an increase in heterogeneity of chemical environments surround the phosphorus centers. Nevertheless, the CP-MAS experiment does not show any relevant decrease of the mobility or reorganization in the amorphous region of the polymer, which clearly indicates that, differently from Ca^{2+} , Na^+ does not leads to the formation of a less mobile, non-crystalline fraction in the system.

Even though the phosphorus NMR analysis indicates a change in the rigid fraction of the polymer, which is probably related to the crystalline region, the level of the change is still not clear, as the single – pulse spectrum analysis is not easily integrable due to the overlap of the signals. In order to better understand the structural changes in the polymer in the presence of each of the additives $^{13}\text{C}\{^1\text{H}\}$ CP heteronuclear correlation (CP-HETCOR) spectra were recorded at 25 kHz MAS and 298 K sample temperature (Figure 3.1 – 11). This method makes use of a combination of a classic heteronuclear correlation analysis, where, through the use of high field (850 MHz) and fast MAS speed (25 kHz), proton resolution can be obtained. The ^{13}C NMR signals can be assigned to specific sites and conformations in the polymer chain, and the presence of e.g. all-trans conformations in alkyl chains is a good indicator for the presence of a crystalline phase. Differences in the ^1H line width can be interpreted with aspects from the *wideline separation* (WISE) analysis. This method first introduced by Spiess *et al.*²¹⁴ is capable to evaluate qualitatively large-amplitude molecular motions through the reduction of ^1H dipolar line width, separating different overlapping ^1H NMR lines with the use of a cross polarization step from protons to carbons. The WISE

experiment provides a 2D spectrum where for every ^{13}C resonance a proton wide-line spectrum is obtained, which reflects how the dipolar couplings of the protons around the carbons are changed for each case, allowing the understanding of changes in local mobility on a nanometer scale. In contrast to the classical WISE experiment which is performed under quasi-static experiments, the $^{13}\text{C}\{^1\text{H}\}$ CP-HETCOR experiments performed under fast MAS, provides a 2D correlation spectrum, where the ^1H line width is not completely dominated by the strong dipolar couplings in dense ^1H systems, so that the central position of the signals reflect the isotropic ^1H chemical shift, while the line width of the signal is still determined by the local dipolar couplings and thus the local molecular mobility. In the spectrum of the neat UPPE-C20-Hydroxy, the broad signal observed at approximately 33 ppm in the ^{13}C dimension is typical of all-*trans* conformations of alkyl chains in most likely crystalline regions of the polymer.²¹⁵ The monitoring of this signal shows clearly how the different additives are capable to influence the crystallinity in the system. The narrowing of the line width for the ^1H signal relative to the all-*trans* conformation indicates a shortening of these conformations and consequently a higher mobility. Tris and NaCl (Figures 3.1 – 11C and 11D) shows a reduction of the signal at 33 ppm, which can however still be clearly observed and is in agreement to the results observed from ^{31}P CP-MAS measurements. The influence of CaCl_2 on the structure of the polymer is clearly stronger (Figure 3.1 – 11B). The all-*trans* signal at 33 ppm is practically suppressed in the presence of CaCl_2 , indicating that this interaction with calcium acts as the driving force for the disruption of the crystalline phase. However, why does the interaction with Na^+ not produce the same effect? Even though both ions present similar radius, the fact of Ca^{2+} be a divalent ion results in the need for the reorganization of the system to neutralize the cation.

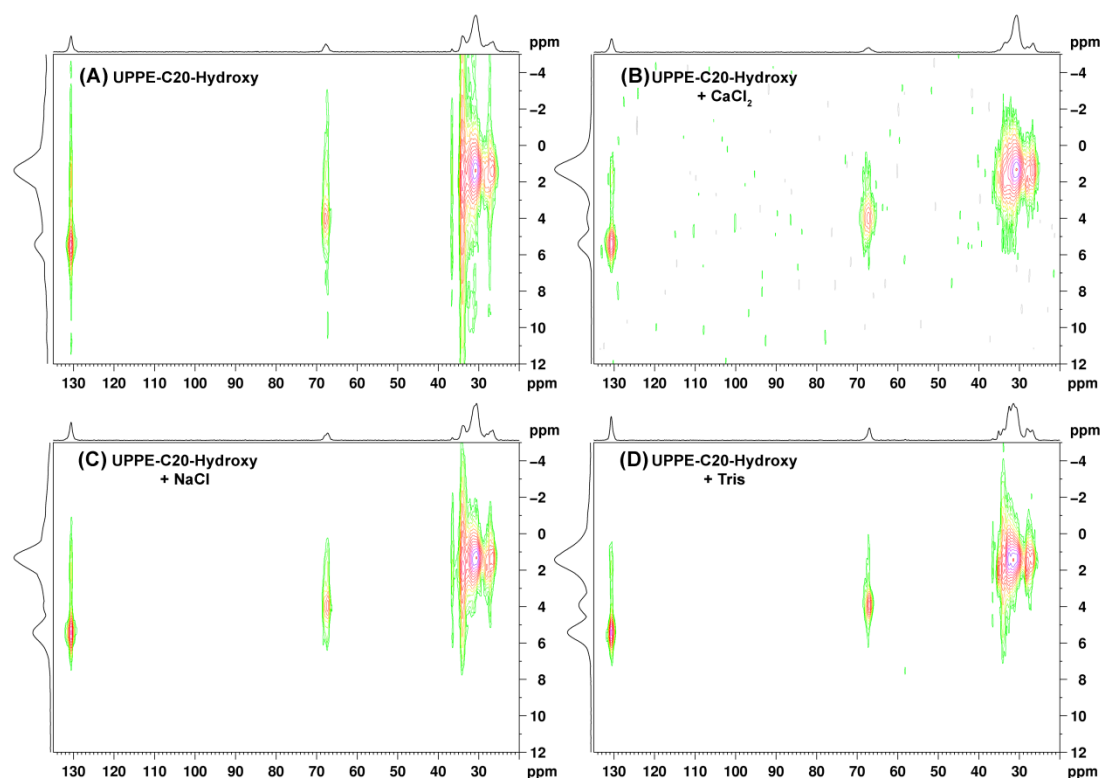


Fig. 3.1 – $11\ ^{13}\text{C}\{^1\text{H}\}$ CP heteronuclear correlation (CP-HETCOR) spectra (850 MHz, Avance III) obtained at 298K and 25 kHz from: (A) neat polymer UPPE-C20-Hydroxy, (B) UPPE-C20-Hydroxy + CaCl_2 , (C) UPPE-C20-Hydroxy + NaCl and (D) UPPE-C20-Hydroxy + Tris buffer.

Figure 3.1 – 12 shows the wide-angle X-ray diffraction measurements for UPPE-C20-Hydroxy before and after exposition to the additives. The pure polymer does not present any reflection pattern similar to polyethylene, the closest example for comparison of crystalline structure of the polymer UPPE-C20-Hydroxy, which could be related to formation of hydrogen bonding between the –OH groups in the side chain. Such alignment could result in a distorted crystalline structure in comparison to the expectation for all-*trans* polyethylene-like chains. Nevertheless, the previously indicated change on the morphology of the polymer after exposition to the additives could be further confirmed by X-ray diffraction measurements. The pure unsaturated polymer is a semi-crystalline material, presenting a halo amorphous around $2\theta=20^\circ$ and other three signals attributed to the crystalline part at $2\theta=18.1^\circ$, 19.8° and 21.6° . The exposition of the polymer to CaCl_2 provides a substantial change in the diffractogram, with the suppression of the signals at $2\theta=18.1^\circ$ and 19.8° and enhancement of a signal at $2\theta=21.1^\circ$, which could indicate a new ordering in the system, which would be in agreement with the previous data obtained by solid-state

NMR. As expected, NaCl does not produce strong changes in the system, but still disturbs the crystalline structure, resulting in the suppression of the signal at $2\theta=18.1^\circ$. In the case of Tris buffer a change in the crystalline structure was also seen, and as expected from the solid state NMR the main structure formed by the all-*trans* chain conformation can still be observed. At the same time the increase of the signal at $2\theta=21.1^\circ$ is also observed. Besides the change in the refraction patterns, the analysis of the low-angle region of the diffractograms shows that the interplanar spacing in the crystalline structures is also affected. The pure polymer shows initially a refraction at $2\theta=4.1^\circ$, which is related to an interplanar space of 2.15 nm. A similar space is observed for the polymer after the exposition to NaCl, with $2\theta=4.07^\circ$ and interplanar space of 2.16 nm. The addition of CaCl_2 shifts the refraction to $2\theta=3.37^\circ$, which indicates an increase in the interplanar space to 2.61 nm. The introduction of Tris generates two different interplanar spaces in the polymer, with 2.38 nm relative to the diffraction at $2\theta = 3.73^\circ$ and 3.17 nm for $2\theta = 2.78^\circ$. In the of Ca ions, the change in the interplanar space can be probably related to the increase of the amorphous portion in the material due to the disruption of the crystalline arrangement due to the interaction. In the case of Tris, a possible explanation for the presence of two different interplanar space values is the allocation of molecules of the organic molecule Tris in the amorphous region summed to the disruption of the crystalline structure, increasing the free volume in the material.

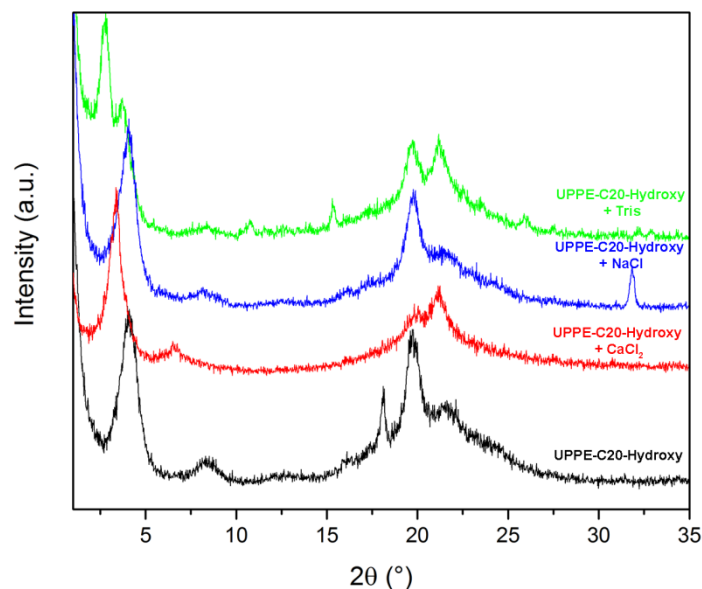


Fig. 3.1 – 12 XRD diffractograms of the neat polymer UPPE-C20-Hydroxy and the mixtures with the additives CaCl_2 , NaCl, and Tris buffer.

The changes on the crystallinity of the samples could also be evidenced by DSC measurements (Figure 3.1 – 13). Figure 3.1 – 13A shows the first heating step for the samples of UPPE-C20-Hydroxy with and without the presence of the additives. As can be seen, the neat polymer and polymer after exposition to NaCl presents similar curve, with a clear melting event around 80°C and another less relevant event around 50 °C. The introduction of Tris shifts the main melting event to lower temperatures (74 °C), while the other event is still visualized around 50 °C. The introduction of calcium provides the most relevant change in the melting profile of the sample, with the reduction of the crystallinity (total area of the melting peak) and a new melting event around 20 °C, which indicates, as expected from the previous measurements, that the crystallinity is more affected in the presence of this additive. Such assumptions are clearly confirmed at the second heating step of the samples (Figure 3.1 – 13B). Besides the recrystallization process, which could be a consequence of the cooling rate applied, the pure polymer and the polymer plus NaCl show similar behavior in comparison to the first heating step, while the influence of Tris in the crystallization is so that smaller crystallites are formed and the melting point is reduced. CaCl₂ shows again the highest influence in the crystallization. The sample can barely crystallize after being once melted in the presence of calcium ions, reinforcing the idea that strong coordination interaction with calcium ions is preferential in comparison to the formation of a crystalline structure.

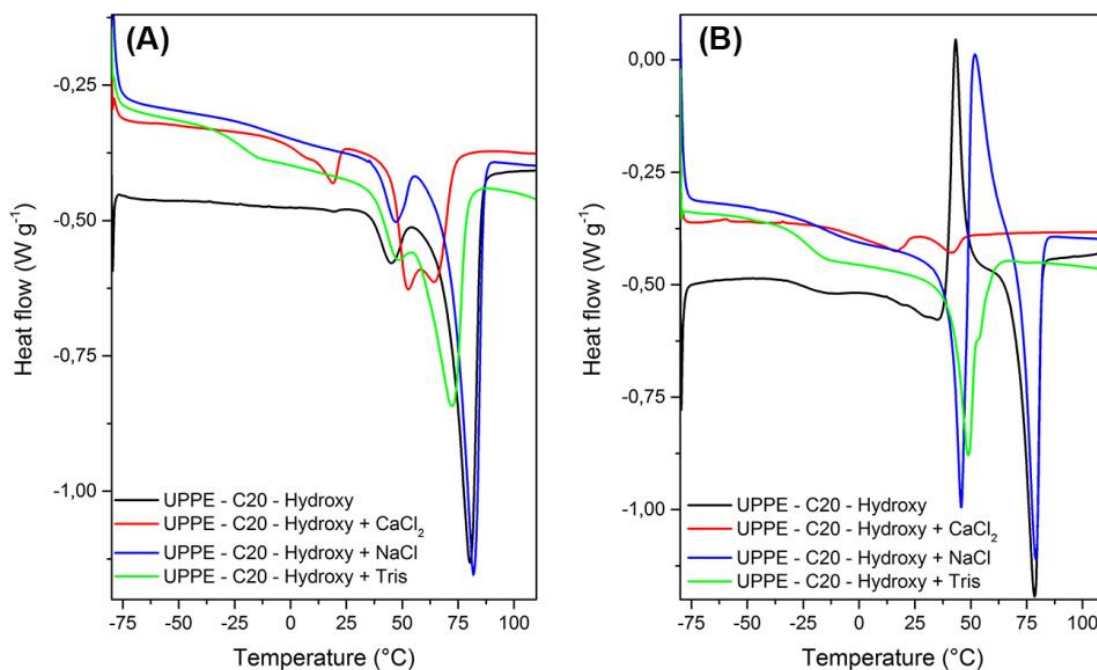


Fig. 3.1 – 13 DSC curves of the neat polymer UPPE-C20-Hydroxy (black) and the mixtures with the additives CaCl₂ (red), NaCl (blue) and Tris buffer (green): (A) first heating step and (B) second heating step.

Therefore, the experiments with the positive control evidence a relevant influence of calcium in the mobility and order of the polyphosphoester UPPE-C20-Hydroxy. The analysis was further performed for the polymer PPE-C20-Phenoxy, however in this case sodium ions were substituted by a mixture of Tris and CaCl₂, in order to verify a possible synergetic effect (due to the higher hydrophobicity of the polymer system in question). The results are presented in Figure 3.1 – 14.

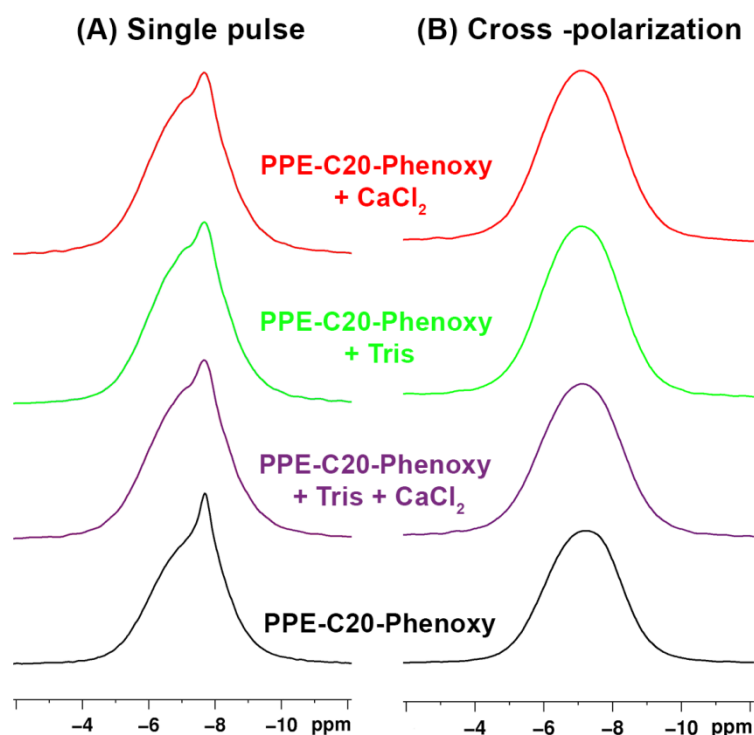


Fig. 3.1 – 14 ³¹P MAS-solid state NMR spectra (500 MHz, Avance III) at 298K and 10 kHz from the neat polymer PPE-C20-Phenoxy (black) and after exposition to a mixture of Tris buffer and CaCl₂ (lila), Tris buffer (green) or CaCl₂ (red): (A) single-pulse and (B) cross-polarization experiments.

Only minor changes are observed in the single pulse spectra independently of the additive to which the polymer was exposed, even for the mixed Tris and CaCl₂. The analysis of the CP-MAS spectra shows no change in the structural order of the rigid fraction in the polymer structure. Such results indicate that none or only minor changes in the polymer mobility are caused by the addition of calcium ions in case when no hydroxyl groups are present. This is in agreement with the previous hypothesis presented in section 3.1.4. The polymer PPE-C20-Methyl also does not show relevant changes in the ³¹P MAS NMR spectra (Figure 3.1 – 15) upon the addition of Tris and CaCl₂, although an overall shift to higher field can be observed. The introduction of the additives makes the peaks broader and the weak asymmetry in the original polymer structure in the single pulse, probably due to the crystalline and amorphous phases, vanishes. This system shows higher melting point (65° C) and higher crystallinity is therefore expected, which should result in a less effective distinction between both mobile and rigid phases.

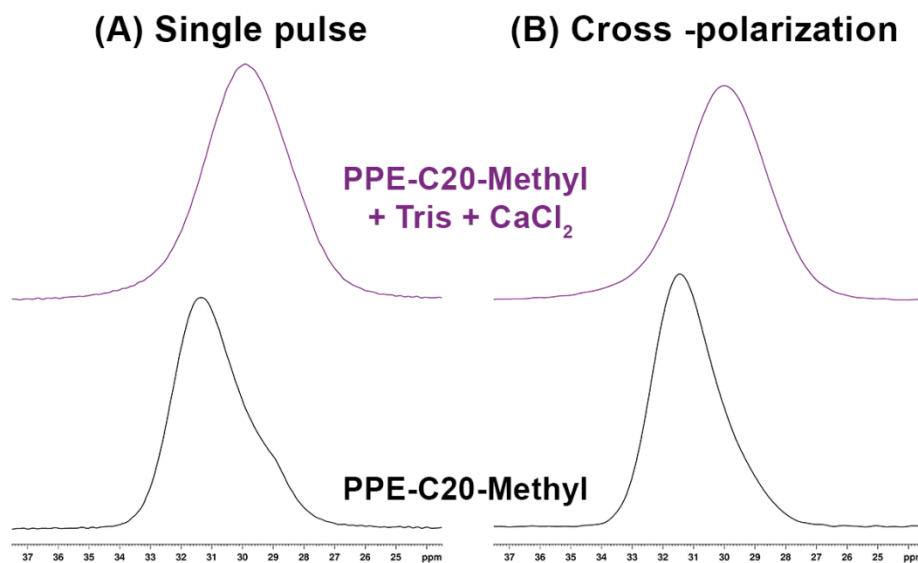


Fig. 3.1 – ^{31}P MAS – solid state NMR spectra (500 MHz, Avance III) at 298K and 25 kHz from the neat polymer PPE-C20-Methyl (black) and after exposition to a mixture of Tris buffer and CaCl_2 (lila): (A) single-pulse and (B) cross-polarization experiments.

In order to evaluate the potential that surface degradation could have in the calcium interactions, a calcium phosphate crystallization experiment, inspired in the previous published works,^{216, 217} was performed with nanoparticles from PPE-C20-Phenoxy, and prepared with a non-ionic surfactant (D- α -Tocopherol polyethylene glycol succinate (TPGS)). The experiment was performed in pH 10 (Figures 3.1 – 16A and 16B) and pH 7 (Figures 3.1 – 16C and 16D). As can be clearly seen, at pH 10 crystallization occurs preferentially at the surface of the particles, due to the accumulation of calcium ions at the surface of the nanoparticles, meanwhile at pH 7 most of the crystallization occurs in the bulk of the solution, although a good adhesion of the particles can still be observed to the calcium phosphate aggregates. This short experiment reinforces therefore the idea of stronger interactions in the presence of $-\text{OH}$ groups in the side chain of the polyphosphoester.

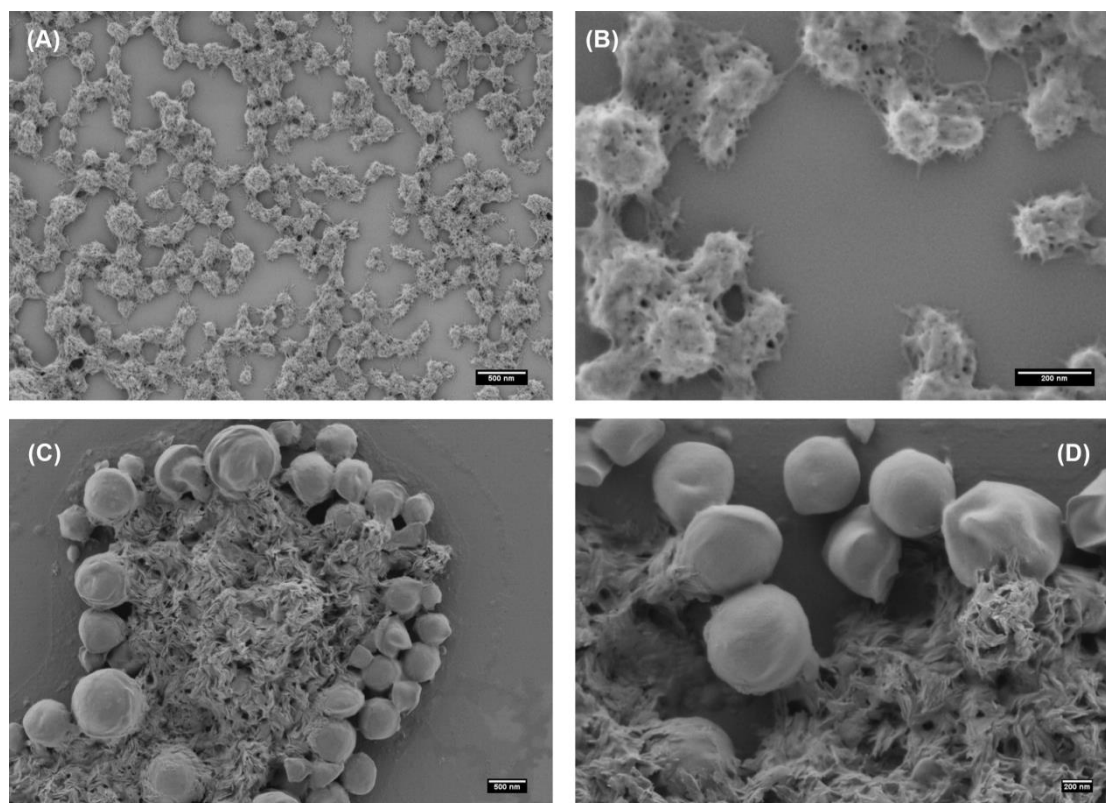


Fig. 3.1 – 16 SEM micrographies of the calcium phosphate crystallization experiments performed with the PPE-C20-Phenoxy nanoparticles at pH 10 (A and B) or pH 7 (C and D), at 37°C.

3.1.6 Paclitaxel loaded nanoparticle synthesis

As shown above, the PPE nanoparticles interact with the “model bone tissue”, this protocol should allow the development of a drug delivery system for local application in bone cancer therapies. With this goal, paclitaxel (PTX), a strong anti-mitotic drug, was selected and the miniemulsion/solvent-evaporation methodology was used to produce PTX loaded-PPE nanoparticles by co-precipitation of both drug and polymer during solvent evaporation. Four PTX-loaded PPE nanoparticle formulations, with 1.5, 5, 10 and 15 wt% PTX (and a control without the addition of PTX) were produced using the PPE-C20-Phenoxy. Table 3.1 – 2 summarizes the main physicochemical properties of these materials. The nanoparticles mean diameters were determined to be between 160-200 nm; it can be clearly seen that the size distribution (standard deviation) increased with the amount of PTX introduced initially to the particle preparation. The angle dependence of the hydrodynamic radius (Figure 3.1 – 17) was also evaluated and revealed a similar angle dependence for all

formulations, which indicates that, independent of the drug loading ratio, the shape of the particles in solution is approximately the same and isotropic. Two possible applications of the PTX-loaded NPs could be either their application on the bone cement before implantation or by injection over infected tissue. The zeta potential was measured after an exhaustive dialysis process. The zeta potential was, independent of the loading, in the range of -48 mV for all formulations, except for the formulation with the highest drug content (PPE-NP-15).

Table 3 – X Summary of the properties of the paclitaxel-loaded PPE nanoparticles (Alexandrino *et al.*; *J. Mater. Chem. B*, 2014, **2**, 1298-1306, <http://pubs.rsc.org/en/Content/ArticleLanding/2014/TB/c3tb21295e#ldivAbstract> - Reproduced by permission of The Royal Society of Chemistry).

Sample	Paclitaxel loading ratio ^a (wt%)	Mean diameter ± S.D. (nm) ^b	Zeta potential (mV) ^c	Encapsulation efficiency (%) ^d	$\Delta H_M \pm 1$ (J/g) ^e
PPE-NP	0	162 ± 38	-47.6±9,4	-	74.9
PPE-NP-1	1.5	170 ± 33	-44.3±9,0	70	70.4
PPE-NP-5	5	179 ± 73	-49.0±13,5	100	69.2
PPE-NP-10	10	173 ± 98	-48.7±11,8	98	66.3
PPE-NP-15	15	200 ± 100	-29.0±13,6	93	57,9

^aTheoretical weight percentage of paclitaxel;

^bDetermined via dynamic light scattering in a NICOMP Particle Size Analyzer;

^cElectrophoretic mobility determined using a Zetasizer;

^dEncapsulation efficiency determined by HPLC;

^eMelting enthalpy determined by differential scanning calorimetry.

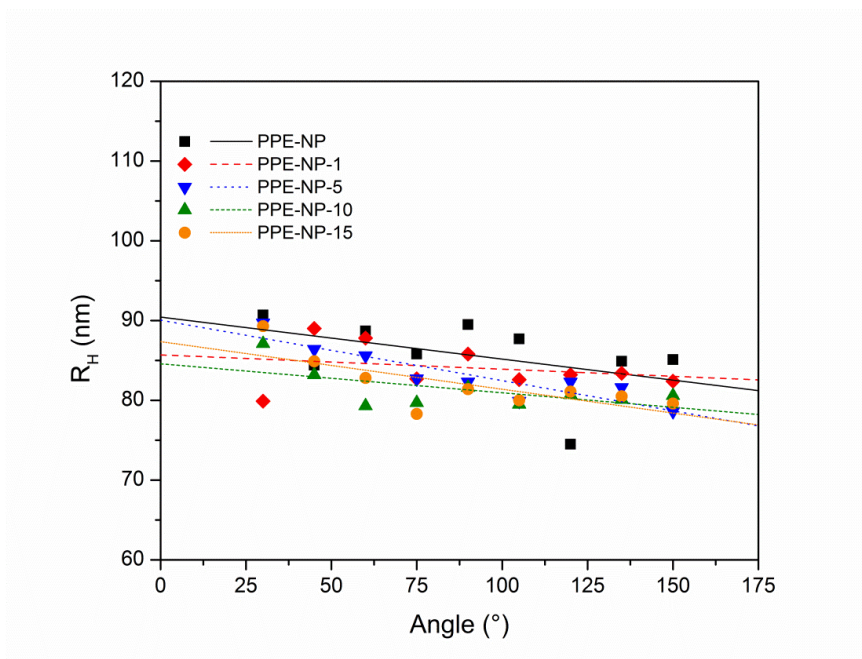


Fig. 3.1 – 17 Multi-angle DLS scattering of the “placebo” PPE nanoparticles and the Paclitaxel loaded PPE nanoparticles formulations (Alexandrino *et al.*; *J. Mater. Chem. B*, 2014, **2**, 1298-1306, <http://pubs.rsc.org/en/Content/ArticleLanding/2014/TB/c3tb21295e#ldivAbstract> - Reproduced by permission of The Royal Society of Chemistry).

3.1.7 Drug encapsulation efficiency

An important factor for drug delivery vehicles is the encapsulation efficiency of the drug of interest. As the PPEs used herein are hydrophobic materials, PTX was chosen as a model drug with a low water solubility in the range of $1 \mu\text{g mL}^{-1}$.²¹⁸ For all formulations, encapsulation values between 70-100% were obtained (compare Table 3.1 – 2), proving that the miniemulsion/solvent-evaporation technique is a robust technique that can be also applied for obtaining drug loaded PPEs nanoparticles.

The drug loading and encapsulation efficiency of the PPE-NPs is comparable with other published nanoparticle systems. Feng and coworkers, for example, reported on several polyester-based nanoparticles for PTX delivery, reaching drug loading up to 12% and encapsulation efficiencies over 90%.^{183, 219, 220} Only very recently, Wooley and coworkers presented in an elegant work a very high PTX loading (up to 65 wt%) by covalent linkage of PTX to a PPE-block copolymer for micellar delivery.²²¹

3.1.8 Thermal characterization

DSC was used to evaluate the dispersion of the drug within the nanoparticles. Figure 3.1 – 18 shows the DSC scans of the PPE nanoparticles synthesized in this study versus pure PTX. Homogeneous incorporation of PTX in the nanoparticles can be detected if no crystallization peak of the drug can be observed in the different formulations. The appearance of a melting point would suggest inhomogeneous incorporation or the formation of crystals within the nanoparticles. PTX, as received, is a crystalline powder, with a melting point around 220 °C-240 °C (variation depends on the water content).²¹⁸ At temperatures above the melting point, PTX decomposes; hence only one heating ramp was performed. In our setup, the DSC scan for PTX showed a melting transition at 228 °C. For all PPE-containing samples (control nanoparticles, mixture of control nanoparticles and PTX (20 wt%), and the PTX-loaded nanoparticles) a melting transition at ca. 50 °C can be detected. For all the formulations with PTX content up to 10 wt%, only the melting transition of the PPE can be detected indicating a homogeneous dispersion without agglomerates inside the nanoparticles. For the sample with 15 wt% PTX incorporated, however, a slight endothermic response in the region of the melting point of the drug was observed, similar to the physical mixture of the nanoparticles and PTX indicating phase separation, i.e. the formation of drug crystals, for loading higher than 10 wt%. Another important result that can be determined from these experiments is the change in the melting enthalpy with increasing amount of PTX incorporated in the nanoparticles (compare Table 3.1 – 2). The comparison of the melting enthalpies reveals a lowering in the melting enthalpy with increasing drug content. This behavior can be related to a lowering in the degree of crystallinity of the polymer by the inclusion of an ‘impurity’ in the polymer matrix, leading to defects during the crystallization. Once again the effect was more evident for the sample PPE-NP-15, supporting also the formation of separated PTX domains. Since the polymer has a low glass transition temperature (around -50 °C), the mechanical stability of the nanoparticles is directly related to the degree of crystallinity of the polymer. Loading of the nanoparticles with the drug leads to a lowering of the degree of crystallinity and the nanoparticles become softer, what could possibly explain the increase in the particle size and size distribution due to partial agglomeration and particle fusion during the evaporation process, especially for the sample PPE-NP-15.

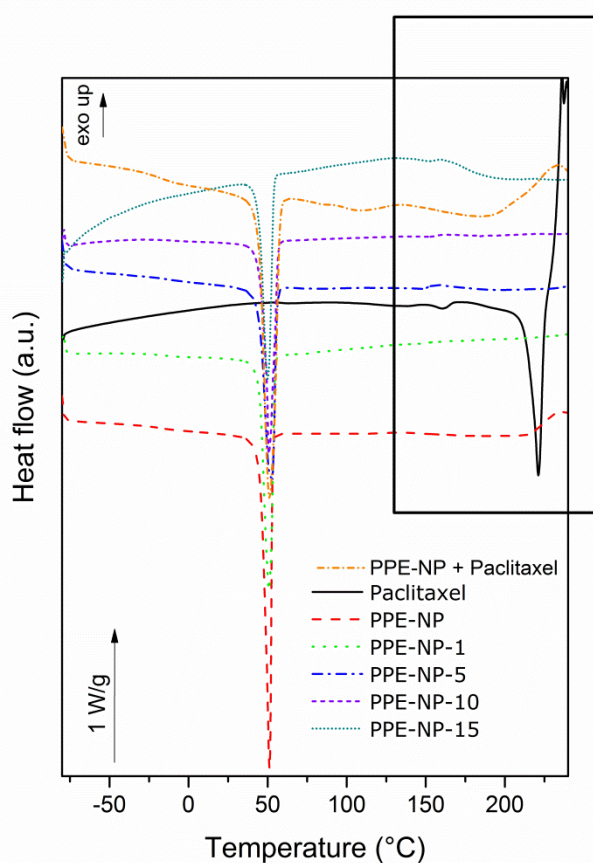


Fig. 3.1 – 18 Differential scanning calorimetry obtained for PTX, the placebo nanoparticles NP-PPE, the mixture of paclitaxel and placebo nanoparticles and the formulations with up to 15 wt% paclitaxel (Alexandrino *et al.*; *J. Mater. Chem. B*, 2014, **2**, 1298-1306, <http://pubs.rsc.org/en/Content/ArticleLanding/2014/TB/c3tb21295e#ldivAbstract> - Reproduced by permission of The Royal Society of Chemistry).

3.1.9 Effect of PPE-NPs and PPE-NPs loaded with paclitaxel on *in vitro* cell viability

The investigation of the cytotoxicity properties of the nanoparticles with and without Paclitaxel was performed in collaboration by Dr. Sandra Ritz. For the analysis of the cytotoxicity of these PPE nanoparticles we first evaluated the effect without drug loading on the metabolic activity of HeLa and Saos-2 cells lines. The cells were treated with $75 \mu\text{g mL}^{-1}$ to $600 \mu\text{g mL}^{-1}$ of nanoparticle dispersion for 24 h or 48 h and no cytotoxicity was detected, as displayed in Fig. 3.1 – 19, proving the biocompatibility under these conditions for the herein investigated PPEs.

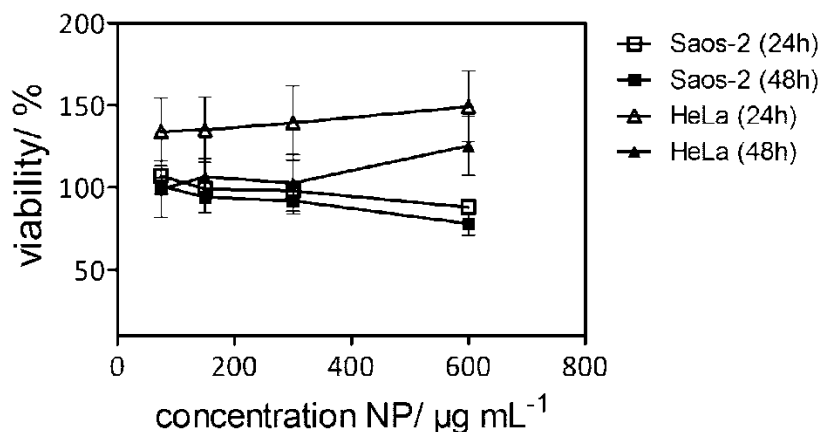


Fig. 3.1 – 19 Effect of polyphosphoester nanoparticles PPE-NPs on *in vitro* cell viability. (A) HeLa and Saos-2 cells treated with increasing concentrations of PPE-NP ($75\text{--}600 \mu\text{g mL}^{-1}$) for 24 h and 48 h. Cell viability was measured by CellTiter-Glo[®] luminescence assay. Mean values \pm standard deviation calculated from 4 replicates (Tests performed in collaboration by Dr. Sandra Ritz) (Alexandrino *et al.*; *J. Mater. Chem. B*, 2014, **2**, 1298-1306, <http://pubs.rsc.org/en/Content/ArticleLanding/2014/TB/c3tb21295e#ldivAbstract> - Reproduced by permission of The Royal Society of Chemistry).

The cytotoxic effect of PTX-loaded PPE-NP-1 (1.5% wt) was analyzed on two different cancer cell lines (HeLa, Figure 3.1 – 20A and Saos-2, Figure 3.1 – 20B) and compared to PTX dissolved in DMSO and the chemotherapeutic compound Taxomedac[®]. The reference compounds, PTX/DMSO and Taxomedac, revealed generally a higher toxicity for osteoblastoma cells (Saos-2, $\text{EC}_{50} \sim 10 \text{ nM}$) for PTX when compared to the cervix cancer cells (HeLa, $\text{EC}_{50} \sim 25 \text{ nM}$) which is indicated by lower EC_{50} values. Figure 3.1 – 21 shows the bright field image of HeLa cells treated. The PPE-NPs with the low PTX loading (PPE-NP-1, 1.5 wt%) were less effective compared to the pure PTX/DMSO or Taxomedac which was reflected by an approximated EC_{50} value of 10-25 nM for Saos-2 cells (Figure 3.1 – 20B) and $>100 \text{ nM}$ for the HeLa cells (Figure 3.1 – 20A). The lower EC_{50} value of the drug loaded nanoparticle could probably be attributed to the loading efficiency (70% for the PPE-NP-1) or a different drug transfer mechanism.²²¹ The actual drug availability is lower when PTX is encapsulated in comparison with the free drug, thus the EC_{50} depends in the first case also of the nanoparticles concentration. Figure 3.1 – 20C and 3.1 – 20D shows that the cytotoxic effect on Saos-2 cells can be improved by the application of PPE-NPs with increased compound loading. For example $1 \mu\text{g mL}^{-1}$ NP loaded with 10 wt% or 15 wt% of PTX showed a 75% reduction in cell viability, where the same concentration of nanoparticles

loaded with 1 wt% PTX showed nearly no effect. Figure 3.1 – 20D highlights this dependence of PPE-NP concentration, PTX loading and cytotoxicity for a fixed concentration of 30 nM PTX. The highest effect was obtained for 30 nM pure PTX/DMSO ($0 \mu\text{g mL}^{-1}$ PPE-NP, 40% remaining cell viability), followed by the PPE-NPs with the highest PTX loading (15 wt%, 55% remaining cell viability) and further decreasing with lower PTX loading. These *in vitro* cell tests confirm that the drug can be loaded into the PPE nanoparticles and that it is still active, while a low load of PTX in wt% per polymer results in a lower effect. This would indicate that the release from a highly loaded nanocarrier is easier achieved compared to lower loaded one. The delivery pathway is most likely a mixture of several ones. One delivery mechanism has been described recently which is especially attractive as it occurs rapidly for hydrophobic drugs at the cell membrane within minutes. As the nanoparticles only shortly touch and then detach again this mechanism has been termed “kiss-and-run” leaving behind the respective hydrophobic cargo.²²¹ This appears to be reasonable when the supposed release from the nanoparticles may need release from the surface of the nanocarrier to a lipophilic surface like the cell membrane or an endosomal membrane. Therefore with a higher loading a higher concentration right at or below the surface would occur.

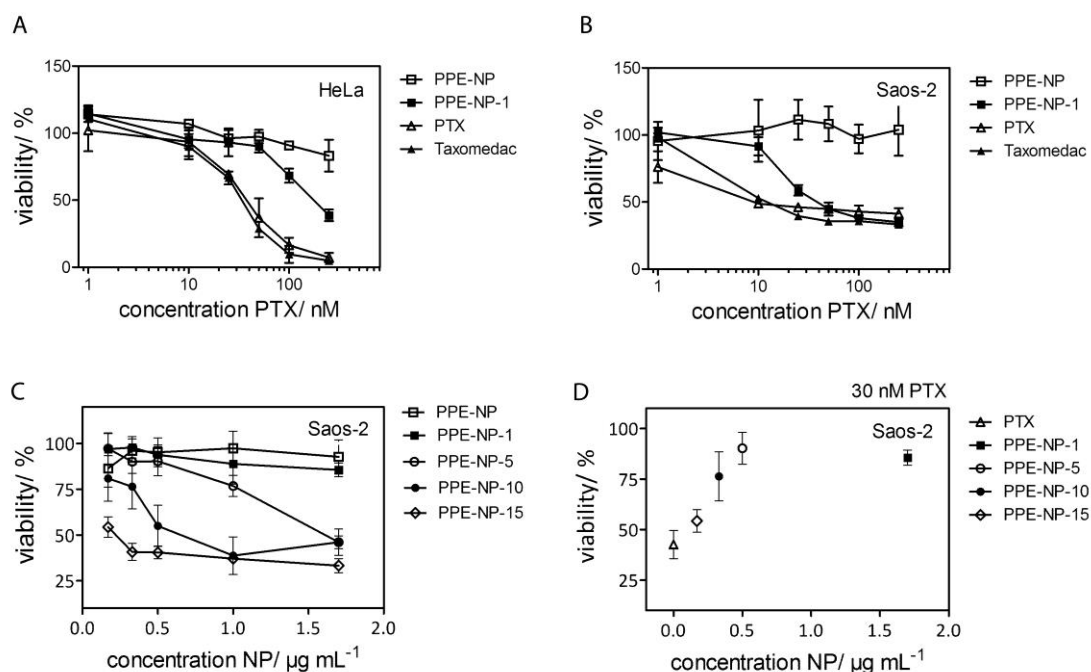


Fig. 3.1 – 20 Effect of polyphosphate nanoparticles (PPE-NPs) and PPE-NPs loaded with Paclitaxel (PTX) on *in vitro* cell viability. (A, B) Dose-response curves (1-250 nM) of paclitaxel loaded PPE-NP-1 (1.5 wt% PTX) in comparison to PPE-NP, PTX (0.1% DMSO) and Taxomedac in HeLa (A) and Saos-2 (B) cells. Cell viability was measured by PrestoBlue[®] staining after

48 h treatment. (C,) Viability of Saos-2 cells in dependence of increased polymer concentration PPE-NP and PTX loading. PPE-NP-1, -5, -10, and -15 wt% correspond to 1.5, 5, 10, 15 wt% PTX loading. (D) Relation between cell viability, NP concentration and PTX loading for a fixed concentration of 30 nM PTX. Mean values \pm standard deviation calculated always from 4 replicates (all tests performed in collaboration by Dr. Sandra Ritz) (Alexandrino *et al.*; *J. Mater. Chem. B*, 2014, **2**, 1298-1306, <http://pubs.rsc.org/en/Content/ArticleLanding/2014/TB/c3tb21295e#!divAbstract> - Reproduced by permission of The Royal Society of Chemistry).

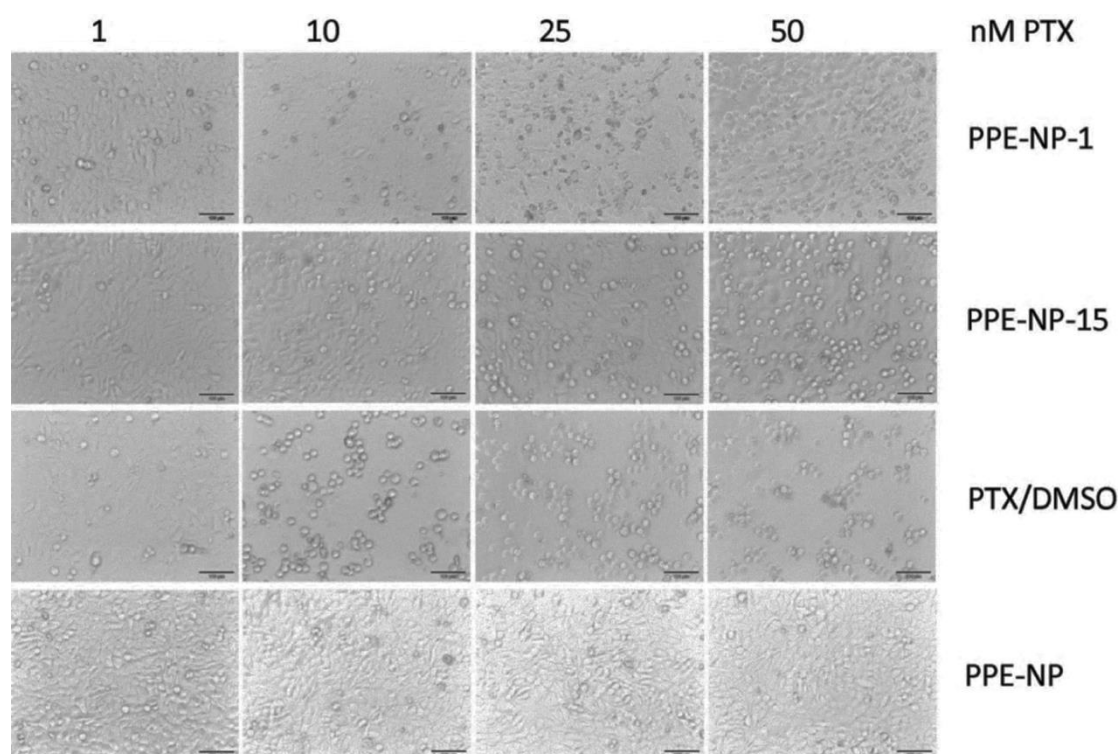


Fig. 3.1 – 21 Bright field images of HeLa cells treated with increasing concentrations of PTX and PTX loaded PPE-NPs (24h). Cells treated with the control nanoparticle PPE-NP showed a dense cell layer, whereas cells treated with PTX and PTX loaded nanoparticles showed a round, detached morphology, supporting the cell viability studies with Prestoblu assay. Bar scales 100 μ m (all tests performed in collaboration by Dr. Sandra Ritz) (Alexandrino *et al.*; *J. Mater. Chem. B*, 2014, **2**, 1298-1306, <http://pubs.rsc.org/en/Content/ArticleLanding/2014/TB/c3tb21295e#!divAbstract> - Reproduced by permission of The Royal Society of Chemistry).

3.1.10 Calcium phosphate attachment studies of drug-loaded nanoparticles

As a final prove that the PTX-loaded PPE-NP's are suitable to target bone tissue we investigated whether the drug loading affects the PPE-NPs attachment on the calcium-phosphate cement.

Figure 3.1 – 22 shows the SEM pictures for the pure MBCP+ (Figure 3.1 – 22A) and the granules after the exposition to the nanoparticles PPE-NP, PPE-NP-1 and PPE-NP-15 (Figure 3.1 – 22B-D). From these images it can be clearly stated that the loaded PPE nanoparticles exhibit a high surface attachment with the calcium phosphate granules, even after vigorous washing steps. This proves that the phosphate groups are located at the surface of the PPE NPs and further indicates homogeneous drug dispersion within the nanoparticles. These attachment properties combined with the encapsulation efficiency and excellent toxicity data makes the herein presented PPE-NPs an ideal platform for further in vivo studies to generate a powerful anti- cancer drug delivery vehicle.

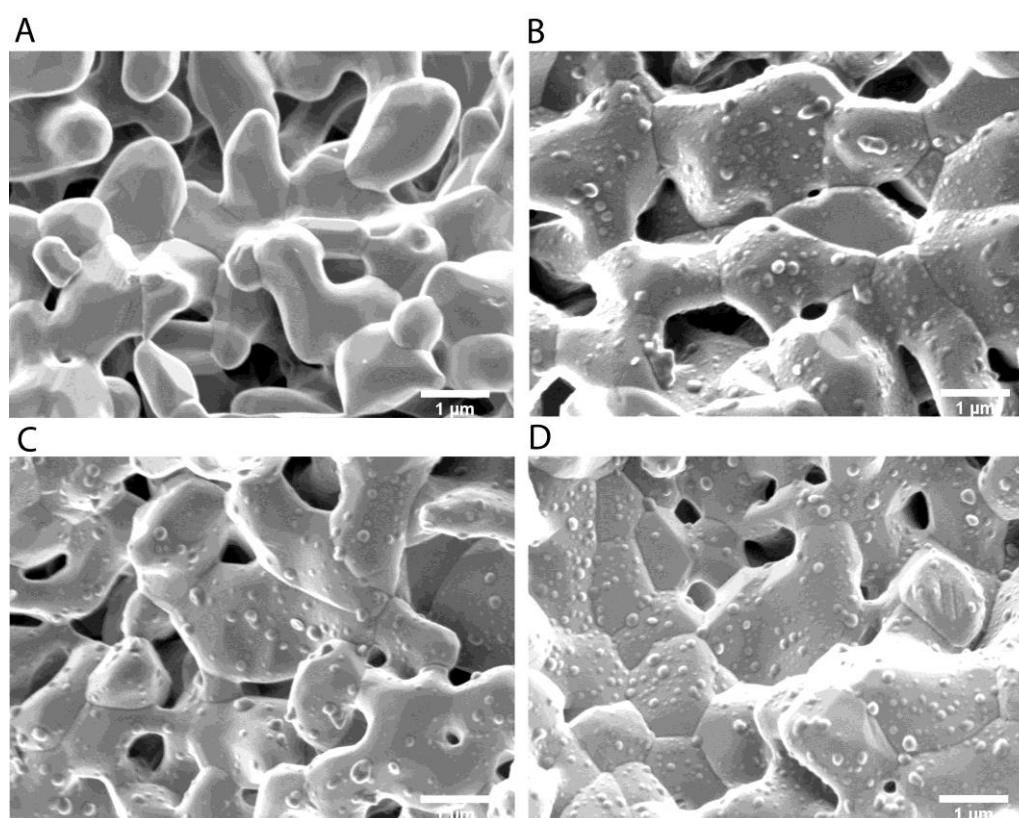


Fig. 3.1 – 22 Scanning electron micrographs of the calcium phosphate attachment experiments: (A) MBCP+; (B) MBCP+/ PPE-NP; (C) MBCP+/ PPE-NP-1; (D) MBCP+/ PPE-NP-15. Bar scales 1 μm (Alexandrino *et al.*; *J. Mater. Chem. B*, 2014, **2**, 1298-1306,

<http://pubs.rsc.org/en/Content/ArticleLanding/2014/TB/c3tb21295e#!divAbstract> -

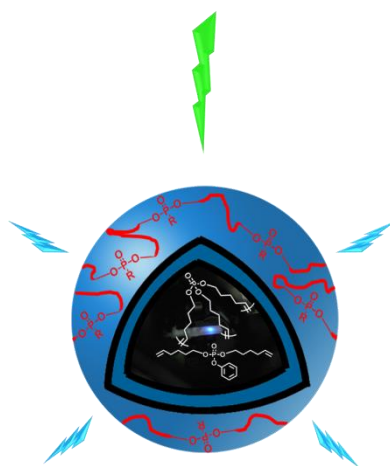
Reproduced by permission of The Royal Society of Chemistry).

3.1.11 Conclusion

A new class of nanoparticles based on potentially biodegradable and biocompatible polyphosphoesters with potential inherent bone adhesion abilities was developed using materials produced through different olefin metathesis approaches. The hydrophobic polyphosphates or polyphosphonates were prepared by metathesis protocol (ADMET and ROMP) and the miniemulsion/solvent-evaporation method proportioned stable nanoparticles dispersions, with low size distribution and also an effective method for loading of a hydrophobic drug (up to 10 wt%). Solid state NMR provided insights about how the interaction between the synthetic PPEs here prepared and calcium ions can be controlled, demonstrating that a specific and strong interaction is observed between those ions and polyphosphoesters bearing a hydroxyl group in the pendant side chain. The control of such interaction is a primordial know-how in the development of new solutions aiming the treatment of bone diseases and tissue engineering. *In vitro* studies proved that the polyphosphate nanoparticles are non-toxic against HeLa or Saos-2 cells for concentrations up to 600 mg ml⁻¹ or 300 mg ml⁻¹, respectively, and that the polyphosphate nanoparticles loaded with Paclitaxel exhibit a similar cytotoxicity as the commercial available Taxomedac® against osteosarcoma cells (Saos-2). The introduction of the hydrophobic drug did not influence the capacity of interaction of these nanoparticles with calcium phosphate, which creates the opportunity for the development of composite systems with bone cements that could also be applied for the delivery of Paclitaxel. Therefore, the nanoparticles developed in this work showed a high potential for the development of systemic or local treatment. Further studies are in progress to understand the drug transfer mechanism, material degradation as well as *in vivo* validation are required to assess the potential for a clinical application.

3.2 Full PPE core-shell nanocapsules for potential oxygen and temperature detection

Upconversion is a phenomenon of high interest in the scientific community, due to potential applications in biomedical, optical, and energy applications. The high sensitivity of this process against oxygen and the hydrophobicity of the dyes systems are great challenges but also offer potential handles for manipulation. In this chapter, a photon upconversion system was encapsulated in a PPE nanocapsule (with a linear PPE as shell) and organophosphates or hyperbranched unsaturated polyphosphates (as core), which were recently reported as very efficient protective matrix against oxygen. This is the first colloidal system with merely PPE colloids for UC. The decay rates of the upconversion signal in presence of oxygen were evaluated as well as the temperature dependence of the relative upconversion efficiency of the systems. All upconversion measurements were performed with the collaboration of Dr. Dmitry Busko.



3.2.1 Motivation

Luminescence based phenomena continuously attracts the attention of the scientific community and nowadays especially in the development of solutions in biomedical fields, as for example bioimaging, phototherapy and oxygen, pH and temperature detection.²²² Up to date, diverse strategies have been developed based on fluorescent proteins,²²³ quantum dots,²²⁴ etc., which are mostly based on Stokes shift emission, i.e. the emission of lower-energy photons promoted by the use of higher-energy photons.²²² Few processes can nevertheless produce higher-energy photons under stimulation with lower-energy ones, generating thus an anti-Stokes emission,^{222, 225} which in bioimaging applications results in advantages such as high signal-to-noise ratio and superior photo stability. Between the anti-Stokes processes available, the triplet-triplet annihilation (TTA) upconversion process stands out in comparison with other anti-Stokes emission phenomena like second harmonic generation or two-photon absorption, showing advantages as the use of incoherent and low intensity light.^{222, 226}

The TTA upconversion is a photochemical process based normally on an interaction between at least two chromophores, a sensitizer and an annihilator or emitter.²²² Basically, the upconversion cycle starts with the sensitizer being excited by lower energy photons, followed by a fast intersystem crossing process (ISC), with the lowest triplet state being occupied; in the next step the energy of the previously formed triplet state is “transferred” to an adequate triplet state of the emitter molecule, and finally two triplet states of the emitter molecules are combined to form a higher energy singlet state, which will provide later on a higher energy photon through decay. Many different molecules can be combined to act as chromophores in the TTA upconversion process, providing an almost unlimited flexibility in the wavelength region for the spectral emission of this process,^{222, 226} which simultaneously increases the number of possible applications.

Although the TTA upconversion process could occur in infinity cycles in an ideal system, in reality two main concurrent processes interfere: natural triplet decay and triplet quenching by oxygen.²²⁶ Diverse attempts have been made aiming for the optimization of the protection of upconversion systems in aerated environments, as the use of rubbery polymer matrices^{227, 228} or solvents and polymers containing unsaturated double bonds to chemically quench singlet oxygen species.^{13, 14} Marsico *et al.*¹⁴ showed the potential of hyperbranched unsaturated polyphosphoesters (hbUPPEs) in the long term protection of TTA upconversion systems formed by palladium tetrabenzoporphyrin (PdTBP) and

3,9(10)-bis(3,3-dimethylbut-1-yn-1-yl)perylene. Polyphosphoesters are of high interest for biomedical applications, due to the potentially biodegradability and biocompatibility as well as the structural versatility which allows an easy modification of the backbone, the side chains and the end groups to tailor the functionality and solubility profile.^{121, 201} Nevertheless, the direct use of the rather soft (T_g below room temperature) hydrophobic hbUPPEs in biomedical fields is limited due to the difficulty to disperse this kind of materials in the blood stream. An alternative is the development of core-shell systems like nanocapsules with a “hard” shell. The strategy of adding oxygen scavenging materials in the core in micro- and nanocapsules systems has been demonstrated to be effective in the development of oxygen resistant TTA upconversion systems.^{229, 230} As a shell material, linear polyphosphoesters, previously applied in the development of paclitaxel nanocarriers for bone cancer strategy, emerge as potential candidates, due to their crystallinity and evidenced biocompatibility.¹

Herein, is presented in this Thesis the preparation of the first fully PPE core shell nanocarriers with a crystalline PPE shell and an amorphous PPE liquid core, a system that sums to the biodegradability and potential biocompatibility of the PPEs explored in the previous chapter the potential oxygen barrier properties of the PPE liquid cores. In the inside, a TTA upconversion dye system composed of a sensitizer and an emitter was loaded, in order to evaluate the oxygen barrier properties. All upconversion measurements were performed in collaboration with Dr. Dmitry Busko. The hbUPPE polymer or an organophosphate monomer with oxygen scavenging properties is used as core material with linear polyphosphate or polyphosphonate as shell material. Stable colloids are obtained for both core materials, and the protection against oxygen and the thermal dependence of the systems is evaluated.

3.2.2 Experimental part

3.2.2.1 Materials

The synthesis of the monomers and the polymerization of linear and hyperbranched polyphosphoesters accomplished by ADMET, was previously described in the literature.^{2, 13, 14, 16, 204} The hyperbranched PPEs possess molecular weight of ca M_w 6,000 g mol⁻¹. Sodium dodecyl sulfate (SDS) was purchased from Sigma-Aldrich. Chloroform (analytical grade), used for the preparation of the nanocapsules and nanodroplets systems, was purchased from

VWR and the water purified by reverse osmosis (Milli-Q, Millipore®). Perylene was purchased from Aldrich and purified by sublimation before use. Platinum (II) octaethylporphyrin (PtOEP) was purchased from Aldrich and used without further purification. All chemicals, unless otherwise stated, were used as received.

3.2.2.2 Nanodroplet and nanoparticle preparation

Hyperbranched PPE nanodroplets and PPE-C20-Phenoxy nanoparticles were synthesized using an adopted combination of the miniemulsion technique and the solvent-evaporation strategy.²⁰² In a glass vial protected from light, 30 mg of the hyperbranched PPE were dissolved in 1.25 g of chloroform. To this solution certain volumes of the stock solutions of perylene and PtOEP in chloroform ($500 \mu\text{g ml}^{-1}$) were added, adjusting the final dyes concentrations to the volume of hyperbranched polymer. 5 g of Milli-Q water containing 10 mg of SDS were added to the chloroform solution and stirred during over a period of 60 min for the formation of the pre-emulsion. Then, the pre-emulsion was submitted to a pulsed ultrasonication process in an ice bath during 120 s (30 s sonicated and 10 s paused) at 70% amplitude by a $\frac{1}{4}$ " tip Brason 450 W sonifier. The obtained miniemulsion was kept at 30 °C in an oil bath over a period of 8 h to completely evaporate the organic solvent.

The average particle size and particle size distribution were obtained by dynamic light scattering (DLS) in a submicron particle sizer NICOMP® 380 equipped with a detector to measure the scattered light at 90°.

3.2.2.3 Nanocapsule preparation

Core-shell PPE nanocapsules and other nanocapsules were synthesized by an adopted combination of the miniemulsion technique and the solvent-evaporation strategy (Figure 3.2 – 1).²⁰² In a glass vial protected from light, 30 mg of the linear polymer (PPE or PMMA) and 60 mg of PPE monomers or hyperbranched PPE were dissolved in 1.25 g of chloroform. To this solution certain volumes of the stock solutions of perylene and PtOEP in chloroform ($500 \mu\text{g ml}^{-1}$) was added, adjusting the final concentration to the volume of hyperbranched polymer. Ultrasonication conditions similar to the ones presented in the section 3.2.2.2 were applied. The obtained miniemulsion was kept at 30 °C in an oil bath

over a period of 8 h to completely evaporate the organic solvent. Particle size and charge were measured as described in section 3.2.2.2. The particle morphology was studied by scanning electron microscopy (SEM) using a Zeiss LEO Gemini 1530 microscope. Transmission electron microscopy (TEM) was performed in a JEOL 1400 microscope, after a drop cast of the nanoparticle dispersion onto a carbon coated copper grid.

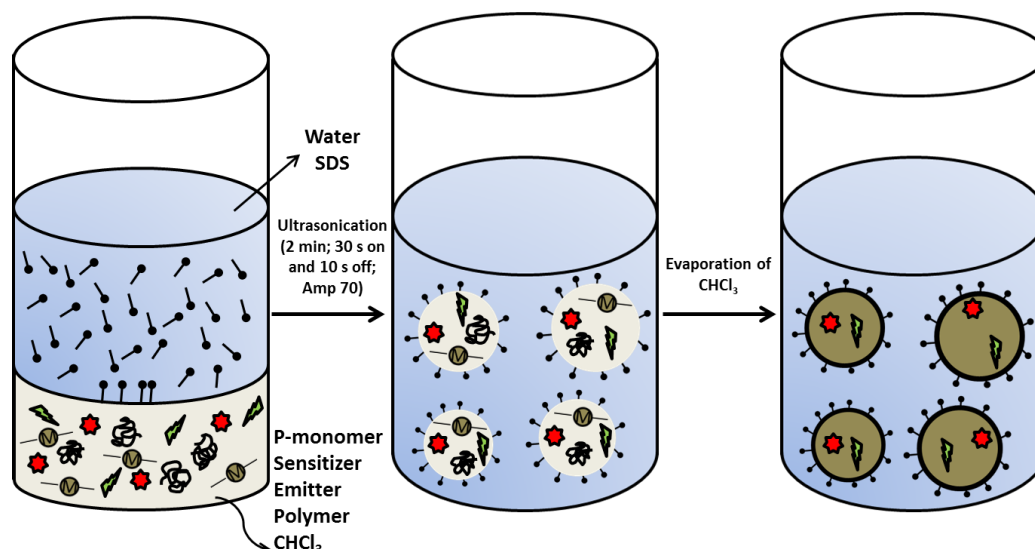


Figure 3.2 – 1 General miniemulsion/solvent-evaporation approach for the preparation of nanocapsule systems.

3.2.2.4 TTA-UC measurements

For the measurement of the luminescence spectra of the samples, a special optical glass cuvette (1 mm thickness) was filled with approximately 300 μL of the colloidal dispersion under nitrogen atmosphere (Glovebox system Mecabox MF82-1) and then sealed to prevent oxygen contamination. The luminescence spectra were obtained using the setup shown in Figure 3.2 – 2.²³¹ The measurement setup, constructed by Dr. Dmitry Busko, utilizes the DPSS laser (DJ532-40 (Thorlabs Inc.), 532 nm, 40 mW) as an excitation source. A round continuously variable neutral density filter (Thorlabs Inc.) placed on revolving optical holder was used to attenuate smoothly the beam power. The laser beam was guided by ultrabroadband mirrors (MaxMirror, Semrock Inc.) and finally focused by an achromatic lens (NA = 0, 24) onto the sample. The luminescence emission generated by the sample was collected by the same achromatic lens, thus the excitation- and observation-spots were completely spatially overlapped. The excitation light ($\lambda_{\text{exc}} = 532 \text{ nm}$) was rejected by notch

filter NF01-532U-25 (Semrock Inc.). The emission spectra were registered by CCD-spectrometer (C10083CA, Hamamatsu Inc.). For the measurements in presence of oxygen, the samples were unsealed and exposed to atmospheric oxygen. The samples were again closed before measurement and the variation of the luminescence spectra was recorded during a determined period of time (50 to 800 s).

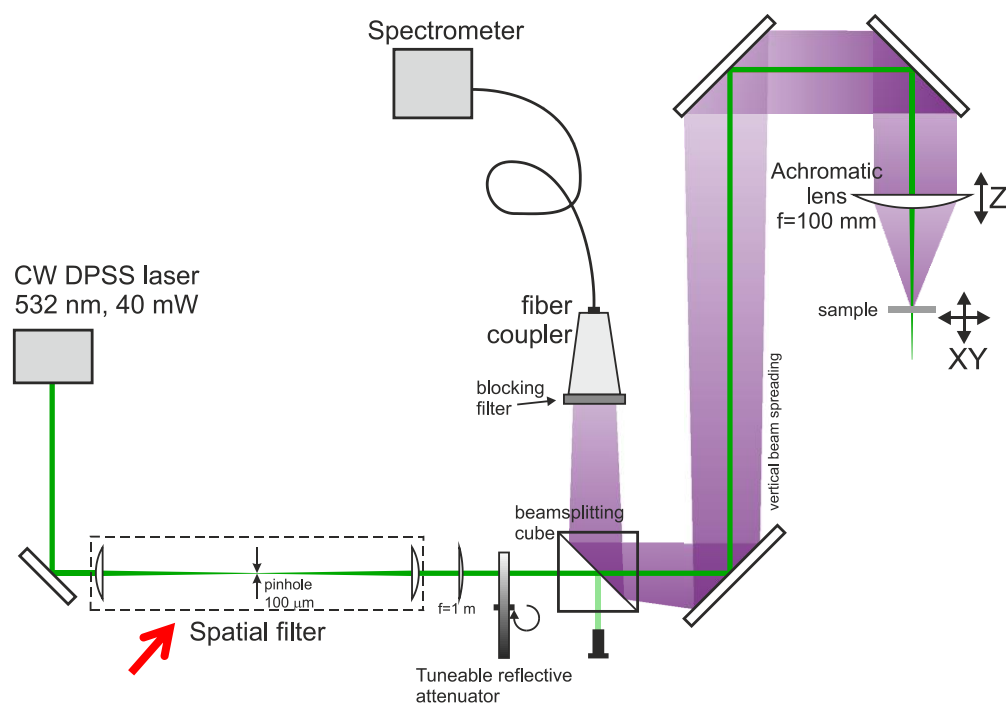
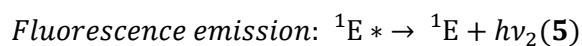
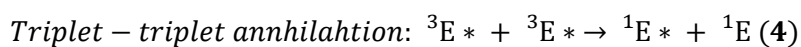
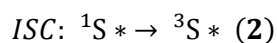
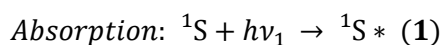


Fig. 3.2 – 2 Representative scheme of the measurement setup used for record of the luminescence spectra (Figure gently provided by Dr. Dmitry Busko ²³¹).

The temperature dependent measurements were performed in the same setup measurement showed in Figure 3.2 – 2, with substitution of the regular sample holder by a thermo stabilized stage from LINKAM Inc. The stage allows measurement within -190 to 120 °C, with 0.1 °C accuracy. Temperature control is obtained through a cooling system, consisted of cold water or liquid nitrogen. The sample solutions were placed in a thinner optical glass tubes (VitroCom, thickness 400 μm), aiming faster thermal equilibrium conditions, in oxygen free atmosphere. All the samples were sealed prior measurement. Four cyclic measurements were performed in a sequence for each sample, with lowest temperature 20 °C and highest temperature 60 °C. A luminescence spectrum was recorded every 5 °C.

3.2.3 Organophosphate core shell PPE colloids for TTA upconversion

In order to construct a better understanding of the PPE colloids features in TTA upconversion, a detailed explanation of the most accepted mechanism is presented beforehand. A TTA upconversion process scheme is represented by Figure 3.2 – 3 and equations (1) – (5).²²⁶ Sensitizer molecules (S), typically comprised by heavy-metal complexes with porphyrin, phthalocyanine, polyimines or cyclometalated ligands or organic sensitizers as iodo-substituted dyes or C₆₀ derivatives,²²² are excited with lower-energy photons (eq. 1) and through a fast intersystem crossing process (ISC) the system is converted to the lowest excited triplet state (eq. 2). Then, the sensitizer can interact with the emitter (E) chromophore and transmit the energy to it through a triplet-triplet transfer process (TTT, eq. 3). Emitter molecules are comprised normally by polycyclic aromatic hydrocarbons and heterocyclic dyes, and a large library is available up to date.²²² The excited triplet state of the emitter must have an adequate triplet energy state for the efficient TTT and a slow decay rate (e.g. long lifetime), so the number of excited species can be raised, increasing that way the efficiency of the triplet-triplet annihilation process (eq.4). The TTA process results in the formation of one singlet ground state emitter molecule and a excited singlet state of emitter, which finally undergoes fluorescence emission decay, resulting in a photon with higher energy than the ones used for the excitation of the sensitizer (eq. 5).



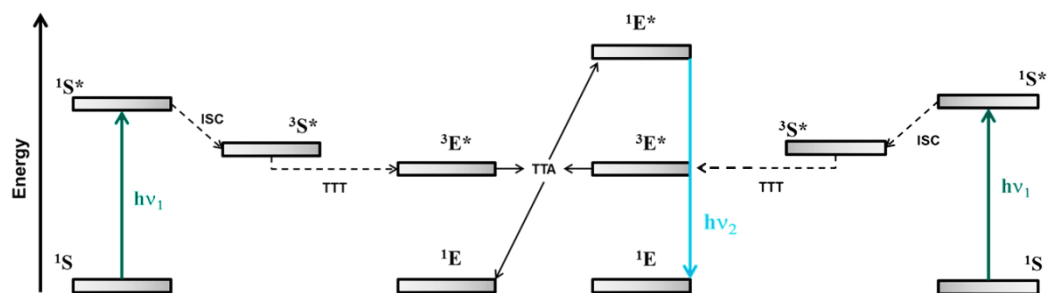
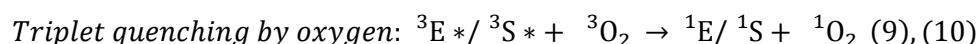
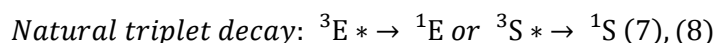


Fig. 3.2 – 3 Schematic energy-level diagram of the triplet-triplet annihilation photon upconversion process.

As previously mentioned, despite the upconversion process, two others processes can interfere with the final emission: natural triplet decay and oxygen triplet quenching (eq. 7 – 10).²²⁶ The natural triplet decay is closely related to the mobility of the system, since it is related to a forbidden transition. Such transitions are usually slower than allowed ones, as for example the singlet-singlet transition of the emitter in the upconverted photon emission. In case the system shows lower mobility, the “incapacity” to perform the energy transfer process (eq. 3) or TTA process (eq. 4) will allow a slower non radiative decay path to be followed, in the form of phosphorescence emission by sensitizer. The role of oxygen is without no doubt one of the most crucial in TTA upconversion systems. Being initially in a triplet ground state, oxygen can react with triplet states formed in the system and generate singlet oxygen,²²⁶ a higher reactive species, which can further degrade the chromophores in the system. Especially polycyclic compounds, such as anthracene derivatives, which are typically used in the TTA-UC, presents high reactivity against oxygen via a Diels-Alder mechanism, resulting in a typically irreversible damage for the upconversion system and consequent quenching of the fluorescence.²³²



Recently, our group has made advances in the development of a large library of hyperbranched unsaturated PPEs, which can act as an excellent protective matrix for oxygen sensitive systems, for example, the triplet-triplet annihilation upconversion systems.^{13, 14} As previously mentioned, Marsico *et al.* introduced the potential of hyperbranched unsaturated polyphosphoesters (hbUPPEs) as oxygen scavenging materials.^{13, 14} Through the measurement of T_1 relaxation times via NMR for proton, carbon and phosphorus

(Figure 3.2 – 4) and calculations of the HOMO and LUMO energies for fragments of hyperbranched polymers, the authors concluded that the double bonds are responsible for the interaction with singlet oxygen.

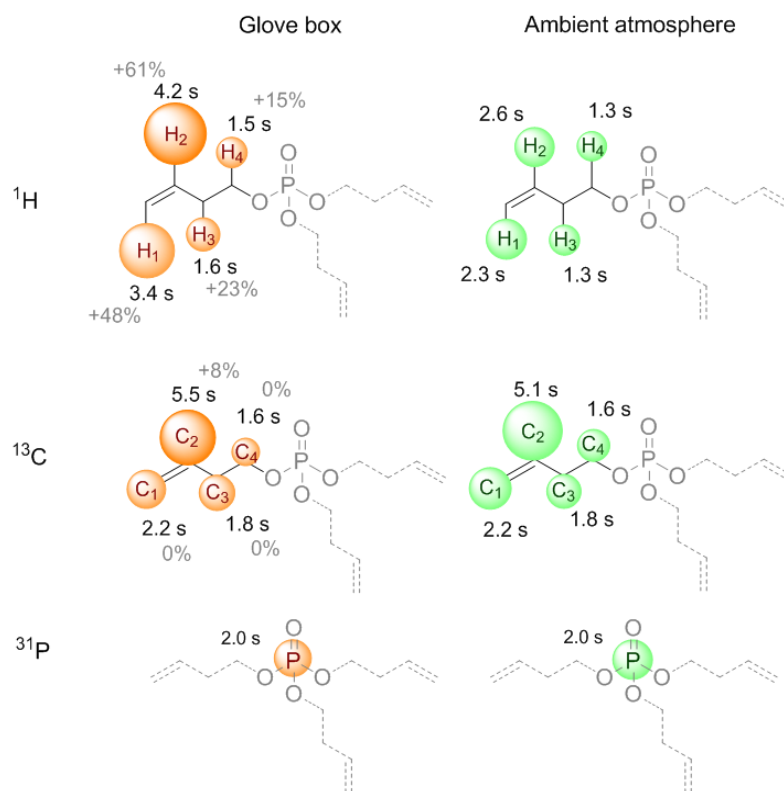


Fig. 3.2 – 4 T_1 relaxation time measurements from proton, ^{13}C and ^{31}P for the hyperbranched unsaturated polyphosphates measured in oxygen free and 21% oxygen atmosphere, performed by Dr. Filippo Marsico and collaborators. The increased relaxation times of the protons measured under oxygen free atmosphere (glove box – 2 ppm O_2) suggest a strong interaction between the π -orbitals and the free electrons in the oxygen molecules (Reprinted with permission from Marsico *et al. J. Am. Chem. Soc.*, 2014, 136 (31), pp 11057–11064. Copyright © 2014, American Chemical Society).¹⁴

Despite the higher protection level observed in the hyperbranched systems, organophosphates were also able to exhibit an outstanding performance in bulk TTA upconversion samples.¹³ Nevertheless, the high hydrophobicity of these systems is a limiting parameter in the application of these materials aqueous environments. Herein we transfer them into an aqueous dispersion: the formation of nanocapsules was performed using the less viscous organophosphates as core. Previous experience in our group have showed that

the use of highly hydrophobic cores as hexadecane and heptadecane have been highly effective for the formation of capsule-like morphologies with different polymers as shell materials, as for example PMMA. Aiming to use a similar strategy, firstly four different materials were combined accordingly to their hydrophobicity. As core materials, two different organophosphates were applied, containing different carbon chain lengths, providing materials with varied hydrophobicity and density of phosphate units. 1-phenyl heptadecane (PHD) was used for preparation of one control system for further comparison. As shell material candidates, two linear acrylate polymers (PMMA and P(BuMA)), used as control, and two linear PPEs were selected. The hydrophobicity of the shell materials candidates was measured by contact angle with water from films prepared by spin-coating and PMMA and PPE-C20-Methoxy showed a contact angle of approximately 75° and P(BuMA) and PPE-C20-Phenoxy approximately 90°. The more hydrophobic core, C11-Ph-P, was combined with the less hydrophobic shell materials, in order to increase the insolubility of the shell material in the organophosphate core and induce the phase separation. The same reasoning was applied for C6-Ph-P. The herein used PPEs are semi-crystalline polymers, which could be a factor in favor of the protection of the core against oxygen, as previously observed in other systems as cellulose capsules.²³² In addition with this approach a fully biodegradable system (PPE) is achieved for the first time, which could be of great interest for biomedical applications. PtOEP and perylene were chosen to serve as sensitizer and emitter, respectively (Figure 3.2 – 5).

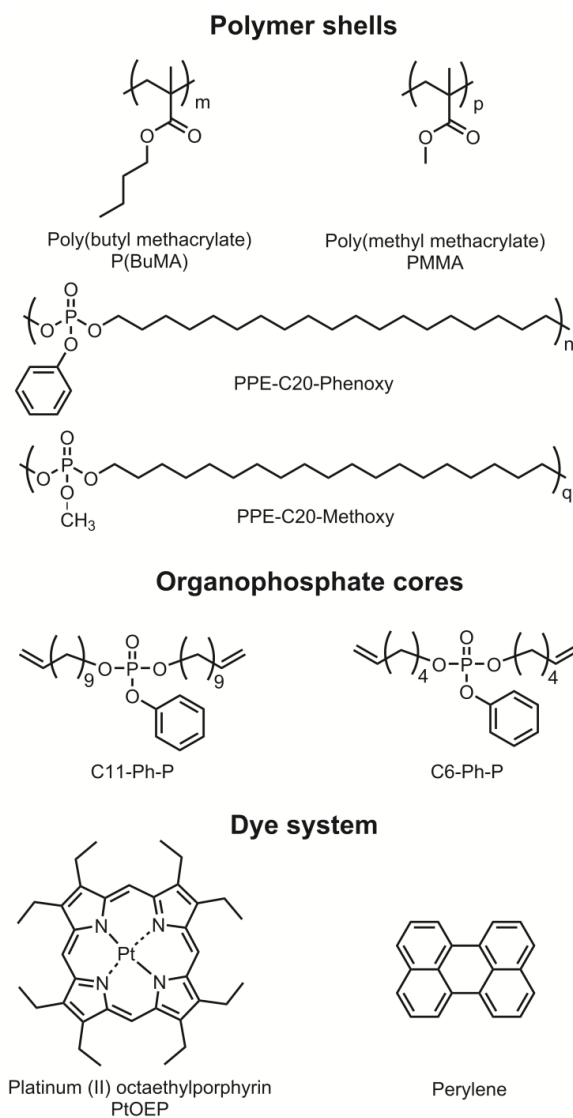


Fig. 3.2 – 5 Chemical structures of the materials used in the PPE nanocapsules with UC properties.

The size and size distribution determined by light scattering are shown in Table 3.2 – 1. The sample prepared with P(BuMA) showed the largest size distribution and a thin layer of the phase separated liquid core in the bottom of the flask, which confirms that this system did not lead to an efficient encapsulation. In case of no encapsulation of the core, larger size distributions are expected due to coalescence and phase separation of the liquid cores. All the samples, except for the one prepared with P(BuMA), proved to be stable even after 3 months kept at room temperature, without relevant increase of the average size and size distribution. It should be noted that the morphological characterization of the systems containing an organophosphate as core and a PPE as shell is difficult. Nanocapsules can be visualized by TEM, if the core and the shell exhibit different densities (as it is mostly

the case with a solvent and a payload inside and a dense polymer shell). For the full-PPE systems the visualization by TEM is difficult, since the core and the shell material present similar electronic density (Figure 3.2 – 6).

Table 3.2 – 1 Mean diameter and size deviation of the four polymer shell/organophosphate core systems.

Sample	Mean diameter \pm S.D. (nm) ^a
P(BuMA)/C6-Ph-P	213 \pm 100
PMMA/C11-Ph-P	185 \pm 64
PPE-C20-Phenoxy/C6-Ph-P	196 \pm 81
PPE-C20-Methoxy/C11-Ph-P	239 \pm 81
PPE-C20-Phenoxy/PHD	164 \pm 66

^a Determined via dynamic light scattering using a NICOMP Particle Size Analyzer.

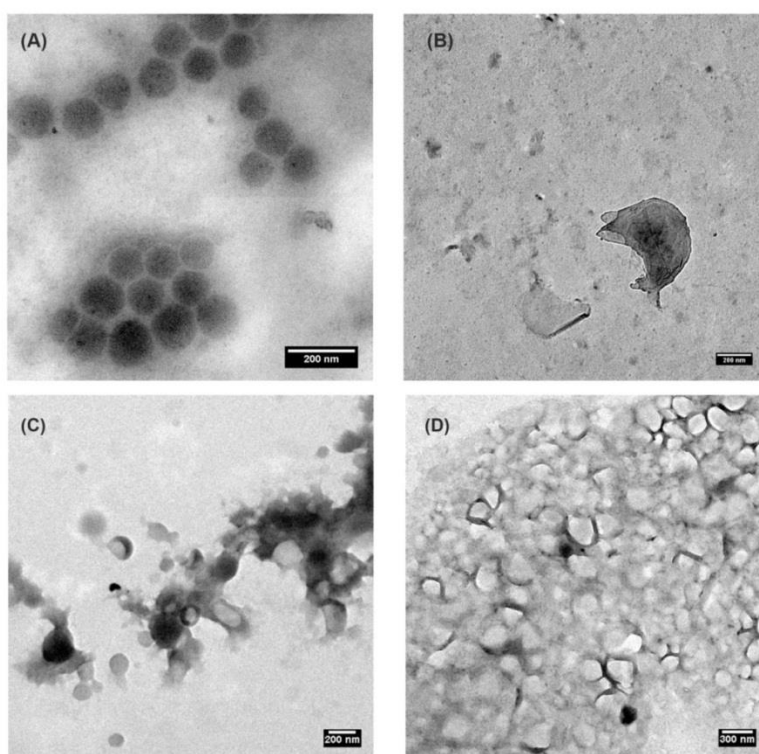


Fig. 3.2 – 6 TEM images of the PPE-C20-Methoxy/C11-Ph-P (A and B) and PMMA/C11-Ph-P: for the organophosphate core/PPE shell systems no core-shell morphology can be observed due to the similar electronic density of core and shell materials (A), except for samples where the shell was broken and the core has leaked (B). On the other hand, the capsule

morphology could be easily observed for the systems containing PMMA as shell material (C) or 1-phenyl-heptadecane (PHD) as core material (D).

In order to verify the upconversion capacity of the dispersions, the luminescence spectra of the emission of the samples in oxygen-free atmosphere was measured. Figure 3.2 – 7 presents the spectra obtained between 400 – 850 nm. For further comparison, a sample with 1-phenyl-heptadecane (PHD) as core material was produced, with the PPE-C20-Phenoxy as the shell material. PHD was previously applied in the preparation of upconversion nanocapsules systems, providing good results at *in vitro* experiments for cell bioimaging.⁴⁶ The green arrow indicates the wavelength used for excitation of the system (532 nm). Upconverted photons emitted by perylene were obtained for 4 of 5 systems, with the maximum intensity at approximately 475 nm. The exception was the system containing P(BuMA) as shell material, which reinforces the possibility of lower or non-encapsulation in this sample. A strong phosphorescent signal generated by the sensitizer dye can be observed at 645 nm.

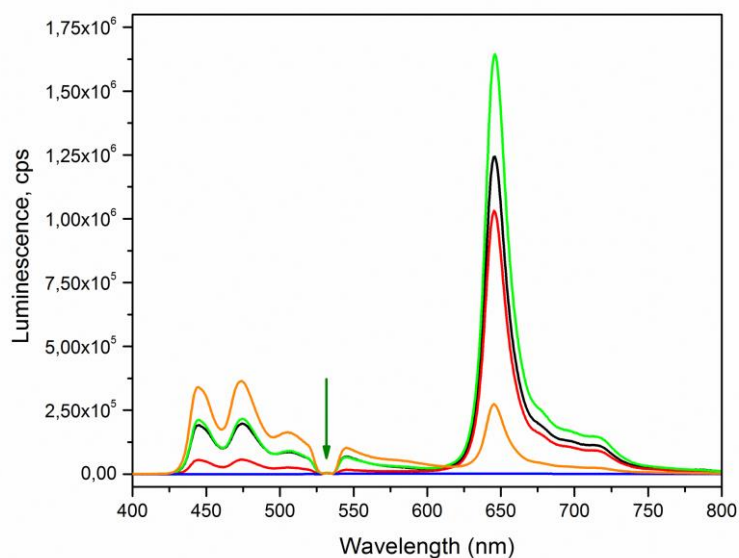


Fig. 3.2 – 7 Luminescence spectra of the four polymer shell/organophosphate core systems: P(BuMA)/C6-Ph-P (— blue —), PMMA/C11-Ph-P (— red —), PPE-C20-Phenoxy/C6-Ph-P (— green —) and PPE-C20-Methoxy/C11-Ph-P (— black —); reference system PPE-C20-Phenoxy/PHD spectrum (— orange —) ($\lambda_{exc} = 532 \text{ nm}$; $P_{exc} = 15 \text{ mW}$ - all the measurements were performed at the same measurement spot).

The most important factor of the TTA UC is the upconversion efficiency.^{222, 233} The calculation can be done either as the upconversion quantum yield (QY_{UC}) or upconversion quantum efficiency (QE_{UC}).²²² However, in colloidal systems the determination of such values is complicated due to the loss of photons by scattering, the difficulties to control the number of species in the same volume and to measure the absorption of the excited radiation. Therefore, an empirical method²³³ is applied: the ratio of the integrals from the upconverted photons (I_{UC}) and from the phosphorescence ($I_{Phosphorescence}$) is calculated for each system. For each upconverted photon measured, two photons are originally generated: one which is irradiated in a non-radioactive way and the measured photon. Thereby, the relative upconversion efficiency %UC can be calculated as:

$$\%UC = \frac{2xI_{UC}}{(2xI_{UC}+I_{Phosphorescence})} \times 100 \quad (11)$$

It is important to stress that this relation is only valid for internal comparison between the TTA upconversion systems prepared in this work, containing the same dye system. This relation should not be applied for comparison with other upconversion systems. Figure 3.2 – 8 shows the calculated efficiency for each of the systems for a concentration of sensitizer and emitter of $1 \times 10^{-5} \text{ mol L}^{-1}$ and $2 \times 10^{-4} \text{ mol L}^{-1}$, respectively. As it seen in Figure 3.2 – 7, the efficiency of the system containing polyphosphoesters as the shell material is higher than the PMMA, with efficiency around 30 – 40% for the PPE shell systems. The values for these systems are still low in comparison with other systems reported in previous works, were nanocapsules systems could show efficiency up to 95%.²³³ Nevertheless, as will be explained in the upcoming discussion, the comparison must be carefully done, since diverse parameters can play a role in the efficiency of the upconversion, as the dye system or the concentration.

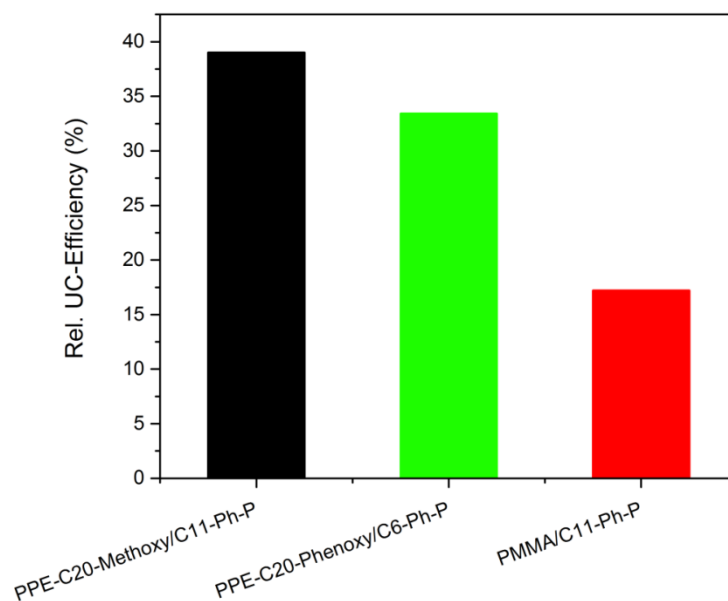


Fig. 3.2 – 8 Relative upconversion efficiency for the polymer shell/organophosphate core systems, with $[\text{PtOEP}] = 1 \times 10^{-5} \text{ mol L}^{-1}$ and $[\text{Perylene}] = 2 \times 10^{-4} \text{ mol L}^{-1}$.

3.2.4 Effect of emitter concentration

Due to the higher upconversion efficiency, which means the more efficient use of the created sensitizer triplet population for emission of upconverted photons in the full polyphosphate samples, the systems PPE-C20-Phenoxy/C6-Ph-P and PPE-C20-Methoxy/C11-Ph-P were further analyzed in relation to the effect of the increase of the emitter concentration. The strong phosphorescence seen in encapsulated systems is normally not observed in experiments using the same core material as bulk matrix for upconversion for the perylene/PtOEP dye system. This observation was done previously by Marsico *et al.*¹³ and the spectrum for the PtOEP/perylen system in C6-Ph-P is reproduced in the Figure 3.2 – 9. A possible explanation for such effect in encapsulated systems is the lower mobility of some of the dyes. Due to interactions with the polymer shell membrane in the confined system, less interaction between the two dyes is afforded, resulting in higher number of sensitizer molecules that lost the energy of the triplet state not through a triplet-triplet transfer process but rather through a natural decay process, as phosphorescence.

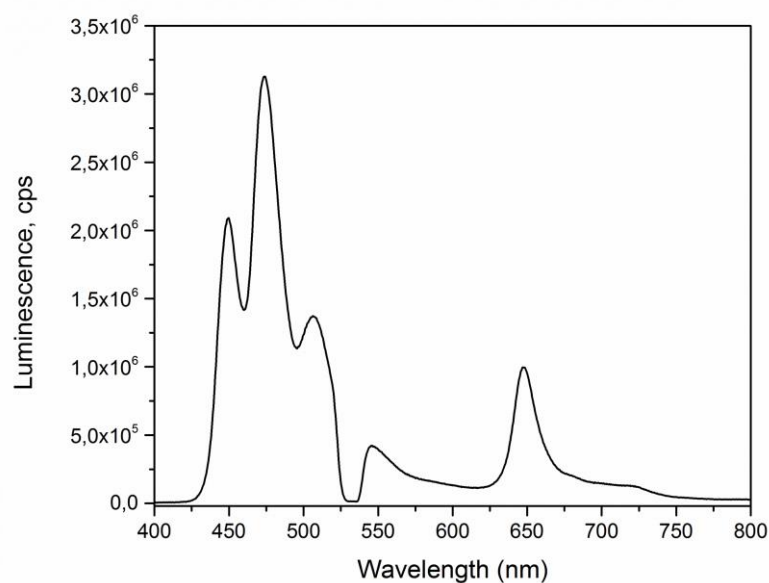


Fig. 3.2 – 9 Luminescence spectrum for the system PtOEP/perylene diluted in C6-Ph-P measured under oxygen free conditions ($[PtOEP] = 1 \times 10^{-5} \text{ mol L}^{-1}$ and $[Perylene] = 1 \times 10^{-3} \text{ mol L}^{-1}$; $\lambda_{exc} = 532 \text{ nm}$; $P_{exc} = 15\text{mW}$).

To test this hypothesis, the effect of concentration increase of one of the components was analyzed. Increasing the emitter concentration whereas the concentration of the sensitizer is kept constant should increase the probability that the energy transfer process between triplet states occurs, resulting in an increase of the upconversion efficiency. The concentration of emitter was varied from $2 \times 10^{-4} \text{ mol L}^{-1}$ up to $1 \times 10^{-3} \text{ mol L}^{-1}$. The results at oxygen free atmosphere can be seen in Figures 3.2 – 10 and 3.2 – 11. Figures 3.2 – 10A and 10B show the changes in the spectra of the samples accordingly to the emitter concentration and Figure 3.2 – 11 shows the variation of the relative efficiency. As can be seen, the addition of higher amounts of emitter leads to an increase on the efficiency for both systems as expected, but especially for the system containing C6-Ph-P as the core material, where an almost 2.5 fold increase was observed.

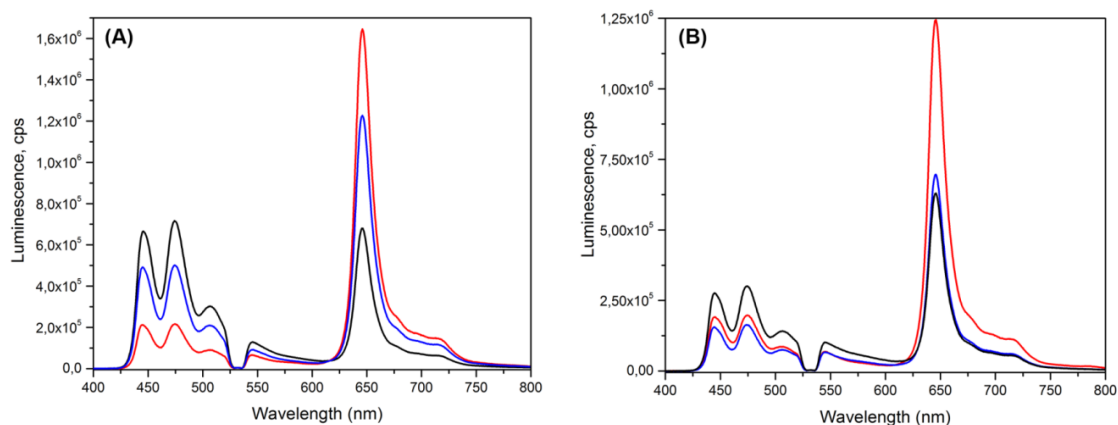


Fig. 3.2 – 10 Luminescence spectra for the systems (A) PPE-C20-Phenoxy/C6-Ph-P and (B) PPE-C20-Methoxy/C11-Ph-P, with $[PtOEP] = 1 \times 10^{-5} \text{ mol L}^{-1}$ and $[Perylene] = 2 \times 10^{-4} \text{ mol L}^{-1}$ (red), $5 \times 10^{-4} \text{ mol L}^{-1}$ (blue) or $1 \times 10^{-3} \text{ mol L}^{-1}$ (black) ($\lambda_{exc} = 532 \text{ nm}$; $P_{exc} = 15\text{mW}$ - all the measurements were performed at the same measurement spot).

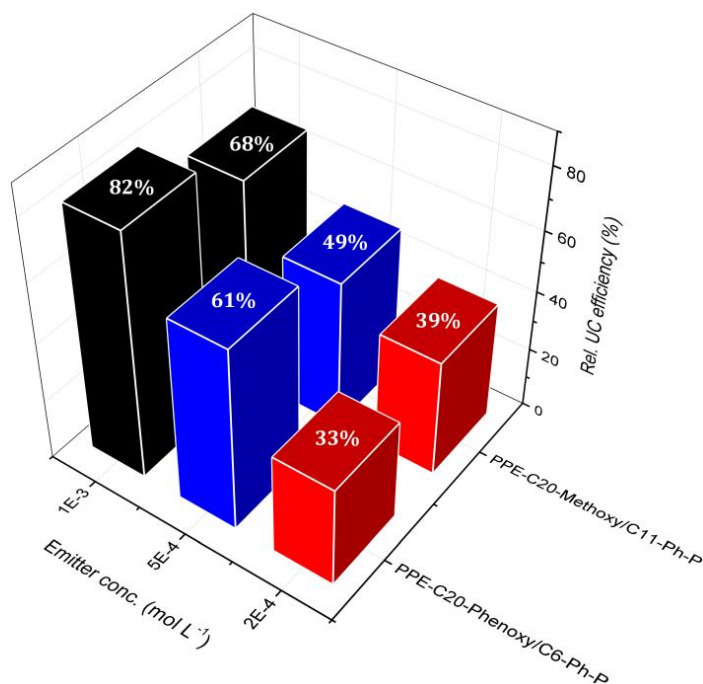


Fig. 3.2 – 11 Relative upconversion efficiency for the polymer shell/organophosphate core systems in dependence on the concentration of emitter ($[PtOEP] = 1 \times 10^{-5} \text{ mol L}^{-1}$, $\lambda_{exc} = 532 \text{ nm}$; $P_{exc} = 15\text{mW}$ - all the measurements were performed at the same measurement spot).

3.2.5 hbUPPE nanodroplets and core/PPE shell nanocapsules

In comparison to bifunctional organophosphate monomers, hyperbranched unsaturated PPEs present a higher density of terminal double bonds and at the same time possess low viscosity values, even though higher than the viscosity of the organophosphate monomers previously studied. In order to analyze the influence of such properties on the oxygen barrier properties and upconversion behavior of colloidal systems, a hyperbranched unsaturated polymer (PPE-(C6)₃) was synthesized based on trihexenylphosphate, a trifunctional monomer similar to C6-Ph-P. Nanocapsules systems with PPE – (C6)₃ as core material and two different classes of PPE as shell material, the polyphosphate PPE-C20-Phenoxy and the polyphosphonate PPE-C20-Methyl, were synthesized. The structures of the hyperbranched polymer and polyphosphonate are represented in Figure 3.2 – 12. The upconversion system PtOEP/Perylene was used with concentration of $1 \times 10^{-5} \text{ mol L}^{-1}$ and $1 \times 10^{-3} \text{ mol L}^{-1}$, respectively.

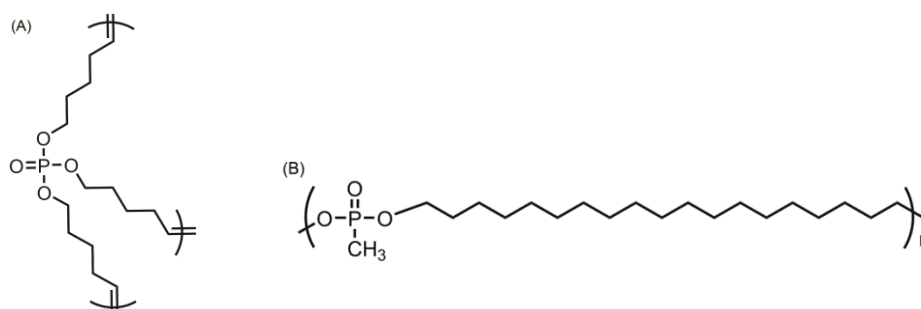


Fig. 3.2 – 12 Chemical structure from (a) hyperbranched unsaturated polyphosphate PPE-(C6)₃ and (b) polyphosphonate PPE-C20-Methyl.

The size and size distribution obtained for these systems are shown in Table 3.2 – 2 and Figure 3.2 – 13 shows the UV-Vis spectra obtained for both core shell systems, at excitation wavelength 532 nm. The spectrum of the system PPE-20-Phenoxy/PPE-C6-Ph and all the spectra were normalized to the phosphorescence signal for better comparison (due to the different signal intensities resulting of the different solid contents).

Table 3.2 – 2 Mean diameter and size deviation of the core/shell hbUPPEs based systems.

Sample	Mean diameter \pm S.D. (nm)
PPE-C20-Phenoxy/PPE-(C6) ₃	143 \pm 49
PPE-C20-Methyl/PPE-(C6) ₃	249 \pm 76

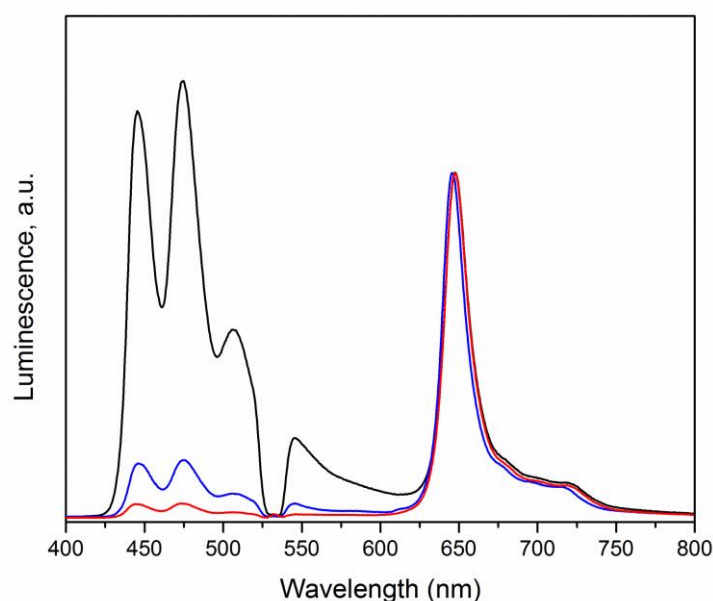


Fig. 3.2 – 13 Luminescence spectra of the PPE shell/hbUPPE core systems PPE-C20-Phenoxy/PPE-(C6)₃ (— blue —), PPE-C20-Methyl/PPE-(C6)₃ (— red —) and of the organophosphate core system PPE-C20-Phenoxy/PPE-C6-Ph (— black —) ($\lambda_{\text{exc}} = 532$ nm; $P_{\text{exc}} = 15$ mW - all the measurements were performed at the same measurement spot).

The system containing an organophosphate as the core material presents higher efficiency in comparison to the systems with the hyperbranched polymer as the core material. A relative upconversion efficiency of 38% was obtained for the system PPE-C20-Phenoxy/PPE-(C6)₃ and of 13% for the system PPE-C20-Methyl/PPE-(C6)₃, which are approximately 2 and 6-fold, respectively, lower than the value obtained previously for the organophosphate system. Two factors can possibly explain these results: lower encapsulation efficiency for the hyperbranched core systems and/or the higher viscosity of

the hyperbranched polymer in comparison to the organophosphate. These factors will be discussed in the upcoming sections.

On the other hand, if the higher viscosity of the hyperbranched system can be a possible drawback in the development of more efficient upconversion systems, it allows the development of stable colloidal systems without a stabilizing shell. Nanodroplets were prepared using the miniemulsion/solvent-evaporation strategy. It resulted in a stable colloidal system with size distribution similar to the core-shell systems previously described (Figure 3.2 – 14).

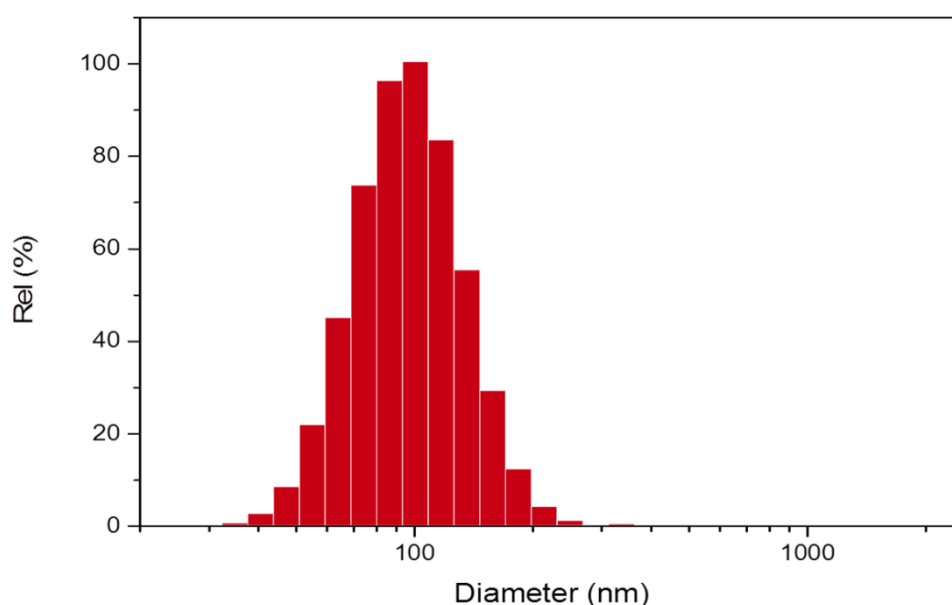


Fig. 3.2 – 14 DLS analysis of the nanoparticles produced from the hbUPPE PPE-(C6)₃ by miniemulsion/solvent-evaporation technique. Mean diameter: 101 ± 30.5 nm determined by light scattering in a NICOMP Particle Size Analyzer.

Figure 3.2 – 15 shows the emission spectrum of the system PPE-(C6)₃. The relative upconversion efficiency for this system was almost equal to that measured for the core shell system PPE-C20-Phenoxy/PPE-(C6)₃, and was estimated as 39%. Even though this system shows lower efficiency than previously obtained for the organophosphate, a highly interesting property was noticed: the nanodroplet system formed an almost transparent colloidal dispersion, as can be seen in the comparison with the system PPE-C20-Phenoxy/C6-Ph-P (Figure 3.2 – 16). The absence of the semi-crystalline shell and the smaller size of the nanodroplets resulted in less scattering, which may be the main

reasons for the observed characteristic. This property could be of great interest in the development of displays based on colloidal upconversion materials.

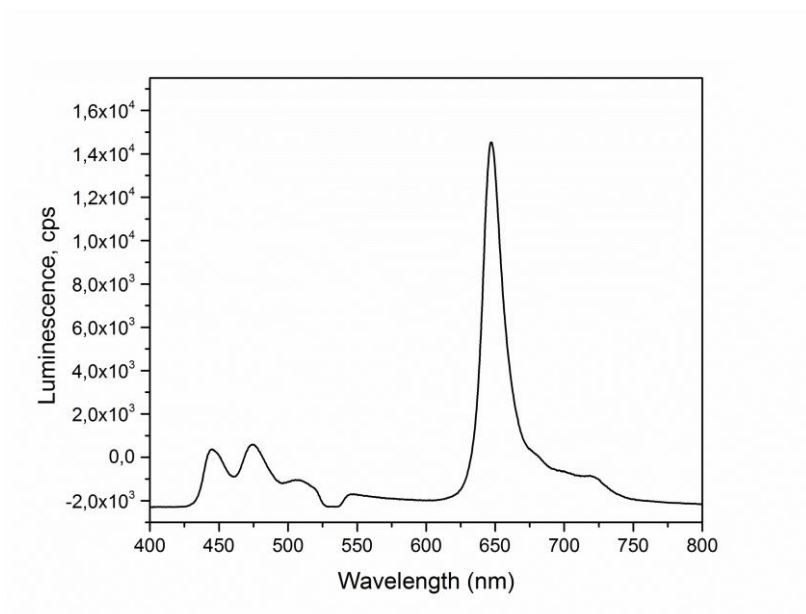


Fig. 3.2 – 15 Luminescence spectrum of the nanodroplet system based on the unsaturated hyperbranched polymer PPE-(C6)₃ ($\lambda_{exc} = 532$ nm; $P_{exc} = 15$ mW).

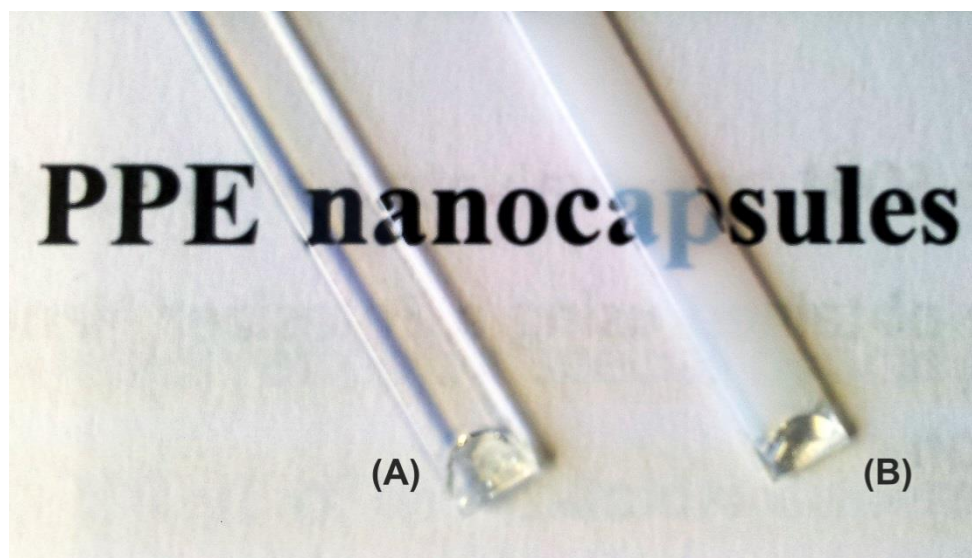


Fig. 3.2 – 16 (A) PPE-(C6)₃ nanodroplets and (B) PPE-C20-Phenoxy/C6-Ph-P nanocapsules in a 400±40 μ m thick optical glass cuvette.

3.2.6 Core/shell PPE colloids interactions with O₂

Upconversion process is highly sensitive to the presence of oxygen and many efforts have been made aiming the development of UC systems capable to work in oxygen-rich environment.^{232, 234, 235} To evaluate the oxygen protection provided by herein proposed systems, the temporal behavior of the upconversion signal in the presence of air was measured and the results are presented in the Figure 3.2 – 17. It is obvious that an upconversion signal is observed for all systems containing the organophosphate as core material, while for the system containing PHD no UC signal was detected in the presence of oxygen. Even though the time scale of the experiments is rather short, a clear protective effect in the presence of the organophosphate is clear, showing a dependence on the shell material. Although the PPE-C20-Methoxy presents the same core material as PMMA, the living time of the upconversion signal is higher for the polyphosphoester shell. Recently, Svagan *et al.* have reported the preparation of highly oxygen protective pristine cellulose nanofibers composites with nanocellulose-based capsules containing an upconversion system.²³² The high oxygen barrier property of pristine cellulose nanofibers films is attributed to its semicrystalline structure and optimal packing.^{232, 236} The crystallinity possibly play a role in oxygen barrier properties of these systems. PPE-C20-Methoxy and PPE-C20-Phenoxy are semi-crystalline materials, with melting point around 65°C and 45°C, respectively, while PMMA is an amorphous material, and both PPE material shells present higher protection efficiency against oxygen.

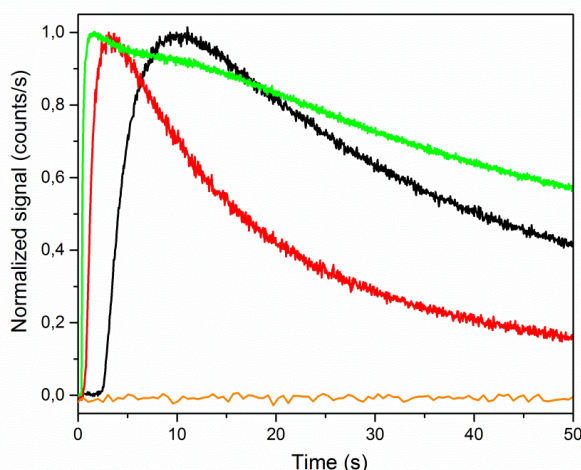


Fig. 3.2 – 17 Normalized upconversion signal versus time for the systems PMMA/C11-Ph-P (—), PPE-C20-Phenoxy/C6-Ph-P (—), PPE-C20-Methoxy/C11-Ph-P (—)

and the reference system PPE-C20-Phenoxy/PHD (—) ($\lambda_{\text{exc}} = 532 \text{ nm}$; $P_{\text{exc}} = 15\text{mW}$ - all the measurements were performed at the same measurement spot).

The effect of the emitter concentration in the oxygen resistance was also verified (Figure 3.2 – 18). The increase of the emitter concentration resulted in longer periods of upconversion signal emission. It is well known that high reactive species as singlet oxygen can easily degrade dyes as perylene.²³⁷ The increase of photogeneration of the singlet oxygen by porphyrins and metalloporphyrins dyes was also reported by many authors.²³⁸⁻²⁴⁰ Increment of the perylene concentration boost the concentration of species, which can react with the generated singlet oxygen, while the concentration of the porphyrin-based dye PtOEP is kept constant. Thus, the singlet oxygen produced is “scavenged” also by one of the components of the system, resulting in the increase of time for decay of the upconversion signal.

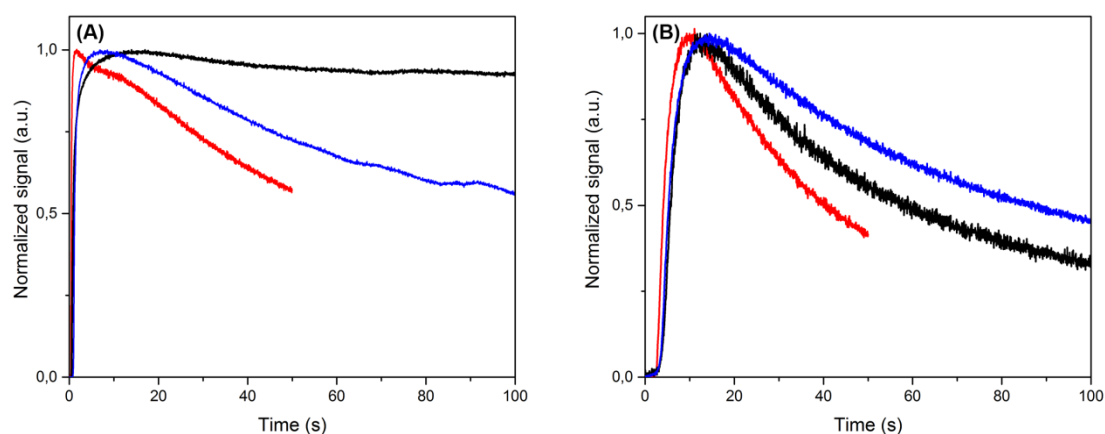


Fig. 3.2 – 18 Normalized upconversion signal versus time for the systems (A) PPE-C20-Phenoxy/C6-Ph-P and (B) PPE-C20-Methoxy/C11-Ph-P, with $[\text{PtOEP}] = 1 \times 10^{-5} \text{ mol L}^{-1}$ and $[\text{Perylene}] = 2 \times 10^{-4} \text{ mol L}^{-1}$ (red curve), $5 \times 10^{-4} \text{ mol L}^{-1}$ (blue curve) or $1 \times 10^{-3} \text{ mol L}^{-1}$ (black curve) ($\lambda_{\text{exc}} = 532 \text{ nm}$; $P_{\text{exc}} = 15\text{mW}$ – all the measurements were performed at the same measurement spot).

A second parameter that can interfere in the efficiency and the resistance against oxygen is the chemical characteristics of the dyes used for the upconversion system. 9, 10-diphenylanthracene or DPA (Figure 3.2 – 19) is a polycyclic aromatic hydrocarbon with emission in the UV region of the light spectrum. It is well known that in comparison to perylene, DPA has a faster reaction with singlet oxygen.²⁴¹⁻²⁴³ Therefore, a system containing DPA as the emitter should be less resistant to the oxygen at the same concentration of dyes. Figure 3.2 – 20A shows the emission spectra in oxygen free atmosphere for a samples

containing $1 \times 10^{-3} \text{ mol L}^{-1}$ of emitter (DPA or perylene) and Figure 3.2 – 20B shows the extinction of the upconverted signal in presence of oxygen. As expected, even though good upconversion efficiency (76%) is obtained for the system with DPA, the kinetics of oxygen reaction with DPA is clearly faster than with perylene. This observation reveals that even though the organophosphate core is capable to slow down the reaction of singlet oxygen with the dyes, the overall reaction kinetic will be dependent on the reactivity of the dye system against the singlet oxygen generated.

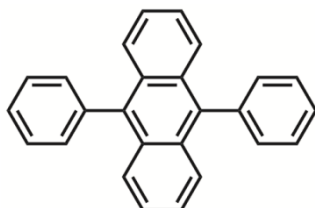


Fig. 3.2 – 19 Chemical structure of 9,10-diphenylanthracene.

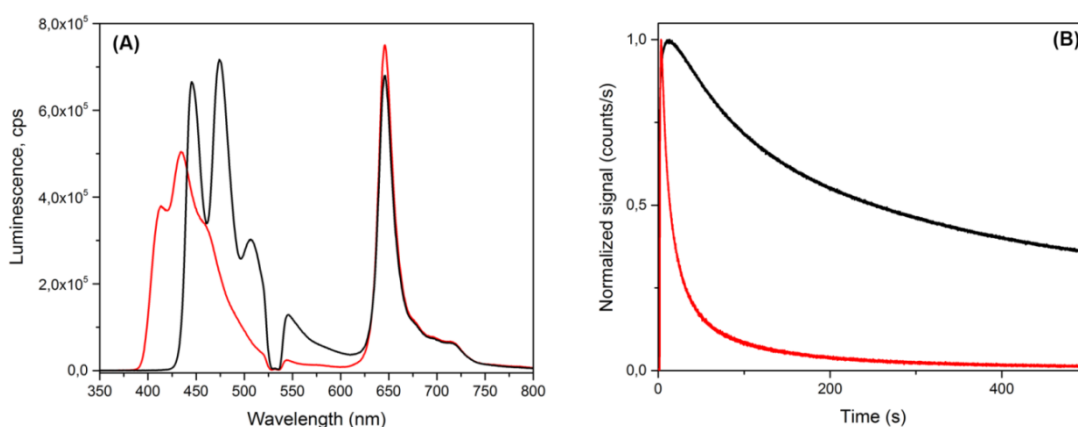


Fig. 3.2 – 20 Comparison between two emitter dyes – perylene (black) and DPA (red): (A) Luminescence spectra for the system PPE-C20-Phenoxy/C6-Ph-P, with $[\text{PtOEP}] = 1 \times 10^{-5} \text{ mol L}^{-1}$ and $[\text{emitter}] = 1 \times 10^{-3} \text{ mol L}^{-1}$; and (B) normalized upconversion signal versus time ($\lambda_{\text{exc}} = 532 \text{ nm}$; $P_{\text{exc}} = 15 \text{ mW}$ - all the measurements were performed at the same measurement spot).

The hbUPPE systems were also investigated in relation to their protection against oxygen. According to Marsico *et al.*¹³, for bulk upconversion systems the hbUPPE showed longer lifetime of the upconversion signal in the presence of oxygen in comparison to the organophosphates. The higher viscosity and the scavenging properties of this material seems to effectively slower the diffusion of oxygen in these systems. However, the same effect was observed in the colloidal systems. Figure 3.2 – 21 shows the kinetic of the upconversion

signal against oxygen for the three systems prepared using a hbUPPE in comparison to the system PPE-C20-Phenoxy/C6-Ph-P. As can be seen, the slowest decay rate of the upconversion signal in the presence of oxygen was obtained for the systems containing PPE-C20-Phenoxy as the shell material, independently of the core material used. Studies of oxygen absorption in oil-in-water emulsions from n-alkanes suggest that the solubility of a gas in an emulsion can be estimated from the solubility in pure liquids.²⁴⁴ Due to the small volume fraction of the oil phase and small volume fraction of the droplets in relation to the volume fraction of the water phase the diffusion properties of oxygen are mostly similar to the one in pure water. In comparison to the bulk system, the colloidal system will present a higher surface area for contact with oxygen dissolved in the water phase and the small volume of the core will show less influence in the diffusion of oxygen to meet the dyes system. In this scenario, the influence of the shell material in the final decay rate of the upconversion signal in the presence of oxygen is increased.

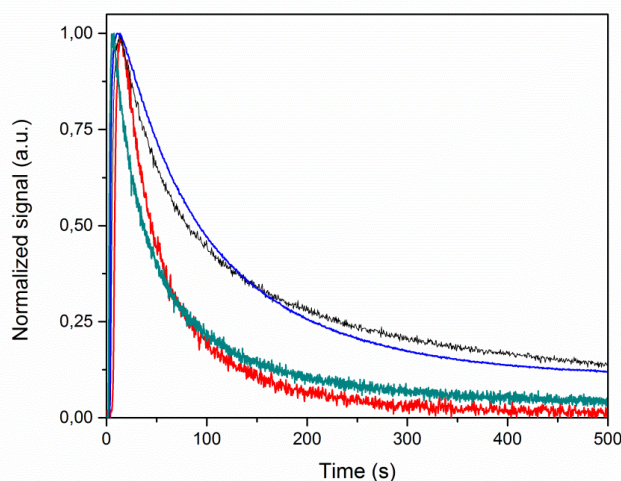


Fig. 3.2 – 21 Normalized upconversion signal versus time for the systems PPE-(C6)₃ (—), PPE-C20-Phenoxy/C6-Ph-P (—), PPE-C20-Phenoxy/PPE-(C6)₃ (—) and PPE-C20-Methyl/PPE-(C6)₃ (—) ($\lambda_{\text{exc}} = 532 \text{ nm}$; $P_{\text{exc}} = 15\text{mW}$ - all the measurements were performed at the same measurement spot).

3.2.7 Temperature dependent measurements

To date, the development of nanothermometers based on upconversion has not been largely explored and mostly achieved with lanthanide upconversion nanoparticles,

which can show different emission intensity according to the temperature.²²² Herein we explore the temperature-dependent properties of the TTA photon upconversion systems developed in this work. Each of the systems was submitted to four cycles of consecutive measurement between 20 °C and 60 °C. Figure 3.2 – 22 shows the spectra obtained at the first cycle of temperature change for the systems PPE-C20-Phenoxy/PPE-(C6)₃ (Figure 3.2 – 22A), PPE-(C6)₃ (Figure 3.2 – 22B) and PPE-C20-Phenoxy/C6-Ph-P (Figure 3.2 – 22C). Invariably the intensity of the upconversion emission and the phosphorescence emission reduced with the increase of the temperature for all systems and recovered back during the cooling step. The sensitivity of the phosphorescent signal to temperature was previously reported by Chu and coworkers, which observed a reduction of the emission intensity of PtOEP in 78% between 25 °C and 74 °C in the absence of oxygen.²⁴⁵

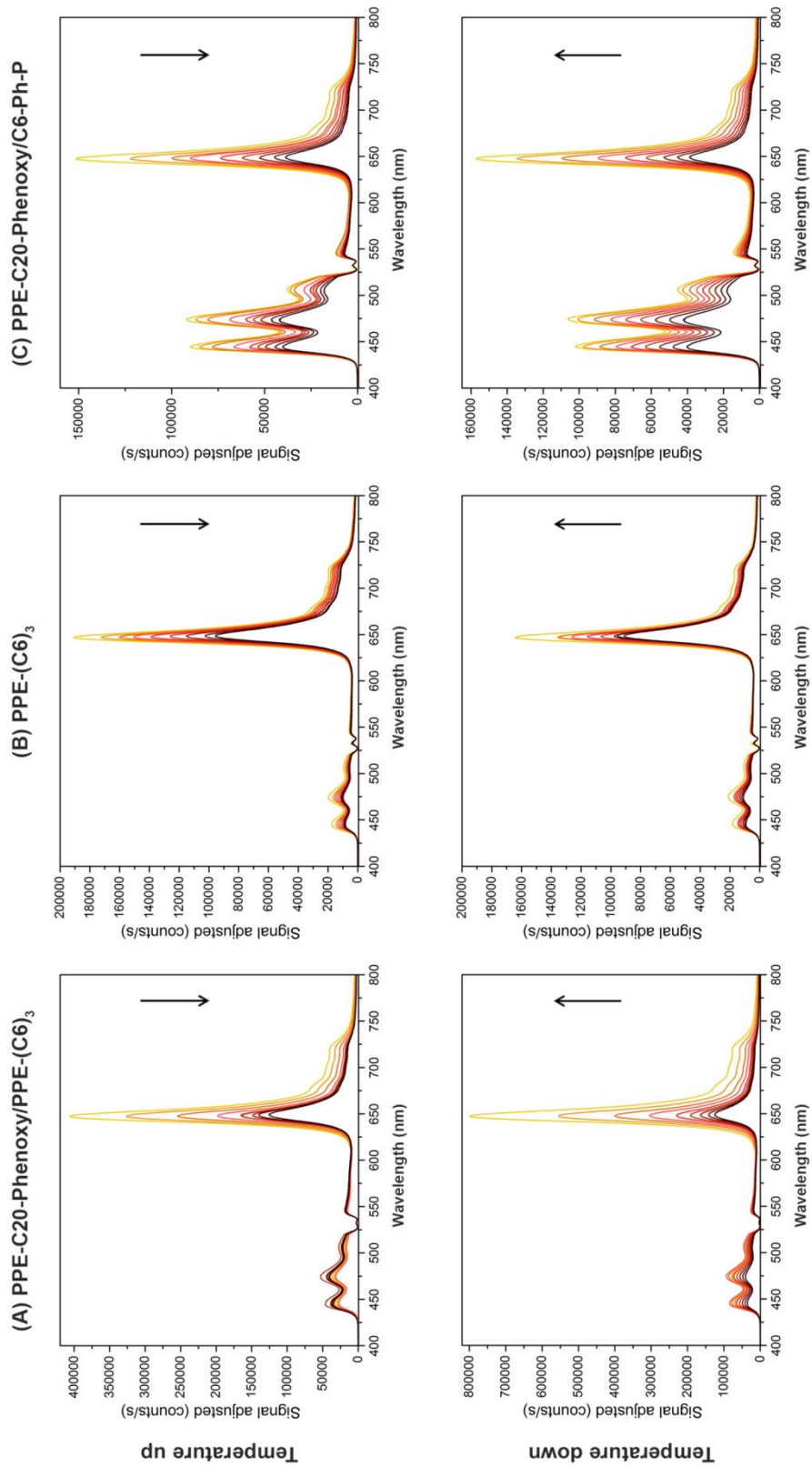


Fig. 3.2 – 22 First cycle luminescence temperature dependent spectra obtained between 20 and 60°C each 5°C: (A) PPE-C20-Phenoxy/PPE-(C6)₃, (B) PPE-(C6)₃ and (C) PPE-C20-Phenoxy/C6-Ph-P. The arrows indicate the direction of temperature variation. All the measurements performed at $P_{exc} = 15$ mW and with the same measurement spot.

However, the ratio between upconversion emission and phosphorescence emission at each of the 3 systems was considerably different at each case. Figure 3.2 – 23 shows the relative upconversion efficiency obtained during four cycles measurements, between 20 °C and 60 °C. The results were approximately reproducible during the cycles, presenting higher efficiency within the cooling step. The organophosphate core PPE-C20-Phenoxy/C6-Ph-P and the hyperbranched nanodroplets PPE-(C6)₃ show lower temperature dependence in comparison to the system hyperbranched core system PPE-C20-Phenoxy/PPE-(C6)₃. Meanwhile, whereas for the systems PPE-(C6)₃ and PPE-C20-Phenoxy/C6-Ph-P an increase between 10 – 15% was observed, the system PPE-C20-Phenoxy/PPE-(C6)₃ shows an increase around 40%. Remarkably, the system PPE-C20-Phenoxy/PPE-(C6)₃ showed two temperature ranges where the efficiency was mostly constant: during the heating step between 45°C and 60°C and during the cooling step between 60 °C and 35 °C. The temperature points where the efficiency starts to change more remarkably are in agreement with the melting and crystallization temperatures for the pure polymer PPE-C20-Phenoxy. The system PPE-C20-Phenoxy/C6-Ph-P showed lower influence from the shell material and seems to have a transition temperature at lower temperatures, supposedly around 30 °C.

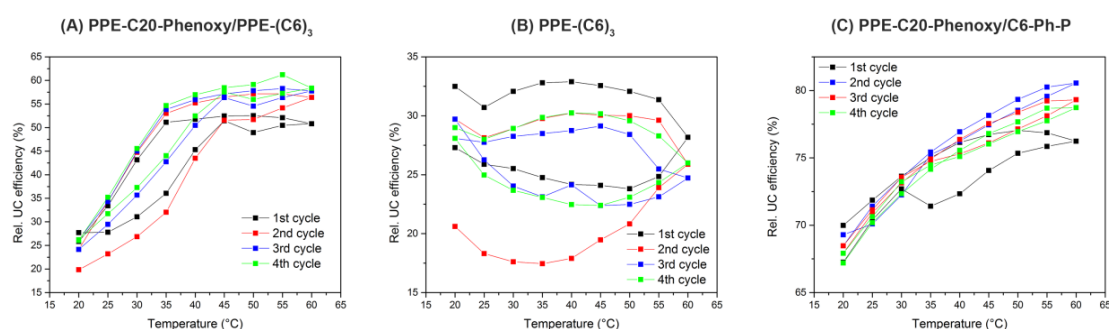


Fig. 3.2 – 23 Four cycles of relative upconversion efficiency changes against temperature: (A) PPE-C20-Phenoxy/PPE-(C6)₃, (B) PPE-(C6)₃ and (C) PPE-C20-Phenoxy/C6-Ph-P (all the measurements performed at $P_{exc} = 15$ mW and with the same measurement spot).

To better understand the differences between the systems, 3 “bulk” systems were measured in the same temperature range: PPE-C20-Phenoxy nanoparticles containing the dye system, the bulk hyperbranched polymer PPE-(C6)₃ and the bulk organophosphate C6-Ph-P. Figure 3.2 – 24 shows the relative upconversion efficiency obtained for each system after a four cycle measurement. The bulk systems PPE-(C6)₃ and C6-Ph-P showed an approximately linear behavior in the temperature range. Nevertheless, while for the organophosphate the increase was close to 5%, the hbUPPE showed an increase higher than

20% of efficiency, which is a consequence of the higher dependency of the viscosity with temperature for macromolecular systems. The PPE-C20-Phenoxy nanoparticle system showed the lowest efficiency between the samples. However, an interesting behavior was noticed between the cycles: a similar dependence with the melt and crystallization temperatures of the polymer matrix could be again observed. Another interesting fact is that the efficiency increased after each cycle, from first to the third cycle, where it kept constant afterwards. A possible reason for such behavior resides in the increase of the mobility of the dyes in the matrix after the melting of the polymer, which could lead to a re-dissolution of the dyes after each cycle, resulting in the random redistribution of the dyes in the frozen state of the particles. Thus, in case the re-dissolution process allows the approximation of the molecules of the dye system, higher efficiency could be reached.

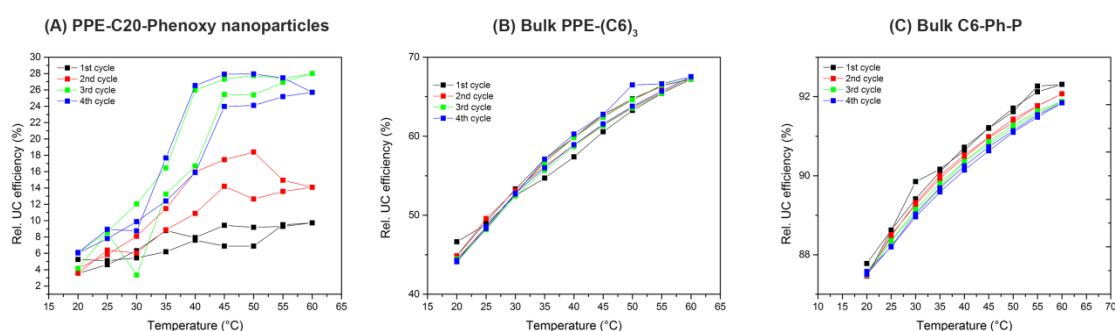


Fig. 3.2 – 24 Four cycles of relative upconversion efficiency changes against temperature: (A) PPE-C20-Phenoxy nanoparticles, (B) bulk PPE-(C6)₃ and (C) bulk C6-Ph-P (all the measurements performed at $P_{exc} = 15$ mW and with the same measurement spot).

The similar behavior between the nanoparticles and the system PPE-C20-Phenoxy/PPE-(C6)₃ also indicates that the gain of mobility is the crucial fact for the increase of efficiency of UC. The melt of the shell material allows the dyes entrapped inside or in the surface of the shell to have enough mobility to participate in the upconversion process. The final efficiency of the PPE-C20-Phenoxy/PPE-(C6)₃ is approximately the sum of the increase corresponding to the bulk hbUPPE and to the nanoparticles. However, these results do not explain the difference with the system PPE-C20-Phenoxy/C6-Ph-P. In order to clarify the problem, calorimetric experiments were performed in the emulsions and the curves for the systems PPE-C20-Phenoxy/C6-Ph-P and PPE-C20-Phenoxy/PPE-(C6)₃ are presented in Figure 3.2 – 25. As can be seen, the melting point of the organophosphate system was reduced to approximately 35 °C meanwhile the melting point in the hbUPPE system is not affected. The apparent plasticization effect of the organophosphate in the shell

could lead to a higher mobility of the dyes and results in a lower dependence of the UC efficiency on temperature.

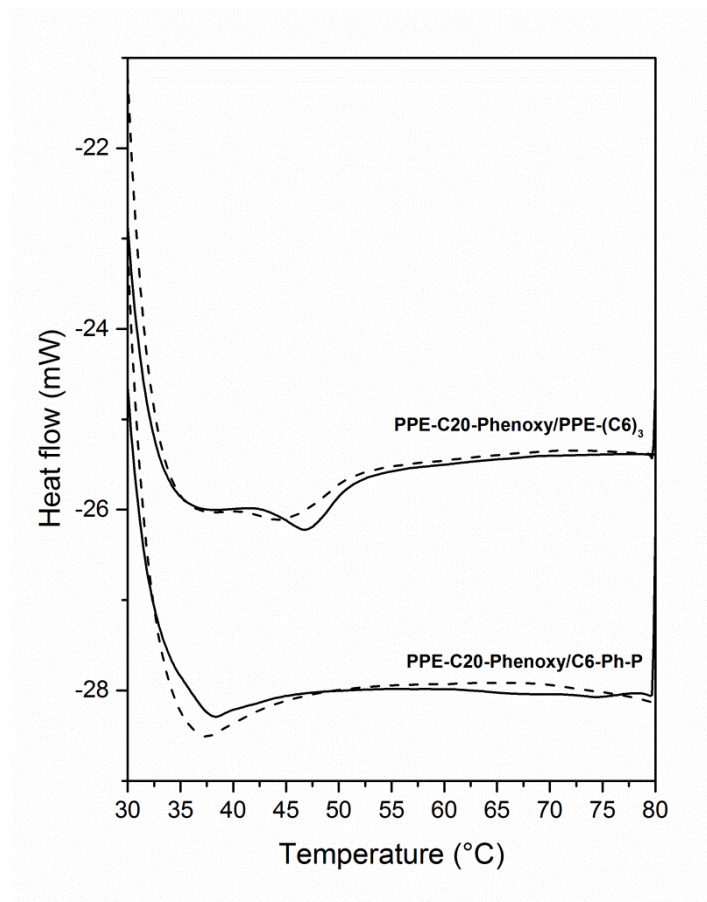


Fig. 3.2 – 25 Differential scanning calorimetry curves for the first (straight) and second (dashed) heating curves of the PPE-C20-Phenoxy/PPE-(C6)₃ and PPE-C20-Phenoxy/C6-Ph-P dispersions.

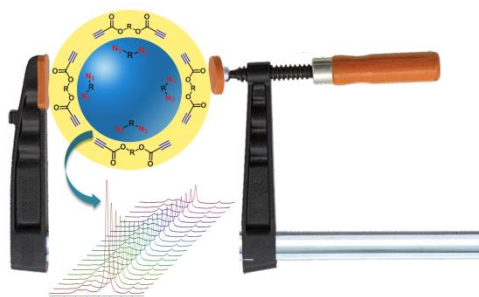
3.2.8 Conclusion

Potentially biodegradable and biocompatible PPE upconversion colloidal systems were successfully developed using the miniemulsion/solvent-evaporation protocol. Systems containing an organophosphate monomer as the core and a linear semi-crystalline saturated polyphosphate as shell showed higher relative UC efficiency in comparison to the same system containing a hyperbranched unsaturated polyphosphate as the core material. The higher viscosity of the hbUPPE in comparison to the organophosphate allowed the synthesis of stable nanodroplets dispersion, which showed similar relative upconversion efficiency in comparison to the encapsulated system, with the advantage of a high level of transparency,

which could be of interest in the development of display systems based on aqueous dispersions. All systems showed upconversion emission when exposed to atmospheric oxygen, with a lifetime of the UC signal up to 12 min. The upconversion signal decay rate was independent of the core material, but presented a dependence on the shell material. Temperature dependent measurements showed an approximate linear dependence of the relative upconversion efficiency with the temperature. The exception was the encapsulated hbUPPE system, which demonstrated that higher dependency of the signal with temperature and the thermal transitions of the shell component material, which is related to partition of dyes between the core and the shell during the phase separation during the solvent-evaporation process. The results here presented form a base for the development of *in vivo* oxygen and temperature detection systems. The tailoring possibilities of the polyphosphoester materials create opportunities for the future development of functional possible shells, for the development of upconversion based on organophosphate monomers and hyperbranched polyphosphate cores.

3.3 Kinetics of copper-free azide alkyne cycloaddition polymerization (Cu-free AACP) in miniemulsion⁴

The interface as a “screw clamp”: this section covers the study of the influence of the a minimized interface in the copper-free 1,3 – dipolar azide alkyne cycloaddition. Miniemulsion droplets surface were used as a template for the reaction and the reaction was followed by NMR spectroscopic methods. The influence of the miniemulsion in the temperature dependence was compared to a solution polymerization system, as well as the structural features. The reaction at the oil-water interface proved to exhibit higher rate constants, increased molecular weights and higher regioselectivity compared to the reaction in solution. Finally, the results obtained in this approach were applied in the reaction of monofunctional reactants, as approach for the preparation of amphiphilic molecules as, for example, surfactants. This chapter reproduces content previously published in a paper.⁴



(Alexandrino *et al.*; *Chem. Commun.*, 2014,**50**, 10495-10498, <http://pubs.rsc.org/en/Content/ArticleLanding/2014/CC/C4CC04119D#!divAbstract> -Reproduced by permission of The Royal Society of Chemistry.)

3.3.1 Motivation

“Click chemistry” refers to a series of chemical reactions that must follow several criteria: *modular, wide in scope, inoffensive and easily removable by-products, stereospecific, readily available starting materials and reagents, no solvent or benign solvent and simple to purify.*²⁴⁶

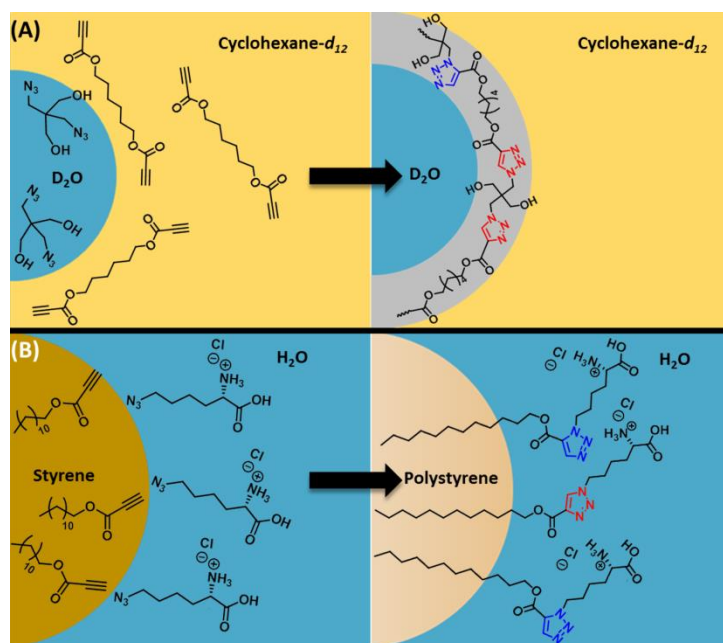
The 1,3-dipolar Huisgen cycloaddition between alkynes and azides (AAC) is certainly the most successful and widespread type of these reactions resulting in the formation of 1,2,3-triazoles.²⁴⁷ The AAC is currently applied and studied in many fields as peptidomimetic strategies,²⁴⁸ medicinal chemistry,²⁴⁹ drug delivery systems,²⁵⁰ and polymer chemistry.²⁵¹⁻²⁵³ The reaction developed by Huisgen was originally a thermally activated relatively slow reaction, which generated a mixture of two regioisomers: 1,4- and 1,5- disubstituted 1,2,3- triazoles.²⁵⁴ Later, Sharpless and coworkers²⁵⁵ and Medal and coworkers²⁵⁶ obtained regioselective products (1,4-disubstituted 1,2,3-triazoles) with high yields by the use of copper catalysts at mild conditions. Ruthenium catalysts have also been used for preparation of 1,5-disubstituted 1,2,3-triazoles²⁵⁷ and recently iridium has been used for the preparation of regioselective products from electron rich internal alkynes.²⁴⁷ However, the removal of metal catalysts can be challenging especially for biological applications.^{258, 259} Some approaches to metal-free AAC have been successfully developed, as the use of strained cyclooctynes,^{259, 260} activated alkynes^{259, 261} and electron deficient alkynes.^{259, 262, 263} From the different alkyne derivatives, the electron deficient propiolates are of special interest due to the straightforward synthesis by esterification of the alcohol of choice with propiolic acid.²⁶²

The absence of a catalyst and the bioorthogonal functional groups make this reaction highly interesting for the preparation of materials for biomedical applications, e.g. the formation of bioconjugates, nanocarriers, or biodegradable surfactants. However, still elevated temperatures, which may e.g. denature biomolecules, are necessary to obtain reasonable reaction rates. Another interesting aspect of this reaction is the feasible combination of two immiscible molecules via interfacial click reaction, either generating a polymeric shell or an amphiphilic material, e.g. surfactant, via orthogonal chemistry.

This work explores the possibilities of the copper-free click reaction between propiolates and azides at the droplet interface of a stable miniemulsion. First, we investigate the effects on reaction kinetics of an $A_2 + B_2$ polyaddition with respect to conversion and molecular weights of the resulting polyesters which are compared to solution protocols at

different temperatures. Then the droplet interface is also used to generate a surfactant via *in situ* click reaction followed by a reaction in the stabilized miniemulsion, i.e. the radical polymerization of styrene. In the miniemulsion, droplets with a very high total surface area in comparison to conventional emulsions or a homogeneous reaction system are generated.²⁶⁴ These monodisperse droplets can be used as nanocontainers for reactions inside or at the interface of the droplets.²⁶⁴

The kinetics of the reaction and the structural features of both systems were characterized in detail by various NMR spectroscopic techniques and gel permeation chromatography (GPC). Previously, our group has successfully developed an facile method to produce nanocapsules by copper-free click polymerization for encapsulation of functional molecules using a water soluble azide (2,2-bis(azidomethyl)propan-1,3-diol, BAP) and an organic soluble alkyne (hexane-1,6-diyil dipropiolate, HDDP).⁶⁸ From these results, the detailed investigation of the copper-free click reaction at the interface of a miniemulsion on the polymerization of HDDP and BAP at the interface and the use of this methodology to synthesize amphiphilic molecules, like surfactants, attracted our interest (Scheme 3.3 – 1).



Scheme 3.3 – 1 Polyadditions performed at the interface: (A) system used for evaluating the kinetics of the polymerization between HDDP and BAP in an inverse miniemulsion system (cyclohexane- d_{12} /D $_2$ O); (B) *in-situ* surfactant formation during the radical polymerization of polystyrene nanoparticles using the click reaction to stabilize a direct miniemulsion (water/styrene). The different possible regioisomers 1,4- and 1,5- disubstituted 1,2,3-triazoles are highlighted here in red and blue, respectively

(Alexandrino *et al.*; *Chem. Commun.*, 2014,**50**, 10495-10498, <http://pubs.rsc.org/en/Content/ArticleLanding/2014/CC/C4CC04119D#ldivAbstract> -

Reproduced by permission of The Royal Society of Chemistry).

3.3.2 Experimental part

3.3.2.1 Materials

For the study of the polymerization reactions, hexane-1,6-diyl dipropiolate (HDDP) and 2,2-bis (azidomethyl)propan-1,3-diol (BAP) were synthesized according to literature procedures.^{255, 265} 1,6-hexanediol, propiolic acid, DMF, benzene, DMSO-*d*₆, D₂O, chloroform-*d* and sulfuric acid were obtained from Sigma-Aldrich. 2,2-bis(bromomethyl)-1,3-propanodiol was obtained from Wako Chemicals, and sodium azide from Servay. All chemicals were used without further purification.

For the *in situ* surfactant system, the ester of dodecanol and propiolic acid (Sigma-aldrich), DoDP, was prepared using a similar approach for the synthesis of HDDP. *N*- ϵ -azido-L-lysine, used in the direct system, was obtained from Iris Biotech GmbH and used without further purification. The initiator VA044 was obtained from Wako Chemicals. Styrene was obtained from Sigma-Aldrich and previously purified by filtration through basic alumina. The surfactant P(E-B-*b*-EO), poly((ethylene-*co*-butadiene)-*b*-(ethylene oxide))²⁶⁶ was used for the preparation of the inverse miniemulsion systems. Cyclohexane-*d*₁₂ was obtained from Deutero GmbH. Decamethylcyclopentasiloxane was obtained from Merck.

3.3.2.2 Miniemulsion polyaddition of HDDP and BAP

For the study of the kinetics of the azide-alkyne cycloaddition in miniemulsion, 0,9 mg of NaCl and 6.2 mg (approximately 2.8×10^{-5} mol) of BAP were dissolved in 100 mg of D₂O. 1000 mg of a stock solution of cyclohexane-*d*₁₂/P(E-B-*b*-EO) (0.6 wt%) was added and the mixture was stirred at 1500 rpm for 1 h. Meanwhile, a second solution composed of 7.4 mg (approximately 2.8×10^{-5} mol) of HDDP was dissolved in 200 mg cyclohexane-*d*₁₂/P(E-B-*b*-EO) (0.6 wt%). For complete dissolution of HDDP, a gentle heat was applied to the solution for a few seconds. After 1 h, the pre-emulsified mixture was submitted to a pulsed ultrasonication process in an ice bath for 60 s (2.5 s sonication, 5 s

paused) at 70% amplitude using a 1/8" tip Branson 450W sonifier. 500 μL of the obtained miniemulsion was immediately transferred into a conventional NMR tube. A NMR spectrometer (Bruker Avance III 700 MHz) was previously equilibrated at the temperature of the experiment (298K or 323K). 100 μL of the second solution containing the HDDP monomer and one droplet of decamethylcyclpentasiloxane, used as reference for the spectrum, were added with a syringe to the NMR tube, homogenized and the tube was immediately introduced in the spectrometer. For each experiment, 100 ^1H spectra were collected consecutively, using 64 transients with an 11 ms long 90° pulse. A 12600 Hz spectral width together with a recycling delay time of 5 s, resulting in a total time of 8 min for the collection of each spectrum and a total time of 800 min, was used for each experiment.

3.3.2.3 Solution polymerization of HDDP and BAP

6,2 mg of BAP was dissolved in 600 mg of $\text{DMSO-}d_6$ and, separately, a second solution of 7,4 mg of HDDP in 600 mg of $\text{DMSO-}d_6$ was also prepared. 300 μL of each solution was added to a NMR tube containing one droplet of decamethylcyclpentasiloxane. The tube was immediately introduced in the NMR spectrometer with the temperature of the experiment previously equilibrated (298K or 323K). For each experiment, the same procedure applied for the miniemulsion experiments was followed, resulting in a total time of 800 min.

3.3.2.4 *In-situ* surfactant formation in direct miniemulsion

Initially, the disperse phase containing 750 mg of styrene, 17.4 mg (7.3×10^{-5} mol) of dodecyl propiolate DoDP and 10 mg of hexadecane was prepared. The continuous phase composed of 3 g of Milli-Q water and 15.2 mg (7.3×10^{-5} mol) of *N*- ϵ -azido-L-lysine hydrochloride was added and the mixture was left to stirring at 1000 rpm in an oil bath at 70 $^\circ\text{C}$ over a period of 1 hour. Then, the mixture was submitted to a pulsed ultrasonication process while cooling in an ice bath over 120 s (30 s sonication and 10 s paused) at 70% amplitude using a 1/4" tip Branson 450W sonifier. The first "emulsion" system was returned to the oil bath and left to stir at 300 rpm in an oil bath at 70 $^\circ\text{C}$ for an additional 1 h. Then, the same ultrasonication program was applied. To the miniemulsion, 500 mg of Milli-Q

water containing 37.5 mg (1.2×10^{-4} mol) of the initiator VA044 was added and the system was left to stir at 300 rpm overnight in an oil bath at 300 rpm at 70°C. The average particle size and particle size distribution was obtained by dynamic light scattering (DLS) in a submicron particle sizer NICOMP® 380 equipped with a detector to measure the scattered light at 90°. For comparison a control experiment without the presence of DoDP and *N*- ϵ -azido-L-lysine was performed under the same conditions, however no stable emulsion was obtained.

3.3.2.5 2D ^1H - ^{15}N HMBC analysis

^1H -NMR (850 MHz) and ^{15}N -NMR (86 MHz) were performed on Bruker Avance III 850 NMR spectrometers with a 5 mm TXI probe equipped with a z-gradient. The spectra were obtained with $\pi/2$ -pulse lengths of 11 μs (^1H) and 32 μs (^{15}N) and a sweep width of 10330 Hz (20,6 ppm) for ^1H and 43000 Hz (500 ppm) for ^{15}N , all nuclei with a relaxation delay of 1.3s. Proton and carbon spectra were referenced using the remaining solvent signals (DMSO- $\text{d}_5\text{H}_1=2.49$ ppm) as an internal standard. The nitrogen setup was done with $\text{CH}_3^{15}\text{NO}_2$ with a value of 0 ppm.

Long-range correlation between ^1H - ^{15}N was recorded with 2D HMBC (heteronuclear multiple bond correlation) via heteronuclear zero and double quantum coherence optimized for long range couplings with a low-pass J-filter to suppress one-bond correlations. No decoupling during acquisition using gradient pulses for selection was used. The average indirect coupling constants used was $^nJ_{\text{NH}}=4\text{Hz}$ (^1H - ^{15}N), to optimize the observable intensities of cross peaks from multiple bond ^1H -X correlation.

3.3.2.6 2D DOSY ^1H NMR analysis

Diffusion-ordered NMR spectroscopy (DOSY-NMR)^{267, 268} experiments were collected with a 5 mm TXI $^1\text{H}/\text{X}$ z-gradient probe (850 MHz, Avance III) with a gradient strength of 5,350 [G/mm]. The gradient strength of the probe was calibrated by analysis of a sample of $^2\text{H}_2\text{O}/^1\text{H}_2\text{O}$ at a defined temperature and compared with the theoretical diffusion coefficient of $^2\text{H}_2\text{O}/^1\text{H}_2\text{O}$ (values taken from Bruker diffusion manual)²⁶⁹ at 298,3K.

The diffusion coefficients were derived from the mono-exponential function:²⁷⁰

$$\ln\left(\frac{I(G)}{I(0)}\right) = -\gamma^2 \delta^2 G^2 \left(\Delta - \frac{\delta}{3}\right) D,$$

where $I(G)$ and $I(0)$ are the intensities of the signals with and without gradient, γ the gyromagnetic ratio of the nucleus (^1H in these measurements), G is the gradient strength, δ the duration of the pulse field gradient (PFG), D the diffusion coefficient in m^2/s and Δ the “diffusion time” between the beginning of the two gradient pulses. The relaxation delay between scans was 3 s. In this work, the diffusion times (d_{20}) were optimized for the QXI probe to 80 ms, while the gradient pulse length was kept at 1.6 ms. The optimization was realized by comparing the remaining intensity of the signals at 2% and 95% gradient strength. In the measurement 32 strengths of gradients (from 2% to 95%) were used with sixteen scans.

3.3.2.7 Gel permeation chromatography (GPC) analysis

The apparent molecular weight was determined by gel permeation chromatography (Agilent Technologies 1260 Infinity). The samples were immediately lyophilized after 13 h of reaction and directly analyzed by GPC. Solutions of the final materials with concentrations of 1 mg mL^{-1} were prepared in DMSO, injected at a flow of 1 mL min^{-1} with DMF as eluent phase. The signal was detected with a UV-Vis detector S-3702 (Soma) and the molecular weight was obtained with the software PSS-WinGPC UniChrom (PSS) against PS standards.

3.3.2.7 Statistics analysis

The curves of the kinetics measurements were fitted using the software Origin 9.0. For the kinetics at 323K a 2nd order exponential curve was used, while a 1st order was applied for the data obtained at 298K.

3.3.3 Kinetics evaluation: miniemulsion vs solution

Aiming the evaluation of the polymerization in the kinetics involving the azide-alkyne cycloaddition, ^1H NMR spectroscopy was used for the *in situ* measurement of the polymerization kinetics²⁷¹ over a period of 800 min for the various reactions. Both solution and inverse miniemulsion polymerizations were carried out in either $\text{DMSO-}d_6$, or

cyclohexane- d_{12} as continuous phase and D_2O as dispersed phase respectively. Temperatures of 298K and 323K with a delay time of approximately 8 min between each spectral acquisition were used. Figure 3.3 – 1A-D presents an overlay of the four different polymerizations 1H NMR spectra. The evolution of the integral of the alkyne proton was followed over time in comparison to an internal standard (0.07 ppm from decamethylcyclopentasiloxane). The results of the consumption of HDDP over time are plotted in Figure 3.3 – 2.

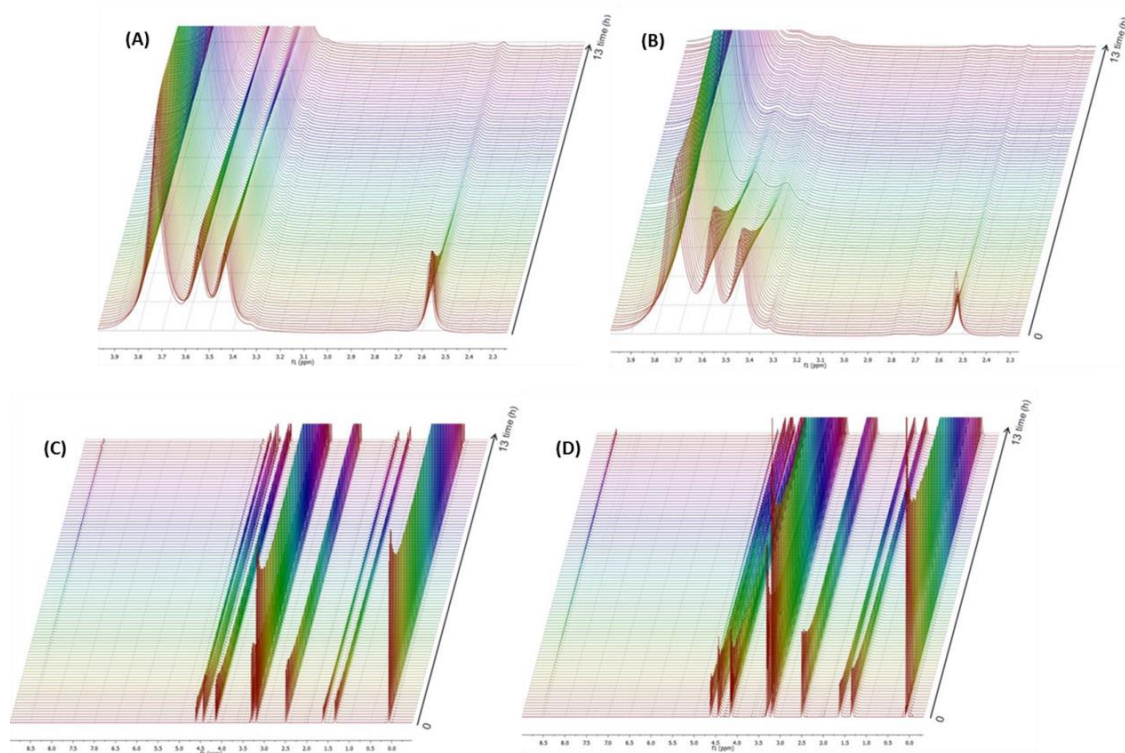


Fig. 3.3 – 1 Overlay of the 1H NMR spectra for the polyaddition of BAP and HDDP conducted in (a) inverse miniemulsion (cyclohexane- d_{12}/D_2O) at 298K, (b) inverse miniemulsion (cyclohexane- d_{12}/D_2O) at 323K, (c) solution ($DMSO-d_6$) at 298K and (d) solution ($DMSO-d_6$) at 323K (Alexandrino *et al.*; **Chem. Commun.**, 2014,**50**, 10495-10498, <http://pubs.rsc.org/en/Content/ArticleLanding/2014/CC/C4CC04119D#!divAbstract> - Reproduced by permission of The Royal Society of Chemistry).

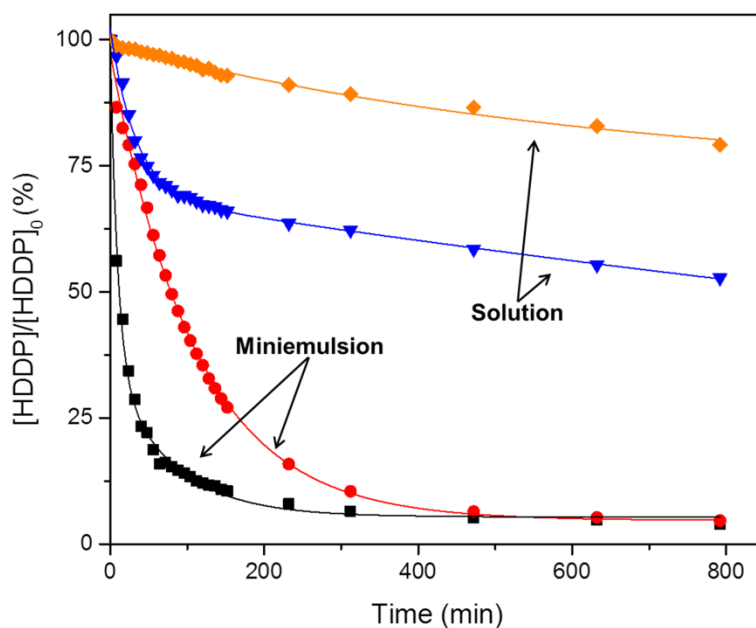


Fig. 3.3 – 2 Conversion of HDDP for the polyaddition with BAP in miniemulsion (water/cyclohexane $c = 1.94 \times 10^{-2}$ mol/L) at 323 K (■) and 298 K (●) and in solution (DMSO- d_6 , $c = 2.76 \times 10^{-2}$ mol/L) at 323 K (▼) and 298 K (◆), as determined by ^1H NMR (Alexandrino *et al.*; *Chem. Commun.*, 2014, **50**, 10495-10498, <http://pubs.rsc.org/en/Content/ArticleLanding/2014/CC/C4CC04119D#!divAbstract> - Reproduced by permission of The Royal Society of Chemistry).

As can be seen from Figure 3.3 – 2, the miniemulsion system resulted in a faster consumption of the HDDP monomer in comparison to a solution polymerization. Considering the system as a second order reaction, the following method can be applied to obtain the values of k_2 :²⁷²

$$\frac{1}{1-x} = k_2 t, \text{ with } x = 1 - \frac{[\text{HDDP}]}{[\text{HDDP}]_0} \quad (1)$$

Applying this equation across the different reaction conditions for the first hour (Figure 3.3 – 3), at 298K, the miniemulsion polymerization system showed a **25-fold** increase in the value of k_2 compared to the solution polymerization. At 323K a **12-fold** increase was measured. The values can be observed at Table 3.3 – 1. The increase in the rate of reaction can be explained in terms of the so called “pseudo-phase model”, which relates the

partitioning of monomers at the interface with the characteristics of the reagents with both solvents.^{273, 274}

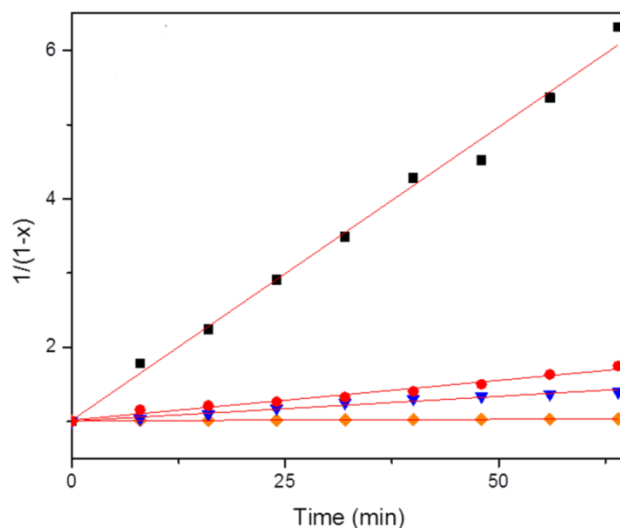


Fig. 3.3 – 3 Second-order reaction kinetics treatment for the first hour of the polyaddition of BAP and HDDP in miniemulsion (water/cyclohexane $c = 1.94 \times 10^{-2}$ mol/L) at 323 K (■) and 298 K (●) and in solution (DMSO- d_6 , $c = 2.76 \times 10^{-2}$ mol/L) at 323 K (▼) and 298 K (◆) (Alexandrino *et al.*; *Chem. Commun.*, 2014,50, 10495-10498, <http://pubs.rsc.org/en/Content/ArticleLanding/2014/CC/C4CC04119D#!divAbstract> - Reproduced by permission of The Royal Society of Chemistry).

Table 3.3 – 1 k_2 values for the second-order reaction kinetics treatment for the first hour of the polyaddition of HDDP and BAP in each of the four systems (Alexandrino *et al.*; *Chem. Commun.*, 2014,50, 10495-10498, <http://pubs.rsc.org/en/Content/ArticleLanding/2014/CC/C4CC04119D#!divAbstract> - Reproduced by permission of The Royal Society of Chemistry).

Sample	k_2 (min ⁻¹)
Miniemulsion 298K	$1.1 \times 10^{-2} \pm 6.0 \times 10^{-4}$
Miniemulsion 323K	$8 \times 10^{-2} \pm 2.6 \times 10^{-3}$
Solution 298K	$4.4 \times 10^{-4} \pm 4.9 \times 10^{-4}$
Solution 323K	$6.7 \times 10^{-3} \pm 4.2 \times 10^{-4}$

Bravo-Díaz and Romsted have modelled the reactivity of “macro”emulsions and “micro”emulsions in terms of the pseudo-phase model.²⁷⁴ Miniemulsions are kinetically stable systems, similar to macroemulsions, however with the additional kinetic stabilization against diffusion and collisions. The system studied herein uses a non-ionic surfactant, which avoids the interference of charges in the kinetics of the reaction, as observed by Engberts and coworkers for the kinetics of cycloadditions in microemulsions.²⁷⁵ Thus, this system is a better comparison to the solution polymerization. Two assumptions have been made for the application of the pseudo-phase model:

- (a) the distribution of the components is a thermodynamic equilibrium, which can be represented by the partition coefficient;
- (b) the interfacial region is in a dynamic equilibrium state.²⁷⁴

The partition coefficient depends on the solubility of the components in each of the solvents; therefore the level of acceleration observed will be directly linked to the chemical properties of the components of the system.

3.3.4 Effect of the temperature

As an additional factor, two reaction temperatures were examined: for the miniemulsion polymerization, an increase on the k_2 -value from 298K to 323K of approximately **7-fold** and for the solution polymerization an increase of approximately **15-fold** was observed. This difference can be rationalized in terms of mobility. The increase of the temperature directly affects the Brownian mobility of the molecules in the system. In a miniemulsion system one monomer is confined inside the droplet and has limited space and therefore limited mobility at the interface, while in the homogeneous reaction both monomers have a similar mobility and are thus significantly more influenced by temperature variations.

3.3.5 Evaluation of the method in the polymer structure features

The evolution of the molecular weight for both polymerization methods was followed by GPC (Table 3.3 – 2 and Figure 3.3 – 4). The data highlights that higher molecular

weights are achieved in the miniemulsion systems at both temperatures compared to the solution polymerizations. This may be explained by considering two factors: (1) in solution the overall concentration is lower than at the interface of nanodroplets resulting in a decreased molecular weight of the polymer (up to $M_w = 4500 \text{ g mol}^{-1}$ (vs. PS)); and (2) in the heterophase system, the polymer precipitates, and is confined to, the interface resulting in higher conversions and molecular weights (up to $M_w = 10\,000 \text{ g mol}^{-1}$ in miniemulsion at 323K).

Table 3.3 – 2 Relative molecular weights after 13 h of polymerization for the miniemulsion and solution polymerization, at 298K and 323K (Alexandrino *et al.*; *Chem. Commun.*, 2014, **50**, 10495-10498, <http://pubs.rsc.org/en/Content/ArticleLanding/2014/CC/C4CC04119D#!divAbstract> -

Reproduced by permission of The Royal Society of Chemistry).

Method	T (K)	M_w^a (g mol^{-1})	\mathcal{D}^a
Miniemulsion	298	6,000	1.9
Miniemulsion	323	9,800	2.3
Solution	298	4,600	1.8
Solution	323	4,100	1.6

^a Weight average of the molecular weight (g mol^{-1}) and molecular weight dispersity determined via GPC in DMF vs PS standards.

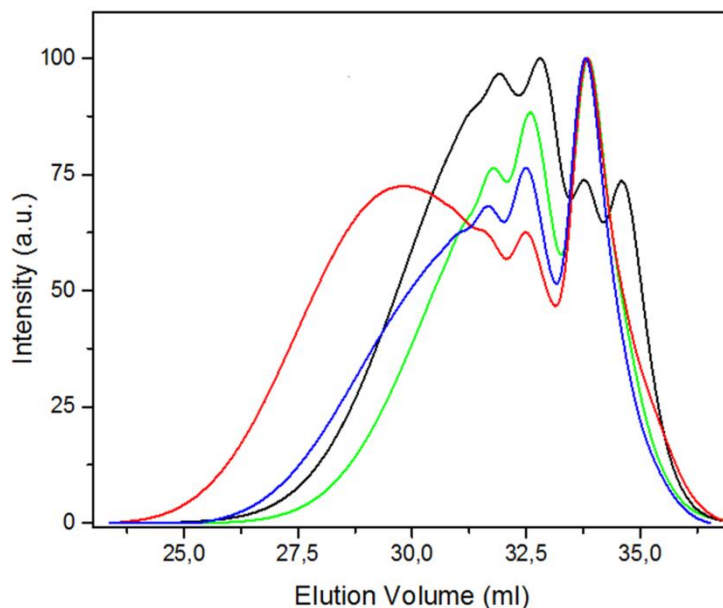


Fig. 3.3 – 4 Comparison of the GPC elugrams (UV detection, DMF) for the polyaddition of BAP and HDDP in miniemulsion (water/cyclohexane $c = 1.94 \times 10^{-2}$ mol/L) at 323K (—) and 298K (—) and in solution (DMSO- d_6 , $c = 2.76 \times 10^{-2}$ mol/L) at 323K (—) and 298K (—) (Alexandrino *et al.*; *Chem. Commun.*, 2014, **50**, 10495-10498, <http://pubs.rsc.org/en/Content/ArticleLanding/2014/CC/C4CC04119D#!divAbstract> - Reproduced by permission of The Royal Society of Chemistry).

The final morphology obtained from the miniemulsion systems is, as expected, the formation of nanocapsules with a mean diameter of 190 ± 60 nm. This could be confirmed by SEM, TEM and light scattering measurements (Figure 3.3 – 5A-C and Figure 3.3 – 6) and agrees well with what has been previously reported by our group.⁶⁸

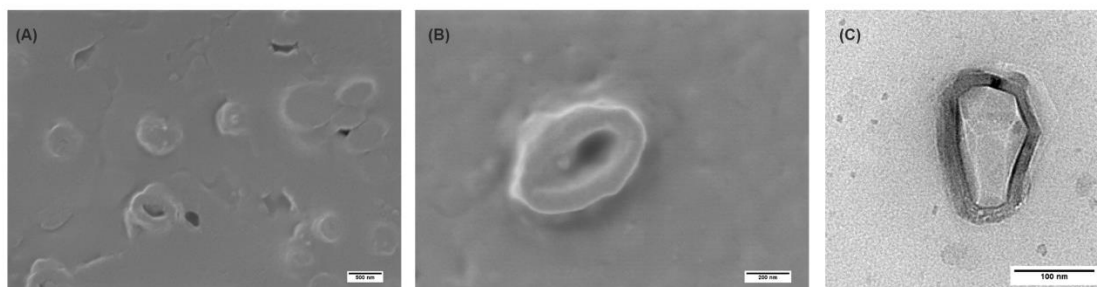


Fig. 3.3 – 5 SEM (A and B) and TEM (C) micrographs obtained for the after the click polymerization at 323K in miniemulsion (Alexandrino *et al.*; *Chem. Commun.*, 2014, **50**, 10495-10498,

<http://pubs.rsc.org/en/Content/ArticleLanding/2014/CC/C4CC04119D#!divAbstract>

Reproduced by permission of The Royal Society of Chemistry).

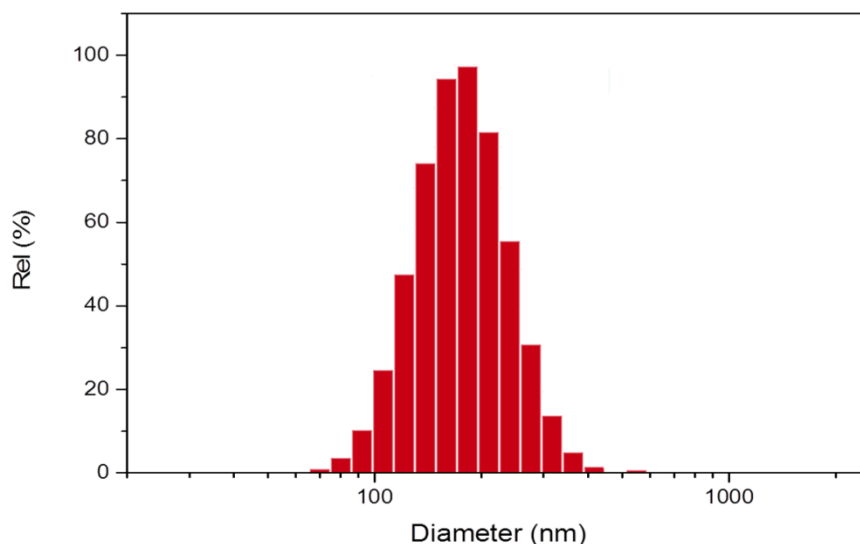


Fig. 3.3 – 6 DLS analysis in cyclohexane of the polymeric nanocapsules obtained in inverse miniemulsion polymerization at 323K (Alexandrino *et al.*; **Chem. Commun.**, 2014, **50**, 10495-10498, <http://pubs.rsc.org/en/Content/ArticleLanding/2014/CC/C4CC04119D#!divAbstract> - Reproduced by permission of The Royal Society of Chemistry).

An interesting aspect of the interfacial reaction is whether there is an influence on the microstructure of the polymer. Tang and coworkers²⁶² have used metal-free alkyne-azide polymerization to produce a series of polymers with diazides and dipropiolates in solution and found a high tendency for the formation of 1,4-triazoles (over 90%). Both possible regioisomers (1,4- and 1,5-triazole) can be differentiated by two distinct singlets between 7 and 10 ppm in the ¹H NMR spectrum.²⁷⁶ Both products of the polymerization in solution and in miniemulsion were analysed via ¹H NMR spectroscopy (DMSO-*d*₆) and several signals can be detected in the triazole region (Figure 3.3 – 7A). Interestingly, an inversion in the relative intensities of these peaks is observed depending on the polymerization methodology. Previously, ¹H-¹⁵N HMBC (hetero nuclear multiple bond correlation) NMR spectroscopy was used as a powerful tool to distinguish different triazole isomers.²⁷⁶ The ¹H - ¹⁵N HMBC analysis of the polymer obtained by miniemulsion polymerization is shown in Figure 3.3 – 7B. As can be clearly seen from the H-N correlation, the signals between 8.6 and 8.7 ppm (in the H NMR) are related to the same regioisomer, while the two signals around 8.24 ppm correlate to each other. The values are in agreement with the values observed by

Alfonso and coworkers²⁷⁶ and indicated that the three signals at lower field of the spectrum stem from the 1,4-disubstituted 1,2,3-triazoles, while the two signal at higher field correspond to the 1,5-disubstituted 1,2,3-triazole derivatives. Miniemulsion thus preferentially produces the 1,4-triazole regioselective polymer (approximately 91%). Solution polymerization also predominates with the 1,4-isomer, however it appears to be of a different 1,4- species.

To elucidate the nature of this second 1,4-derivative (8.65 ppm and 8.61 ppm), diffusion-ordered NMR spectroscopy (DOSY) ¹H-NMR analysis was performed. Figure 3.3 – 8 shows the spectrum for the product of the miniemulsion polymerization at 323 K. The diffusion coefficient for the signal at ca. 8.61 ppm is higher (approximately $9.0 \times 10^{-11} \text{ m}^2 \text{ s}^{-1}$) than the one observed for the other peaks (approximately $5.5 \times 10^{-11} \text{ m}^2 \text{ s}^{-1}$). The fact that the peaks have a well-defined shape, suggests that it originates from a smaller, faster diffusing species of defined architecture and one that is not related to the molecular weight distribution of the polymer. A plausible explanation is the formation of cyclic oligomers. Considering the surface curvature of the droplet and the lower mobility of the reactants after precipitation at the interface, a lower probability for the formation of cyclic structures for the miniemulsion polymerization in comparison to the solution polymerization is expected. This assumption is in agreement with the change in the intensity between both methods observed in the 1D-¹H NMR (Figure 3.3 – 7A).

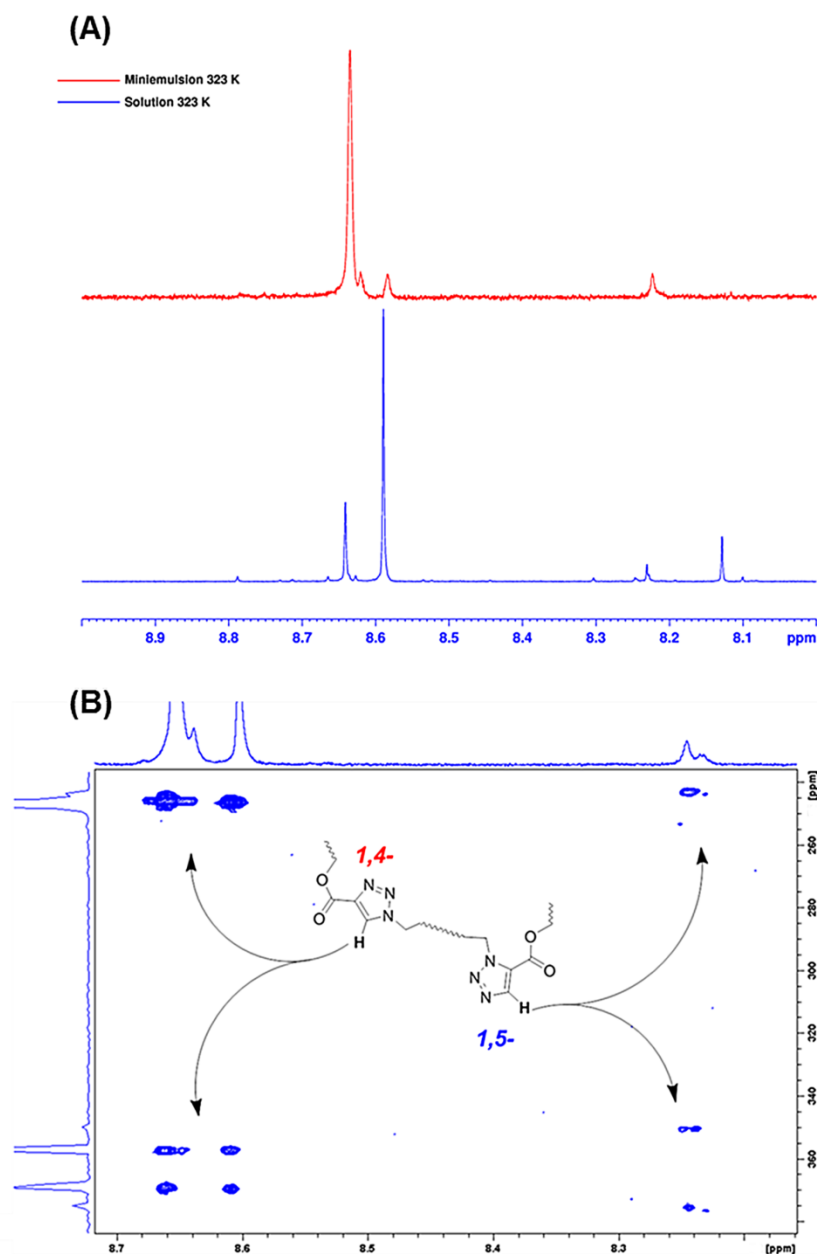


Fig. 3.3 – 7 (A) ^1H -NMR spectra in $\text{DMSO-}d_6$ (700 MHz, Avance III) from the triazole proton region for the product of polymerization in miniemulsion (red) and in solution (blue) at 323K; (B) 2D ^1H - ^{15}N HMBC (850 MHz, Avance III) analysis of the polymer obtained by miniemulsion polymerization at 323K in $\text{DMSO-}d_6$. The upper spectrum corresponds to the ^1H spectrum, the spectrum on the left is the internal calculation of the cross peaks in the ^{15}N -frequency range (Alexandrino *et al.*; *Chem. Commun.*, 2014,**50**, 10495-10498, <http://pubs.rsc.org/en/Content/ArticleLanding/2014/CC/C4CC04119D#!divAbstract> - Reproduced by permission of The Royal Society of Chemistry).

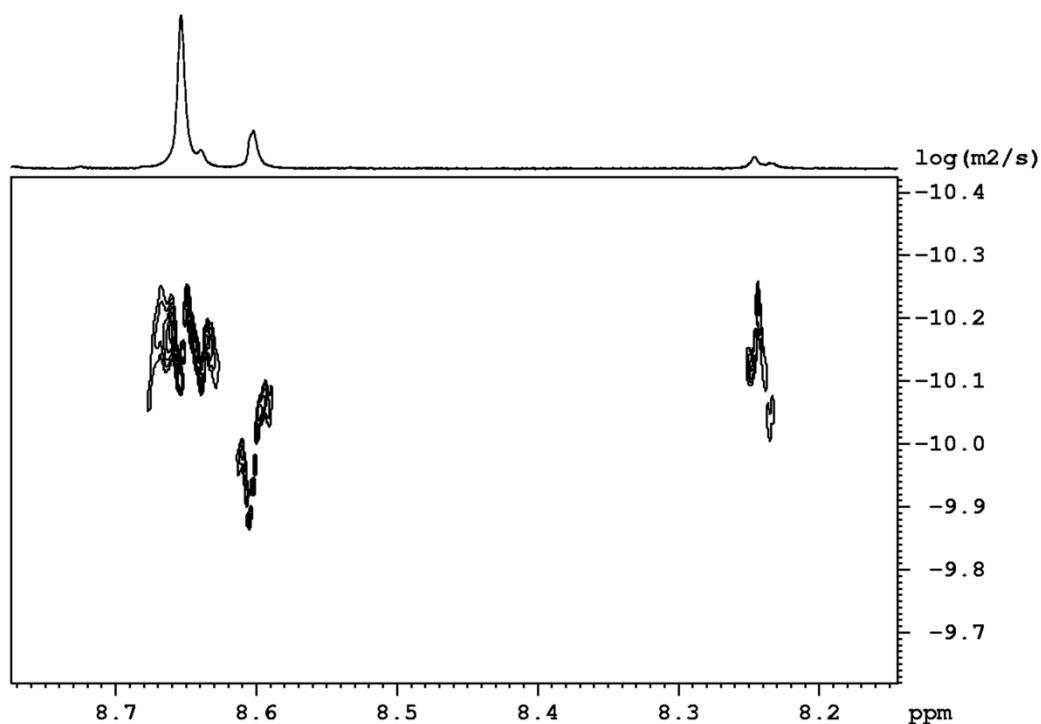


Fig. 3.3 – 8 DOSY ¹H-NMR (850 MHz, Avance III) measurement for the product of miniemulsion polymerization at 323K in DMSO-*d*₆ (Alexandrino *et al.*; *Chem. Commun.*, 2014,50, 10495-10498, <http://pubs.rsc.org/en/Content/ArticleLanding/2014/CC/C4CC04119D#!divAbstract> - Reproduced by permission of The Royal Society of Chemistry).

3.3.6 *In situ* surfactant formation by Cu-free azide-alkyne cycloaddition

The miniemulsion polyaddition is a clear example of the interfacial “screw clamp” and has the potential to accelerate certain reactions, in mild conditions to give an easy pathway for the formation of amphiphilic molecules as protein conjugates or surfactants. To further exemplify this effect and the use of this approach in the preparation of amphiphilic molecules, a monofunctional system was used to generate a surfactant *in situ*, using mild conditions with the capability to stabilize a direct miniemulsion polymerization system. This is the first example for a chemical reaction that can be applied *in situ* to generate a surfactant that stabilizes a miniemulsion of monomer droplets for instantaneous polymerization. Previously, aliphatic carboxylic acids were deprotonated in heterophase to generate ionic surfactants^{277, 278} while metallosurfactants and transition metal acetyl

acetates have also been produced *in situ*.^{279, 280} The generation of a surfactant *in situ* can have advantages such as faster stabilization of the (mini)emulsion and less secondary nucleation processes.²⁸¹ Here, we used the interfacial “screw clamp” for mediating a click reaction in a direct miniemulsion between dodecyl propiolate dispersed in styrene as the organic phase and *N*- ϵ -azido-L-lysine hydrochloride dissolved in the aqueous phase. The emulsion was produced by stirring and the subsequent application of ultrasound. The nanodroplets were formed with a high surface area and stabilized at the same time by the *in situ* generated, i.e. “clicked”, surfactant (compare Scheme 3.3 – 1). The formation of the *in situ* surfactant was proved by TOF-ES MAS analysis of a lyophilized system containing chloroform as disperse phase, where the fragment with m/z 411.31 could be observed (Figure 3.3 – 9). After the addition of a radical initiator (VA044) to the aqueous phase, stable polystyrene nanoparticle dispersion with mean diameter of ca. 300 nm could be obtained (Figure 3.3 – 10). The isomeric ratio in this reaction could not be determined by NMR spectroscopy due to the presence of a broad amine peak, which overlaps the signal of the triazole ring (Figure 3.3 – 11).

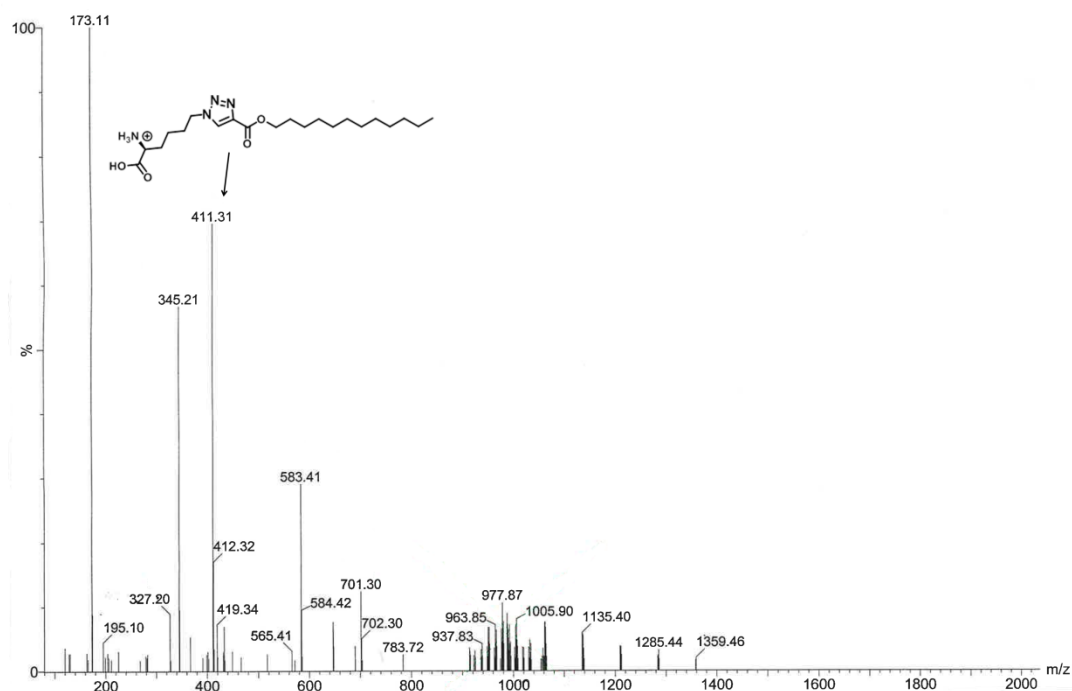


Fig. 3.3 – 9 TOF ES – MS spectra of the *in situ* surfactant (the strong signals at m/z 173.11 and 345.21 are attributed to pure lysine) (Alexandrino *et al.*; *Chem. Commun.*, 2014, **50**, 10495-10498,

<http://pubs.rsc.org/en/Content/ArticleLanding/2014/CC/C4CC04119D#!divAbstract> -

Reproduced by permission of The Royal Society of Chemistry).

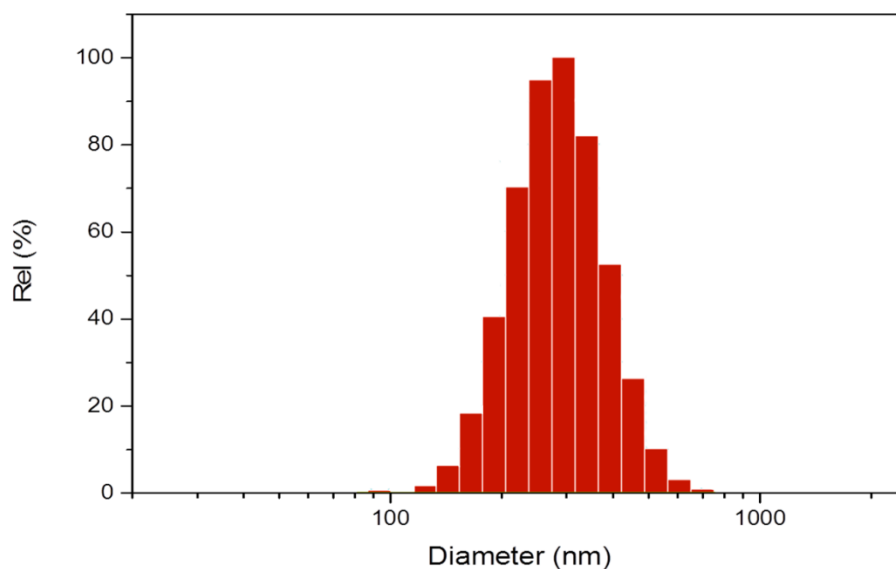


Fig. 3.3 – 10 DLS analysis of polystyrene nanoparticles produced by radical polymerization in direct miniemulsion after *in situ* formation of surfactant via interfacial click chemistry (Alexandrino *et al.*; **Chem. Commun.**, 2014, **50**, 10495-10498, <http://pubs.rsc.org/en/Content/ArticleLanding/2014/CC/C4CC04119D#!divAbstract> -

Reproduced by permission of The Royal Society of Chemistry).

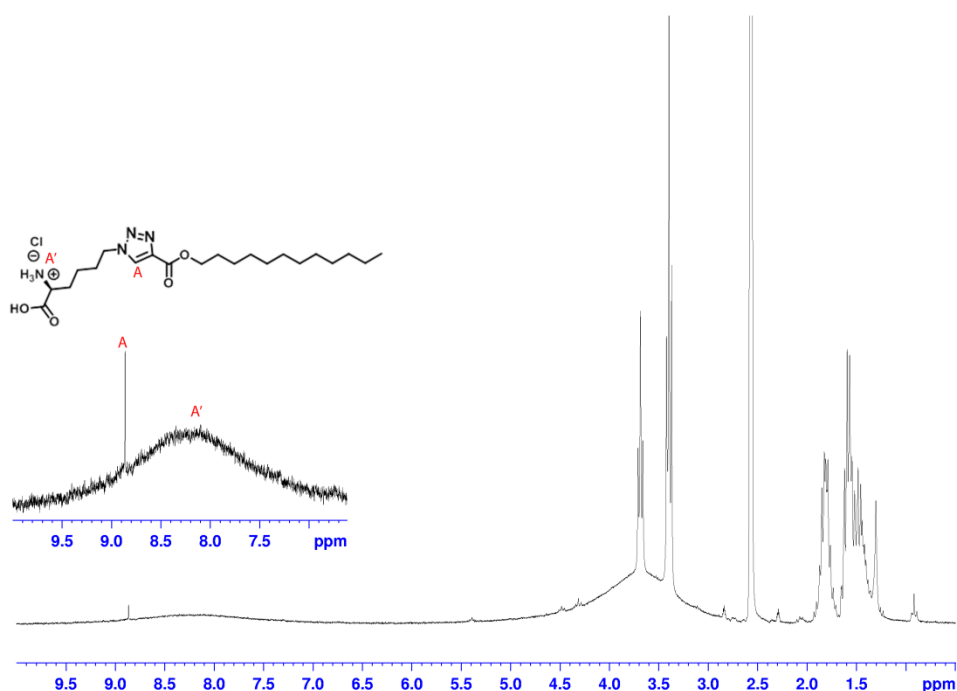


Fig. 3.3 – 11 $^1\text{H-NMR}$ in $\text{DMSO-}d_6$ (250 MHz at 298 K) of the *in situ* surfactant. Highlighted is the broad amino proton around 8.0 ppm overlapping partially the triazole peak (Alexandrino *et al.*; *Chem. Commun.*, 2014, **50**, 10495-10498, <http://pubs.rsc.org/en/Content/ArticleLanding/2014/CC/C4CC04119D#ldivAbstract> - Reproduced by permission of The Royal Society of Chemistry).

3.3.7 Conclusion

Aqueous miniemulsion was used as a synthetic tool to mediate the metal-free 1,3-dipolar cycloaddition between propiolates and azides. A detailed kinetic investigation via NMR spectroscopy was conducted for the copper-free click polyaddition between HDDP and BAP. This $\text{A}_2 + \text{B}_2$ polyaddition was studied both in solution and in a biphasic system, i.e. miniemulsion, with one monomer being confined in the dispersed phase (water) and the second being dissolved in the continuous phase. Conducting the reaction in miniemulsion leads to a significant acceleration of the reaction leading to higher molecular weights at lower temperatures compared to the reaction in solution. Detailed NMR analyses of the microstructure of the final materials indicated that the polyaddition at the interface of

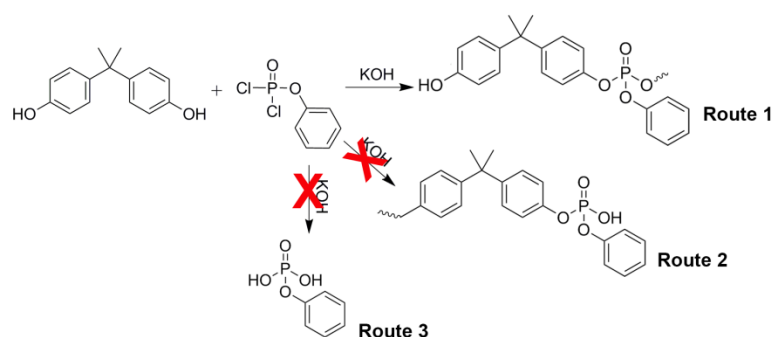
miniemulsion droplets leads to the probable formation of less cyclic oligomers and a high regioselectivity towards the 1,4-triazole isomers.

The catalyst-free 1,3-dipolar cycloaddition in heterophase can be a powerful tool for bioapplications e.g. the encapsulation or bioconjugation of temperature sensitive biomolecules, such as proteins, that can be mediated at the water interface. Herein, we also used the interfacial “screw clamp” to generate a surfactant *in situ* as an example capable of stabilizing styrene nanodroplets of which could subsequently conduct a radical polymerization.

This approach could be especially useful for biological materials due to bioorthogonality, mild conditions (low temperature, no catalyst) and the tolerance to water.

3.4 Polyphosphoester colloids: efficiency of miniemulsion vs interfacial polycondensation

Interfacial polycondensation (IP) is a valuable polymerization tool in the preparation of unique structures and morphologies. This work explores the efficiency of an inverse miniemulsion in the preparation of a bisphenol-A based polyphosphate latex, using ^{31}P NMR for the analysis of the structural features provided by the interfacial area minimization. $^1\text{H} - ^{31}\text{P}$ 2D-HMBC revealed less deactivation reactions in the inverse miniemulsion in comparison to classic interfacial polycondensation.



3.4.1 Motivation

The development of poly(phosphoester)s (PPEs) and polycondensation are closely related, since the pioneering work of Arvin in 1934.¹⁰⁷ The work described the preparation of a synthetic PPE, based on bisphenol-A with potential flame retardant properties through a polycondensation approach in solution. Indeed, polycondensation is a valuable tool for the development of a variety of polymeric structures and can be performed through three different approaches: in melt, in solution or as interfacial polycondensation.²⁸² Inspired by the early works of Schotten and Baumann^{47, 48} and followed by the preparation of aliphatic polyamides by Magat *et al.*²⁸³ in 1955, its first industrial application, interfacial polycondensation (IP) reactions are nowadays widely applied in the industrial production of polycarbonates,²⁸² the development of membranes for reverse osmosis^{284, 285} and encapsulation of a variety of different materials.²⁸⁶⁻²⁸⁸

For the IP both monomers are separately dissolved two immiscible solvents and the reaction occurs at or in a thin region at the interfacial region between the phases, followed by the precipitation of the insoluble oligomers and polymers formed in the interfacial region.²⁸⁹ For the mechanistic description of each IP different conditions have to be considered, as the equilibrium processes involved, the localization of the reaction and the solubility parameters of all reactants and products, which will directly the efficiency of the process and the level of undesired side reactions (e.g. deactivation of the monomers by hydrolysis or cyclization).^{282, 289} Therefore, an IP is influenced by both chemical reaction parameters and physical transport processes at the interfacial region.²⁸⁹ Herein, we investigate the polycondensation of bisphenol-A and dichlorophenylphosphate (DCPP) under different biphasic conditions: a classical and a miniemulsion IP. Both protocols involve a basic aqueous solution of bisphenol-A and the organic phase with DCPP. We recently studied the formation of nanocarriers and the kinetics of a click-type polyaddition in miniemulsion.⁴ In this work the influence of the surface area on the efficiency of a polycondensation is analysed using the phosphorus atoms in the polymer structure as a probe for the structural features provided by each approach, as well as the influence on the molecular weight of the polymer and the morphology of the particles obtained by miniemulsion. This work has two separate goals: first, we present the first example for the preparation of PPE colloids by IP, and second, with the phosphorus being present in the polymer structure and the hydrolytically-labile DCPP a detailed NMR-analysis of the reaction and the products by ³¹P NMR spectroscopy is possible. This enables a deep insight in the efficiency of the IP in

mini-emulsion compared to the classical approach and provides at the same time more insights about the influence of the minimization of surface area in interfacial polymerization reactions and a platform for the preparation of potentially flame-retardant nanoparticles.

3.4.2 Experimental part

3.4.2.1 Materials

For the study of the polymerization reactions, the monomer bisphenol-A was obtained from FLUKA and the monomer dichlorophenylphosphate was obtained from Sigma-Aldrich. Cyclohexane was obtained from VWR Chemicals and deionized water was produced in-house. The surfactant polyglycerol polyricinoleate (PGPR) was obtained from DANISCO and NaOH or KOH were obtained from Sigma-Aldrich. All chemicals were used without further purification.

3.4.2.2 Synthesis of BPA – PPE by inverse mini-emulsion

Figure 3.4 – 1 presents a scheme of the inverse mini-emulsion approach used in this work. In a glass vial protected from light to avoid oxidation from bisphenol A, 0.568 mmol of bisphenol A (130 mg) were dissolved in 5 g of Milli-Q water and 1,19 mmol KOH (67.32 mg). In some samples, NaOH was also used at the same molar concentration as KOH. After the complete dissolution of all components, a solution of 7.5 mg of cyclohexane and 100 mg PGPR was added and the system was pre-emulsified by stirring at 1000 rpm during a period of 60 min. Then, the pre-emulsion was submitted to a pulsed ultrasonication process in an ice bath during 180 s (20 s sonicated and 10 s paused) at 90% amplitude by a ½" tip Brason 450 W sonifier. To this first emulsified system, a second aliquot of 5 g of cyclohexane and 30 mg of PGPR was added and the system was further stirred over a period of 30 min. After this process, the system was once again ultrasonicated with the same procedure used previously. A fresh solution of 30 mg PGPR, 131.41 mg (0.623 mmol) phenyldichlorophosphate in 5 g of cyclohexane was prepared and immediately dropped through a septum cap in the emulsified system under stirring (300 rpm) with a syringe, over a period of 5 min under room temperature. The reaction was left stirring overnight. The final dispersion obtained was also redispersed in water. 1 mg of the dispersion was mixed with

5 g of Milli-Q water and 5 mg of SDS. The dispersion was submitted to ultrasonication process in an ice bath during 60 s (10 s sonicated and 5 s paused) at 17% amplitude by a ½" tip Brason 450 W sonifier. The emulsified system was left stirring (250 rpm) open for evaporation of the cyclohexane.

The average particle size and particle size distribution were obtained by dynamic light scattering (DLS) in a submicron particle sizer NICOMP® 380 equipped with a detector to measure the scattered light at 90°. The particle morphology was studied by scanning electron microscopy (SEM) using a microscope Zeiss LEO Gemini 1530. EDX analysis was performed in a microscope HITACHI SU8000 with a Bruker AXS Xflash 5010 (SDD=silicon drift detector, with a chip size of 10mm²) using their software Quantax ESPRIT, version 1.9.4. Previous to the measurement a thin carbon coating layer was deposited using a vacuum coating system Leica EM MED020. Transmission electron microscopy (TEM) was performed in a JEOL 1400 microscope, after drop cast of the nanoparticle dispersion onto a carbon coated copper grid. Cryo-TEM imaging was performed using a cryogenic holder in the same microscope. The sample was prepared directly from the inverse miniemulsion system, following and adapted version of the literature procedure.²⁹⁰ For the NMR analysis described in the following sections, the samples were firstly liophilized and subsequently dissolved in DMSO-*d*₆.

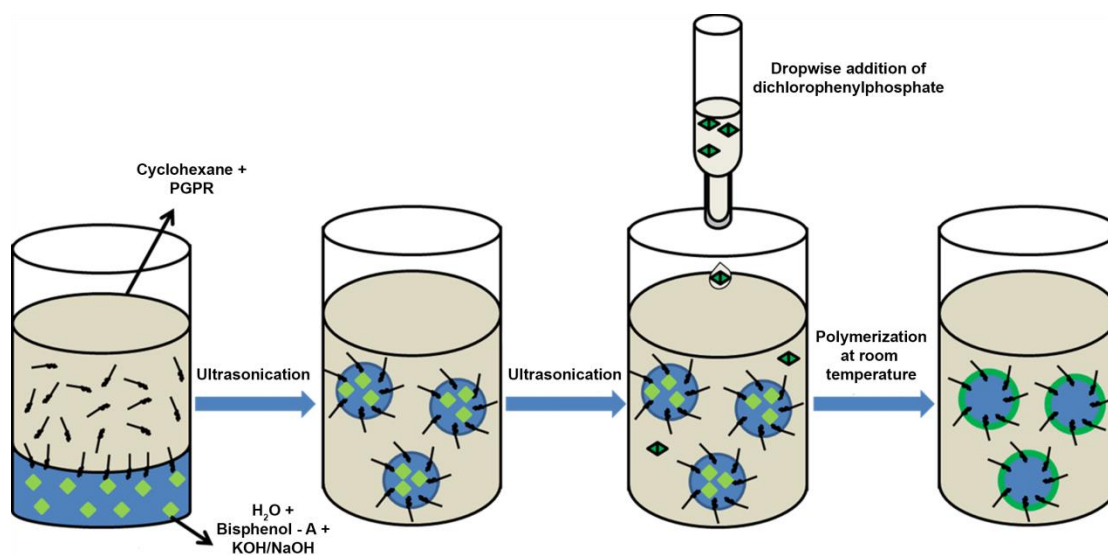


Fig. 3.4 – 1 General inverse miniemulsion polycondensation approach for the preparation of PPE colloids.

3.4.2.3 Synthesis of BPA-PPE by interfacial polymerization

A classical interfacial polymerization approach was used for the synthesis of BPA-PPE.²⁹¹ In the usual procedure, a glass protected from light was used and 1 equivalent of bisphenol-A (502 mg or 2.19 mmol) was dissolved in two equivalents of KOH aqueous solution (247.5mg or 4.4 mmol in 5 g of deionized water). After complete dissolution the system was stirred at 1000 rpm. The organic phase was freshly prepared and was composed by 3.75 g of cyclohexane and 1 equivalent of dichlorophenylphosphate (463 mg). The organic phase added dropwise under the stirring aqueous phase and left reacting during 5-10 min. After this period, the stirring was stopped a polymer was formed between the two phases. The water phase was extracted with a syringe and the samples were lyophilized and subsequently dissolved in DMSO-*d*₆, prior the NMR analysis described in the following sections.

3.4.2.4 ¹H and ³¹P {H} NMR analysis

The ¹H NMR experiments were recorded with a 5 mm BBFO 1H/X z-gradient on the 500 MHz spectrometer with a Bruker Avance III system. ¹H-NMR spectra were recorded 128 transients using an 11.9 μs long 90° pulse and a 10000 Hz spectral width together with a recycling delay of 5 s.

For ³¹P {H} spectra measurements (202 MHz), an 1H powergate decoupling method using 30° degree flip angle was used, which had a 11 μs long 90° pulse for phosphor. Overall 128 numbers of scans were admitted with a relaxation delay of 2 s and a spectral width of 20000 Hz.

3.4.2.5 2D ¹H-³¹P HMBC analysis

Long-range correlation between ¹H-³¹P was measured with 2D HMBC (heteronuclear multiple bond correlation) via heteronuclear zero and double quantum coherence optimized for long range couplings with a low-pass J-filter to suppress one-bond correlations. No decoupling during acquisition using gradient pulses for selection was used. The average indirect coupling constants used was ⁿJ_{PH}=5Hz (¹H-³¹P), to optimize the observable intensities of cross peaks from multiple bond ¹H-X correlation. The spectra were obtained with

$\pi/2$ -pulse lengths of 11.9 μs (^1H) and 11 μs (^{31}P) and a sweep width of 8000 Hz (16 ppm) for ^1H and 20000 Hz (100 ppm) for ^{31}P , all nuclei with a relaxation delay of 1.3 s.

3.4.2.6 Size exclusion chromatography (SEC) analysis

The apparent molecular weight was determined by size – exclusion chromatography (Agilent Technologies 1260 Infinity). The lyophilized samples were dissolved in DMSO with concentrations of approximately 1 mg mL⁻¹ and directly analyzed by SEC. The solutions were injected at a flow of 0.8 ml min⁻¹ with a 5 g L⁻¹ LiBR in DMSO solution as eluent phase at 80 °C. A GRAM PSS column, with linear porosity, particle size 10 μm and dimensions of 0.8 x 30 cm was used. The signal was detected with a refractive index detector (RI -101 ERC) and the molecular weight was obtained with the software PSS-WinGPC UniChrom (PSS) against PMMA standards ($M_p = 800\text{-}2000000 \text{ g mol}^{-1}$).

3.4.3 Bisphenol A-based polyphosphate by inversion miniemulsion: miniemulsion vs classic interfacial polycondensation

Typical challenges for polycondensation reactions are the limited molecular weights and potential side-reactions that may occur during the procedure. Especially the hydrolysis of the electrophile under Schotten-Baumann conditions is a limiting factor for the molecular weight and the overall conversion/yield. The general reaction is showed in Figure 3.4 – 2. The formation of bisphenol-A terminal groups due to limitations for further reaction, is the most efficient route to achieve higher molecular weights. The formation of phosphoric acid derivatives by the hydrolysis of the P-chlorides at the interface should be avoided in order to obtain higher degrees of polymerization.

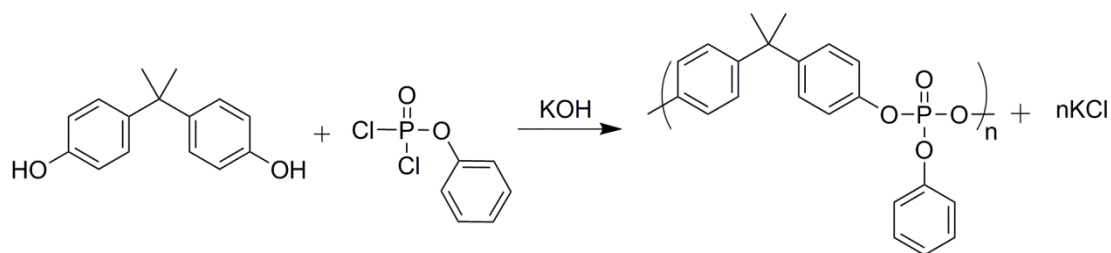


Fig. 3.4 – 2 Polycondensation reaction between bisphenol A and dichlorophenylphosphate.

IPs have been already studied in miniemulsion relying on the crosslinking of different polymers for the formation of nanocapsules and nanoparticles, with the goal of encapsulation of the various compounds.^{54, 60, 292-294} To date, no report on the preparation of PPE colloids by IP has been reported, nor has the efficiency been compared to a classical interfacial polycondensation. The preparation of BPA-PPE by classic IP is a typical example for PPEs²⁹¹ with striking potential for flame retardant polymers.¹⁰⁸ With the recent ban on halogenated flame retardants, a revival of phosphorus-containing flame retardants is ongoing and also classical polycondensations as industrially interesting platform are receiving again more interest.¹² The approach introduced in this work is a useful strategy for the development of flame-retardant nanoparticles based on phosphorus containing polymers, a strategy already explored with hydroxyapatite nanoparticles by Ke *et al.*²⁹⁵ and in the development of nanocoatings by Mostafa and Elbasuney,²⁹⁶ which could also be used in the development of phosphorus containing nanocarriers for potential biomedical applications.¹ Therefore, the comparison between macroscopic and nanoscopic interfaces is especially interesting for fundamental studies of the IP for the preparation of PPEs, but also for other polymers.

The reaction was conducted under basic conditions (with KOH or NaOH as the respective base) to increase the nucleophilicity of the phenolic OH-groups. DCPD is added drop-wise after emulsification or under stirring (Fig. 3.4 – 1). In the case of the miniemulsion IP the base acts at the same time as the osmotic stabilizer. After the miniemulsion IP, PPE nanoparticle dispersions were obtained directly. The size and size distribution determined by dynamic light scattering are shown in Table 3.4 – 1.

Table 3.4 – 1 Mean diameter and size deviation of the systems BPA-PPE-KOH and BPA-PPE-NaOH obtained in inverse miniemulsion.

Sample	Mean diameter \pm S.D. (nm) ^a
BPA-PPE-KOH (miniemulsion)	732 \pm 255
BPA-PPE-NaOH (miniemulsion)	927 \pm 205

^a Determined via dynamic light scattering using a NICOMP Particle Size Analyzer.

The final product was characterized in detail by $^1\text{H-NMR}$ spectroscopy (Figure 3.4 – 3). The signals highlighted are related to the expected polymer structure, while others signals attributed to the surfactant (PGPR) are also observed. The signals of the polymer were confirmed by comparison with the product of reaction of a classical IP. The overlay of the miniemulsion polymerization product in comparison to the one obtained by classical IP (Figure 3.4 – 4), both with KOH as deprotonating agent, reveals that in both cases the signals for terminal bisphenol A units, at δ 6.6 ppm, indicating that the molecular weight is limited independent of the polymerization approach. The molecular weight distributions by both methods were confirmed by size exclusion chromatography (SEC) (the elugram is presented at Figure 3.4 – 6). Higher molecular weights and a broader molecular weight distribution were obtained at the inverse miniemulsion system in comparison to the classical IP.

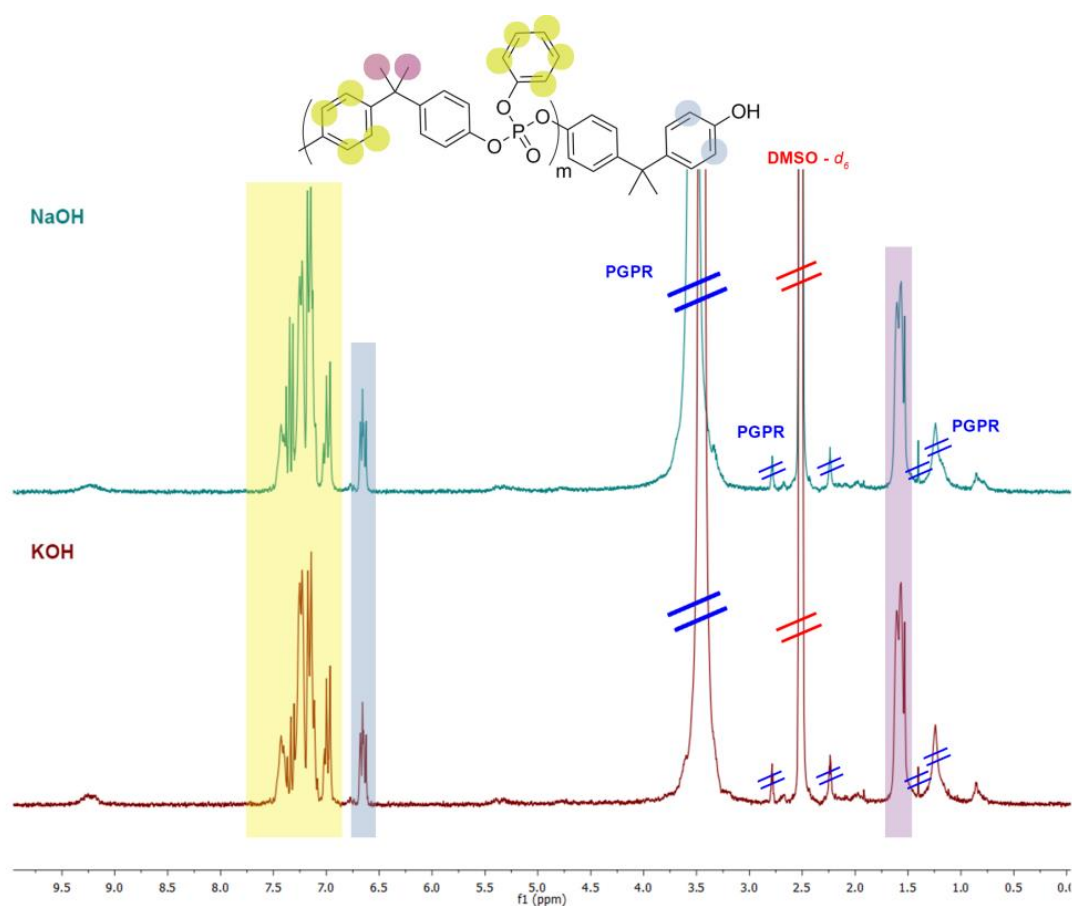


Fig. 3.4 – 3 $^1\text{H-NMR}$ spectra in $\text{DMSO-}d_6$ (500 MHz, Avance III) from the polymer BPA-PPE produced by polymerization in inverse miniemulsion with KOH or NaOH as osmotic and deprotonation agent.

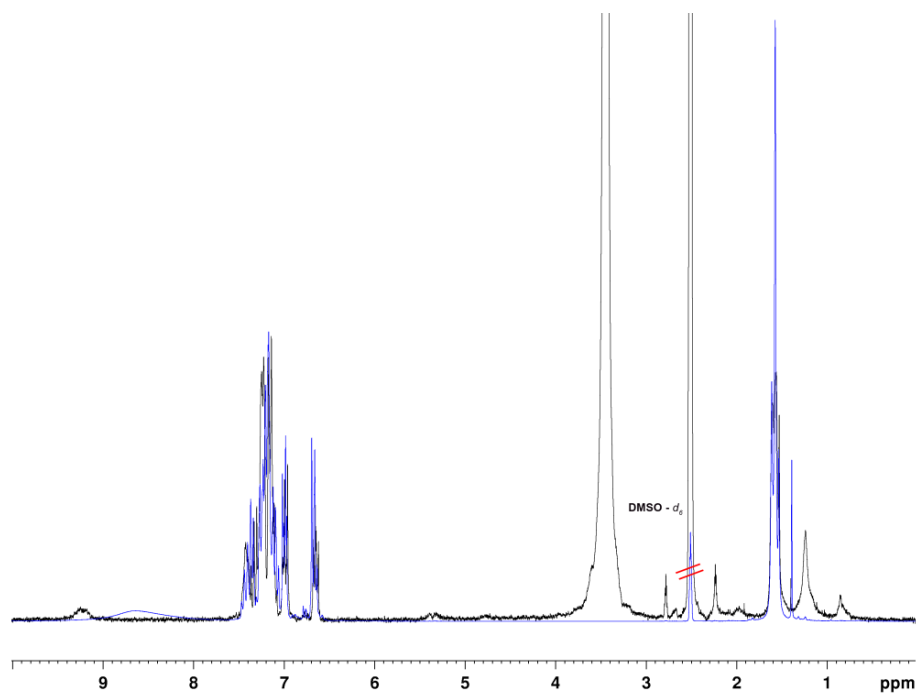


Fig. 3.4 – 4 $^1\text{H-NMR}$ spectra in $\text{DMSO-}d_6$ (500 MHz, Avance III) from the polymer BPA-PPE made by polymerization in inverse miniemulsion (black) or classic interfacial polymerization (blue).

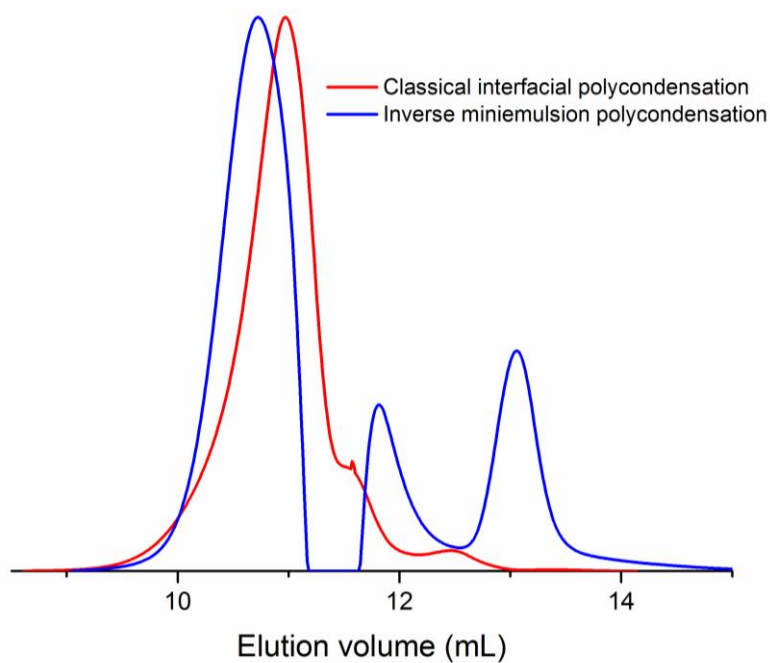


Fig. 3.4 – 5 SEC elugram of BPA-PPE prepared by a classical IP (red) and an inverse miniemulsion IP (blue).

The $^{31}\text{P}\{\text{H}\}$ NMR spectra of BPA-PPE prepared by miniemulsion IP was recorded in $\text{DMSO-}d_6$ and compared with the polymer obtained by the classical IP (Figure 3.4 – 6). In order to determine the chemical shift corresponding to the polymer, an aromatic phosphoric acid triester (triphenylphosphate) was measured as a control. The polymers produced by miniemulsion IP exhibit four different resonances in the $^{31}\text{P}\{\text{H}\}$ NMR, independently of the use of KOH or NaOH. The most intense signal (δ -17 ppm) is localized close to the chemical shift of triphenylphosphate, indicating the resonance of the in-chain repeat unit. In the case of the classical interfacial polymerization approach, three signals were observed, more importantly, the signal for the P-triester was less intense.

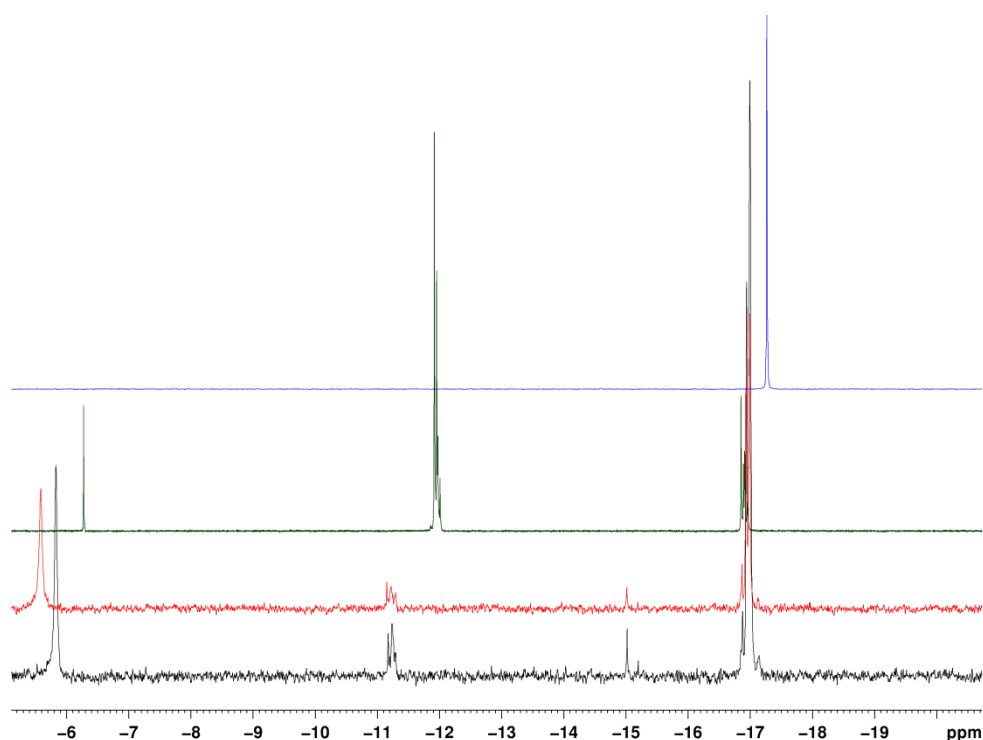


Fig. 3.4 – 6 $^{31}\text{P}\{\text{H}\}$ -NMR spectra in $\text{DMSO-}d_6$ (202 MHz) at 298K from the polymer BPA-PPE made by polymerization in inverse miniemulsion with KOH (black) or NaOH (red) as osmotic and deprotonation agent or classic interfacial polymerization (green) with KOH as deprotonation agent. As reference, triphenylphosphate (blue) was also measured in $\text{DMSO-}d_6$.

To assign the peaks from the ^{31}P NMR spectra to the phosphorus centers in the polymers, 2D $^1\text{H-}^{31}\text{P}$ HMBC correlation spectroscopy was applied to the polymer synthesized via the miniemulsion IP with KOH as osmotic and deprotonating agent (Figure 3.4 – 7). All signals can be correlated to the aromatic region of the ^1H NMR spectrum. As previously

pointed, the signal at approximately -17 ppm is characteristic for a tri-aromatic phosphoester and is therefore attributed to the internal part of the polymer. The second signal at approximately -15 ppm shows direct correlation with the region of terminal bisphenol-A groups (δ 6.6-6.7 ppm in the ^1H NMR). 85% phosphoric acid solution presents chemical shift at 0 ppm and is usually used as reference in ^{31}P NMR measurements.²⁹⁷ The peak closer to $\delta = 0$ ppm, at -5.8 ppm, must have a structure similar to phosphoric acid and the most probable structure is the product of hydrolysis of phenyl dichlorophosphate.^{298, 299} Thereby, the peak at ca. -11ppm can be attributed to the phosphoric diesters, i.e. the terminal units.

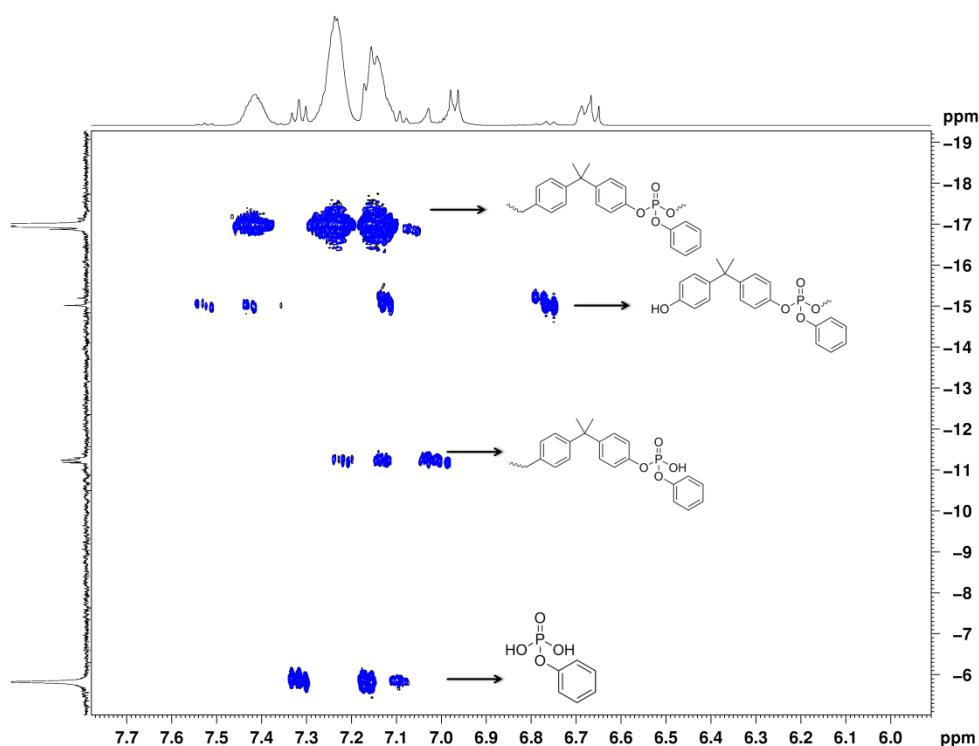


Fig. 3.4 – 7 2D ^1H - ^{31}P HMBC (500 MHz, Avance III)) analysis of the polymer BPA-PPE obtained by inverse miniemulsion polymerization in $\text{DMSO-}d_6$ at 298K. The upper spectrum corresponds to the ^1H spectrum, the spectrum on the left is the internal calculation of the cross peaks in the ^{31}P -frequency range.

The increase of the surface area apparently reduces the possibility of deactivation reactions, which can be related to an increase in the local concentration of bisphenolate species available for reaction with DCPD induced by the smaller volume of the aqueous droplets compared to a macroscopic interface. Leong and coworkers proved that for longer reaction times a decrease of the molecular weight is observed in the IP of BPA-PPE in the

presence of a phase-transfer catalyst (cetyltrimethylammonium chloride). This decreased molecular weights were not observed in the miniemulsion IP.²⁹¹ These findings correlate also with recent findings from our group on increased reaction kinetics in an interfacial Huisgen-type polyaddition in miniemulsion.⁴ An increase in the local concentration at the droplet interface of the second monomer reduces the probability of the hydrolysis of the phosphoric acid chlorides, resulting in materials with a lower level of phosphoric acid terminal units. Figure 3.4 – 8 presents the superposition of the 2D ^1H - ^{31}P HMBC spectra of the polymer BPA-PPE produced by both approaches and confirms the previously expected decrease of the concentration of phosphoric acid terminal units in the inverse miniemulsion system.

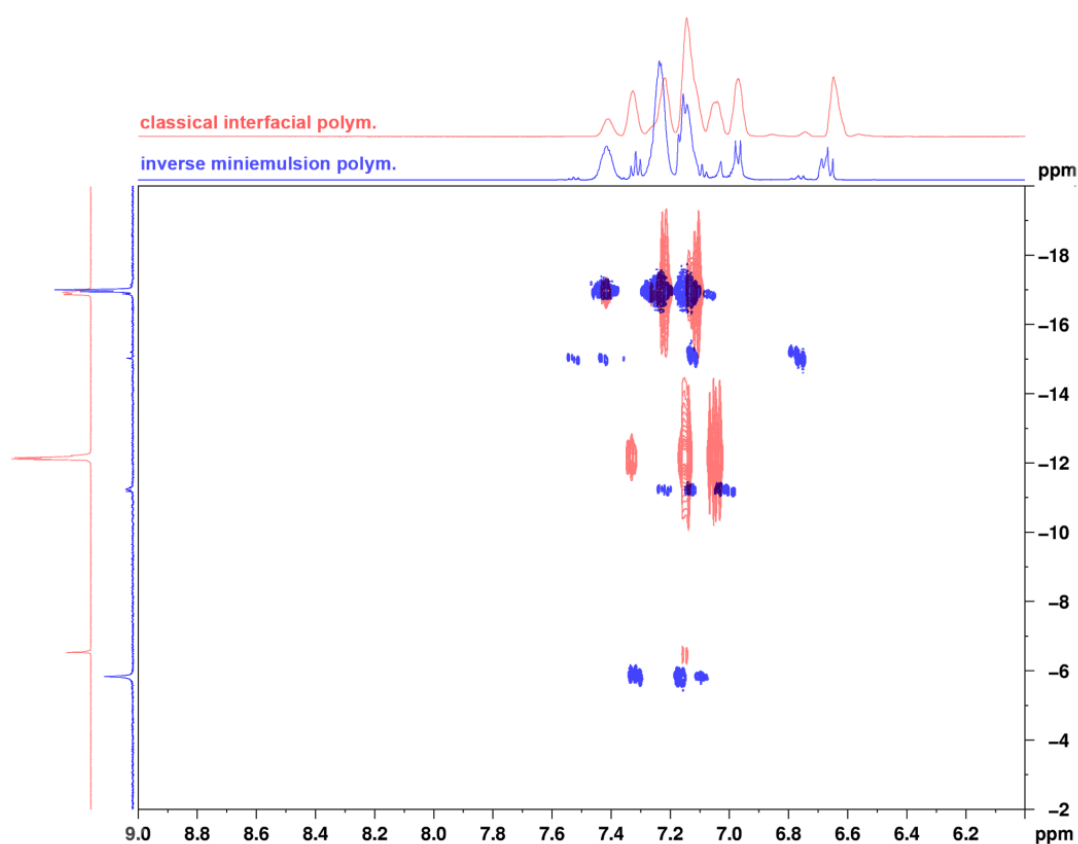


Fig. 3.4 – 8 Comparison between the 2D ^1H - ^{31}P HMBC spectra (500 MHz, Avance III) of the polymer BPA-PPE obtained by inverse miniemulsion polymerization (blue) and by a classical interfacial (red) polymerization approach (in $\text{DMSO}-d_6$ at 298K). The upper spectra corresponds to the ^1H spectrum, the spectra on the left is the internal calculation of the cross peaks in the ^{31}P -frequency range. The signals for the classical interfacial polymerization spectrum were increased in order to make the correlation at approximately -6 ppm visible.

3.4.4 Morphological analysis of BPA-PPE colloids obtained by inverse miniemulsion

As previously presented in section 2.1.4 of this work, the final morphology obtained in a miniemulsion phase separation process in a system composed by three phases is essentially dependent of the interfacial tension equilibria between those phases. SEM micrographies in Figure 3.4 – 9 reveals the morphology obtained after the polymerization of the polymer BPA-PPE in inverse miniemulsion with KOH (Figure 3.4 – 9A and B) or NaOH (Figure 3 – 9C and D) as the osmotic agent. As can be observed, a mixture between deflated or not spheres was obtained in both cases. Deflated spheres are commonly observed in the formation of capsule-like structures due to the evaporation or leakage of the liquid core. Nevertheless the most remarkable feature of this system was the presence of cubic structures attached to the particle surface, which could be observed for almost every particle (between one and 5 cubes per particle in average).

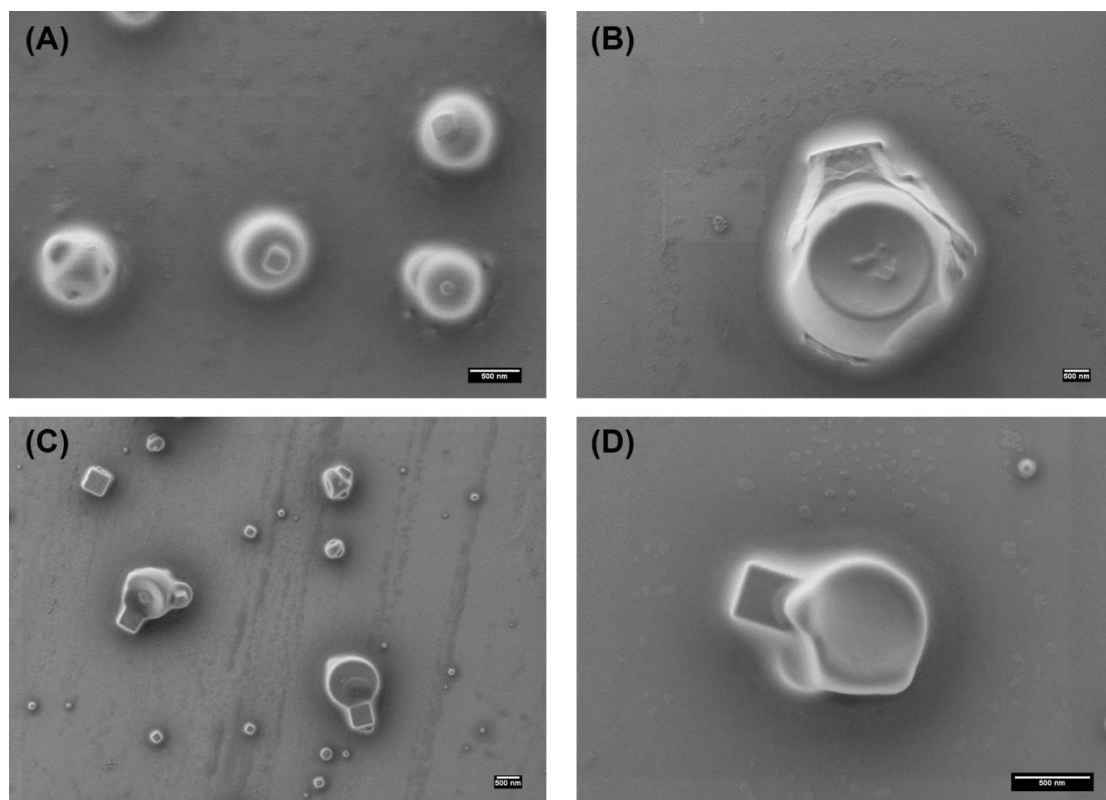


Fig. 3.4 – 9 SEM micrographies obtained for the product of the polycondensation of BPA-PPE in inverse miniemulsion using KOH (A-B) or NaOH (C-D) as the osmotic and deprotonation agent.

In order to understand such morphology, TEM analysis was performed. Figure 3.4 – 10 presents the TEM micrographies for the system with KOH as the osmotic agent. The images reveal that no core-shell morphology can be easily observed for this system, which does not confirm the possible formation of capsule-like systems. Another feature is the position of the cubes formed: in most of the cases the cubes are partially penetrated in the particles surface.

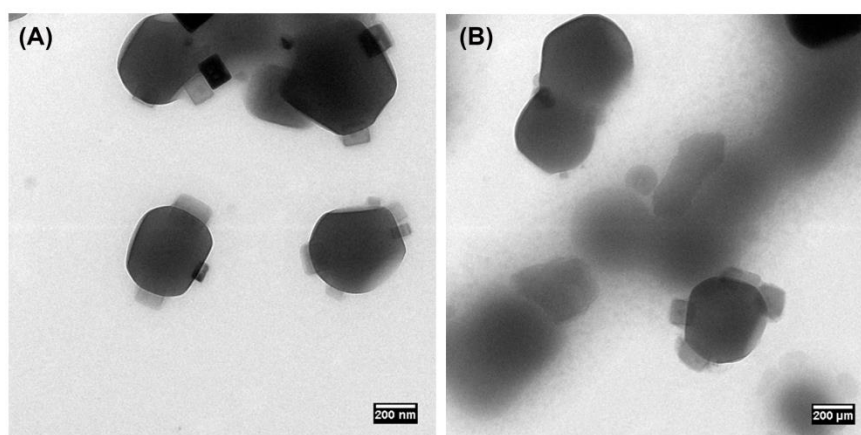


Fig. 3.4 – 10 TEM micrographies obtained for the product of the polycondensation of BPA-PPE in inverse miniemulsion using KOH as the osmotic and deprotonation agent.

At this point, it is still unclear the reason and mechanism for the formation of such structures. In an attempt of a closer look to the structure formed, the particles were firstly embedded in a cross-linked resin; thin slices were obtained by microtomy and thereby the cross section of the particles was analyzed by TEM (Figure 3.4 – 11A and B) and the surface of the resin was analyzed by SEM (Figure 3.4 – 11C and D). The polymer was stained with osmium tetroxide and it is seen with darker contrast at TEM and lighter at SEM measurements. TEM images show that most of the particles are solid particles in most of the cases, even though the fact that some of the particles have the same contrast as the background indicates that the resin could penetrate and fill the particles in some cases, a fact that is mostly seen in the SEM images. In general, after embedding the particles in the resin an increase in the diameter was observed, which is also a potential indication that a swallowing process happened. The crystals were less often observed, and when observed there was no penetration in the particle surface.

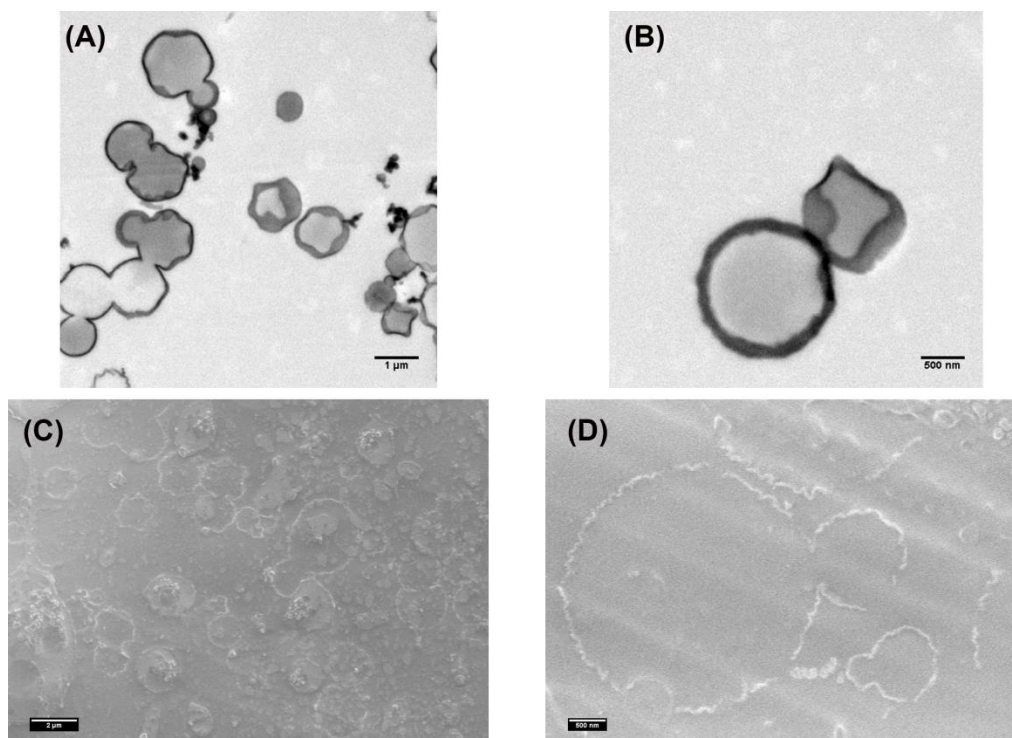


Fig. 3.4 – 11 TEM (A and B) and SEM (C and D) micrographies obtained from microtomed slices or the surface of the resin, respectively, for a resin containing embedded particles obtained from the polycondensation of BPA-PPE in inverse miniemulsion using KOH as the osmotic and deprotonation agent.

After redispersion of the particles obtained in inverse miniemulsion system in water, the cubic structures could not anymore be observed, for both systems, resulting in round particles, as can be seen in Figure 3.4 – 12, indicating that the material composing such structures was probably soluble in water.

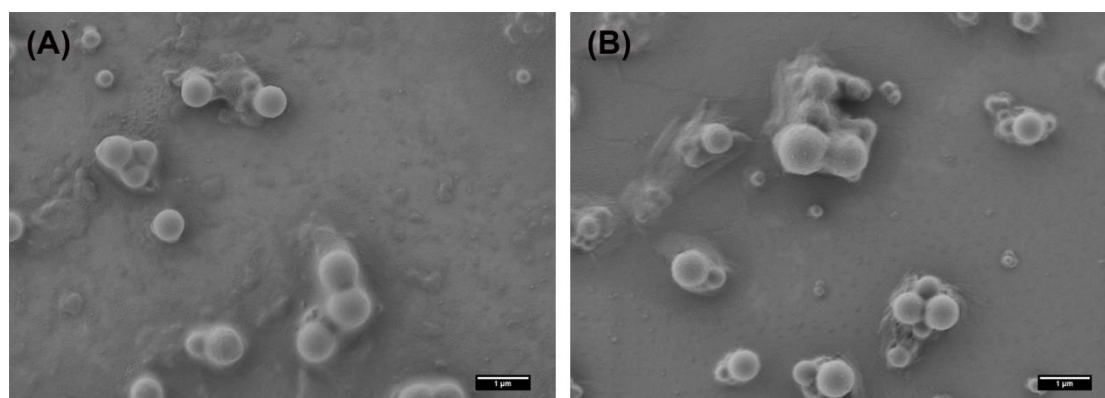


Fig. 3.4 – 12 SEM micrographies of the particles of BPA – PPE after redispersion in water/SDS (0.6 wt%): KOH (A) or NaOH (B) as the osmotic and deprotonation agent.

Aiming the determination of the composition of the cubic structures, EDX analysis (Figure 3.4 – 13) was performed in the product obtained direct from the miniemulsion. A sample containing KOH as osmotic and deprotonating agent was analyzed and revealed that the cubes are composed by potassium and chlorine, i.e. potassium chloride, a by-product of the polycondensation reaction.

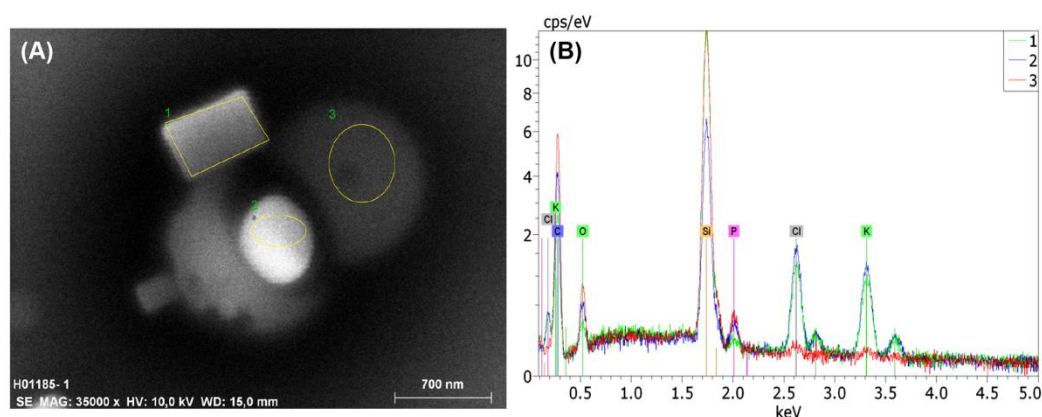


Fig. 3.4 – 13 EDX analysis of the BPA-PPE particles obtained in inverse miniemulsion using KOH as the osmotic and deprotonation agent.

So, potassium chloride formed during the interfacial polycondensation is crystallized in the surface of the particles. The question right now is: when and why? To verify the presence of the crystals in the inverse miniemulsion dispersion, cryogenic TEM analysis was performed with a sample before the re-dispersion (Figure 3.4 – 14). As can be seen, any presence of KCl crystals was observed, showing that the crystallization from the inverse miniemulsion is phenomenon that happens during the drying process of the samples in the sample preparation.

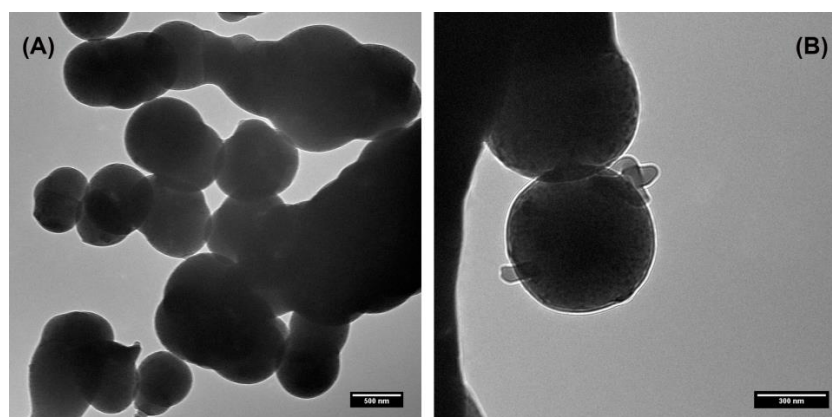


Fig. 3.4 – 14 Cryo-TEM micrographs obtained from BPA-PPE particles in the inverse miniemulsion system.

With this information, the best scenario to explain the formation of such crystals is the case presented in Figure 2.1 – 3 in section 2.1.4: the interfacial tension equilibrium leads to a partial encapsulation of the water droplet; the crystallization occurs through the evaporation of this water droplet (Figure 3.4 – 15).

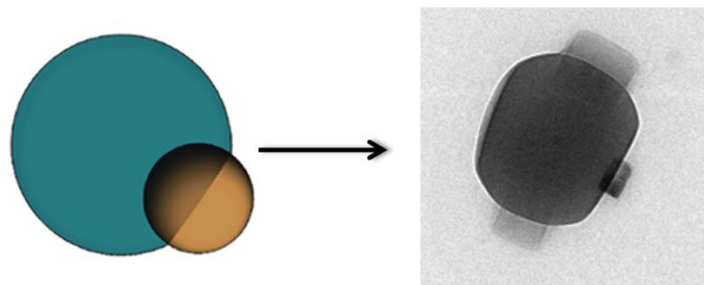


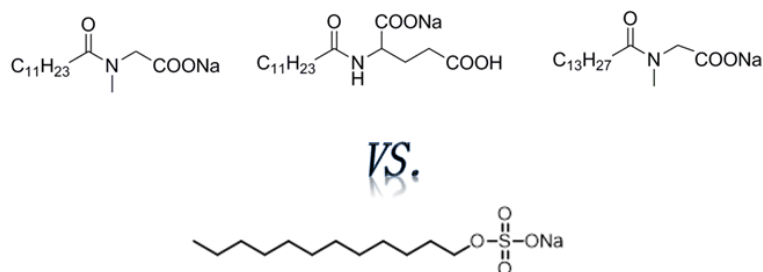
Fig. 3.4 – 15 Most possible scenario obtained for the inverse miniemulsion polymerization of BPA-PPE: partial encapsulation of the water droplet.

3.4.5 Conclusion

This work introduced the first interfacial polycondensation (IP) in miniemulsion for the preparation of poly(phosphoester)s (PPE). In comparison to a classical interfacial polycondensation, higher molecular weights were achieved in the inverse miniemulsion system. This study follows two different goals: Besides the potential of the PPE colloids acting as a flame-retardant additive, we used the NMR-active phosphorus as an inherent probe to study the influence of the minimization of the surface area on the efficiency of the IP in miniemulsion (vs. classic system). A lower amount of hydrolysis of the phosphoric acid dichloride was achieved in the miniemulsion IP, which is probably related to an increase in the local concentration at the surface of the aqueous droplets, as previously rationalized by other polyaddition reactions.⁴ The increase of the surface area apparently reduces the contact between phosphoric acid dichloride and the aqueous droplet phase, reducing therefore the possibility of hydrolysis and thus the interfacial area of contact is a determinant factor in the efficiency of the reaction. The particles produced in this work are composed of a well-known flame-retardant and have potential for further application as an additive for flame resistant improvement of other polymers compositions. The applicability of this material is topic of further studies at the moment.

3.5 Stabilization of nanoparticles synthesized by miniemulsion polymerization using “green” amino-acid based surfactants³⁰⁰

This section covers the use of PPE nanoparticles in the study of biocompatible amino-acid based surfactants, published Baier et al.³⁰⁰ Polystyrene (PS) nanoparticles were synthesized using a classical direct miniemulsion radical polymerization technique, while poly(l-lactide) (PLLA) and polyphosphate (PP) - the same PPE-C20-Phenoxy presented in previous sections- nanoparticles were synthesized by direct miniemulsion/solvent-evaporation technique. The surfactant concentration was varied between 3-6 mg surfactant mL⁻¹ water during the preparation of all nanoparticles system. In this study, three different amino-acid based surfactants were used: sodium lauroyl sarcosinate (SLS), sodium lauroyl glutamate (SLG) and sodium myrityl sarcosinate (SMS).



3.5.1 Motivation

The use of different stabilizing molecules allows the modification of the nanoparticles surface even in the formation of nanoparticles with different types of surfactants. The most commonly used surfactant is anionic sodium dodecyl sulphate (SDS). Despite the fact that SDS is not carcinogenic when applied directly to the skin or when consumed, it is known that SDS deactivates enzymes and can denature proteins. Therefore, such surfactant cannot be applied in strategies involving enzyme triggered release approaches. This fact implies in the need for the search of new stabilizing molecules with similar effective of SDS and adding at the same time special features as biocompatibility and biodegradable structures. In this scene, amino-acid based surfactants are a good alternative to classical ionic surfactants because of their biocompatibility and biodegradation. Due to the fact that the surfactant remains bound to the surface of the final particle system, it is necessary to achieve minimal toxicity. The structures of the surfactants are depicted in Figure 3.5 – 1. As standard for comparison, sodium dodecyl sulphate (SDS) was used. The influence of the surfactant concentration in the stability, size, size distribution, morphology and surface tension was evaluated. Poly(L-lactide) (PLLA) and polystyrene (PS) nanoparticles were also evaluated in comparison to polyphosphate nanoparticles (PP), based on the previous introduced PPE-C20-Phenoxy. These particles were prepared by Abdulkader Baki. The evaluation of the surface tension was performed by Dr. Grit Baier and the cytotoxic characterization was performed by Dr. Stephanie Tomcin.

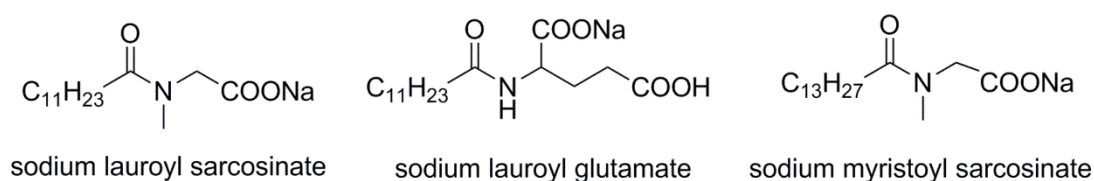


Fig. 3.5 – 1 Chemical structures of the amino-acid based surfactants.

3.5.2 Experimental part

3.5.2.1 Materials

Styrene (Merck) was purified by distillation under reduced pressure before use. All the other reagents and solvents were used as received. The oil-soluble initiator

2,20-azobis(2-methylbutyronitrile) (V59) from Wako Chemicals, Japan, was used as initiator. Hexadecane was purchased from Aldrich. Biomer1L9000 was kindly supplied by Biomer, Germany (Mn: 66,500 g mol⁻¹, Mw: 145,000 g mol⁻¹ determined by GPC in chloroform). The HPLC-grade organic solvent chloroform was purchased from Merck. Sodium dodecyl sulfate (SDS) was purchased from Merck, sodium myristoyl sarcosinate (SMS) and sodium lauroyl glutamate (SLG) were kindly provided by Schill and Seilacher, and sodium lauroyl sarcosinate (SLS) was purchased from AppliChem. The polyphosphate polymer (PP) was synthesized as previously mentioned in the section 3.1 of this Thesis, being previously hydrogenated before the use with a Pd/C catalyst (5% Pd/C) purchased from Aldrich. Demineralized water was used in all experiments.

3.5.2.2 Synthesis of polystyrene nanoparticles (PS-NPs)

The polystyrene nanoparticles were synthesized by Abdulkader Baki. Briefly, a total monomer amount of 6 g styrene, 250 mg hexadecane, and 100 mg V59 as initiator were mixed and added to the aqueous phase (24 g water and different amounts of SLS, SLG, SMS and SDS). After 1 h of stirring at 1000 rpm, the mixture was homogenized by ultrasonication for 120 s at 90% intensity (Branson sonifier W450 Digital, ½" tip) at 0 °C in order to prevent polymerization of the monomer(s). Polymerization was carried out at 72 °C under stirring for 12 h. For the characterization all polymeric nanoparticles were dialyzed for 48 h (MWCO: 12,000 g mol⁻¹) in order to remove the residual surfactant-if any.

3.5.2.2 Synthesis of poly(L-lactide) nanoparticles (PLLA-NPs) or polyphosphate nanoparticles (PP-NPs)

PLLA-NPs and PP-NPs were synthesized using a miniemulsion/solvent-evaporation approach. The PP nanoparticles were synthesized as described in the section 3.1.2.2, with the amount of surfactant being adapted to similar values used in the synthesis of PS-NPs and PLLA-NPs. PLLA-NPs (synthesized by Abdulkaber Baki) were synthesized through the following approach: 300 mg PLLA was dissolved in 10 g of chloroform at 40 °C. Afterwards the aqueous phase consisting of 24 g water and different amounts of surfactant (SLS, SLG, SMS and SDS) was added to the chloroform phase. The polymeric NPs were cleaned by dialysis (MWCO: 12,000 g mol⁻¹) over 48 h in order to remove the residual surfactant - if any.

For all nanoparticle samples, the average size and the size distribution of the NPs by means of dynamic light scattering (DLS) were measured with diluted dispersions (40 mL sample was diluted in 1 mL water) on a PSS Nicomp Particle Sizer 380 (Nicomp Particle Sizing Systems, USA) equipped with a detector at 90° scattering mode at 20 °C. The zeta potential of the NPs was measured in 1×10^{-3} M potassium chloride solution with a Zeta Nanosizer (Malvern Instruments, U.K.) at 20°C. Scanning electron microscopy (SEM) images were recorded by using a field emission microscope (LEO (Zeiss) 1530 Gemini, Oberkochen, Germany) working at an accelerating voltage of 170 V. Generally, the samples were prepared by diluting the NP dispersion in demineralized water to about 0.01% solid content; then one droplet of the sample was placed onto silica wafers and dried under ambient conditions over night. Surface tension measurements were performed by Dr. Grit Baier in a DuNouy ring method with a DCAT21 tensiometer (Dataphysics) at 25 °C.

3.5.2.2 MTS assay for determination of cell viability

All cytotoxicity evaluation was performed by Dr. Stephanie Tomcin. The HeLa cells were kept in Dulbecco's Modified Eagle Medium (DMEM) without Phenolred supplemented with 10 vol% fetal calf serum (FCS), 100 units penicillin and 1 vol% GlutaMAX™ (all from Invitrogen, Germany). Cells were grown in a humidified incubator at 37 °C and 5% CO₂. A MTS assay was performed to show if the synthesized nanoparticles have a toxic influence on HeLa cells. Therefore cells were detached using 0.5% trypsin (Gibco, Germany) and seeded out in 96 well plates (Becton Dickinson, USA) at a density of 0.8×10^5 cells/well. After re-adhesion overnight cells were incubated with each nanoparticle at a concentration of 75, 150, 45, 600, 750 and 1000 mg mL⁻¹ for 24 h in a humidified incubation at 37 °C and 5% CO₂. After incubation time the MTS assay was done in medium following the manufacturer's protocol of CellTiter 961 Aqueous One Solution Cell Proliferation Assay (Promega, USA). MTS (3-(4,5-dimethylthiazol-2-yl)-5-(3-carboxymethoxyphenyl)-2-(4-sulfophenyl)-2H-tetrazolium, inner salt) is reduced NADH-dependent by cells to a colored formazan product which is soluble in culture medium. The concentration of formazan (directly proportional to the number of live cells) is photometrically detectable as absorption at 490 nm. The absorption signal was obtained by using a Plate Reader Infinite M1000 (Tecan, Germany).

3.5.3 Results and discussion

After the synthesis, the nanoparticles were purified by dialysis against deionized water. Table 3.5 – 1 summarizes the results obtained for the size and size distribution, and for the zeta potential.

Table 3.5 – 1 Mean diameter, standard deviation and zeta-potential of PS, PLLA and PP nanoparticles synthesized via miniemulsion strategy (Reproduced from ³⁰⁰, © 2014 WILEY-VCH Verlag GmbH & Co. KGaA, Weinheim).

Sample	Mean diameter (nm)	Standard deviation (%)	Zeta potential – pH 7 (mW)
PS-SDS-72 (control)	100	11	-55
PS-SLS-72	100	11	-52
PS-SLS-108	90	10	-55
PS-SLS-144	85	9	-53
PS-SLG-72	95	3	-51
PS-SLG-108	90	16	-47
PS-SLG-144	85	17	-50
PS-SMS-72	92	17	-59
PS-SMS-108	85	11	-54
PS-SMS-144	80	12	-57
PLLA-SDS-72 (control)	90	30	-49
PLLA-SLS-72	130	26	-58
PLLA-SLS-108	120	30	-52
PLLA-SLS-144	100	30	-58
PLLA-SLG-72	190	28	-57
PLLA-SLG-108	180	28	-65
PLLA-SLG-144	140	30	-47
PLLA-SMS-72	160	18	-50
PLLA-SMS-108	140	30	-57
PLLA-SMS-144	125	30	-55
PP-SDS-72 (control)	130	13	-48
PP-SLS-72	135	24	-53
PP-SLS-108	120	20	-49
PP-SLS-144	115	20	-47
PP-SLG-72	190	23	-53

Stabilization of nanoparticles using “green” amino-acid based surfactants

PP-SLG-108	200	20	-59
PP-SLG-144	180	27	-59
PP-SMS-72	170	29	-56
PP-SMS-108	150	17	-52
PP-SMS-144	130	19	-60

The data in Table 3.5 – 1 show that all investigated surfactants and polymers can be used to produce stable nanoparticles dispersions using the miniemulsion technique. As expected, the increase of the surfactant concentration leads to a decrease in the mean diameter of the nanoparticles. For all PS nanoparticles, narrow size distributions were obtained, independently of the surfactant used. These dispersions also presented smaller mean diameter than what was obtained for PLLA and PP nanoparticles. The use of the miniemulsion/solvent-evaporation for the preparation of nanoparticles from PLLA and PP resulted and broader size distribution in comparison to the one obtained by miniemulsion radical polymerization in the synthesis of PS nanoparticles. In general, the use of amino-acid based surfactants resulted in bigger nanoparticles in comparison to SDS at the same surfactant concentration. The zeta-potential data reveals similar range of zeta-potential for all the systems, around -50 mW, which represents a very good colloidal stability for all the systems.

Figure 3.5 – 2 shows the surface tension measured for the surfactant/water solution and the PS, PLLA and PP nanoparticles stabilized with 72 mg of surfactant. The surface tension values measured are a reflex of the amount of surfactant necessary to stabilize the droplets and final particles during miniemulsion synthesis of the nanoparticles. Lower surface tension values indicate that less surfactant is at the particle surface, and therefore more surfactant is in the water phase resulting in lower surface tension values for the dispersion. The surface tension for PS nanoparticles stabilized with SDS was the same observed for the amino acid based surfactants. For PLLA nanoparticles, slightly higher values of surface tension were obtained with SDS as surfactant in comparison to the same nanoparticles with amino-acid based surfactants, which means that less amounts of surfactant are necessary to stabilize the droplets in this system. For the PP nanoparticles, higher values of surface tension were observed for the amino-acids based surfactant in comparison to SDS, especially for SLG. In pure water, the amino-acid based surfactants showed slightly lower surface tensions in comparison to SDS.

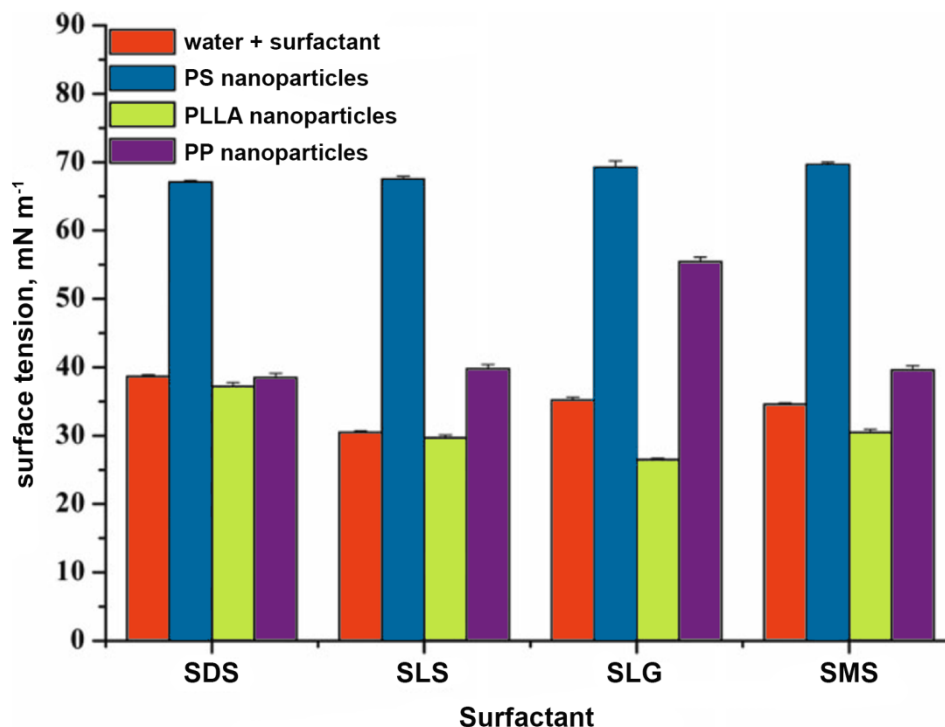
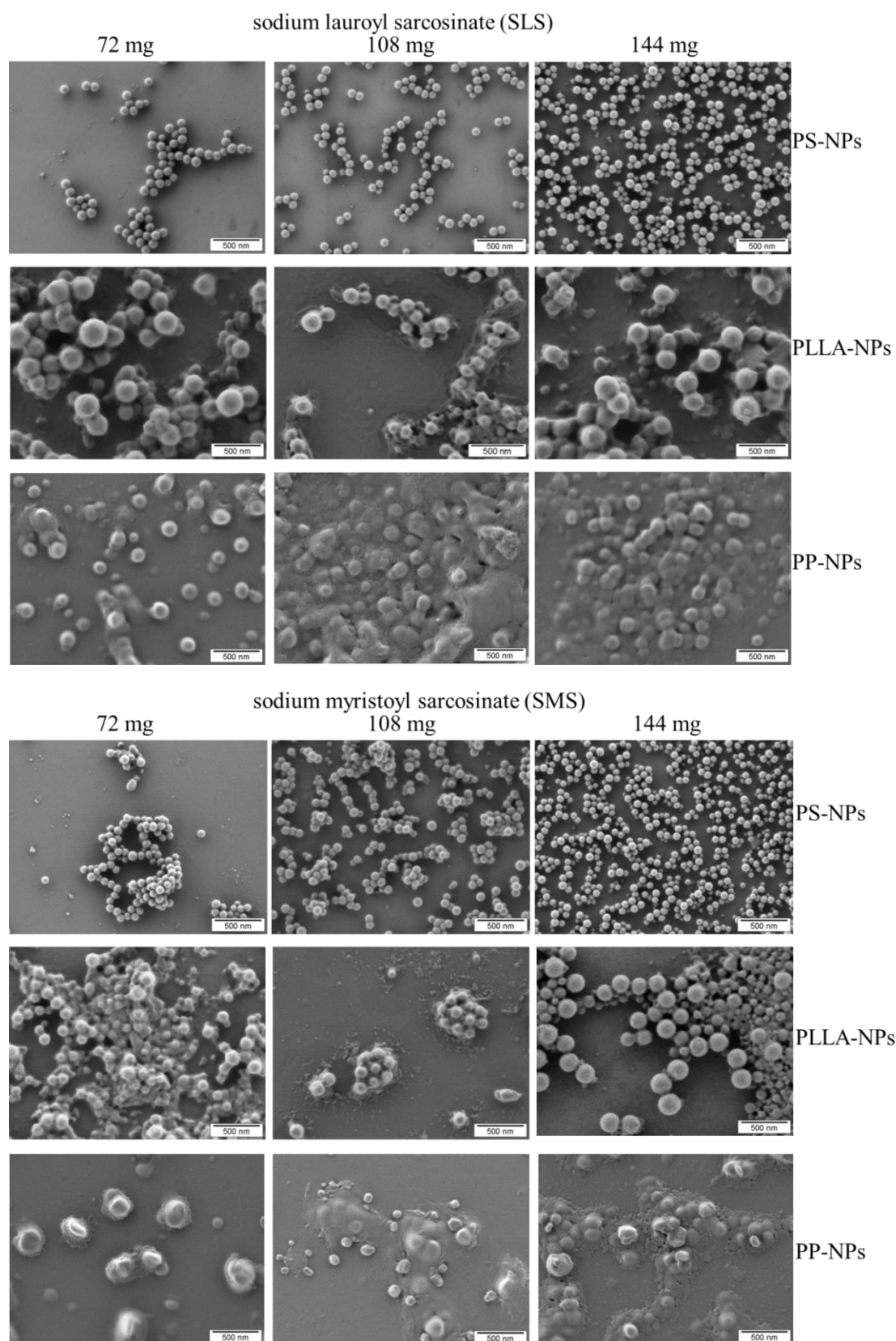


Fig. 3.5 – 2 Surface tension measured for the surfactant/water solution and the PS, PLLA and PP nanoparticles stabilized with 72 mg of surfactant in 24 g of water (3 mg mL^{-1}). The measurements were performed by Dr. Grit Baier (Reproduced from ³⁰⁰, © 2014 WILEY-VCH Verlag GmbH & Co. KGaA, Weinheim).

The morphological characterization of the nanoparticles was done by scanning electron microscopy (SEM) and the results are depicted in Figure 3.5 – 3. PS and PLLA nanoparticles resulted in spherical and low polydisperse distribution, independently of the surfactant used. Due to the low melting point and crystallinity, PP nanoparticles do not show a perfect spherical morphology. Larger size distribution and sometimes film formation was observed for this system.



(continue in the next page)

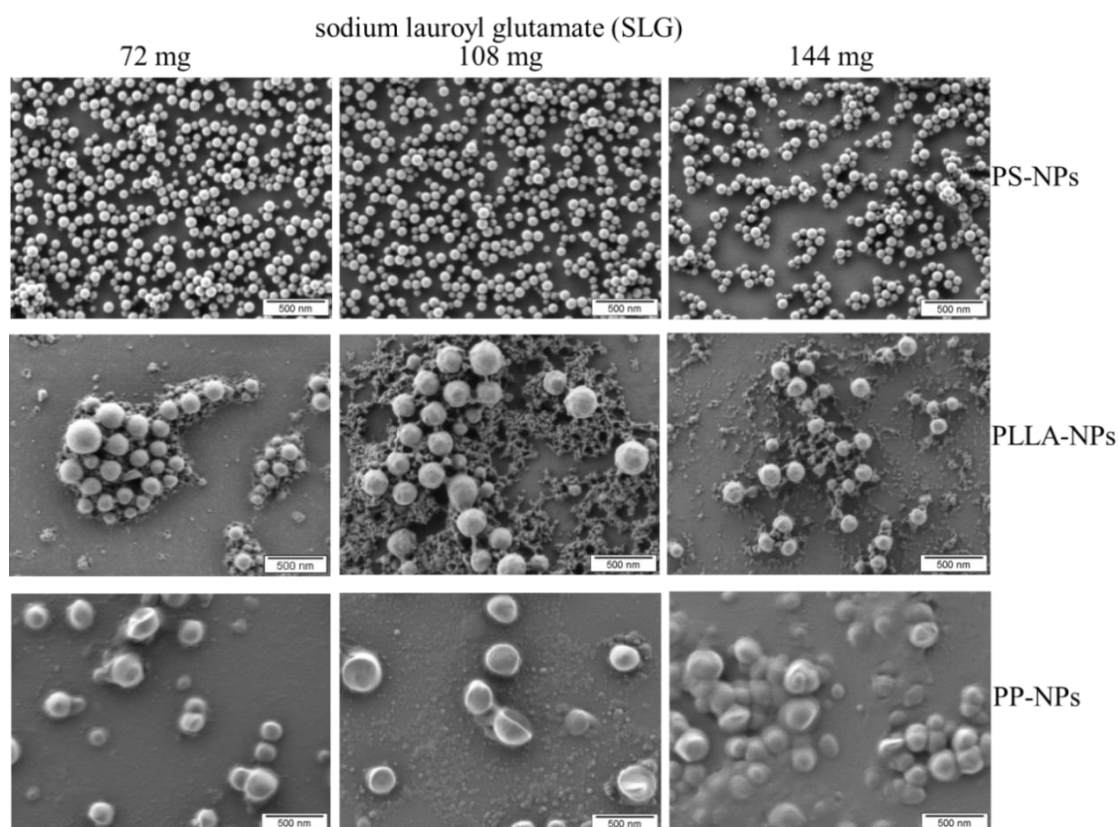


Fig. 3.5 – 3 SEM micrographies of PS, PLLA and PP nanoparticles stabilized with different amounts of SLS, SLG and SMS (Reproduced from ³⁰⁰, © 2014 WILEY-VCH Verlag GmbH & Co. KGaA, Weinheim).

In order to ensure the biocompatibility of the nanoparticles stabilized with amino-acid based surfactants, MTS assays were performed in PLLA and PP nanoparticles with each of the four surfactants. Figure 3.5 – 4 shows the influence of the nanoparticles prepared with 3 mg mL^{-1} surfactant on HeLa cells after 24 h incubation time. PLLA nanoparticles stabilized with SLS and SLG showed no toxicity for concentrations up to $1000 \text{ }\mu\text{g mL}^{-1}$. Significant toxicity was observed with SMS-stabilized nanoparticles at $600 \text{ }\mu\text{g mL}^{-1}$, which is still far away to the usual concentration administered in biomedical applications. PP nanoparticles presented even lower toxicity, demonstrating the high potential of these poly(phosphoester) nanoparticles in the development of biomedical strategies.

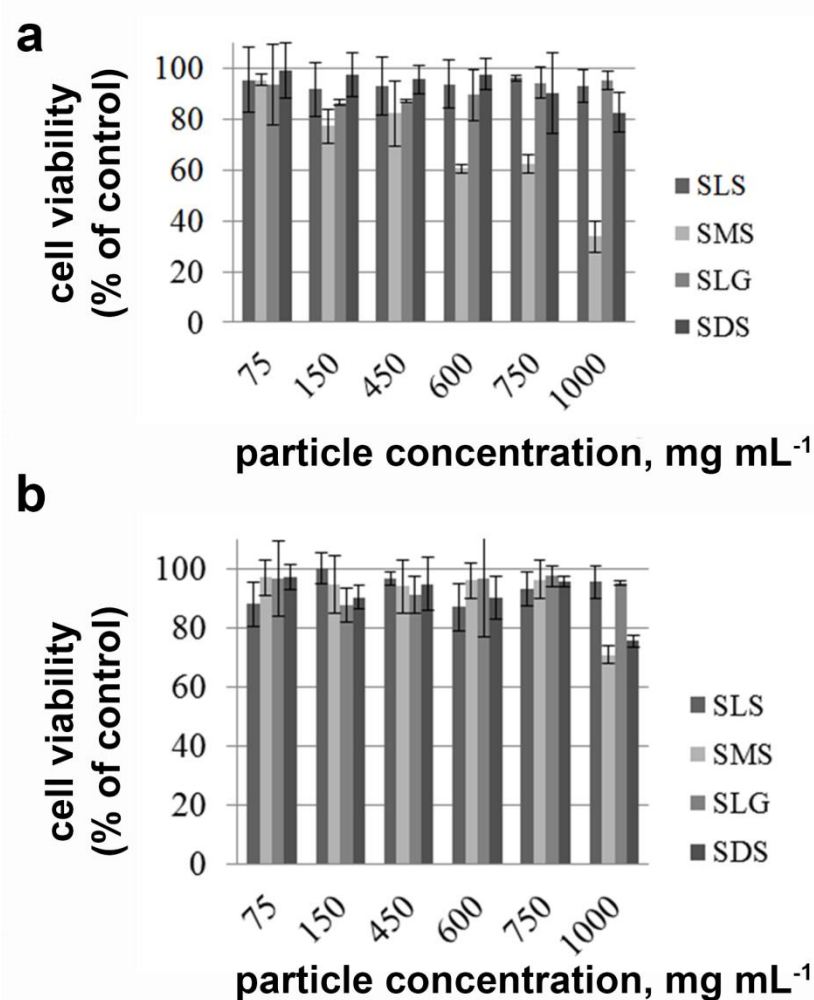


Fig. 3.5 – 4 MTS assay (measured by Dr. Stephanie Tomcin) of (a) PLLA and (b) PP nanoparticles stabilized with the amino-acid based surfactants SLS, SMS and SLG, in relation to the control nanoparticles stabilized with SDS (all samples prepared with 3 mg mL⁻¹ surfactant) (Reproduced from ³⁰⁰, © 2014 WILEY-VCH Verlag GmbH & Co. KGaA, Weinheim).

3.5.4 Conclusion

In conclusion, these “green” surfactants are environmentally friendly, biodegradable and capable to form stable non-toxic nanoparticles with different classes of polymers through the miniemulsion strategy. The amino-acid based surfactants are an effective alternative for substitution of the classical surfactant SDS and in combination with the potential of the polyphosphoesters nanoparticles can provide less toxic and more effective biomedical therapies.

4 Outlook

Polyphosphoester colloids have been proven in this work as an efficient tool for the development of diverse applications. From biomedical, especially involving strategies targeting bone diseases and bone tissue engineering, to optical and energetic applications, with the good protection provided to upconversion systems.

For biomedical applications, the tailorability of polyphosphoesters allows further steps in the development of new polymeric structures with higher interaction and different mechanical properties, for use mainly in the development of new platforms for tissue engineering. The knowledge produced in this work about the mechanism involving the control of the interaction between calcium ions and PPEs is vital for the development of new materials with potential to act at the same time in the therapy and replacement/growing of bone areas affected by different diseases. The colloids prepared in this work can, in cooperation with the calcium cement, already work as an efficient medium for the treatment of patients affected by bone cancer and other bone diseases. Further *in vivo* studies are still necessary to verify the availability of this strategy.

The full PPE upconversion colloids produced in this thesis showed higher efficiency of the upconversion signal in relation to phosphorescence in comparison to systems containing other standard materials as PMMA as the shell. In addition, the materials produced with the phosphoester core, both the organophosphates and hyperbranched polyphosphoester, were capable to show upconversion signal in the presence of oxygen during short periods of time, even though in a smaller scale in comparison to results obtained in bulk phase. The systems also presented an interesting and reproducible dependence of the efficiency according to the temperature, which seems to be related to the melting point of the shell and mobility of the dyes. Such properties make these systems potential candidates for the development of oxygen and temperature sensors, for both *in vivo* and external applications. The production of an almost transparent miniemulsion capable to produce upconversion photons is also of high interest and the use of the non-linear properties of the TTA upconversion phenomenon together with such characteristic can be a valuable option for the development of 3D upconversion displays. The versatility of polyphosphoesters also provides opportunities for the development of light responsive polymeric shells, which could produce special chemical responses using the photons produced internally by the upconversion phenomenon.

This work also explored the properties proportionated by the surface area reduction in miniemulsion systems, demonstrating how the interface can be used as a shortcut for the production of new molecules and influence both the kinetics and structural properties of polymers. Such information is of essential importance for the development of new polymeric nanocapsules and amphiphilic molecules, including new polyphosphoester nanocapsules for potential application in drug delivery systems.

5 Appendix

5.1 Curriculum Vitae

Name: Evandro Mendes Alexandrino

Birthday: 09.07.1986 in Osasco—São Paulo (Brazil)

Nationality: Brazil

Professional Experience

06/2015 - today	Ultima (Deutschland) GmbH as Project Chemist
06/2008 - 03/2010	SABIC Innovative Plastics (Campinas—São Paulo, Brazil) as Technology Trainee

Education

05/2012 – 07/2015	Max Planck Institute for Polymer Research (Mainz - Germany) PhD Thesis
03/2010 - 02/2012	University of Campinas - UNICAMP (São Paulo - Brazil) Master in Physical Chemistry Dissertation title: “Polymer composites of poly(ether imide)/polyaniline: preparation and characterization”
03/2004 - 12/2009	University of Campinas - UNICAMP (São Paulo - Brazil) Bachelor in Chemistry with Technological Attributions
03/2001 - 12/2003	ETE Guaracy Silveira (São Paulo - Brazil) High School
03/2002 - 06/2003	ETE Guaracy Silveira (São Paulo - Brazil) Electronics Technician

Publications List

Papers - Alexandrino, E. M.; Buchold, P.; Wagner, M.; Fuchs, A.; Kreyes, A.; Weiss, C.; Landfester, K.; Wurm, F. R.; A molecular “screw-clamp”: accelerating click reactions in miniemulsions, *ChemComm*; 2014; 10495-10498.

- **Alexandrino, E. M.**; Ritz, S., Baier, G.; Marsico, F.; Mailänder, V.; Landfester, K.; Wurm, F. R.; Paclitaxel-loaded polyphosphate nanoparticles: a potential strategy for bone cancer treatment, *J. Mater. Chem. B*; 2014, 2, 1298 - 1306. (featured on the cover page)
- **Alexandrino, E. M.**; Conceição, T. F.; Felisberti, M. I. *J. App. Polym. Sci.*; 2014, 16, 131, 40619.
- Baier, G.; Baki, A.; Tomcin, S; Mailänder, V.; **Alexandrino, E.**; Wurm, F.; Landfester, K.; Stabilization of nanoparticles synthesized by miniemulsion polymerization using “green” amino-acid based surfactants, *Macromol. Symp.*; 2014, 337, 9 -17.
- Steinbach, T.; **Alexandrino, E. M.**; Wurm, F. *Polym. Chem.*, 2013, 4, 3800 - 3806.
- Steinbach, T.; **Alexandrino, E. M.**; Wahlen, C.; Landfester, K.; Wurm, F. *Macromolecules*; 2014, 47, 4884-4893.

Conferences

- 10th Zsigmondy Colloquium, 2014, Konstanz - Germany (**Poster**).
- 245th ACS Spring Meeting, 2013, New Orleans - USA (**Poster**). **Honored with an “1st place Outstanding Research Poster Award”.**
- Makromolekulares Kolloquium Freiburg, 2013, Freiburg - Germany (**Poster**).
- European Polymer Federation Conference, 2011, Granada - Spain (**Poster**)
- 8th Conference on Solid State Chemistry, 2008, Bratislava - Slovak (**Poster**)

5.2 Acknowledgments

A thesis is the result of intensive work summed to the great support of diverse persons and institutions.

I would like to firstly thank the Max Planck Society for the financial support for the development of this work and Professor Dr. K. Landfester for giving me the opportunity to be part of her research group in the last three years. I also would like to thank the professors Dr. M. Maskos and R. Zentel for their time and interest to be part of the doctoral commission of this work.

I would thank Dr. F. R. Wurm for all the support and scientific discussions in the last three years and for betting on taking me as one of his first students. I also would like to thank Dr. M. Wagner, which was more than an extreme competent colleague but a mentor and a friend for me.

To all the technicians in the Max Planck Institute for Polymer Research a special thank you. Without their help, patience and quality this work would not have been possible. Thank you for the wonderful conversations and for the help improving my German skills.

These last 3 years will be unforgettable for me. I got to know many wonderful persons, from different cultures and corners in the world. And from each I could learn at least one invaluable lesson. So first of all, thanks to all my colleagues at the AK Landfester which have made part of this last 3 years for the barbecues, good work environment and especially for the Sommerfest Pokal. Scientifically I would like to thank especially K. Weber, Dr. F. Marsico, Dr. S. Ritz and Dr. D. Busko for their priceless collaborations. I would like to thank also the GOALden Girls for the delightful time together. It was an honour to play for you girls. And between so many colleagues some become friends for a life. I would like to thank especially Dr. C. Wohnhaas, Dr. M. Bernhardt and his family, Dr. B. Freisinger, Dr. K. Schuller, Dr. F. R. Steinmacher, Dr. L. Lv and Dr. F. Kaveh and future doctors K. Piradashvili, B. Ma and D. Estupiñan for your friendship in good and bad times. You really mean a lot to me.

For last but sure not least, I would like to thank my family. Without my family I could never have reached this point of my life. Without the teaching of my parents I am no one. Para a minha família simplesmente obrigado por tudo, sem vocês isso tudo teria sido simplesmente impossível.

6 References

1. E. M. Alexandrino, S. Ritz, F. Marsico, G. Baier, V. Mailander, K. Landfester and F. R. Wurm, *Journal of Materials Chemistry B*, 2014, 2, 1298-1306.
2. T. Steinbach, E. M. Alexandrino, C. Wahlen, K. Landfester and F. R. Wurm, *Macromolecules*, 2014.
3. T. Steinbach, E. Alexandrino and F. Wurm, *Polymer Chemistry*, 2013.
4. E. M. Alexandrino, P. Buchold, M. Wagner, A. Fuchs, A. Kreyes, C. K. Weiss, K. Landfester and F. R. Wurm, *Chemical Communications*, 2014, 50, 10495-10498.
5. A. D. McNaught, A. Wilkinson, I. U. o. Pure and A. Chemistry, *Compendium of Chemical Terminology: IUPAC Recommendations*, Blackwell Science, 1997.
6. R. Cowen and L. Critchley, *Skimming Stones: and other ways of being in the wild*, Hodder & Stoughton, 2012.
7. F. Westheimer, *Science*, 1987, 235, 1173-1178.
8. S. C. L. Kamerlin, P. K. Sharma, R. B. Prasad and A. Warshel, *Q. Rev. Biophys.*, 2013, 46, 1-132.
9. K. N. Weilbaecher, T. A. Guise and L. K. McCauley, *Nat. Rev. Cancer*, 2011, 11, 411-425.
10. B. T. Luk and L. Zhang, *ACS Applied Materials & Interfaces*, 2014, 6, 21859-21873.
11. T. Steinbach, S. Ritz and F. R. Wurm, *ACS Macro Letters*, 2014, 3, 244-248.
12. T. Steinbach and F. R. Wurm, *Angew. Chem.*, 2015, n/a-n/a.
13. F. Marsico, Max Planck Institute for Polymer Research, 2014.
14. F. Marsico, A. Turshatov, R. Peköz, Y. Avlasevich, M. Wagner, K. Weber, D. Donadio, K. Landfester, S. Balushev and F. R. Wurm, *Journal of the American Chemical Society*, 2014, 136, 11057-11064.
15. F. Marsico, A. Turshatov, K. Weber and F. R. Wurm, *Org. Lett.*, 2013, 15, 3844-3847.
16. F. Marsico, M. Wagner, K. Landfester and F. R. Wurm, *Macromolecules*, 2012, 45, 8511-8518.
17. S. Slomkowski, V. Alemán José, G. Gilbert Robert, M. Hess, K. Horie, G. Jones Richard, P. Kubisa, I. Meisel, W. Mormann, S. Penczek and F. T. Stepto Robert, in *Pure Appl. Chem.*, 2011, vol. 83, p. 2229.
18. M. Antonietti and K. Landfester, *Prog. Polym. Sci.*, 2002, 27, 689-757.
19. D. Crespy and K. Landfester, *Beilstein J. Org. Chem.*, 2010, 6, 1132-1148.
20. S. Abbas, K. Hayat, E. Karangwa, M. Bashari and X. Zhang, *Food Eng Rev*, 2013, 5, 139-157.
21. B. Abismaïl, J. P. Canselier, A. M. Wilhelm, H. Delmas and C. Gourdon, *Ultrason. Sonochem.*, 1999, 6, 75-83.
22. M. Ashokkumar, *Ultrason. Sonochem.*, 2011, 18, 864-872.
23. M. K. Li and H. S. Fogler, *J. Fluid Mech.*, 1978, 88, 499-511.
24. M. K. Li and H. S. Fogler, *J. Fluid Mech.*, 1978, 88, 513-528.
25. D. H. Sharp, *Physica D: Nonlinear Phenomena*, 1984, 12, 3-18.
26. M. Sivakumar, S. Y. Tang and K. W. Tan, *Ultrason. Sonochem.*, 2014, 21, 2069-2083.
27. H.-J. Butt, K. Graf and M. Kappl, in *Physics and Chemistry of Interfaces*, Wiley-VCH Verlag GmbH & Co. KGaA, 2004, pp. 4-25.
28. G. W. B. Rton and C. P. O. F. Rrell, *J. Elastomers Plast.*, 1977, 9, 94-101.
29. R. H. Staff, K. Landfester and D. Crespy, in *Hierarchical Macromolecular Structures: 60 Years after the Staudinger Nobel Prize li*, ed. V. Percec, 2013, vol. 262, pp. 329-344.
30. N. Anton, J.-P. Benoit and P. Saulnier, *J. Control. Release*, 2008, 128, 185-199.

31. R. H. Staff, D. Schaeffel, A. Turshatov, D. Donadio, H.-J. Butt, K. Landfester, K. Koynov and D. Crespy, *Small*, 2013, 9, 3514-3522.
32. G. Baier, A. Cavallaro, K. Friedemann, B. Mueller, G. Glasser, K. Vasilev and K. Landfester, *Nanomedicine-Nanotechnology Biology and Medicine*, 2014, 10, 131-139.
33. A. Ethirajan, A. Musyanovych, A. Chuvilin and K. Landfester, *Macromolecular Chemistry and Physics*, 2011, 212, 915-925.
34. A. Musyanovych, J. Schmitz-Wienke, V. Mailaender, P. Walther and K. Landfester, *Macromol. Biosci.*, 2008, 8, 127-139.
35. T. Kietzke, D. Neher, K. Landfester, R. Montenegro, R. Guntner and U. Scherf, *Nat Mater*, 2003, 2, 408-412.
36. R. H. Staff, P. Rupper, I. Lieberwirth, K. Landfester and D. Crespy, *Soft Matter*, 2011, 7, 10219-10226.
37. S. Torza and S. G. Mason, *Journal of Colloid and Interface Science*, 1970, 33, 67-83.
38. T. Trongsatitkul and B. M. Budhlall, *Langmuir*, 2011, 27, 13468-13480.
39. R. H. Staff, I. Lieberwirth, K. Landfester and D. Crespy, *Macromolecular Chemistry and Physics*, 2012, 213, 351-358.
40. F. S. Romanski, J. S. Winkler, R. C. Riccobene and M. S. Tomassone, *Langmuir*, 2012, 28, 3756-3765.
41. Y.-C. Chen, V. Dimonie and M. S. El-Aasser, *Journal of Applied Polymer Science*, 1992, 46, 691-706.
42. M. R. Muscato and D. C. Sundberg, *J. Polym. Sci., Part B: Polym. Phys.*, 1991, 29, 1021-1024.
43. Y. Zhao, J. Fickert, K. Landfester and D. Crespy, *Small*, 2012, 8, 2954-2958.
44. J. Fickert, C. Wohnhaas, A. Turshatov, K. Landfester and D. Crespy, *Macromolecules*, 2013, 46, 573-579.
45. Y. Zhao, D. Döhler, L.-P. Lv, W. H. Binder, K. Landfester and D. Crespy, *Macromolecular Chemistry and Physics*, 2014, 215, 198-204.
46. C. Wohnhaas, V. Mailänder, M. Dröge, M. A. Filatov, D. Busko, Y. Avlasevich, S. Balushev, T. Miteva, K. Landfester and A. Turshatov, *Macromol. Biosci.*, 2013, 13, 1422-1430.
47. C. Schotten, *Berichte der deutschen chemischen Gesellschaft*, 1884, 17, 2544-2547.
48. E. Baumann, *Berichte der deutschen chemischen Gesellschaft*, 1886, 19, 3218-3222.
49. H. Watarai, N. Teramae and T. Sawada, *Interfacial Nanochemistry: Molecular Science and Engineering at Liquid-Liquid Interfaces*, Springer US, 2006.
50. A. G. Volkov, *Liquid Interfaces In Chemical, Biological And Pharmaceutical Applications*, Taylor & Francis, 2001.
51. K. Holmberg, *European Journal of Organic Chemistry*, 2007, 2007, 731-742.
52. D. J. McClements, *Soft Matter*, 2012, 8, 1719-1729.
53. T. M. S. Chang, *Science*, 1964, 146, 524-&.
54. D. Crespy, M. Stark, C. Hoffmann-Richter, U. Ziener and K. Landfester, *Macromolecules*, 2007, 40, 3122-3135.
55. F. Gaudin and N. Sintès-Zydowicz, *Colloids Surf. Physicochem. Eng. Aspects*, 2011, 384, 698-712.
56. Q. Zhang, Y. Shi, X. Zhan and F. Chen, *Colloids Surf. Physicochem. Eng. Aspects*, 2012, 393, 17-26.
57. S. Taheri, G. Baier, P. Majewski, M. Barton, R. Forch, K. Landfester and K. Vasilev, *Journal of Materials Chemistry B*, 2014, 2, 1838-1845.
58. D. Yiamsawas, G. Baier, E. Thines, K. Landfester and F. R. Wurm, *RSC Advances*, 2014, 4, 11661-11663.

59. K. Piradashvili, M. Fichter, K. Mohr, S. Gehring, F. R. Wurm and K. Landfester, *Biomacromolecules*, 2015, 16, 815-821.
60. J. Fickert, P. Rupper, R. Graf, K. Landfester and D. Crespy, *J. Mater. Chem.*, 2012, 22, 2286-2291.
61. G. Baier, A. Musyanovych, M. Dass, S. Theisinger and K. Landfester, *Biomacromolecules*, 2010, 11, 960-968.
62. H. Freichels, M. Wagner, P. Okwieka, R. G. Meyer, V. Mailaender, K. Landfester and A. Musyanovych, *Journal of Materials Chemistry B*, 2013, 1, 4338-4348.
63. E.-M. Rosenbauer, M. Wagner, A. Musyanovych and K. Landfester, *Macromolecules*, 2010, 43, 5083-5093.
64. L. Spornath and S. Magdassi, *Polym. Adv. Technol.*, 2011, 22, 2469-2473.
65. B. Kang, P. Okwieka, S. Schöttler, S. Winzen, J. Langhanki, K. Mohr, T. Opatz, V. Mailänder, K. Landfester and F. R. Wurm, *Angewandte Chemie International Edition*, 2015, n/a-n/a.
66. R. Roux, L. Sallet, P. Alcouffe, S. Chambert, N. Sintès-Zydowicz, E. Fleury and J. Bernard, *ACS Macro Letters*, 2012, 1, 1074-1078.
67. B. Cao, Y. Zheng, T. Xi, C. Zhang, W. Song, K. Burugapalli, H. Yang and Y. Ma, *Biomed. Microdevices*, 2012, 14, 709-720.
68. J. M. Siebert, G. Baier, A. Musyanovych and K. Landfester, *Chemical Communications*, 2012, 48, 5470-5472.
69. U. Paiphansiri, G. Baier, A. Kreyes, D. Yiamsawas, K. Koynov, A. Musyanovych and K. Landfester, *Macromolecular Chemistry and Physics*, 2014, 215, 2457-2462.
70. C.-K. Chen, Q. Wang, C. H. Jones, Y. Yu, H. Zhang, W.-C. Law, C. K. Lai, Q. Zeng, P. N. Prasad, B. A. Pfeifer and C. Cheng, *Langmuir*, 2014, 30, 4111-4119.
71. K. Malzahn, F. Marsico, K. Koynov, K. Landfester, C. K. Weiss and F. R. Wurm, *ACS Macro Letters*, 2014, 3, 40-43.
72. P. B. Cardoso, A. Musyanovych, K. Landfester, C. Sayer, P. H. H. de Araújo and M. A. R. Meier, *J. Polym. Sci., Part A: Polym. Chem.*, 2014, 52, 1300-1305.
73. D. Quemener, V. Heroguez and Y. Gnanou, *Macromolecules*, 2005, 38, 7977-7982.
74. D. Quemener, V. Heroguez and Y. Gnanou, *Journal of Polymer Science Part a-Polymer Chemistry*, 2006, 44, 2784-2793.
75. S. V. Kostjuk and F. Ganachaud, *Accounts of Chemical Research*, 2010, 43, 357-367.
76. S. Jiang, T. Qiu, L. He, J. Tan and X. Li, *Colloid. Polym. Sci.*, 2013, 291, 1135-1142.
77. S. Cauvin, A. Sadoun, R. Dos Santos, J. Belleney, F. Ganachaud and P. Hémerly, *Macromolecules*, 2002, 35, 7919-7927.
78. S. Cauvin, F. Ganachaud, V. Touchard, P. Hémerly and F. Leising, *Macromolecules*, 2004, 37, 3214-3221.
79. S. V. Kostjuk, A. V. Radchenko and F. Ganachaud, *Macromolecules*, 2007, 40, 482-490.
80. V. Touchard, C. Graillat, C. Boisson, F. D'Agosto and R. Spitz, *Macromolecules*, 2004, 37, 3136-3142.
81. S. Cauvin, F. Ganachaud, M. Moreau and P. Hémerly, *Chem. Commun.*, 2005, 2713-2715.
82. M. Barrère, C. Maitre, M. A. Dourges and P. Hémerly, *Macromolecules*, 2001, 34, 7276-7280.
83. A. De Gunzbourg, J.-C. Favier and P. Hémerly, *Polym. Int.*, 1994, 35, 179-188.
84. C. Maitre, F. Ganachaud, O. Ferreira, J. F. Lutz, Y. Paintoux and P. Hémerly, *Macromolecules*, 2000, 33, 7730-7736.
85. A. Musyanovych and K. Landfester, in *Surface and Interfacial Forces – From Fundamentals to Applications*, eds. G. Auernhammer, H.-J. Butt and D. Vollmer, Springer Berlin Heidelberg, 2008, vol. 134, pp. 120-127.

86. N. Altinbas, C. Fehmer, A. Terheiden, A. Shukla, H. Rehage and C. Mayer, *J. Microencapsulation*, 2006, 23, 567-581.
87. C. Limouzin, A. Caviggia, F. Ganachaud and P. Hemery, *Macromolecules*, 2003, 36, 667-674.
88. M. Barrère, F. Ganachaud, D. Bendejacq, M. A. Dourges, C. Maitre and P. Hémerly, *Polymer*, 2001, 42, 7239-7246.
89. D. Crespy and K. Landfester, *Macromolecules*, 2005, 38, 6882-6887.
90. M. Ruppert, K. Landfester and U. Ziener, *J. Polym. Sci., Part A: Polym. Chem.*, 2010, 48, 4929-4937.
91. J. Nicolas, B. Charleux, O. Guerret and S. Magnet, *Macromolecules*, 2005, 38, 9963-9973.
92. J. P. Rao and K. E. Geckeler, *Progress in Polymer Science*, 2011, 36, 887-913.
93. H. Fischer, *Chemical Reviews*, 2001, 101, 3581-3610.
94. P. B. Zetterlund, J. Wakamatsu and M. Okubo, *Macromolecules*, 2009, 42, 6944-6952.
95. P. B. Zetterlund, *Polymer Chemistry*, 2011, 2, 534-549.
96. M. J. Monteiro, *Macromolecules*, 2010, 43, 1159-1168.
97. B. Charleux, F. D'Agosto and G. Delaître, in *Hybrid Latex Particles*, eds. A. M. van Herk and K. Landfester, Springer Berlin Heidelberg, 2010, vol. 233, pp. 125-183.
98. M. E. Thomson and M. F. Cunningham, *Macromolecules*, 2010, 43, 2772-2779.
99. B. Charleux, M. J. Monteiro and H. Heuts, *Chemistry and Technology of Emulsion Polymerisation, Second Edition*, 2013, 105-143.
100. Y. Guo, J. Liu and P. B. Zetterlund, *Macromolecules*, 2010, 43, 5914-5916.
101. Y. Guo, V. L. Teo, S. S. Ting and P. B. Zetterlund, *Polym. J.*, 2012, 44, 375-381.
102. Y. Guo and P. B. Zetterlund, *ACS Macro Letters*, 2012, 1, 748-752.
103. K. Matyjaszewski and N. V. Tsarevsky, *Journal of the American Chemical Society*, 2014, 136, 6513-6533.
104. M. Butusov and A. Jernelöv, *Phosphorus: An Element that could have been called Lucifer*, Springer, 2013.
105. Y. C. Wang, Y. Y. Yuan, J. Z. Du, X. Z. Yang and J. Wang, *Macromol. Biosci.*, 2009, 9, 1154-1164.
106. T. W. Steinbach, Frederik R., *Angewandte Chemie International Edition*
- 2015.
107. *United States Pat.*, 1936.
108. C. W. E, Google Patents, 1952.
109. S. Banerjee, S. K. Palit and S. Maiti, *J. Polym. Sci., Part A: Polym. Chem.*, 1994, 32, 219-227.
110. G. B. Quistad, N. Zhang, S. E. Sparks and J. E. Casida, *Chem. Res. Toxicol.*, 2000, 13, 652-657.
111. S. Penczek, J. Pretula, P. Kubisa, K. Kaluzynski and R. Szymanski, *Prog. Polym. Sci.*
112. K. Kishore, P. Kannan and K. Iyanar, *J. Polym. Sci., Part A: Polym. Chem.*, 1991, 29, 1039-1044.
113. S. Monge and G. David, *Phosphorus-Based Polymers: From Synthesis to Applications*, Royal Society of Chemistry, 2014.
114. S. Penczek, *Models of Biopolymers By Ring-Opening Polymerization*, Taylor & Francis, 1989.
115. S. Penczek, J. B. Pretula, K. Kaluzynski and G. Lapienis, *Isr. J. Chem.*, 2012, 52, 306-319.
116. J. Wen and R.-X. Zhuo, *Macromolecular Rapid Communications*, 1998, 19, 641-642.

117. K. Oussadi, V. Montembault, M. Belbachir and L. Fontaine, *Journal of Applied Polymer Science*, 2011, 122, 891-897.
118. W. Vogt and R. Pflüger, *Die Makromolekulare Chemie*, 1975, 1, 97-110.
119. Y. Iwasaki, T. Kawakita and S.-i. Yusa, *Chem. Lett.*, 2009, 38, 1054-1055.
120. S. Zhang, A. Li, J. Zou, L. Y. Lin and K. L. Wooley, *ACS macro letters*, 2012, 1, 328-333.
121. S. Zhang, H. Wang, Y. Shen, F. Zhang, K. Seetho, J. Zou, J.-S. A. Taylor, A. P. Dove and K. L. Wooley, *Macromolecules*, 2013, 46, 5141-5149.
122. G. Lapienis and S. Penczek, *Macromolecules*, 1974, 7, 166-174.
123. G. Lapienis and S. Penczek, *Macromolecules*, 1977, 10, 1301-1306.
124. H. Yasuda, M. Sumitani and A. Nakamura, *Macromolecules*, 1981, 14, 458-460.
125. S. Penczek, K. Kaluzynski and J. Pretula, *Journal of Applied Polymer Science*, 2007, 105, 246-254.
126. M. Steinmann, J. Markwart and F. R. Wurm, *Macromolecules*, 2014, 47, 8506-8513.
127. T. Steinbach, C. Wahlen and F. R. Wurm, *Polymer Chemistry*, 2015, 6, 1192-1202.
128. K. Tauber, F. Marsico, F. R. Wurm and B. Schartel, *Polymer Chemistry*, 2014, 5, 7042-7053.
129. K. Kazanskii, V. Kuznetsova, J. Pretula and S. Penczek, *Polym. Gels Networks*, 1996, 4, 335-349.
130. I. van der Veen and J. de Boer, *Chemosphere*, 2012, 88, 1119-1153.
131. H. M. Stapleton, S. Klosterhaus, A. Keller, P. L. Ferguson, S. van Bergen, E. Cooper, T. F. Webster and A. Blum, *Environ. Sci. Technol.*, 2011, 45, 5323-5331.
132. S.-Y. Lu and I. Hamerton, *Prog. Polym. Sci.*, 2002, 27, 1661-1712.
133. C.-Y. Sun, S. Dou, J.-Z. Du, X.-Z. Yang, Y.-P. Li and J. Wang, *Advanced Healthcare Materials*, 2014, 3, 261-272.
134. J. Zou, F. Zhang, S. Zhang, S. F. Pollack, M. Elsabahy, J. Fan and K. L. Wooley, *Advanced Healthcare Materials*, 2014, 3, 441-448.
135. C.-Y. Sun, Y.-C. Ma, Z.-Y. Cao, D.-D. Li, F. Fan, J.-X. Wang, W. Tao and X.-Z. Yang, *Acs Applied Materials & Interfaces*, 2014, 6, 22709-22718.
136. F. Zhang, S. Zhang, S. F. Pollack, R. Li, A. M. Gonzalez, J. Fan, J. Zou, S. E. Leininger, A. Pavia-Sanders, R. Johnson, L. D. Nelson, J. E. Raymond, M. Elsabahy, D. M. P. Hughes, M. W. Lenox, T. P. Gustafson and K. L. Wooley, *Journal of the American Chemical Society*, 2015, 137, 2056-2066.
137. Y.-C. Ma, J.-X. Wang, W. Tao, H.-S. Qian and X.-Z. Yang, *Acs Applied Materials & Interfaces*, 2014, 6, 16174-16181.
138. K. W. Li, W. Dang, B. M. Tyler, G. Troiano, T. Tihan, H. Brem and K. A. Walter, *Clin. Cancer. Res.*, 2003, 9, 3441-3447.
139. S. Zhang, J. Zou, M. Elsabahy, A. Karwa, A. Li, D. A. Moore, R. B. Dorshow and K. L. Wooley, *Chemical Science*, 2013, 4, 2122-2126.
140. Y. Hao, J. He, M. Zhang, Y. Tao, J. Liu and P. Ni, *Journal of Polymer Science Part a-Polymer Chemistry*, 2013, 51, 2150-2160.
141. H.-Q. Mao and K. W. Leong, *Non-Viral Vectors for Gene Therapy, 2nd Edition: Part 1*, 2005, 53, 275-306.
142. J. Wen, H. Q. Mao, W. P. Li, K. Y. Lin and K. W. Leong, *J. Pharm. Sci.*, 2004, 93, 2142-2157.
143. J. Wang, P. C. Zhang, H. Q. Mao and K. W. Leong, *Gene Ther.*, 2002, 9, 1254-1261.
144. T.-M. Sun, J.-Z. Du, L.-F. Yan, H.-Q. Mao and J. Wang, *Biomaterials*, 2008, 29, 4348-4355.
145. J. Xie, S. Lee and X. Chen, *Adv. Drug Deliv. Rev.*, 2010, 62, 1064-1079.
146. T. P. Gustafson, Y. H. Lim, J. A. Flores, G. S. Heo, F. Zhang, S. Zhang, S. Samarajeewa, J. E. Raymond and K. L. Wooley, *Langmuir*, 2014, 30, 631-641.

147. A. C. A. Wan, H.-Q. Mao, S. Wang, K. W. Leong, L. K. L. Ong and H. Yu, *Biomaterials*, 2001, 22, 1147-1156.
148. Y. Hacchou, T. Uematsu, O. Ueda, Y. Usui, S. Uematsu, M. Takahashi, T. Uchihashi, Y. Kawazoe, T. Shiba, S. Kurihara, M. Yamaoka and K. Furusawa, *J. Dent. Res.*, 2007, 86, 893-897.
149. D. S. W. Benoit, M. P. Schwartz, A. R. Durney and K. S. Anseth, *Nat Mater*, 2008, 7, 816-823.
150. Q. Li, J. Wang, S. Shahani, D. D. N. Sun, B. Sharma, J. H. Elisseeff and K. W. Leong, *Biomaterials*, 2006, 27, 1027-1034.
151. X. Z. Yang, T. M. Sun, S. Dou, J. Wu, Y. C. Wang and J. Wang, *Biomacromolecules*, 2009, 10, 2213-2220.
152. I. Teraoka, 2002.
153. W. Schärtl, *Light Scattering from Polymer Solutions and Nanoparticle Dispersions*, Springer Berlin Heidelberg, 2007.
154. B. J. Berne and R. Pecora, *Dynamic Light Scattering: With Applications to Chemistry, Biology, and Physics*, Dover Publications, 2000.
155. T. Cosgrove, *Colloid Science: Principles, Methods and Applications*, John Wiley & Sons, 2010.
156. M. Freeling and V. Walbot, *The Maize handbook*, Springer-Verlag, 1994.
157. W. Zhou and Z. L. Wang, *Scanning Microscopy for Nanotechnology: Techniques and Applications*, Springer, 2007.
158. D. B. Williams and C. B. Carter, *Transmission Electron Microscopy: A Textbook for Materials Science*, Springer, 2009.
159. L. Reimer and H. Kohl, *Transmission Electron Microscopy: Physics of Image Formation*, Springer, 2008.
160. C. S. S. R. Kumar, *Transmission Electron Microscopy Characterization of Nanomaterials*, Springer, 2013.
161. H. Förster, in *Characterization I*, eds. H. Karge and J. Weitkamp, Springer Berlin Heidelberg, 2004, vol. 4, pp. 337-426.
162. A. H. Kitai, *Solid State Luminescence: Theory, Materials, and Devices*, Chapman & Hall, 1993.
163. L. Mueller, *Journal of the American Chemical Society*, 1979, 101, 4481-4484.
164. A. Bax and M. F. Summers, *Journal of the American Chemical Society*, 1986, 108, 2093-2094.
165. W. Schoefberger, J. Schlagnitweit and N. Müller, in *Annual Reports on NMR Spectroscopy*, ed. A. W. Graham, Academic Press, 2011, vol. Volume 72, pp. 1-60.
166. K. Hatada and T. Kitayama, *NMR Spectroscopy of Polymers*, Springer, 2004.
167. W. S. Veeman and D. G. Cory, in *Advances in Magnetic and Optical Resonance*, ed. W. Warren S, Academic Press, 1989, vol. Volume 13, pp. 43-56.
168. V. I. Chizhik, Y. S. Chernyshev, A. V. Donets, V. Frolov, A. Komolkin and M. G. Shelyapina, *Magnetic Resonance and Its Applications*, Springer International Publishing, 2014.
169. V. L. Keedy, *OncoTargets Ther.*, 2012, 5, 153-159.
170. J. T. Buijs and G. van der Pluijm, *Cancer Lett.*, 2009, 273, 177-193.
171. G. A. Clines and T. A. Guise, *Expert Rev Mol Med*, 2008, 10, 1-16.
172. D. R. Clohisy and P. W. Mantyh, *Cancer*, 2003, 97, 866-873.
173. M. A. Lopez-Heredia, G. J. B. Kamphuis, P. C. Thune, E. C. Oner, J. A. Jansen and X. F. Walboomers, *Biomaterials*, 2011, 32, 5411-5416.
174. T. Tani, K. Okada, S. Takahashi, N. Suzuki, Y. Shimada and E. Itoi, *In Vivo*, 2006, 20, 55-60.

175. A. Spina, L. Sorvillo, F. Di Maiolo, A. Esposito, R. D'Auria, D. Di Gesto, E. Chiosi and S. Naviglio, *J. Cell. Physiol.*, 2013, 228, 198-206.
176. S. Magnetto, S. Boissier, P. D. Delmas and P. Clezardin, *Int J Cancer*, 1999, 83, 263-269.
177. T. H. Wang, H. S. Wang and Y. K. Soong, *Cancer*, 2000, 88, 2619-2628.
178. C. Luo, Y. Wang, Q. Chen, X. Han, X. Liu, J. Sun and Z. He, *Mini-Rev. Med. Chem.*, 2012, 12, 434-444.
179. H. Gelderblom, J. Verweij, K. Nooter and A. Sparreboom, *Eur. J. Cancer*, 2001, 37, 1590-1598.
180. A. Jager, D. Gromadzki, E. Jager, F. C. Giacomelli, A. Kozłowska, L. Kobera, J. Brus, B. Rihova, M. El Fray, K. Ulbrich and P. Stepanek, *Soft Matter*, 2012, 8, 4343-4354.
181. F. Danhier, N. Lecouturier, B. Vroman, C. Jerome, J. Marchand-Brynaert, O. Feron and V. Preat, *J. Control. Release*, 2009, 133, 11-17.
182. C. Fonseca, S. Simoes and R. Gaspar, *J. Control. Release*, 2002, 83, 273-286.
183. L. Mu and S. S. Feng, *Pharmaceutical Research*, 2003, 20, 1864-1872.
184. X. Jiang, H. Xin, J. Gu, X. Xu, W. Xia, S. Chen, Y. Xie, L. Chen, Y. Chen, X. Sha and X. Fang, *Biomaterials*, 2013, 34, 1739-1746.
185. S. S. Feng, L. Mu, K. Y. Win and G. F. Huang, *Curr. Med. Chem.*, 2004, 11, 413-424.
186. P. Lopez-Gasco, I. Iglesias, J. Benedi, R. Lozano, J. M. Teijon and M. D. Blanco, *J. Microencapsul.*, 2011, 28, 417-429.
187. L. Brannon-Peppas and J. O. Blanchette, *Adv. Drug Deliv. Rev.*, 2004, 56, 1649-1659.
188. F. C. J. van de Watering, P. Laverman, V. M. Cuijpers, M. Gotthardt, E. M. Bronkhorst, O. C. Boerman, J. A. Jansen and J. van den Beucken, *Biomed. Mater.*, 2013, 8.
189. M. Salerno, E. Cenni, C. Fotia, S. Avnet, D. Granchi, F. Castelli, D. Micieli, R. Pignatello, M. Capulli, N. Rucci, A. Angelucci, A. Del Fattore, A. Teti, N. Zini, A. Giunti and N. Baldini, *Curr. Cancer Drug Targets*, 2010, 10, 649-659.
190. S. W. Choi and J. H. Kim, *J Control Release*, 2007, 122, 24-30.
191. I. Ozcan, K. Bouchemal, F. Segura-Sanchez, O. Ozer, T. Guneri and G. Ponchel, *J Pharm Sci*, 2011, 100, 4877-4887.
192. D. Wang, S. Miller, M. Sima, P. Kopeckova and J. Kopecek, *Bioconjug Chem*, 2003, 14, 853-859.
193. S. Zhang, J. E. Wright, N. Ozber and H. Uludag, *Macromol Biosci*, 2007, 7, 656-670.
194. M. E. Davis, Z. Chen and D. M. Shin, *Nat. Rev. Drug Discov.*, 2008, 7, 771-782.
195. J. N. Yewle, D. A. Puleo and L. G. Bachas, *Bioconjugate chemistry*, 2011, 22, 2496-2506.
196. K. Aoki, N. Alles, N. Soysa and K. Ohya, *Advanced drug delivery reviews*, 2012, 64, 1220-1238.
197. A. Tautzenberger, A. Kovtun and A. Ignatius, *Int. J. Nanomedicine*, 2012, 7, 4545-4557.
198. E. Cenni, S. Avnet, D. Granchi, C. Fotia, M. Salerno, D. Micieli, M. G. Sarpietro, R. Pignatello, F. Castelli and N. Baldini, *Journal of biomaterials science. Polymer edition*, 2011.
199. P. Anderson, L. Kopp, N. Anderson, K. Cornelius, C. Herzog, D. Hughes and W. Hthh, *Expert Opin. Investig. Drugs*, 2008, 17, 1703-1715.
200. A. Bamias, E. Kastritis, C. Bamia, L. A. Mouloupoulos, L. Melakopoulos, G. Bozas, V. Koutsoukou, D. Gika, A. Anagnostopoulos, C. Papadimitriou, E. Terpos and M. A. Dimopoulos, *J. Clin. Oncol.*, 2005, 23, 8580-8587.
201. S. Y. Zhang, A. Li, J. Zou, L. Y. Lin and K. L. Wooley, *ACS Macro Lett.*, 2012, 1, 328-333.

202. A. Musyanovych, J. Schmitz-Wienke, V. Mailander, P. Walther and K. Landfester, *Macromol. Biosci.*, 2008, 8, 127-139.
203. H. Mutlu, L. M. de Espinosa and M. A. R. Meier, *Chem. Soc. Rev.*, 2011, 40, 1404-1445.
204. T. Steinbach, Johannes Gutenberg-Universität Mainz, 2014.
205. R. W. Wagner and J. S. Lindsey, *Pure Appl. Chem.*, 1996, 68, 1373-1380.
206. K. Allen and D. Cornforth, *J. Food Sci.*, 2009, 74, C375-C379.
207. E. De Kort, M. Minor, T. Snoeren, T. Van Hooijdonk and E. Van Der Linden, *Dairy Sci. Technol.*, 2009, 89, 283-299.
208. C. Rulliere, L. Perenes, D. Senocq, A. Dodi and S. Marchesseau, *Food Chem.*, 2012, 134, 712-716.
209. M. P. Ginebra, C. Canal, M. Espanol, D. Pastorino and E. B. Montufar, *Adv Drug Deliv Rev*, 2012, 64, 1090-1110.
210. G. Daculsi, F. Jegoux and P. Layrolle, in *Advanced Biomaterials*, John Wiley & Sons, Inc., 2010, pp. 101-141.
211. O. Gauthier, E. Goyenvalle, J. M. Bouler, J. Guicheux, P. Pilet, P. Weiss and G. Daculsi, *J. Mater. Sci.-Mater. Med.*, 2001, 12, 385-390.
212. O. Gauthier, J. M. Bouler, E. Aguado, P. Pilet and G. Daculsi, *Biomaterials*, 1998, 19, 133-139.
213. J. Baran and S. Penczek, *Macromolecules*, 1995, 28, 5167-5176.
214. K. Schmidt-Rohr, J. Clauss and H. W. Spiess, *Macromolecules*, 1992, 25, 3273-3277.
215. D. L. Vanderhart, *J. Magn. Reson.*, 1981, 44, 117-125.
216. R. Sauer, P. Froimowicz, K. Scholler, J. M. Cramer, S. Ritz, V. Mailander and K. Landfester, *Chem.-Eur. J.*, 2012, 18, 5201-5212.
217. K. Schoeller, A. Ethirajan, A. Zeller and K. Landfester, *Macromolecular Chemistry and Physics*, 2011, 212, 1165-1175.
218. R. T. Liggins, W. L. Hunter and H. M. Burt, *J. Pharm. Sci.*, 1997, 86, 1458-1463.
219. Z. P. Zhang, L. Mei and S. S. Feng, *Expert Opin. Drug Deliv.*, 2013, 10, 325-340.
220. L. Mu and S. S. Feng, *J. Controlled Release*, 2003, 86, 33-48.
221. D. Hofmann, C. Messerschmidt, M. Bannwarth, K. Landfester and V. Mailander, *Chem. Commun.*, 2013, DOI: 10.1039/C1033CC48130A.
222. J. Zhou, Q. Liu, W. Feng, Y. Sun and F. Li, *Chem. Rev.*, 2014.
223. R. Y. Tsien, *Annu. Rev. Biochem.*, 1998, 67, 509-544.
224. X. Michalet, F. F. Pinaud, L. A. Bentolila, J. M. Tsay, S. Doose, J. J. Li, G. Sundaresan, A. M. Wu, S. S. Gambhir and S. Weiss, *Science*, 2005, 307, 538-544.
225. Y. Li, S. Zhou, G. Dong, M. Peng, L. Wondraczek and J. Qiu, *Sci. Rep.*, 2014, 4.
226. T. W. Schmidt and F. N. Castellano, *The Journal of Physical Chemistry Letters*, 2014, 5, 4062-4072.
227. T. N. Singh-Rachford and F. N. Castellano, *Coord. Chem. Rev.*, 2010, 254, 2560-2573.
228. T. N. Singh-Rachford, J. Lott, C. Weder and F. N. Castellano, *Journal of the American Chemical Society*, 2009, 131, 12007-12014.
229. J.-H. Kim and J.-H. Kim, *Journal of the American Chemical Society*, 2012, 134, 17478-17481.
230. Q. Liu, B. Yin, T. Yang, Y. Yang, Z. Shen, P. Yao and F. Li, *Journal of the American Chemical Society*, 2013, 135, 5029-5037.
231. D. Busko, Johannes Gutenberg-Universität Mainz, 2013.
232. A. J. Svagan, D. Busko, Y. Avlasevich, G. Glasser, S. Balushev and K. Landfester, *Acs Nano*, 2014, 8, 8198-8207.
233. C. Wohnhaas, Johannes Gutenberg-Universität Mainz, 2012.

234. P. Duan, N. Yanai and N. Kimizuka, *Journal of the American Chemical Society*, 2013, 135, 19056-19059.
235. Q. Liu, B. Yin, T. Yang, Y. Yang, Z. Shen, P. Yao and F. Li, *Journal of the American Chemical Society*, 2013, 135, 5029-5037.
236. C. Aulin, M. Gällstedt and T. Lindström, *Cellulose*, 2010, 17, 559-574.
237. A. A. Earp, T. Rawling, J. B. Franklin and G. B. Smith, *Dyes and Pigments*, 2010, 84, 59-61.
238. C. E. Diaz-Uribe, M. C. Daza, E. A. Páez-Mozo, F. Martínez O, C. L. B. Guedes and E. Di Mauro, *J. Photochem. Photobiol. A: Chem.*, 2013, 259, 47-52.
239. C. Schweitzer and R. Schmidt, *Chem. Rev.*, 2003, 103, 1685-1758.
240. M. A. Oar, W. R. Dichtel, J. M. Serin, J. M. J. Fréchet, J. E. Rogers, J. E. Slagle, P. A. Fleitz, L.-S. Tan, T. Y. Ohulchanskyy and P. N. Prasad, *Chem. Mater.*, 2006, 18, 3682-3692.
241. M. J. Steinbeck, A. U. Khan and M. J. Karnovsky, *J. Biol. Chem.*, 1993, 268, 15649-15654.
242. H. H. Wasserman, J. R. Scheffer and J. L. Cooper, *Journal of the American Chemical Society*, 1972, 94, 4991-4996.
243. N. J. Turro and M. F. Chow, *Journal of the American Chemical Society*, 1981, 103, 7218-7224.
244. T. H. Ngo and A. Schumpe, *International Journal of Chemical Engineering*, 2012, 2012, 7.
245. C.-S. Chu and Y.-L. Lo, *Sensors Actuators B: Chem.*, 2007, 124, 376-382.
246. H. C. Kolb, M. G. Finn and K. B. Sharpless, *Angewandte Chemie International Edition*, 2001, 40, 2004-2021.
247. S. Ding, G. Jia and J. Sun, *Angew. Chem. Int. Ed.*, 2014, 53, 1877-1880.
248. D. S. Pedersen and A. Abell, *Eur. J. Org. Chem.*, 2011, 2011, 2399-2411.
249. G. C. Tron, T. Pirali, R. A. Billington, P. L. Canonico, G. Sorba and A. A. Genazzani, *Medicinal Research Reviews*, 2008, 28, 278-308.
250. E. Lallana, A. Sousa-Herves, F. Fernandez-Trillo, R. Riguera and E. Fernandez-Megia, *Pharmaceutical Research*, 2012, 29, 1-34.
251. J. A. Opsteen and J. C. M. van Hest, *Chemical Communications*, 2005, 57-59.
252. W. H. Binder and R. Sachsenhofer, *Macromolecular Rapid Communications*, 2008, 29, 952-981.
253. D. Fournier, R. Hoogenboom and U. S. Schubert, *Chemical Society Reviews*, 2007, 36, 1369-1380.
254. R. Huisgen, *Angewandte Chemie International Edition in English*, 1963, 2, 633-645.
255. V. V. Rostovtsev, L. G. Green, V. V. Fokin and K. B. Sharpless, *Angewandte Chemie International Edition*, 2002, 41, 2596-2599.
256. C. W. Tornøe, C. Christensen and M. Meldal, *The Journal of Organic Chemistry*, 2002, 67, 3057-3064.
257. L. Zhang, X. Chen, P. Xue, H. H. Y. Sun, I. D. Williams, K. B. Sharpless, V. V. Fokin and G. Jia, *Journal of the American Chemical Society*, 2005, 127, 15998-15999.
258. J. F. Lutz, *Angewandte Chemie-International Edition*, 2008, 47, 2182-2184.
259. C. R. Becer, R. Hoogenboom and U. S. Schubert, *Angewandte Chemie-International Edition*, 2009, 48, 4900-4908.
260. N. J. Agard, J. A. Prescher and C. R. Bertozzi, *Journal of the American Chemical Society*, 2004, 126, 15046-15047.
261. S. Sawoo, P. Dutta, A. Chakraborty, R. Mukhopadhyay, O. Bouloussa and A. Sarkar, *Chemical Communications*, 2008, 5957-5959.
262. H. Li, J. Wang, J. Z. Sun, R. Hu, A. Qin and B. Z. Tang, *Polymer Chemistry*, 2012, 3, 1075-1083.

263. S. S. van Berkel, A. J. Dirks, S. A. Meeuwissen, D. L. L. Pingen, O. C. Boerman, P. Laverman, F. L. van Delft, J. J. L. M. Cornelissen and F. P. J. T. Rutjes, *ChemBioChem*, 2008, 9, 1805-1815.
264. K. Landfester, *Angewandte Chemie International Edition*, 2009, 48, 4488-4507.
265. L. Wang, Y. Song, R. Gyanda, R. Sakhuja, N. K. Meher, S. Hanci, K. Gyanda, S. Mathai, F. Sabri, D. A. Ciaramitaro, C. D. Bedford, A. R. Katritzky and R. S. Duran, *Journal of Applied Polymer Science*, 2010, 117, 2612-2621.
266. H. Schlaad, H. Kukula, J. Rudloff and I. Below, *Macromolecules*, 2001, 34, 4302-4304.
267. A. Jerschow and N. Müller, *Journal of Magnetic Resonance, Series A*, 1996, 123, 222-225.
268. A. Jerschow and N. Müller, *J. Magn. Reson.*, 1997, 125, 372-375.
269. M. Holz and H. Weingartner, *Journal of Magnetic Resonance (1969)*, 1991, 92, 115-125.
270. J. E. Tanner, *J. Chem. Phys.*, 1970, 52, 2523-&.
271. C. Tonhauser, A. Alkan, M. Schömer, C. Dingels, S. Ritz, V. Mailänder, H. Frey and F. R. Wurm, *Macromolecules*, 2013, 46, 647-655.
272. X. Liu, P. Du, L. Liu, Z. Zheng, X. Wang, T. Joncheray and Y. Zhang, *Polym. Bull.*, 2013, 70, 2319-2335.
273. Q. Gu, C. Bravo-Díaz and L. S. Romsted, *Journal of Colloid and Interface Science*, 2013, 400, 41-48.
274. L. S. Romsted and C. Bravo-Díaz, *Current Opinion in Colloid & Interface Science*, 2013, 18, 3-14.
275. J. B. F. N. Engberts, E. Fernández, L. García-Río and J. R. Leis, *The Journal of Organic Chemistry*, 2006, 71, 6118-6123.
276. M. Corredor, J. Bujons, A. Messeguer and I. Alfonso, *Organic & Biomolecular Chemistry*, 2013, 11, 7318-7325.
277. U. El-Jaby, M. Cunningham and T. F. L. McKenna, *Macromol. Chem. Phys.*, 2010, 211, 1377-1386.
278. G. Yi, L. T. Victoria, S. R. S. Ting and B. Z. Per, *Polymer Journal*, 2012, 44, 375-381.
279. C. R. van den Brom, M. Wagner, V. Enkelmann, K. Landfester and C. K. Weiss, *Langmuir*, 2010, 26, 15794-15801.
280. C. R. van den Brom, N. Vogel, C. P. Hauser, S. Goerres, M. Wagner, K. Landfester and C. K. Weiss, *Langmuir*, 2011, 27, 8044-8053.
281. U. El-Jaby, M. Cunningham and T. F. L. McKenna, *Macromol. Rapid Commun.*, 2010, 31, 558-562.
282. H. Kricheldorf, *Polycondensation: History and New Results*, Imprint: Springer, 2013.
283. M. E. Edward and S. D. Rittler, Google Patents, 1955.
284. K. P. Lee, T. C. Arnot and D. Mattia, *J. Membr. Sci.*, 2011, 370, 1-22.
285. B.-H. Jeong, E. M. V. Hoek, Y. Yan, A. Subramani, X. Huang, G. Hurwitz, A. K. Ghosh and A. Jawor, *J. Membr. Sci.*, 2007, 294, 1-7.
286. Y. Zhang and D. Rochefort, *J. Microencapsulation*, 2012, 29, 636-649.
287. W. Lai, X. Li, H. Liu, L. Han, Y. Zhao and X. Li, *Journal of Chemistry*, 2014.
288. H. Zhang, S. Sun, X. Wang and D. Wu, *Colloids and Surfaces a-Physicochemical and Engineering Aspects*, 2011, 389, 104-117.
289. S. S. Dhumal, S. J. Wagh and A. K. Suresh, *J. Membr. Sci.*, 2008, 325, 758-771.
290. C. V. Iancu, W. F. Tivol, J. B. Schooler, D. P. Dias, G. P. Henderson, G. E. Murphy, E. R. Wright, Z. Li, Z. Yu, A. Briegel, L. Gan, Y. He and G. J. Jensen, *Nat. Protocols*, 2007, 1, 2813-2819.

291. M. Richards, B. I. Dahiyat, D. M. Arm, S. Lin and K. W. Leong, *J. Polym. Sci., Part A: Polym. Chem.*, 1991, 29, 1157-1165.
292. K. Landfester, A. Musyanovych and V. Mailander, *Journal of Polymer Science Part a-Polymer Chemistry*, 2010, 48, 493-515.
293. U. Paiphansiri, J. Dausend, A. Musyanovych, V. Mailander and K. Landfester, *Macromol. Biosci.*, 2009, 9, 575-584.
294. J. X. Guo, Q. H. Pan, C. Huang, Y. B. Zhao, X. B. Ouyang, Y. H. Huo and S. S. Duan, *J. Wuhan Univ. Technol.-Mat. Sci. Edit.*, 2009, 24, 1004-1006.
295. Z. Wang, E. Han and W. Ke, *Surf. Coat. Technol.*, 2006, 200, 5706-5716.
296. S. Elbasuney and H. E. Mostafa, *Particuology*.
297. O. Kühl, *Phosphorus-31 NMR Spectroscopy: A Concise Introduction for the Synthetic Organic and Organometallic Chemist*, Springer Berlin Heidelberg, 2008.
298. M. L. Nielsen, J. V. Pustinger and J. Strobel, *J. Chem. Eng. Data*, 1964, 9, 167-170.
299. S. V. Fridland, M. N. Miftakhov and V. P. Arkhipov, *Zh. Obshch. Khim.*, 1987, 57, 1518-1526.
300. G. Baier, A. Baki, S. Tomcin, V. Mailander, E. Alexandrino, F. Wurm and K. Landfester, *Macromolecular Symposia*, 2014, 337, 9-17.